Author:
Williams, Stephen Michael

Title:
The condition monitoring of damaged steel structures.

The Condition Monitoring of Damaged Steel Structures

By

Stephen Michael Williams

A thesis submitted to the University of Bristol in accordance with the requirements of the degree of Doctor of Philosophy in the faculty of Engineering. The work was performed in the Department of Civil Engineering between October 1993 and October 1996 and the thesis submitted in April 1997.

Abstract

This thesis describes research aimed at the development of methods of identifying hidden corrosion damage in structural steelwork. It was inspired by a need to improve methods of inspection for support structures at an ICI manufacturing works.

A review of non-destructive testing methods for steel structures was conducted. This concluded that a method which measured the local stiffness, the coin-tap test, was suitable. The test was advanced by introducing two new techniques to detect damage from the impulse time history: (a) the computation of either the peak impulse force divided by the total area enclosed by the impulse or the area enclosed by the impulse over an interval centred on it divided by the total area enclosed by the impulse, as measures for identifying local stiffness change; (b) the inspection of the time history for changes in structural vibration ('ringing') as a measure for identifying changes in local damping.

A review of selected methods of pattern recognition for automatic classification of dynamic waveforms was then presented. This introduced the back-propagation neural network, for situations where structures in known conditions were available for training, and the Probabilistic Resource Allocating Network (PRAN), for classifying structures whose condition was not known.

The techniques described were used to detect corrosion damage in a bolted steelwork joint, tensile wire rope, splice plates on the Clifton Suspension Bridge, and between a chequer plate floor and its supporting beam. In each case it was possible to identify corrosion deterioration by the characteristic changes in the waveforms produced by increase in damping or reduction in stiffness.

The study has shown that the coin-tap test is an effective diagnostic tool for identifying corrosion damage in structural steelwork. The PRAN proved to be a valuable method of classifying waveforms automatically when no reference structures were available. A self-contained corrosion monitoring system consisting of coin-tap test apparatus and the pattern recognition algorithms is proposed for on-line inspection.

Acknowledgements

I would like to acknowledge the support of the Department of Civil Engineering at the University of Bristol. I am indebted to Dr. J. W. Smith, my advisor, for the opportunity to pursue this course of study, for guidance and for encouraging me by being positive. Special thanks are also due to Dr. C. Campbell, for sparing time to answer my queries on pattern recognition and Dr. A. Vann, for introducing me to computer pattern recognition by neural networks. Among the technical staff special thanks are due to Mr. Peter Whereat and Mr. Alan Young, who were always friendly and willing to help.

Among my student colleagues special thanks are due to Mr. Arnold Niko, University of Graz, Austria, for sending correspondence, Mr. Reza Ragohzar for sparing time to answer my queries, and Mrs. Zhouhua Lu (Minnie), for sparing time to answer my queries and for allowing me to use her fast computer without which I wouldn't have finished on time. I would also like to thank Reza and especially Minnie for being colleagues I could confide in and for being my friends when it mattered most. Thanks also to Mr. Wang Tat Yeung and Mr. Ali Mafinjad for their work on the wire rope and their co-operation.

I would like to thank the EPSRC for providing financial support for and regular up-to-date information on courses in neural networks.

Among those involved in the on-site tests I would like to thank Mr. Mike Gallon of ICI Engineering for arranging the site visits, Mr. Mike Harvey of ICI Severnside for kindly assisting me with the experimental work and Mr. Ken Williams and Mr. John Mitchell, bridgemasters at the Clifton Suspension Bridge (Bristol), for assisting during the testing.

I would also like to express gratitude to the members of my family, especially Mr. Wayne Williams, my brother, for being a good listener and offering opinion and reassurance, Master Jermaine Williams, my nephew, for calling me on weekends about his football matches and Mrs. Geraldine Williams and Mr. Denis Williams, my mum and dad, for being my role models and for they're love and support without which I would not have found the incentive to complete this work.

Dedication

To my Parents:

Mr. Denis Williams

Mrs. Geraldine Avis Williams

Declaration

I declare that unless otherwise cited in the text, the work contained in this thesis is my own original work. The views expressed in this dissertation are those of the author and not of the University of Bristol.

The following papers are based on the work described in this thesis

1. Williams S. M and Smith J. W (1996)
   Identification of Corrosion Damage in Bolted Joints Using an Intelligent Tap Test. International Conference on Identification in Engineering Systems, University of Wales, Swansea, pp 77-86.

2. Smith J. W and Williams S. M (1997)
   Discussion on Paper 'An Introduction to Neural Computing for the Structural Engineer by Prof. W. M. Watkins, The Structural Engineer, Volume 75 Number 3, pp 38-41, 1997'. Submitted 28 February 1997.

Signed S. Williams.....

Date...4th...June...1997.....

Table of Contents

CHAPTER THREE

Review of Dynamic Methods

CHAPTER FOUR

The Coin-tap Test

List of Figures

List of Tables

Notation

English

A	Area under spectrum between 0 Hz and threshold frequency, area under impulse between defined limits, cross-sectional area.
B	Area under spectrum between threshold and maximum frequency.
c	Coefficient of damping, half-width of time interval for ratio of areas under impulse.
d	Distance, diameter, dimension of force and response vectors.
E	Young's modulus, error function in back-propagation neural network.
U	Total energy transferred during linear elastic collision, strain energy.
U_i	Output of second layer unit i in back-propagation neural network.
f	Force.
$H(j\omega)$	Frequency response function.
$h(\tau)$	Impulse response function.
h	Total signal received by a processing unit in a neural network.
j	Square root of -1.
k	Coefficient of stiffness.
k_c	Contact Stiffness.
k_d	Defect Stiffness.
L	Length.
L_1	Length of first section of rope divided into parts.
L_2	Length of second section of rope divided into parts.
m	Coefficient of mass, hammer mass.
N	Number of components in feature vector.
$p(C_q\|\xi)$	Posterior probability that feature vector ξ belongs to class C_q.
$p(\xi \mid C_q)$	Conditional probability density of feature vector ξ given that it belongs to class C_q.
$p(\xi)$	Probability distribution of feature vectors ξ.
$p(C_q)$	Prior probability of membership of class C_q.

C_q	Class number q.
$P(t)$	Impulsive force (internal to system).
P_{max}	Peak impulse force.
$P(\omega)$	Frequency spectrum of impulse force.
R_f	Ratio of fixed area under impulse or impulse height to total area under impulse (in the time domain).
R_t	Ratio of two areas under spectrum in the frequency domain.
r	Radius.
s	Seconds, Laplace variable, standard deviation.
T	Total posterior response for a PRAN unit over all feature vectors, tension.
v	Velocity.
V_j	Processing unit j in output layer of back-propagation neural network.
W_{jk}	Weight on interconnection between unit j in following layer and unit k in preceding layer.
w_{jk}	Weight on interconnection between unit j in following layer and preceding input distribution component k.

Greek

ω	Angular frequency variable.
τ	Time domain for impulse response function.
τ_i	Duration of impulse force or half period of sine wave.
τ_α	Constant for computation of adaption parameter in PRAN unit.
η	Learning rate for back-propagation neural network.
η_n	Hysteretic damping factor for the nth mode.
δ	Displacement at a point on the structure.
ξ	Feature vector from sampled waveform.
θ	Activation function for back-propagation neural network, angle in radians.
Φ	Phase of spectrum relative to input force.

α	Meaning 'is proportional to' or 'has the form of', momentum constant in back-propagation neural network.
β	Constant that controls the shape of the sigmoid function in a back-propagation neural network unit.
α_κ	Adaption parameter for unit *k* in PRAN.
ν	Frequency.
ν_B	Maximum analysis frequency (bandwidth).
ν_{fol}	Folding or Nyquist frequency.
ν_t	Threshold frequency in ratio of areas under spectrum calculation.
ν_{max}	Maximum frequency in ratio of areas under spectrum calculation.
ν_s	Sampling frequency.
μ	Mean.

<u>Vectors and Matrices</u>

C	Damping matrix (square).
$\boldsymbol{H}$	Horizontal reaction force.
M	Mass matrix (square).
K	Stiffness matrix (square).
$\boldsymbol{O}$	Neural network output vector.
$\boldsymbol{P}$	Point load vector.
$\boldsymbol{T}$	Back-propagation network target vector.
V_A	Vertical reaction force.
$\delta(t)$	Displacement response vector (column).
$\delta(j\omega)$	Fourier transform of displacement response vector.
$f(t)$	Input force vector (external to system).
$f(j\omega)$	Fourier transform of input force vector (external to system).
$\boldsymbol{F}$	Vector representing the variance of a Gaussian function.
$\boldsymbol{m}$	Vector representing the mean of a Gaussian function.
σ	Vector representing the standard deviation of a Gaussian function.

Abbreviations

ASM	American Society for Metals.
ASTM	American Society for Testing and Materials.
ATM	Adaptive template matching.
dB	Decibel.
DFT	Discreet Fourier Transform.
DLAC	Damage location assurance criterion.
EPSRC	Engineering and Physical Sciences Research Council.
eqn.	Equation.
FEM	Finite element model.
FFT	Fast Fourier transform.
FM	Frequency Modulation.
FRF	Frequency response function.
ICI	Imperial Chemical Industries.
ICP	Integrated circuit pre-amplifier.
KBS	Knowledge based systems.
K-nn	K-nearest neighbour.
LHS	Left-hand side (of equation).
Lbf	Pound force.
MAC	Modal assurance criterion.
MDOF	Multi-degree of freedom system.
NDT	Non-destructive testing.
NDE	Non-destructive evaluation.
NM	Nearest mean.
PC	Personal Computer.
PCA	Principal Component Analysis.
PRA/N	Probabilistic Resource Allocating /Network.
RBF	Radial basis function network.
RHS	Right-hand side (of equation).
RMS	Root mean square.
RUS	Resonant ultrasound.

SAC	Signature assurance criterion.
SDOF	Single degree of freedom.
s.f.	Significant figures.
SNR	Signal to noise ratio.
Tr	Trace of a matrix (sum of the diagonal components)
UDM	Uniform distributed load.
WCC	Waveform chain code.
WEM	Weighted error matrix.

1. INTRODUCTION

The condition of all steel structures is subject to decay with time, due to various factors. The first is the environment. Parts of the structure exposed to wind and rain or in which water or dirt may become trapped will eventually begin to corrode. Another factor is fatigue. This is the growth of microscopic cracks in parts of a structure due to repeated loading as in bridges. Condition monitoring is concerned with methods of detecting structural decay so as to prevent substantial failure. The objective of this project was to investigate condition monitoring of damaged steel structures by methods of non-destructive testing (NDT). It was inspired by the specific problem of corrosion damage in structural steelwork used in the petro-chemical industry.

In the petro-chemical industry steel is the primary material used for both process equipment and support structures. Condition monitoring of process equipment such as vessels and piping is a diverse field. Recent trends in NDT have been reviewed by De Bruyn (1996). Although some of these techniques may be relevant, this study focuses on the problem of monitoring corrosion in structural steelwork used for the *support* of such equipment. Furthermore, the study proposes some advances in methods of manual field measurement. It does not address the issues of continuous condition monitoring (Moss and Matthews, 1995) although methods of data interpretation may be relevant.

For petro-chemical structural steelwork the environment is the main cause of decay. Steelwork is exposed to the weather as well as to corrosive fumes and salty air (chemical works are frequently located at coastal sites) and there are also parts of structures` that can trap dirt and moisture. Figure 1.1 shows a support beam severely corroded by fumes and moisture in the air of a chemical storage shed. Whilst the industrial environment has become cleaner in recent years many structures are more than 50 years old and the combination of age and aggressive environment means that maintenance and repair has become very expensive. For example, the recent structural refurbishment, shown in Figure 1.2, of a pipe-bridge at an ICI chemical works was reported to cost £25 million (Gallon, 1993). Therefore the detection of structural decay is important for safety and for maintaining production and is also a cost-effective preventative measure.

Figure 1.1. Support Beam Severely Corroded by Chemical Fumes in a Storage Shed

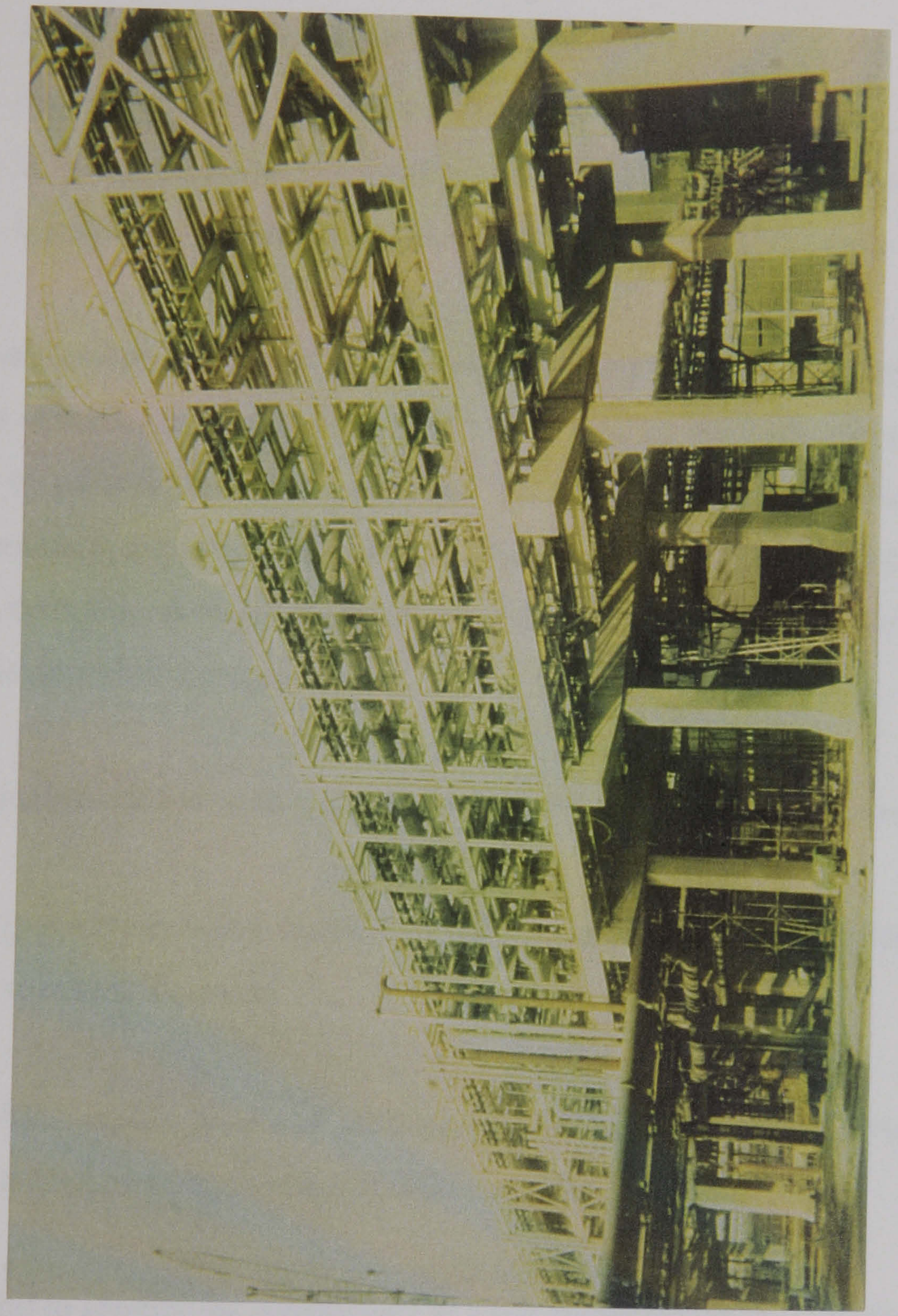

Figure 1.2. Rebuilt Section of a Chemical Works Pipebridge

Visual inspection is the primary method of inspection in the petro-chemical industry. It is satisfactory for detecting substantial corrosion that is not concealed. No specialist equipment is necessary and there is considerable experience of this approach. ICI engineering use four visual categories (ICI, 1990[1] and ICI, 1990[2]) which can be abbreviated as follows:

i) paint intact and no sub-surface corrosion

ii) paint intact but signs of loss of section or scale

iii) paint system broken down as well as insignificant (less than 15%) section loss

iv) significant section loss (more than 15%) or holing, member loss or distortion.

There are several limitations to this current approach. Assessment may not be possible in regions of steelwork that do not permit easy access for the inspector or where the damage is hidden by paint or protective coverings. Furthermore, different individuals may classify the same region of steelwork differently and there is a limit to the resolution of defect size that can be detected. A requirement therefore exists for a non-subjective method of detecting invisible corrosion damage.

The objectives of this work were therefore three-fold and are as follows:

i) to explore viable methods of NDT suitable for detecting hidden corrosion in structural steelwork

ii) to explore the use of intelligent computing methods with a view to the automatic categorisation of field test data

iii) to identify the components of a self-contained, on-line monitoring system for detecting corrosion damage in steel structures.

To achieve this, a review of established NDT methods suitable for steel structures was conducted and these are discussed in Chapter 2. The methods which emerge as showing the greatest potential in this application are described in Chapter 3 which is concerned with

dynamic methods. The requirements of the ideal dynamic method for this application are also identified and described in detail in Chapter 4, which is on the coin-tap test. In Chapter 5 selected techniques in pattern recognition by computer are reviewed with the emphasis on methods suitable for the classification of dynamic NDT data. In Chapter 6 selected methods of pattern recognition are combined with the coin-tap test for the non-destructive testing and automatic classification of test data from two examples of jointed metal structures: a small bolted steel frame and a riveted iron bridge. This exercise is followed up in Chapter 7 by applying the methods to steel wire rope under tension and I-sections under chequer plating. The findings of this study are discussed in Chapter 8 and concluded in Chapter 9.

2. REVIEW OF METHODS OF NON-DESTRUCTIVE TESTING

2.1. Introduction

The literature on non-destructive testing of steel structures is voluminous. It may be classified broadly as follows:

i) methods for examining the quality of manufacture or fabrication, in particular welds of pressure vessels

ii) methods for detecting propagating cracks in structures in service e.g. fatigue cracks in cranes, steel offshore jackets and bridges

iii) methods for general condition assessment i.e. to detect if the structural condition has changed without necessarily focusing on the cause.

In the main this project is concerned with the third group of methods although techniques from (i) and (ii) may be relevant.

There is an abundance of NDT methods in existence. An extensive survey was given by Iffland and Birnstiel (1993). A short review of NDT methods for welded structural steelwork is given in Burdekin (1993) and a review of methods suitable for wire ropes is given in Weischedel (1988). Reviews of recent research work in each field can be found in editions of the British Journal of NDT.

The methods described in the following sections are considered to be relevant to steel structures. Methods that do not involve the exchange of energy between the structure and the testing instrument are generally capable of detecting superficial damage only. These 'passive' methods include visual inspection, liquid penetrant inspection and magnetic particle inspection. Those which do involve the exchange of some energy are capable of detecting damage at various depths in the material depending on the method under

consideration. These 'active' methods of testing include electromagnetic, eddy current, electrical resistance, radiographic, acoustic emission and ultrasonic.

Each of the methods will be discussed in the following sections with a view towards the adoption and development of a method capable of improving the ability to detect corrosion damage in structural steelwork.

2.2. Visual Inspection

This is probably the most widely used NDT method for the inspection of steel structures and assemblies, for quality control and in the field. It is usually used to give an initial appraisal before a more detailed examination by another method.

In the petro-chemical industry, steelwork supporting process equipment is visually inspected and categorised on a regular basis. The procedure also involves the removal of surface layers for detailed inspection where corrosion damage is suspected underneath. In the field of production quality control, visual inspection is used for assessing the quality of welds. The external profile can reveal information concerning the welding process used, as well as the presence of various types of flaw. The results of visual inspection are recorded on a report form.

However, there are several limitations to the use of visual inspection as the only method of structural examination. Visual inspection is inherently subjective because it relies on the judgement of different individuals and one inspector may spot something that another does not or may classify the same fault differently. Furthermore, as there is a limit to the resolution of the eye, there is an associated limit to the size of defect that can be detected. This places a restriction on how early it is possible to detect potentially critical damage. The condition monitoring of support steelwork in the petro-chemical industry presents further specific problems. The first is the inability to inspect regions with poor accessibility. This is a common problem at petro-chemical sites where I-sections can be hidden under chequer plate flooring, or truss joints may be hidden behind concrete fireproofing. Another

common problem is the inability to see corrosion that is hidden by paint or concealed between the interfaces of a joint.

These limitations are clearly difficult to minimise. In the absence of an obvious way of improving the performance of visual inspection in the present application, it was decided to explore the possible use of other methods.

2.3. Liquid Penetrant Inspection

This method is also known as dye penetrant inspection. In this technique a thin coat of penetrant is applied to the cleaned metal surface allowing sufficient time for it to be absorbed into the cracks. The excess liquid is then cleaned off and a developer is applied which draws the absorbed liquid from the cracks. The location of the cracks can be found by visual inspection because the penetrant has a dye or fluorescent material dissolved in it. The effectiveness of the method depends on the ability of the liquid penetrant to wet the testing surface.

Liquid penetrant inspection is frequently used to inspect the quality of manufacture. It works best on structures that have exposed and accessible surfaces such as turbine blades (e.g. Glazkov, 1993), castings, jet engine frames, turbines and circular saw blades. It is probably the simplest and cheapest of NDT methods. It can be used on both ferromagnetic and non-ferromagnetic surfaces and could conceivably be used to detect the microscopic cracks in painted steelwork that lead to corrosion.

However, corrosion damage in structural steelwork tends to be concentrated in moisture traps such as joints, equipment supports and under chequer plate flooring (Gallon, 1993) and in these cases it would be difficult to apply the method which as previously mentioned works best on exposed surfaces. For this reason the technique was not considered further for this study. Further information on this technique can be found in ASTM (1983) and ASM (1976).

2.4. Magnetic Particle Inspection

This method works on the principle that when a magnetic field is applied to the surface of a ferromagnetic material, discontinuities that lie transverse to the field direction will cause a leakage field. Small particles of ferromagnetic material spread over the surface become aligned with the magnetic field, and discontinuities at or near the surface can be identified because they are found at the locations of the field leakage.

Magnetic effects, historically speaking, were the first to be used for the non-destructive testing of quality standards. As early as 1868 Saxby of the Institute of Naval Architects made use of a compass to detect defects and inhomogeneity in cannon tubes. The use of iron filings for the detection of cracks in steel parts results from an observation first made by chance by Hoke in the USA in 1917, and later patented in 1919 (Dobmann and Höller, 1980).

Magnetic particle inspection is extensively used to inspect for cracks in heavy goods vehicle's sub-structures, railway tracks, airframes, plant machinery, crane hooks and steam turbines. The method is a sensitive means of detecting shallow and surface breaking cracks and discontinuities. There is little or no limitation on the size or shape of the part being examined and no elaborate pre-cleaning is necessary as cracks filled with foreign material can still be detected. It is also one of the simplest and cheapest methods of non-destructive testing.

However, the sensitivity of magnetic particle inspection is drastically reduced by a thin non-ferromagnetic coating such as paint. Structural steelwork at ICI chemical sites is regularly painted as part of routine maintenance (Gallon, 1993) and because water can collect underneath damaged paintwork there exists a need to detect corrosion that develops in this way. Therefore this renders magnetic particle inspection unsuitable for this application. Further information on the use of this method for inspecting wire ropes can be found in Winchester (1991). General information may be found in ASTM (1985) and ASM (1976).

2.5. Electromagnetic Inspection

Electromagnetic inspection, also known as the magneto-inductive method, is a method based on magnetism in which the field that magnetises the specimen is derived from an electric current passed through it. The magnetic field is only capable of penetrating to a shallow depth in steel and this determines the maximum depth at which a fault may be detected. Any regions at or near the surface where the composition of the structure being tested changes, or which contains faults, will alter the local magnetic permeability and this in turn produces a leakage field. This leakage field can be detected by the changes in current of a 'probe' circuit that is moved within the external field.

This method represents an advancement on magnetic particle inspection in two respects: firstly the use of an internal electric current as opposed to an external permanent magnet to generate the magnetic field was introduced by Deforest in 1929; and secondly the magnetic particles were replaced by very small field sensitive probes by Förester in 1938 to 1939.

Electromagnetic inspection is commonly used in quality control to sort steels on the basis of chemical composition, hardness, residual stresses, case depth and condition of heat treatment. It can also be used to detect cracks and discontinuities in the surface of ferromagnetic materials.

Compared with conventional physical tests and methods of chemical analysis, electromagnetic induction is a fast, convenient and economical alternative. Furthermore, corrosion damage in steelwork produces compositional changes that could be suited to detection by this method.

However, two common locations for corrosion damage in supporting steelwork are at the joint interfaces and under chequer plate flooring (Gallon, 1993) leading to the requirement that the method be capable of detecting faults under a considerable thickness of steel. The limitation of electromagnetic methods to detecting shallow faults renders it unsuitable for the purposes of this project. Further information on the use of this of this method for

inspecting wire ropes can be found in Weischedel and Ramsey (1989). General information can be found in ASTM (1984), Lord (1985) and ASM (1976).

2.6. Eddy Current Inspection

Eddy current inspection works on a similar principle to electromagnetic inspection in the sense that both methods use an induced sinusoidal electric current. In the eddy current technique a small circular current is induced in the surface layers which generates an associated magnetic field. The presence of any cracks, void, or similar faults will alter the flow of the eddy current which in turn alters the magnetic field it produces. These changes can be detected by an inspection coil that is moved within the field. This differs from electromagnetic inspection in two respects: firstly, the current is induced in the surface of the specimen rather than across the entire cross-section; and secondly, it is the current-fault interaction rather than the field-fault interaction that plays the primary role in detection. This implies an assumption that the magnetic field produced by the eddy current is not significantly affected by variations in the local permeability of the specimen as is the case with electromagnetic inspection.

Some of the earliest applications of sinusoidal eddy currents to the NDT of metals were made by Lewis (1951), Hochschild (1958) and Russell et al. (1962). These methods were based on earlier work aimed at the determination of the physical properties of conducting materials (Hughes, 1879).

Eddy current inspection is commonly used as a quality control tool for the inspection of steel tubes and solid cylinders. The main advantage of this method is that it is largely non-specific, i.e. it can be applied to a wide range of discontinuities including cracks, slivers, and pits and any discontinuity that appreciably alters the eddy current flow.

However, this method would not be suitable for monitoring corrosion damage in structural steelwork in this case for two reasons: Firstly, because eddy current inspection can only be applied to exposed ferromagnetic surfaces and petrochemical steelwork frequently has protective coatings; and secondly, since only a small area can be examined at one time the

inspection of a single typical member of structural steelwork would take an unacceptably long time. For these reasons eddy current testing was not considered further in this project. Further information on the use of this method for inspecting wire ropes can be found in Grimberg et al (1990). General information can be found in ASTM (1984), ASM (1976) and McEleney (1992).

2.7. Electrical Resistance Inspection

Electrical resistance or conductivity testing (inversely proportional to resistance) relies on an electrical current that is passed down the specimen being tested. The presence of any cracks or changes in composition caused by corrosion damage changes the electrical resistance which in turn produces a measurable change in current. As with eddy current testing the method relies on the flow of an electric current that is sensitive to the presence of flaws. However, in this case the current is not restricted to the surface of the specimen and it is the changes in electric current rather than secondary magnetic field that indicate the presence of damage.

The development of electrical resistance inspection as an NDT method has been in progress for several decades. Some of the earliest work was aimed at advancing the method for the purpose of corrosion monitoring in refinery equipment (e.g. Freedman et al, 1958).

In recent times the method has been applied to the monitoring of corrosion damage in reinforcement bars for concrete. However, a great deal of electrical power is required to pass a current down a reinforcement bar of quite modest cross-section and for this reason electrochemical methods are more commonly used. For the determination of the conductivity of metals in quality control, eddy current testing is the preferred choice because unlike electrical resistance it is a non-contact method and therefore potentially faster.

Despite its relative unpopularity electrical resistance has the advantages that, in principle, it is a simple and convenient method and it does not require specialist equipment, However, electrical resistance testing requires a clear path down the member being examined. The

highly jointed structural steelwork used at petro-chemical works is therefore not ideally suited to examination by this method. The method could be applied with some probes covering one small section at a time but this would be too time consuming. Electrical resistance testing was therefore not considered further in this project. Further information on this technique can be found in Hinsley (1959) and Zivica (1993).

2.8. Radiographic Inspection

Radiographic inspection uses a beam of ionising radiation that is passed through the structure being testing to form a direct image on some radiation sensitive film (conventional radiography) or fluorescent screen (fluoroscopy). Types of radiation include charged particles (e.g. alpha, beta, protons), uncharged particles (neutrons) and electromagnetic radiation (gamma rays and X-rays). When the film is developed, regions of damage will contrast with good regions owing to their differing radiation absorptivities. Alternatively the variations in radiation intensity could be monitored with various types of electronic radiation detector (radiation gauging). The radiation beam may be composed of photons or particles with the same energy (monoenergetic) or with a spectrum of energies.

The various aspects of radiography have been developed over several decades for the NDT of structures. X-rays have been found to be effective in the measurement of specimen thickness and have been shown to be capable of measuring thickness changes in the order 0.2% (Halmshaw, 1966). Neutrons provide a significant advantage over X-rays for NDT owing to their ability to measure the thickness of low atomic number materials located within materials of high atomic number. The first reported demonstration of this unusual property was made by Thewlis (1956) by showing the successful neutron radiograph of a piece of waxed string behind 5 cm of lead. Monoenergetic charged particles have been demonstrated to show greater sensitivity to changes in areal density than the previous methods allowing the possibility of detecting variations in composition caused by voids or other such faults. An early example of this application was reported by Jung (1968). Electrons (beta radiation) show particular sensitivity to thin samples and have been used for the analysis of surfaces (Herz, 1969).

Common uses for radiographic inspection include the determination of thicknesses and detection of internal flaws in castings and weldments and the inspection of semiconductor devices for cracks and other faults. Radiography can also be used on forgings and mechanical assemblies although in the latter case it is usually limited to inspection for condition and proper placement of components. The main advantage of this method is that it is deeply penetrating. This would allow the radiographic inspection of corrosion damage under a substantial thickness of steel at the joint interfaces of structural steelwork. The method offers the further advantage of over ultrasonic inspection (also deeply penetrating) that it is more effective at detecting non-planar defects such as voids and inclusions. This might be a useful property in the detection of concealed corrosion products.

However, it would be necessary to use either very long exposure times or higher energy sources to penetrate thick structural steelwork and still obtain good quality radiographic images. The former requirement would make the method unacceptably slow whereas the latter would require heavy shielding making the equipment less portable. For these reasons radiographic inspection was discounted as a possible solution to the current problem. Further information on this technique can be found in ASTM (1989), Rockley (1964) and ASM (1976).

2.9. Acoustic Emission

This is also known as microseism or stress-wave emission. This technique relies on detecting the sub-audible sounds made by a developing crack or during plastic deformation in a structure under stress. Much of the energy released during the process is in the form of heat so that the acoustic emission signal is very small. A very sensitive sensor is required to detect the signal.

One of the earliest studies of acoustic emission was carried out in the late 1940's and early 1950's by Mason et al. (1948). However, its first use as a true surveillance device was probably made by Green et al. (1964). In this application it was used to detect cracks in a pressure vessel for the containment of missiles.

Together with the detection of flaw formation in welds during welding and cooling phases, the detection of cracks in pressure vessels remains the main use of acoustic emission. It can also be used for the surveillance of localised areas of known high potential for flaw development such as the primary coolant systems of a nuclear reactor, or regions of high stress or fatigue in structures.

One of the main advantages is that it does not require much accessibility because the signal internally traverses the steel, radiating in all directions from the fault. It is also possible to locate damage using multiple high sensitivity sensors and the triangulation technique.

However, the acoustic emission signal represents a propagating crack and therefore it cannot be used to give an early warning of damage. Furthermore, the level of the acoustic emission signal is very small and its duration is very short (typically about 0.03 μs in steel) so that false alarms could result if spurious noise signals are mistaken for an acoustic emission signal. This is particularly likely if this is applied to the condition monitoring of structures under normal operating conditions such as the support steelwork at petro-chemical sites. Further information on the use of this method for inspecting wire ropes can be found in Harrop and Summerscales (1989). General information can be found in ASTM (1985) and Scott (1991).

2.10. Ultrasonic Inspection

In this method an ultrasonic *travelling* wave is passed into the structure under examination using a transmitter. This produces stress waves that propagate through the material and are reflected from any interfaces encountered. These might be due to the presence of cracks, changes of phase or composition within the material, or a material to air boundary. The modifications in the frequency content of the signal caused by this event are determined by analysing the spectrum of the reflected signal detected by a receiver placed at another location on the surface.

Perhaps the oldest application of ultrasonic testing was the determination of material transmission properties by manual tuning of a conventional impulse echo instrument

(Roderick and Truell, 1952). The method was later refined to the automatic tuning of test signals by frequency modulation (FM) and applied to the determination of wall thicknesses (Evans, 1959). This method is also known as ultrasonic resonance testing. However, the true forerunner to the use of ultrasonic testing for detecting faults was the technique of examining the shape of an impulse before and after it had interrogated a specimen. Changes in the impulse shape result from the reflection of the signal from or transmission through boundaries separating regions of different density or composition (Gericke, 1963). Today it is possible to detect more subtle impulse shape changes with electronic Fourier analysis (Cooley, 1965).

The ability to measure wall thickness with ultrasonic inspection is frequently exploited in the monitoring of section loss in steel structures. ICI engineering has made limited use of ultrasonic inspection for this purpose (Gallon, 1993). It is also used to examine the micro-structure of polycrystalline metals. However its most common use is in the identification_of cracks in structures and components. The changes in impulse shape produced by interaction with cracks or inclusions within the steel are sensitive to the shape of the fault. This information is crucial in deciding whether the structure should be replaced or repaired.

A recent advance in ultrasonic inspection, which uses the impulse echo technique, allows the testing of steel beneath thick protective coatings and corrosion products (Cygnus Instruments, 1996). This would be advantageous for the inspection of petro-chemical structural steelwork where corrosion develops in moisture traps that are often inaccessible (Gallon, 1993).

However, a clear transmission path on which there may be defects is needed and the structural steelwork typical at petro-chemical sites has a large number of joints. Further information on this technique can be found in ASTM (1988) and Szilard (1982).

Ultrasonic testing can also be used to determine those physical properties of a material that depend on microscopic structure such as elastic moduli, hardness, fracture toughness and tensile strength. This field is known as non-destructive evaluation (NDE). Parameters of the travelling wave, such as velocity and energy loss, that are sensitive to these physical

properties can be measured by experiment. A recent advancement on this technique known as resonant ultrasound (RUS) is a more efficient method that uses ultrasonic *standing* waves (Migliori et al, 1993). RUS requires the determination of parameters such as resonant frequency and damping for resonances in the range 20 kHz to 1 GHz. However, it is presently limited to simple shaped advanced materials with dimensions of the order of 1 mm^3. RUS is an example of a dynamic test, i.e. a technique that uses the dynamic properties of the specimen itself to test its condition.

2.11. Dynamic testing

Dynamic testing is older than usually thought. Originally it involved striking a specimen with a hammer and listening to the sound produced. This approach was used by the ancients to check if their clay pots and glass bottles were sound. Today the potential scope of dynamic testing has considerably broadened owing to the availability of electronic instruments capable of generating and detecting vibrations in the sub-audible range.

In principle it should be possible to detect a wide range of faults with dynamic testing. This is because any fault that affects the local properties, usually stiffness or damping, should affect the dynamic response. It can be applied to any structure that has resonances within the scope of experimental measurement (generally below 20 kHz) such as airframes, engines and bridges. Dynamic testing is an attractive proposition for industrial steelwork because the response is not affected significantly by the presence of paintwork.

There are two main approaches to dynamic testing of structures. The first is to excite the modes of vibration in some way (impulse or periodic function), and to measure the natural frequencies, damping and mode shapes. Changes in these properties during the life of the structure would be indicators of damage. The second approach is to apply an impact and observe the response spectrum or the spectrum of the interacting force. The traditional impact test on pottery and glass and the railway wheel tapper's test are examples of the former. Increased damping reduces the amplitude of the high frequencies and results in a dull thud instead of a ringing tone. The coin-tap test is an example of measurement of the

interacting force that is affected by local stiffness. Damaged material is usually less stiff and results in a lower frequency response locally.

However, it has been found that the sensitivity of methods based on measuring the dynamic response to flaws in steel structures is generally disappointing and that changes in frequency are too small to detect unless there has been major damage (e.g. Stubbs and Osegueda, 1987).

There have been numerous efforts to improve the sensitivity of frequency response methods and these are reviewed in the next chapter. Further general information on dynamic testing can be found in Kozin and Natke (1986). Impact methods such as the coin-tap test have been exploited successfully in other contexts and will be considered in detail in the next chapter.

2.12. Summary and Conclusions

Table 2.1 summarises the findings of the literature review. For the purposes of brevity alternative names have been used for some methods, e.g. microseism for acoustic emission, and the remaining columns contain only a selection of entries. The reader is advised to refer to the appropriate section for full details.

Table 2.1 NDT Methods Suitable for Steel Components and Structures

Method	Typical Uses	Advantages	Limitations†
Visual	Welds, structural appraisal	Cheap	Objectivity
Dye Penetrant	Turbine blades, engine frames	Cheap, simple	Crevices
Mag. Particle	Crane hooks, steam turbines	Cheap, simple	Paint coatings
Electromagnetic	Chemical and physical sorting	Speed	Deep faults
Eddy current	Steel tubes & cylinders	Non-specific	Paint coatings
Conductivity	Concrete reinforcement	Cheap, simple	Jointed steelwork
Radiographic	Castings, weldments	Penetrating	Portability
Microseism	Welds, pressure vessels	Accessibility	Early warnings
Ultrasonic	Section loss in steel	Penetrating	Jointed steelwork
Dynamic	Airframes, engines	Non-specific	Sensitivity

† Regions where testing is *not* possible, or desirable attributes that the method does *not* possess.

None of the available methods of non-destructive testing are entirely satisfactory for damage assessment of structural steelwork. However, dynamic testing methods appear to have some potential advantages for this purpose, particularly those based on impacts, and will be reviewed in more detail in the next chapter.

3. REVIEW OF DYNAMIC METHODS

3.1. Introduction

Although dynamic techniques for NDT have been used for centuries the subject is still capable of considerable development. Since the introduction of the Fast Fourier Transform (FFT) there have been major advances in transducers, electronics and digital analysers. The increasing sensitivity of transducers and increased speed of processing has led to the widespread use of dynamic methods for product development and performance. Experimental observations generally have two major objectives: (a) determining the nature and extent of dynamic response, and (b) verifying theoretical models and predictions (Ewins, 1984). Damage detection can be considered as belonging to the second group where the objective is to *correlate* theoretical and experimental data, or to correlate before and after experimental data, thereby identifying the causes of discrepancies.

Dynamic data are generally either in the time or frequency domain and there are various mathematical techniques to interchange between the two. The techniques arise from a theorem first formulated by Fourier (1822) and extended by Papoulis (1962), which states that any periodic curve may be converted, using a Fourier Transform, into a series of pure sinusoids with harmonically related frequencies. This is known as the frequency spectrum or autospectrum (abbreviated to 'spectrum') and it is a more reliable indicator of dynamic behaviour than the time history. The data may then be converted from the frequency domain into the modal domain. Time domain data does not readily lend itself to harmonic analysis and is therefore more prone to noise and spurious signals. For this reason the frequency domain is generally is generally the basis of the many researches undergone in the field of damage detection with dynamic data.

In the first part of this chapter the theoretical background to dynamic behaviour is briefly outlined. Emphasis is placed on the parameters that can be conveniently measured experimentally. This is followed by a short review of how measured signals may be processed to provide useful data for performance assessment. Finally a review is presented

of damage detection methods that are based on the dynamic behaviour of structures and this is followed by a discussion of the experimental methods for obtaining dynamic data.

3.2. Dynamic Response Theory

The structural dynamic equation of motion for a multi-degree of freedom system (MDOF) is given by equation 3.1:

$$[M]\ddot{\delta}(t)+[C]\dot{\delta}(t)+[K]\delta(t)=f(t) \tag{3.1}$$

Where δ is a d-dimensional vector of the time dependent displacement response at d fixed locations on the structure and $f(t)$ is the external force vector on the system. M, C and K are the mass, damping and stiffness matrices. The Fourier Transform of $f(t)$ is given by:

$$f(j\omega)=\int_{-\infty}^{\infty} f(t)\,.\mathrm{e}^{-\mathrm{j}\omega t}\,.dt \tag{3.2}$$

Therefore

$$f(j\omega)=\int_{-\infty}^{\infty}[M\ddot{\delta}(t)+C\dot{\delta}(t)+K\delta(t)].\mathrm{e}^{-\mathrm{j}\omega t}\,.dt \tag{3.3}$$

$$\delta(t)=\int_{-\infty}^{\infty}\mathrm{A}(\omega)\mathrm{e}^{\mathrm{j}\omega t}\,d\omega \tag{3.4}$$

Equation 3.4 follows from the Fourier theorem. $A(\omega)$ is a function of the response amplitude at frequency ω. The first derivative of $\delta(t)$ is:

$$\dot{\delta}(t)=\frac{d}{dt}\left(\int_{-\infty}^{\infty}\mathbf{A}(\omega)\mathrm{e}^{\mathrm{j}\omega t}\,d\omega\right)$$

$$=\int_{-\infty}^{\infty}\left(\mathbf{A}(\omega)\left(\frac{d}{dt}e^{j\omega t}\right)\right)d\omega$$

Therefore $$\dot{\delta}(t) = j\omega\left(\int_{-\infty}^{\infty} \mathbf{A}(\omega)e^{j\omega t}d\omega\right)$$

Therefore $$\dot{\delta}(t) = j\omega\delta(t) \tag{3.5}$$

Similarly the second derivative of $\delta(t)$ is given by.

$$\ddot{\delta} = -\omega^2\delta(t) \tag{3.6}$$

Substituting equation 3.5 and equation 3.6 into equation 3.3 gives:

$$f(j\omega) = \int_{-\infty}^{\infty}\left(\left[-M\omega^2 + jC\omega + K\right]\delta(t)\right)e^{-j\omega t}.dt$$

$$= \left[-M\omega^2 + jC\omega + K\right]\int_{-\infty}^{\infty}\left(\delta(t)e^{-j\omega t}\right).dt$$

Therefore $$f(j\omega) = \left[-M\omega^2 + jC\omega + K\right]\delta(j\omega) \tag{3.7}$$

Where $\delta(j\omega)$ is the Fourier transform of the response vector $\delta(t)$. The Fourier Transform can take various forms depending on the type of signal being analysed. Equation 3.3 and equation 3.4 represent the transforms for a continuous periodic signal. The Discrete Fourier Transform (DFT) is a Fourier transform that can be applied to periodic signals that are digitised, therefore it is easily implemented on a microprocessor. It generates periodic frequency spectra that are also digitised. However, it has largely been superseded by the FFT which requires less processing time. The DFT equivalent of equation 3.3 and equation 3.4 are detailed in Ewins (1984). The eigensolutions of equation 3.7 are the mode shapes δ_n, modal frequencies ω_n and modal damping σ_n, where σ is the damping factor. Each mode also has a generalised stiffness, mass and damping. Rearranging equation 3.7 leads to an expression for the frequency response function (FRF) of the system, $\boldsymbol{H}(j\omega)$:

$$\boldsymbol{H}(j\omega) = \frac{\delta(j\omega)}{\boldsymbol{f}(j\omega)} = \frac{1}{[-M\omega^2 + jC\omega + K]} \tag{3.8}$$

Equation 3.8 can be written in partial fraction form:

$$H(j\omega) = \sum_{n=1}^{2n} \frac{a_n}{j\omega - P_n} \tag{3.9}$$

Where a_n is known as the residue, P_n is a pole of the system ($= \sigma_n + j\omega_n$) and n is the mode number. The function $\boldsymbol{H}(j\omega)$ is known as the accelerance when the response is measured as the acceleration. This function peaks when $j\omega \cong P_n$, i.e. at the modes of vibration.

The response $\delta(t)$ of a constant parameter linear system to an applied force $\boldsymbol{f}(t)$ can be written as:

$$\delta(t) = h(\tau) * \boldsymbol{f}(t) \tag{3.10}$$

Where $h(\tau)$ is the response of the system to a force spike of unit magnitude as a function of time (τ) and * represents the convolution integral. The FRF can be found by taking the Fourier transform of both sides of equation 3.10, this yields.

$$\delta(j\omega) = H(\nu).\boldsymbol{f}(j\omega) \tag{3.11}$$

Where ν is the frequency, $\delta(j\omega)$ and $\boldsymbol{f}(j\omega)$ are d-dimensional vectors of the Fourier Transform of the response function and the forcing function respectively at angular frequency ω.

The power spectrum, S, of a signal is the product of its amplitude in the frequency domain with the complex conjugate of that amplitude. The FRF can also be defined as

$$H(\nu) = \frac{S_{XF}(\nu)}{S_{FF}(\nu)} \tag{3.12}$$

where $S_{XF} = X(j\omega).F'(j\omega)$, $S_{FF} = F(j\omega).F'(j\omega)$ and the complex conjugate of $F(j\omega)$ is denoted by $F'(j\omega)$. This has the advantage that both S_{XF} and S_{FF} can be averaged. Other approaches to improving the measurement accuracy are described in Maguire, 1984.

The modal parameters σ_n and ω_n that are contained in the system's pole term, P_n (equation 3.9) can be found by curve fitting the measured FRF $\boldsymbol{H}(j\omega)$ at one point due to a particular exciting force vector $\boldsymbol{f}(t)$. The simplest techniques available, known as single degree of freedom (SDOF) analyses, all assume that near a resonance the total response is dominated by the contribution of the mode with the closest natural frequency. In one of them, the peak amplitude or peak picking method, the modal frequency is taken to be that which corresponds to the peak amplitude and the modal damping η_n is estimated from the relations,

$$\eta_n = \frac{\omega_a^2 - \omega_b^2}{\omega_n^2} = \frac{\Delta\omega}{\omega_n} \tag{3.13}$$

where η_n is the hysteretic damping factor for mode n. ω_a and ω_b, which are known as the half-power points, are the frequencies that correspond to the root mean square (RMS) amplitude. This method can only be used when the structure is not so heavily damped that peaks overlap. Furthermore, it is only possible to use this method when the structure is not so lightly damped that there are insufficient data points around the peak to measure its amplitude accurately. It is appropriate in cases where a rough estimate of the modal parameters is sufficient but it is not suitable for determining the structural model. This is because the single-mode assumption is not strictly applicable even for well spaced peaks and the neighbouring modes always contribute a noticeable amount. A more accurate approach that takes account of the contribution of other modes is the circle-fit method which is discussed in detail in Ewins (1984). Finally, the shape of each mode (δ_n) can be found by measuring the response amplitude at various locations on the structure and fitting a smooth curve to the data.

3.3. Data Acquisition

In the previous sections the theory and practice of dynamic methods have been presented. This section describes the computational processes that produce a record of dynamic behaviour from a physical measurement. Data acquisition is often executed by a dedicated instrument such as an oscilloscope or a spectrum analyser. It is concerned with procedures which result in the capture of a digital record of a dynamic event. The output from a transducer is *captured* to produce a digital record in the time domain. If the stored record is to be converted to the frequency domain it is also necessary to use an electronic *window* to prevent a phenomenon known as leakage. There are many other procedures involved in data acquisition and a full treatment is beyond the scope of this thesis but the reader is referred to the text by Ifeachor and Jervis (1993) for further details. The two processes mentioned above will now be discussed in turn.

3.3.1. Data Capture

The analogue output of a transducer is digitised to produce a time record of amplitudes at fixed intervals (the raw data). The main procedures are *sampling*, and *averaging*. These will be discussed in turn.

3.3.1.1. Sampling

For a given analogue signal the sampling theorem by Shannon (1949) places restrictions on the sampling rate. It can be abbreviated to the following statement:

> To recover the signal accurately, it is necessary to sample it at a rate at least twice its highest frequency component.

For a given sampling frequency, ν_s, the highest frequency that can be recovered is 1/2 ν_s. This is known as the folding (or Nyquist) frequency ν_{fol}. If the original signal contains components of higher frequency they will be folded back into the range 0 Hz to ν_{fol}. The consequence of using a lower sampling rate is a phenomenon known as aliasing which is

illustrated in the time domain in Figure 3.1 (a). The analogue signal shown as a solid line is sampled at a rate that is less than twice its frequency (the signal shown represents a pure sinusoid and therefore has only one frequency component). Consequently the alias frequency, which becomes that of the recorded raw data, is approximately half that of the original signal. The distortion of the original signal can be also demonstrated in the frequency domain. The FFT converts the signal into a periodic series of well-separated frequency spectra because the sampling frequency is approximately 2.5 times the bandwidth which is limited to the range 0 Hz $\leq \nu \leq \nu_B$, where ν_B is the maximum analysis frequency, as shown in Figure 3.1 (b). However, if the sampling frequency is not sufficiently large a portion of the image centred on ν_s folds over (aliases) into the original spectrum resulting in distortion, as shown in Figure 3.1 (c). Modern spectrum analysers have anti-aliasing filters which, combined with the high sampling rate, remove the possibility of aliasing. However these filters cause degradation of signals with rapid rise times and therefore should not be used in these cases. The raw data acquired as described above will be contaminated with noise from the physical system and unless measures are taken to remedy this any further computation will be liable to error. The level of noise can be reduced by averaging the raw data in either the time domain or the process domain. These are the first steps in data processing.

3.3.1.2. Averaging

The two principle types of averaging used for dynamic data are process averaging, where *linear* and *exponential* are two examples, and *time* averaging. As its name suggests, the latter process is appropriate for continuously averaging over the duration of a measurement that is contaminated with noise. Process domain averaging is similar to time domain averaging except that averaging is carried out over separate physical measurements. It is appropriate for measurements that have a relatively high degree of intrinsic randomness such as speech and music. In time domain averaging the measurement duration is divided into a number of time records in which the signal will repeat itself exactly. However, the noise component will be always be different owing to its random nature so that averaging all the records it will be found that the noise tends to zero whereas the signal remains the same.

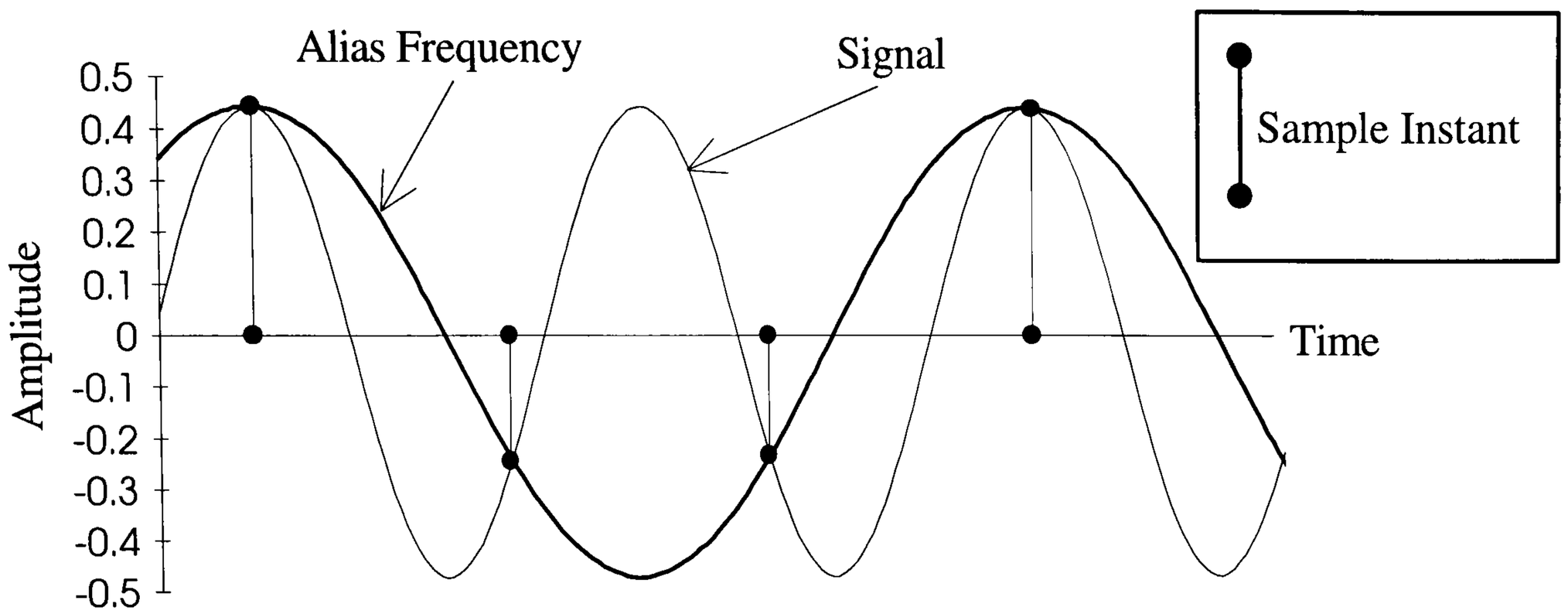

(a) Sampling of a Pure Sinusoidal Signal

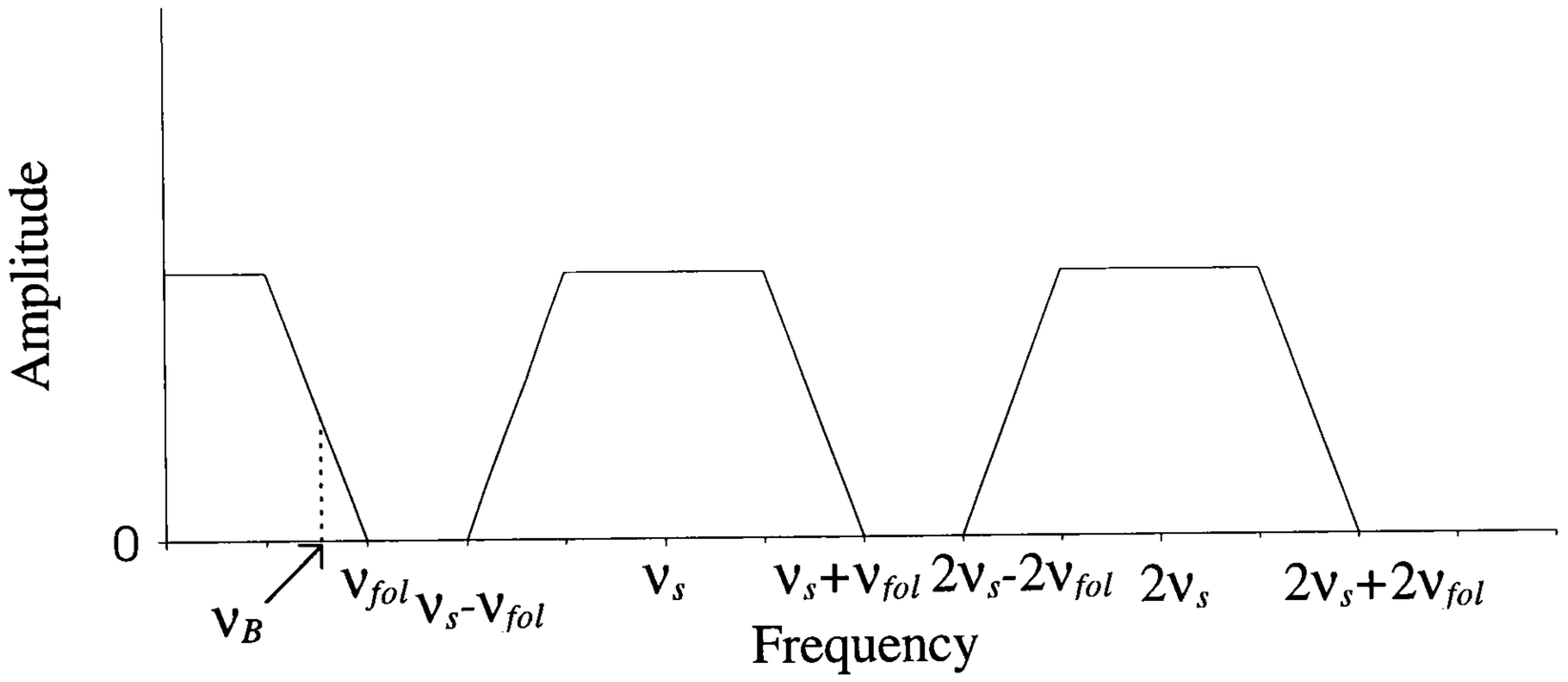

(b) Spectrum of Band Limited Signal

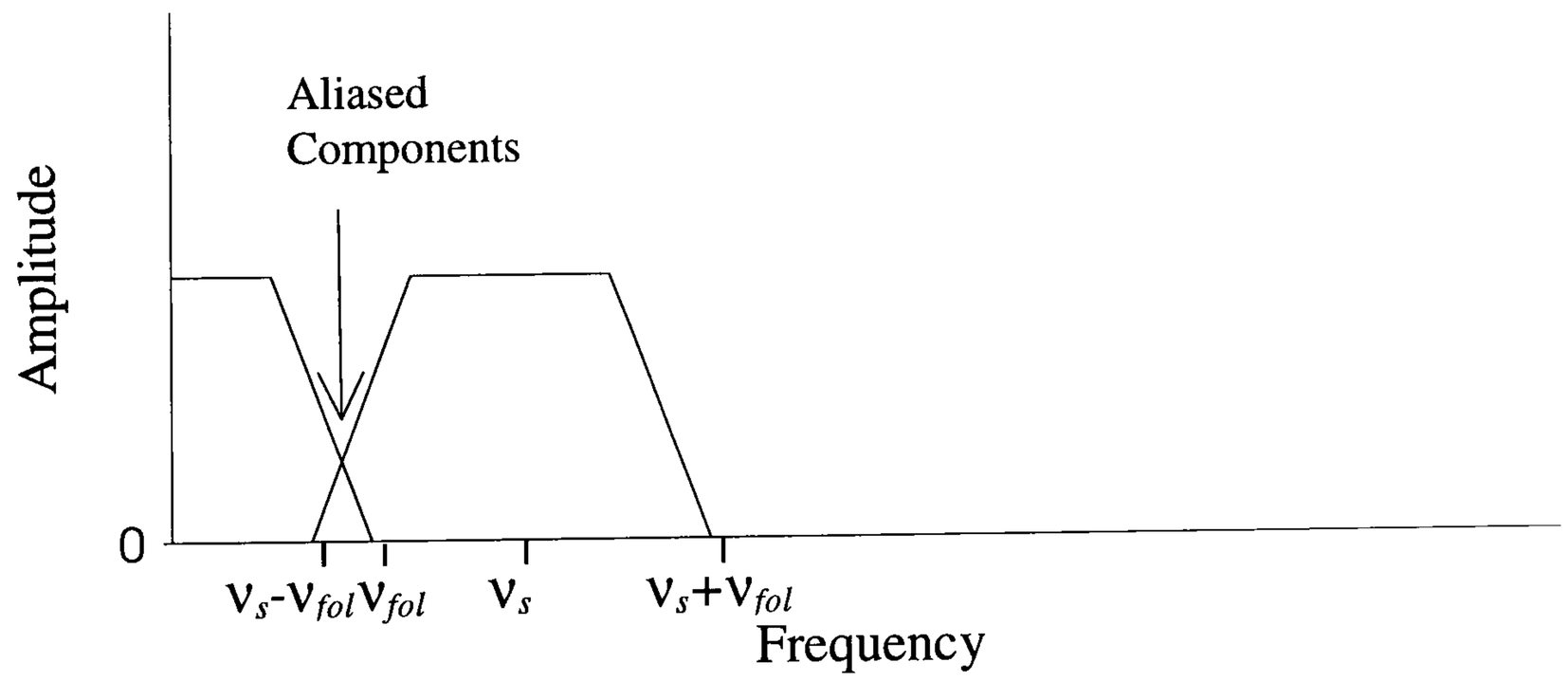

(c) Aliased Spectrum

Figure 3.1. Illustration of Aliasing

On this basis the two components can be separated and the quality, or signal to noise ratio (SNR), can be improved. It is essential that the phase of the signal is the same at the beginning and end of each record when data sampling is initiated (triggered). Therefore, for each record, it is necessary to trigger the start and end of data sampling with another signal that has the same frequency as the noisy signal. The time history of a square wave buried in noise is sketched in Figure 3.2 (a), where the signal waveform is barely discernible. However, after 128 time averages the SNR has improved and the waveform is clearly discernible (Figure 3.2b). This shows the importance of time domain averaging.

By computing the sum of all the records and dividing by the number of them the spectrum analyser performs the task of process domain averaging automatically. Figure 3.2 (c) shows a spectrum with no averages obtained from just one measurement. After five averages a significant improvement in the statistical quality is observable, as shown in Figure 3.2 (d). After ten averages the improvement is even more dramatic with the emergence of a single sinusoidal component, as shown in Figure 3.2 (e), demonstrating the importance of this process.

Exponential averaging is a more sophisticated type of process domain averaging which makes allowance for systems whose dynamic properties vary over the course of several measurements. For example, if the frequency of a sinusoidal component was changing, the linear average might give the impression that there were two or more signals of different frequency in the measurement. The exponential average circumvents this problem by placing a greater weighting factor on recent measurements than on older ones. In this way old data is gradually 'forgotten' and no longer influences the result. However, effectively less data is now available for averaging so poorer statistical stability is obtained.

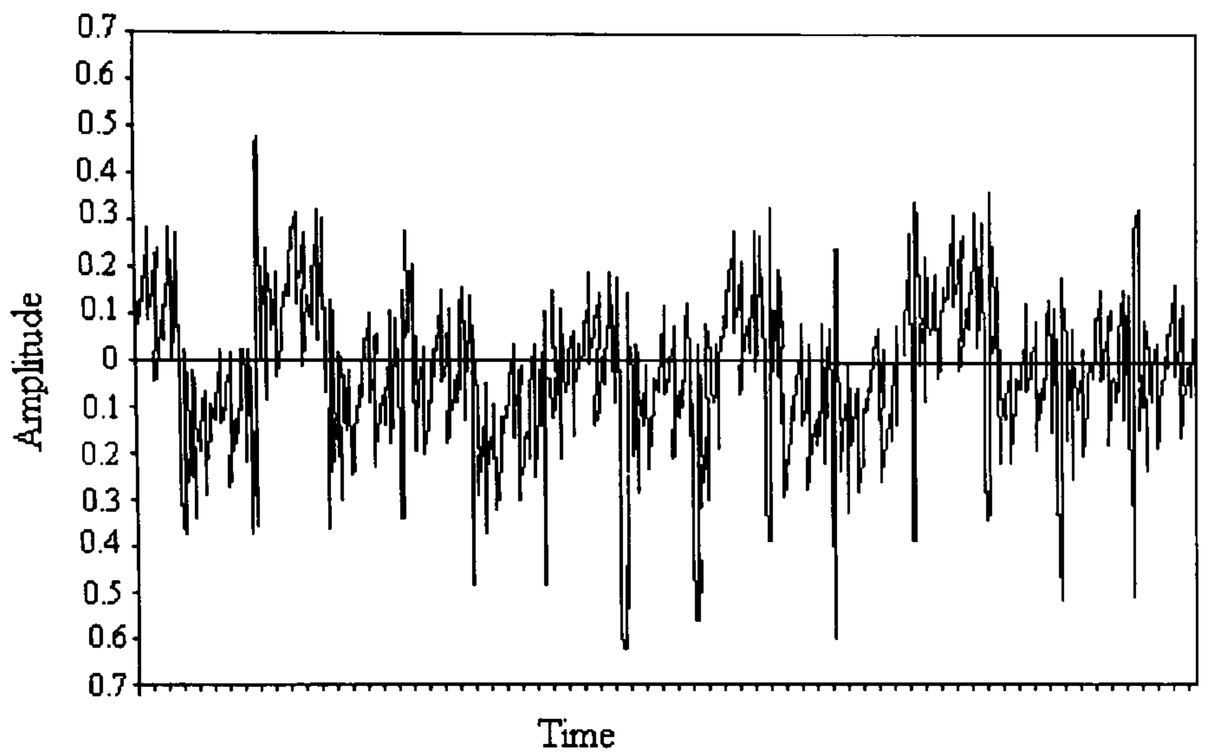

(a) Signal With No Averages

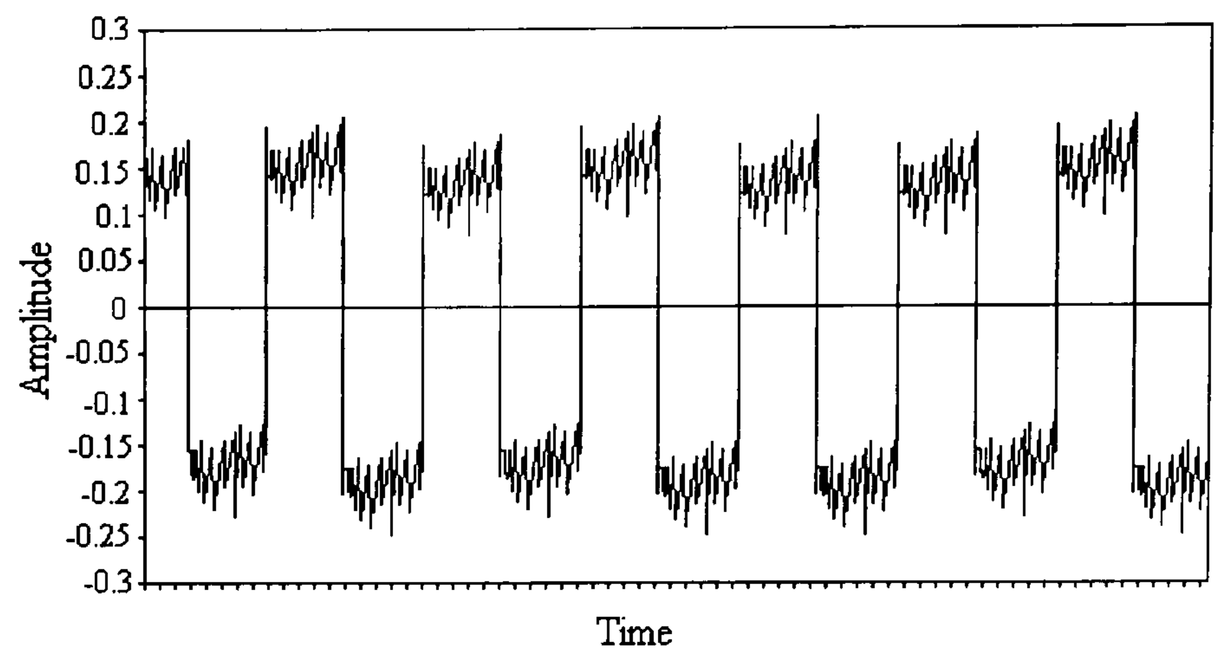

(b) After 128 Time Averages

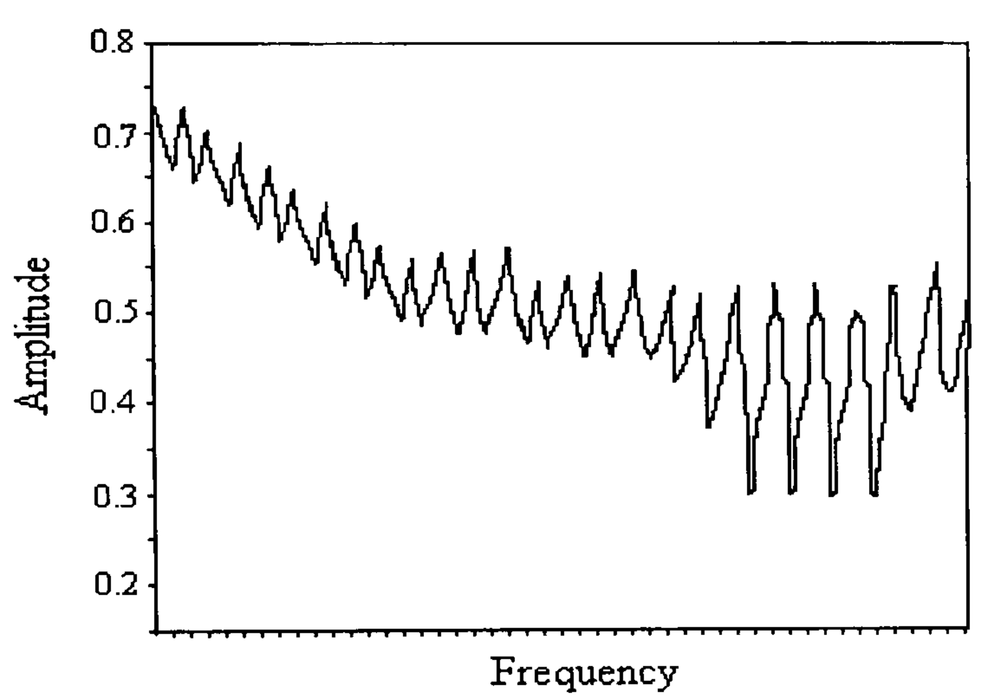

(c) Spectrum With No Averages

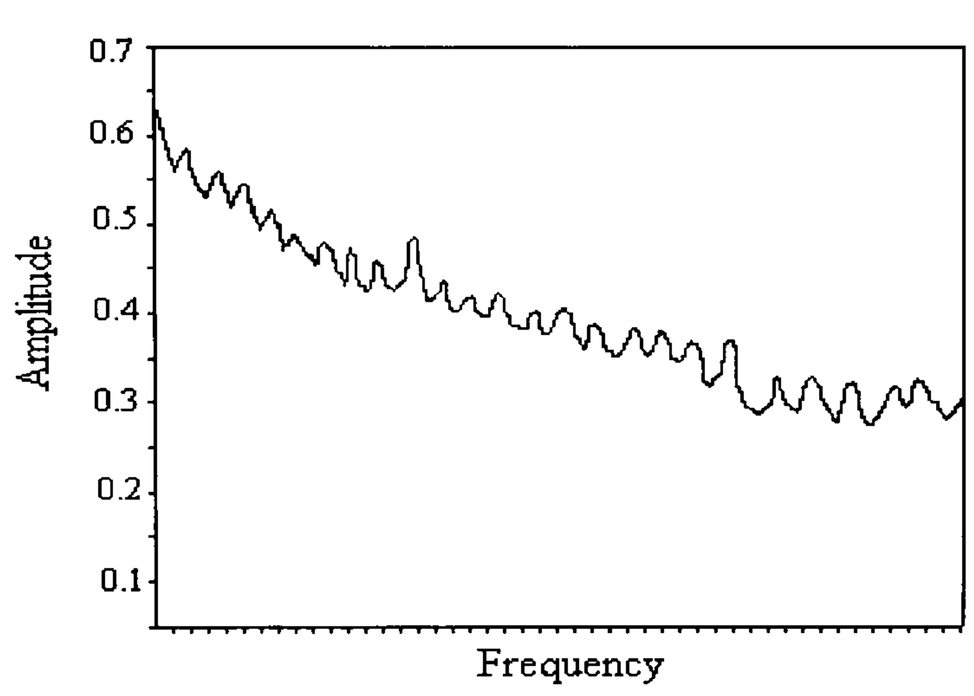

(d) After 5 Linear Process Averages

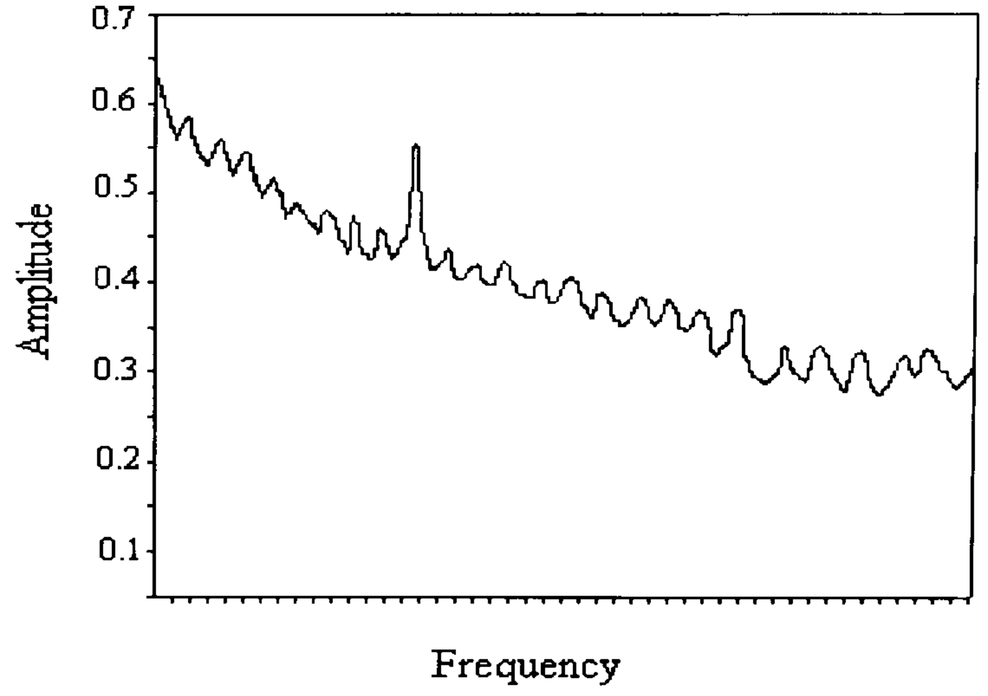

(e) After 10 Linear Process Averages

Figure 3.2. Time and Process Domain Averaging

3.3.2. Windowing

To convert measurement data to the frequency domain a spectrum analyser uses an FFT which requires that the raw data be continuous and periodic in time. In practice this means that the time record (section 3.3.1) should have identical phase at the beginning and at the end. Signals for which this occurs naturally require a rectangular window that essentially leaves the record unmodified. These are discussed below.

There are two instances of signals in which the phase at the beginning and at the end of the record is the same. The first is when the length of the time record is greater than the duration of the signal and therefore the amplitude tends to zero at both ends. An example of this is the transient signal shown in the upper diagram of Figure 3.3 (a) . The periodic signal assumed by the FFT remains continuous at the limits of the record as shown in the lower diagram. The other instance is when the length of the time record is less than the signal duration but equal to an integral of the period of the signal. The period of the sine wave shown in the upper diagram of Figure 3.3 (a) is exactly half that of the record length. Consequently the phases at the record limits are matched and a continuous, synchronous periodic signal is assumed by the FFT as shown in the lower diagram.

However, when the length of the time record is less than the signal duration it is extremely unlikely that it will also be a multiple of its period. For example the sine wave in the upper diagram of Figure 3.3 (a) has three half periods in one record. In a case such as this the assumed periodic signal is asynchronous and has discontinuities at both ends of the record as shown in the lower diagram. This causes the FFT to generate 'pseudo' high frequency spectral lines that might mask real spectral lines of low intensity. This phenomenon, known as leakage, can be overcome by using a window that modifies the signal. The most widely used window of this type is the *Hanning* window, which is discussed below.

The Hanning window constrains the signal to be continuous at each end of the record by forcing its amplitude there to be zero. This is illustrated in Figure 3.3 (b) which shows the effect

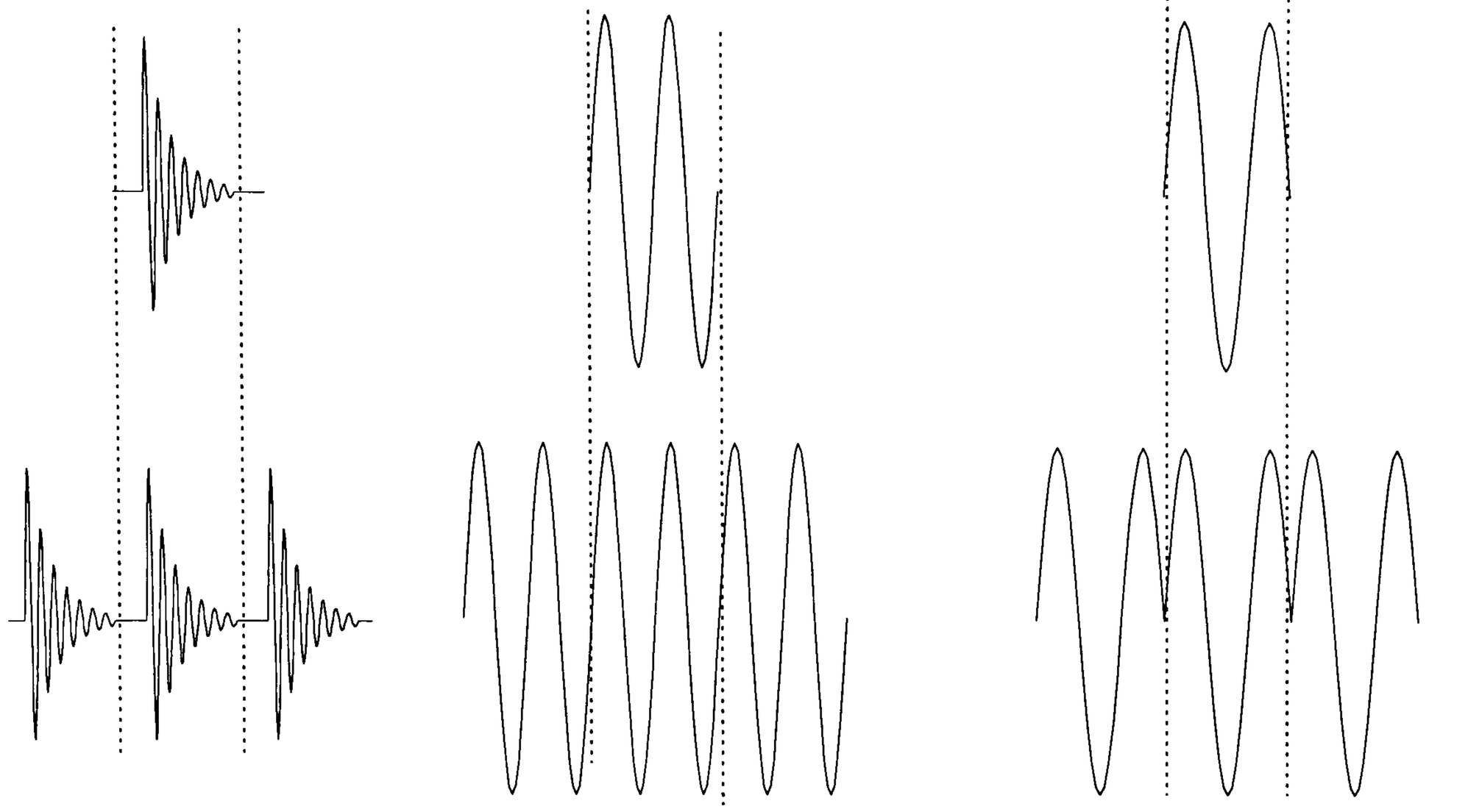

(a) Rectangular Windowed Signals

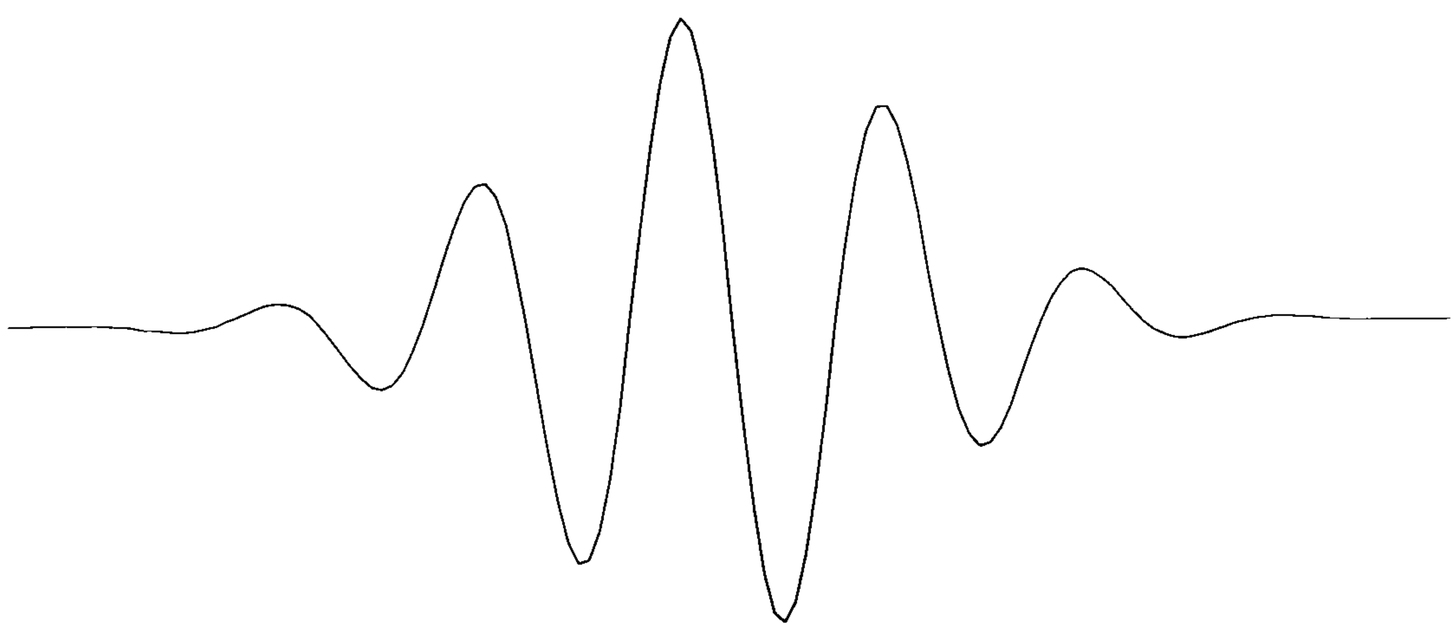

(b) Hanning Windowed Sine Wave

Figure 3.3. Windowing of Signals

of a Hanning window on a sine wave. There is an improvement in frequency resolution owing to the elimination of leakage but, because the raw data is modified, an accompanying reduction in amplitude resolution. There are usually other windows available each of which have different advantages and disadvantages. The choice of which window to use depends on the signal being measured and the balance between frequency and amplitude resolution required.

3.4. Damage Detection

The basic principle behind damage detection is that the frequency and modes of vibration or dynamic response of a structure change when it has been damaged. The change is caused by a change in stiffness at some point due to a fracture, or change in continuity, or a change in damping due to friction at new interfaces in the damaged structure. For the purposes of this report damage detection is achieved either by comparison of experimentally measured changes in the structure's dynamic response caused by damage with those predicted by a theoretical model, or by comparison of experimental measurements before and after damage. In principle it is possible to identify the presence of damage using time domain data. For example Elkordy et al. (1994) detected stiffness reduction in a simple five storey frame by subjecting it to band limited white noise and identifying characteristic changes in the displacement amplitude at certain locations. However, most of the research in the damage detection field has used the frequency domain because it is easier to perform harmonic analysis in the frequency domain. Furthermore, although continuous excitement can be used for damage detection, e.g. Salane and Baldwin (1990), there is a greater tendency to use the impulsive method, particularly impact, owing to its comparative ease of use. Therefore, the following discussion primarily focuses on research in the frequency domain using the impact method. In the first set of techniques to be discussed the parameters are estimated from modal attributes.

The presence of damage is often characterised by reductions in some modal frequencies, a classic indicator of stiffness reduction or mass change. A common approach to damage localisation and detection is to measure the modal *frequency* shifts caused by damage on the real structure and compare them, or parameters computed from them, with those predicted

by a finite element model (FEM) of the structure. A good match between these either validates the model or the structural behaviour whereas a discrepancy would either indicate that the model was inaccurate or that there is structural damage present.

Mannan and Richardson (1990) discuss in theory the effect of localised stiffness reduction on the stiffness matrix of a plate structure. The sensitivity was poor but it was found that the damage sensitivity, which is the percentage reduction in modal frequency for a given localised stiffness reduction, rose with increasing mode number. However, the limited capability of experimental apparatus prevents the excitement of the highest modes of vibration and this places a constraint on techniques based solely on frequency change. For this reason most research has been aimed at improving sensitivity computationally.

Cawley and Adams (1979) describe a method in which the ratio of frequency change for two modes is used to locate damage on a plate structure. In this case the sensitivity of the method was increased by correlating the stiffness matrix with the mode shape. However, the increase in sensitivity becomes less significant when more complex structures requiring a greater number of degrees of freedom are modelled. For example it was found that the detection limit for damage in an offshore type structure was 50% reduction in the stiffness of a major structural member (Stubbs and Osegueda, 1987). Thus, modifications have been made to matrix methods to improve the sensitivity.

Messina et al. (1996) introduced a Damage Location Assurance Criterion (DLAC) as a further improvement to the sensitivity of the Cawley and Adams method. The DLAC gives an index between 0 and 1 that directly compares the experimental frequency shifts with those predicted theoretically. The method was tested on the FEM of a small steel frame and was reported to be capable of detecting a 20% reduction in the stiffness of an element, but the results were highly susceptible to measurement error.

Pandey and Biswas (1994) explored the possibility of using changes in the flexibility matrix (proportional to the inverse of the stiffness matrix). An artificial crack was cut into the centre of an I-beam that was excited with an instrumented hammer. From the response the change in flexibility with position was plotted before and after damage. Information on the

location and extent of damage was present in the results but this method is computationally very complex. The method is claimed to have a number of practical advantages but does not improve on the sensitivity of the stiffness matrix approach.

Park et al. (1988) replaced the stiffness error matrix with a weighted error matrix (WEM). The WEM places a weighting factor on each element of the error matrix and this magnifies those elements most sensitive to the damage. The factors are calculated from the same data used to compute the error matrix. The method was tested on a 600 mm x 100 mm three storey frame and a plate structure. A small notch in one member of the frame and a large H-shaped notch in an element 1/24th the total area of the plate structure were located with this method. The traditional error matrix gave inconclusive results in both cases. The WEM is computationally demanding but the researchers suggest a step-by-step approach to applying the method that minimises computation time.

The shifts in modal frequency that characterise structural damage are accompanied by a reduction in the modal *amplitude* of response near the original modal frequency. Another approach to damage detection is to compare the amplitude at the modal frequency before and after damage. Wu et al. (1992) describe a procedure that compares a band of FRF amplitudes corresponding to the fundamental mode of vibration of a simple three storey frame. However, the best sensitivity obtained was a stiffness reduction of 50% in one of the members showing that this approach does not represent an improvement to the frequency shift approach.

The mode *shape* can also be used to identify damage. One method is to compare the curvature mode shape, which is proportional to the second derivative of the mode shape, for the damaged and undamaged cases. Another is the modal assurance criterion or MAC (Allemang and Brown, 1982). The MAC provides an index between 0 and 1 that is a direct comparison between two mode shapes. It approaches 1 as the similarity between the mode shapes increases (i.e. as damage sensitivity decreases).

Pandey et al. (1991) used the curvature mode shape to determine damage location and size on two simple structures modelled on a computer. The difference in curvature mode shape

between the damaged and the undamaged models was plotted. The damage location became accentuated on these plots and it was possible to distinguish damage down to 1/10th reduction in the Young's modulus of a member. This shows the potential sensitivity of the mode shape method of damage detection. However, in practice it is very difficult to measure mode shapes accurately. Furthermore, it is likely that structures that are more complex than those chosen for this study will be tested, and in these cases the sensitivity would be expected to decrease, as observed by Cawley (1979). It would be useful to know whether mode shape changes are sensitive enough to detect small damages in these cases.

Biswas et al (1989) describe a study aimed at detecting simulated damage on an actual highway bridge. The removal of several bolts from a splice plate was detected by inspection of the changes produced in the MAC. These ranged from 0.86 for the fundamental to 0.2 for the eighth mode showing a consistent increase in damage sensitivity with increasing modal frequency. However, the test was performed under highly controlled conditions, in particular the flow of traffic was temporarily suspended during testing. Opportunities to conduct such tests are rare and it would be more useful to be able to carry out such an experiment during the normal service of the structure.

In the methods previously discussed, damage detection depended on the identification of changes in specific modal attributes. By using such a small proportion of the available data it is possible that potentially valuable information is discarded. Furthermore, small spectral changes could become masked by noise. The following methods attempt to detect damage by calculating parameters from all or most of the frequency domain.

Adaptive Template Matching (ATM) requires the calculation of the minimum tolerance to keep the FRF of the changed structure within that of the unchanged structure. The tolerance increases with degree of structural change. The signature assurance criterion (SAC) provides an index between 0 and 1 that is a direct comparison between two FRFs. The SAC approaches 1 as the similarity between the FRFs increases. Another approach is to convert the FRF amplitudes into a set of parameters more sensitive to change. The slope or curvature differential function is the difference between the first or second derivative respectively of the original structure's FRF and that for the changed structure. Both

functions are examples of a waveform chain code (WCC) and the area under this is sensitive to changes in the FRF.

Samman et al. (1994) used ATM and SAC to detect cracks of 6 mm to 51 mm length on a bridge model. The deck dimensions were 1.22m x 2.57m and it had three girders in which the cracks were made in one of two locations. Crack length discrimination was possible with all methods. In a similar experiment Samman et al. (1991) used slope and curvature differential functions to detect a small simulated crack in the web and flange of a bridge model 65″x 24″ (scale 1:24). These results show that by analysing a greater proportion of the FRF it is possible to detect damage but because the methods are inherently non-specific damage is harder to locate.

3.5. Experimental Procedures

The two basic approaches for obtaining the dynamic response are to use either continuous or impulsive excitation. In the former case the exciting force $f(t)$ can be either periodic or random. For periodic sinusoidal excitation the dynamic response is determined directly either by measuring the response amplitude as a function of time at a fixed frequency (the time history) or by measuring the response amplitude, normalised to the amplitude of the exciting force, over a range of frequencies (the FRF). This is known as the *resonance* or stepped sinusoidal method. In the latter case the excitation may result from the sudden release of a restraining force or it may be due to an *impact* or intermittent force. For impact excitation structural vibrations are excited by applying a sharp impact at one point and the impulse response is recorded at some other point for further analysis. Both techniques can be termed global because, in principle, damage anywhere on the vibrating structure can be detected irrespective of the location of the exciting force.

3.5.1. The Resonance Method

To illustrate the resonance method consider the simple 5-storey frame in Figure 3.4 (a). The shaker provided an excitation force, $f(t) = a \sin \omega t$, at a frequency, ω, determined by an electrodynamic oscillator at the location x = 290 cm, y = 750 cm, z = 0 cm. This frequency

was varied over a certain range and the response $\delta(t)$ was measured at x = 0 cm, y = 750 cm, z = 0 cm by the attached accelerometer. Figure 3.4 (b) shows the accelerance plotted between $\omega/(2\pi)$ = 0 Hz and $\omega/(2\pi)$ = 600 Hz. The first five modes of vibration under horizontal force are also indicated. This is an example of a dynamic response for which the peak amplitude analysis might be appropriate. The modes are well separated and do not overlap considerably. However, there are only one or two data points in the peak regions and an accurate peak amplitude analysis would only be possible if the frequency resolution could be increased. Figure 3.4 (c) shows the shapes of the two modes δ_1 and δ_4. It should be noted that the structure also has modes of vibration perpendicular to the plane shown, but these are not shown in Figure 3.4. The presence of damage or physical change in a system alters the structural characteristics and therefore the dynamic response. The resulting change in FRF or mode shape may then be detected.

3.5.2. The Impact Method

An early example of the impact method as a modern form of quality testing was the railway wheel-tap test which was used to detect cracks in railway wheels (Adams and Cawley, 1985). The inspector would walk alongside the train striking each wheel hard enough to excite structural vibrations. An experienced inspector could judge the wheel condition by the quality of the note produced. This is because new interfaces due to the presence of a crack increase the frictional damping. In the time domain this gives a rapid decay of the vibration resulting in a dull thud instead of a ringing tone. However, it was limited by its inherent subjectivity as the judgement made by more than one inspector testing the same structure could differ considerably.

There existed a need for impact methods that could be computationally analysed. In this respect the introduction of the FFT (Cooley, 1965) was an important advance. The FRF of the structure is determined from the FFT's of the acceleration response $h(\tau)$, and the impact time history $f(t)$ (see equation 3.8).

$$H(j\omega) = \frac{\int_0^\infty h(\tau) e^{-j\omega\tau}.d\tau}{\int_0^\infty f(t) e^{-j\omega t}.dt} \qquad (3.14)$$

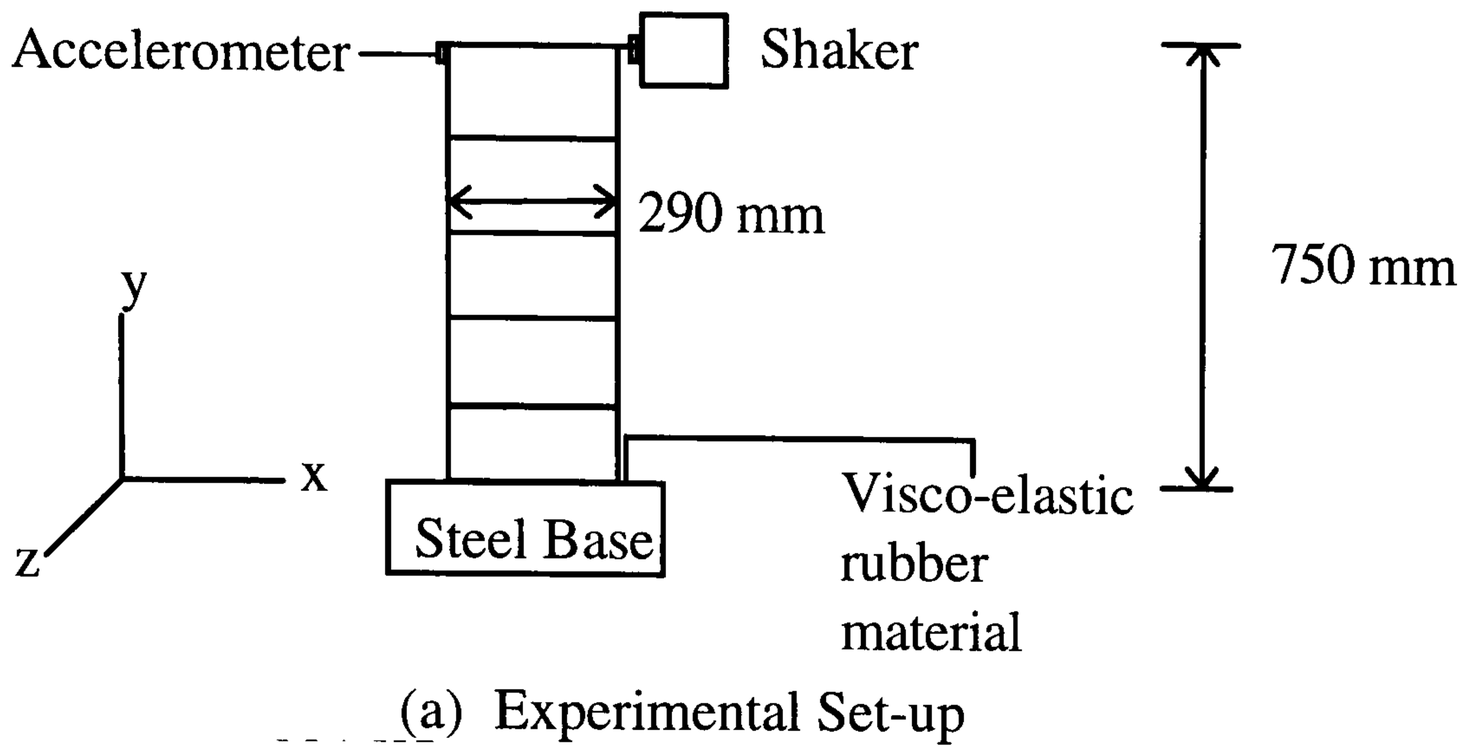

(a) Experimental Set-up

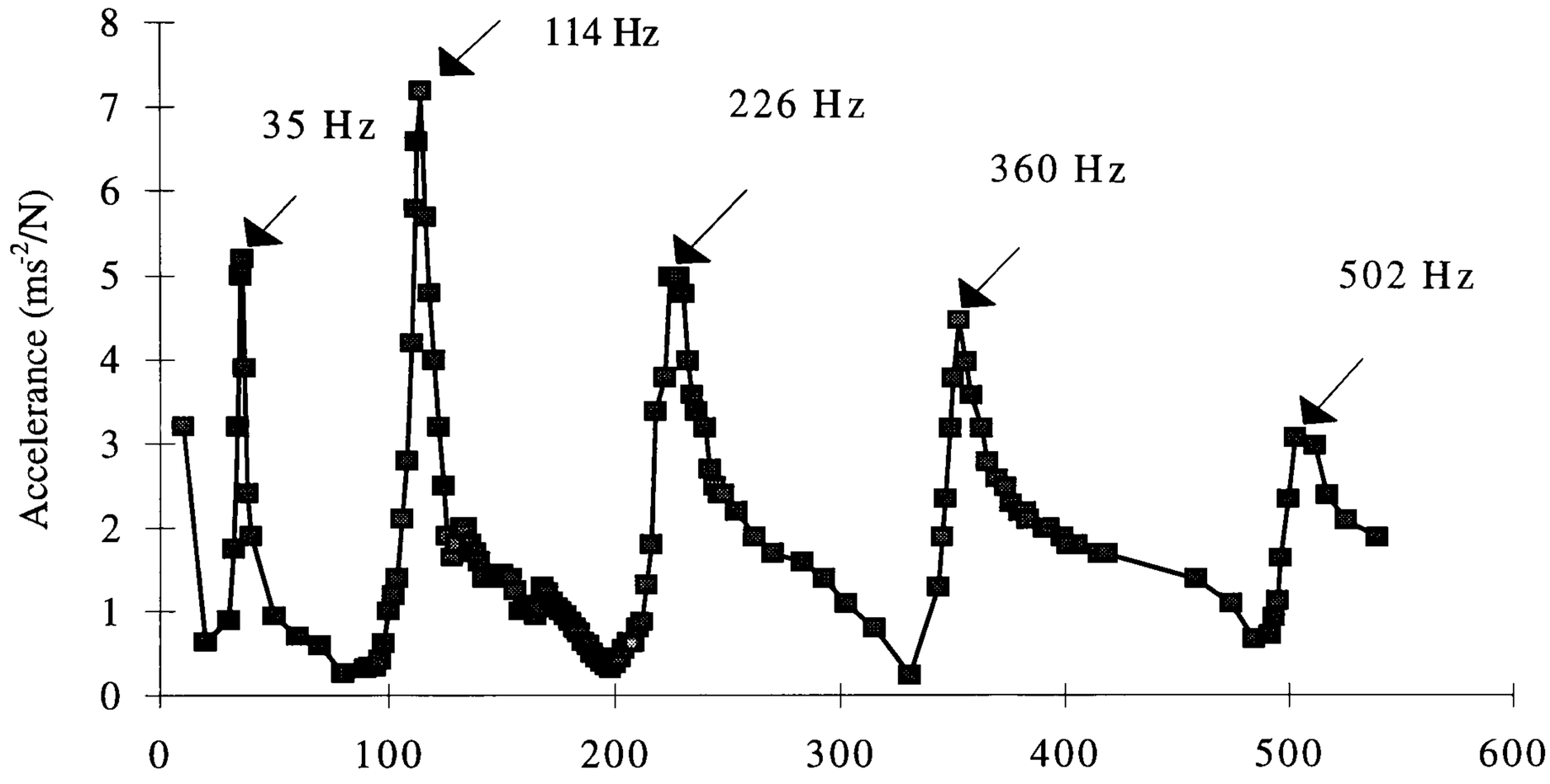

(b) Frequency Response Function

35 Hz 360 Hz

(c) Two Mode Shapes

Figure 3.4. The Resonance Method

Thus the frequency response is obtained in one measurement by exciting the structure with a hammer and evaluating the FFT of the measured acceleration. Halvorsen and Brown (1977) discussed some of the early problems encountered in the development of the computerised impact method. It has since been the subject of rapid development and is now in widespread use. One issue that is still largely unresolved is that of modelling the structural non-linearities induced by an impact (Ewins, 1984). Often a linear model is sufficient but for some systems it is unacceptable as potentially valuable structural dynamic information may be lost. To address this Brandon (1996) has proposed a non-linear methodology for identification with the impact method.

In the field of damage detection of steel structures most of the attention has been focused on the analysis of the *global* response of the structure to an impact. The main drawback with this approach is that it is insensitive to the small structural changes typically caused by damage. However, it has become apparent that the *local* response is more sensitive to damage if it is near to the location of impact. A method that uses measurement of local response to an impact is the coin-tap test developed by Cawley and Adams (1988). This is discussed further in Chapter 4.

3.6. Conclusions

The theoretical and experimental bases of dynamic methods of non-destructive testing has been presented together with a review of recent research progress in that field. The review has shown that the biggest problem faced by researchers is how to improve the sensitivity of dynamic methods so that they are capable of detecting smaller damage. Theoretical modelling has shown that, although new computational techniques such as the WEM and WCC can help, the sensitivity of methods that use *global* response data is generally not satisfactory for practical applications in structural steelwork. Furthermore, damage has been modelled using only stiffness reduction because it is difficult to measure damping changes from global response data. In the case of corrosion damaged steelwork damping changes could be significant and should not be ignored.

It would appear that an effective way to improve the sensitivity would be to measure the *local* response and therefore it was decided to investigate the possibility of applying the coin-tap test to steel structures. The increase in sensitivity over global methods would be advantageous in field measurements where high noise levels can be expected. Furthermore it is possible to detect the changes in damping caused by damage using this method and therefore take advantage of information neglected in the more popular methods based on detecting stiffness changes. Chapter 4 describes the theory and practice of the coin-tap test, and this is followed, in Chapter 5, by a discussion of pattern recognition methods by computer that are suitable for automatic classification of dynamic data. The application of the coin-tap test to real structures is described in Chapter 6 and Chapter 7.

4. THE COIN-TAP TEST

4.1. Introduction

Traditionally this method involved tapping each part of the structure with a coin and listening to the sound caused by the ensuing vibration. Defective areas sounded comparatively "dead" and this could be detected by a skilled inspector (Adams and Cawley, 1985). In the modern method the impact is applied with an instrumented hammer and damage is detected by computational analysis of the time history of the impact force. As the technique only detects defects local to the point of impact it could be quite time consuming if the whole structure is to be tested. This is not necessarily a serious drawback in this application because corrosion damage on petro-chemical steelwork tends to occur at known moisture traps rather than uniformly over the entire structure (Gallon, 1993).

Cawley and Adams (1988) showed that the difference in sound produced by defective areas compared with good areas was due to a change in the input force given to the structure. The differences in the input force caused by local stiffness change allowed the identification of damage. In the absence of damage the force should remain unchanged with location on a perfectly rigid structure. However, in flexible structures it can be expected to vary with location owing to spatial changes in the local stiffness and in the extent to which resonant vibrations are excited. Members with stiff supports at either end are commonly found in structural steelwork. Between the supports the stiffness is very sensitive to the distance from the supports (Owens and Knowles, 1992), these typically being welded or bolted joints. This is also true for wire ropes under tension. Therefore, striking by a hammer may result in significant variation in observed stiffness between blows. An investigation into the effect of this variability on the sensitivity of the coin-tap test when applied to unsupported aluminium beams (Cawley and Adams, 1988) and aluminium plates (Cawley and Adams, 1989) showed that although structural variations reduce the sensitivity of the test, typically sized defects were still detectable. In manual impacts, random variations in location are likely to be the largest source of experimental error and will therefore determine the sensitivity of the method to detect damage.

It is usual to assume a linear structural response in methods of computational damage detection based on global response data. This is because the response is measured with transducers that are normally mounted well away from the location of impact where non-linearities arise. The coin-tap test uses the impact force as the source of dynamic data and therefore the assumptions of linearity are reviewed later in this chapter before computational damage detection based on them can be used.

To facilitate damage detection the total energy and frequency distribution in the impact force is optimised. Two governing factors are velocity of impact and the hammer specifications, particularly tip stiffness and head mass. The hammer specifications can be easily controlled but for manual impacts accurate control over the velocity of impact cannot realistically be achieved. In these cases it is necessary to use methods of computational damage detection that are independent of hammer velocity.

In section 4.2 the validity of a linear model for the input force is tested and this is followed in section 4.3 by a review of methods of damage detection based on the analysis of the interacting force. It discusses existing measures based on detecting local stiffness change and presents two new methods both of which use time domain data. The first makes use of the ratio of peak impact force to the total impulse momentum. The other method uses the force time history to detect changes in structural vibrations caused by local damping. Section 4.4 discusses some technical details involved in the fabrication of two instrumented hammers for use in the coin-tap test, and the findings of this chapter are concluded in section 4.5.

4.2. Linearity in Impact Dynamics

The relationship between the impulsive force and its relative displacement during a dynamic collision is governed by several factors that determine the physical nature of the process. Where there is direct proportionality between the two the system can be said to have linear stiffness. Such processes are generally reversible and occur only when the relative displacement is small. When the linear regime breaks down, non-linear behaviour ensues

and this is characterised by either a more complex polynomial relationship between force and displacement or irreversible plastic deformation.

Consider a mass, m, striking one end of a mass-less spring of stiffness k as shown in Figure 4.1 (a). The velocity of the mass at the moment of impact is v. The force at the supporting surface is $P(t)$.

The mass and spring form a simple oscillator with zero damping and at no time during the collision does any external force act on the system. The displacement time history is obtained by setting the damping, C, and external force, $f(t)$, to zero in equation 3.1. Therefore

$$m\ddot{\delta}(t) + k\delta(t) = 0 \tag{4.1}$$

By inspection it can be seen that this equation can be solved by using a displacement time history of the form

$$\delta(t) = A\sin(\omega_c t) \tag{4.2}$$

where A is the amplitude and ω_c is the angular frequency constant that can be found in terms of k and m by substituting equation 4.2 into equation 4.1. Hence

$$m\omega_c{}^2 = k \tag{4.3}$$

Where,

$$\omega_c = \sqrt{\frac{k}{m}} \tag{4.4}$$

The internal force, $P(t)$, between the mass and spring can be obtained from equation 4.2 together with the spring stiffness, so that,

$$P(t) = (kv/\ \omega_c)\ \sin(\omega_c t) 0 \leq\ t \leq \tau_i \tag{4.5}$$

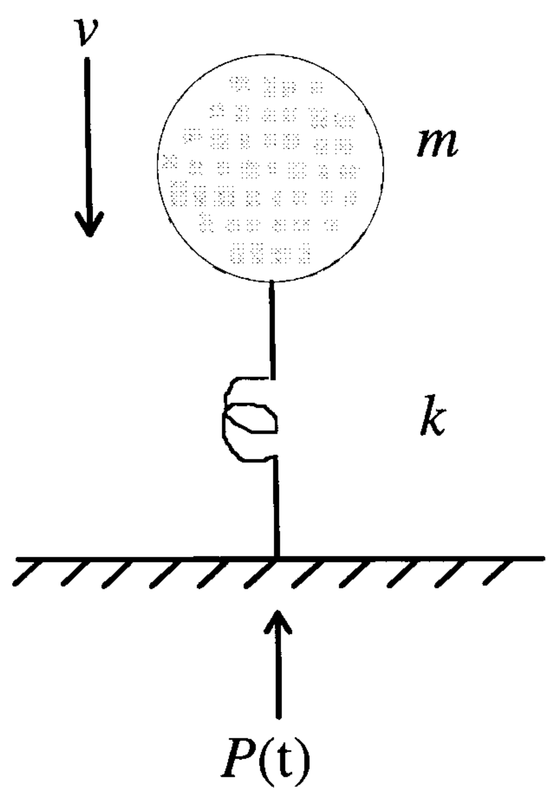

(a) Model

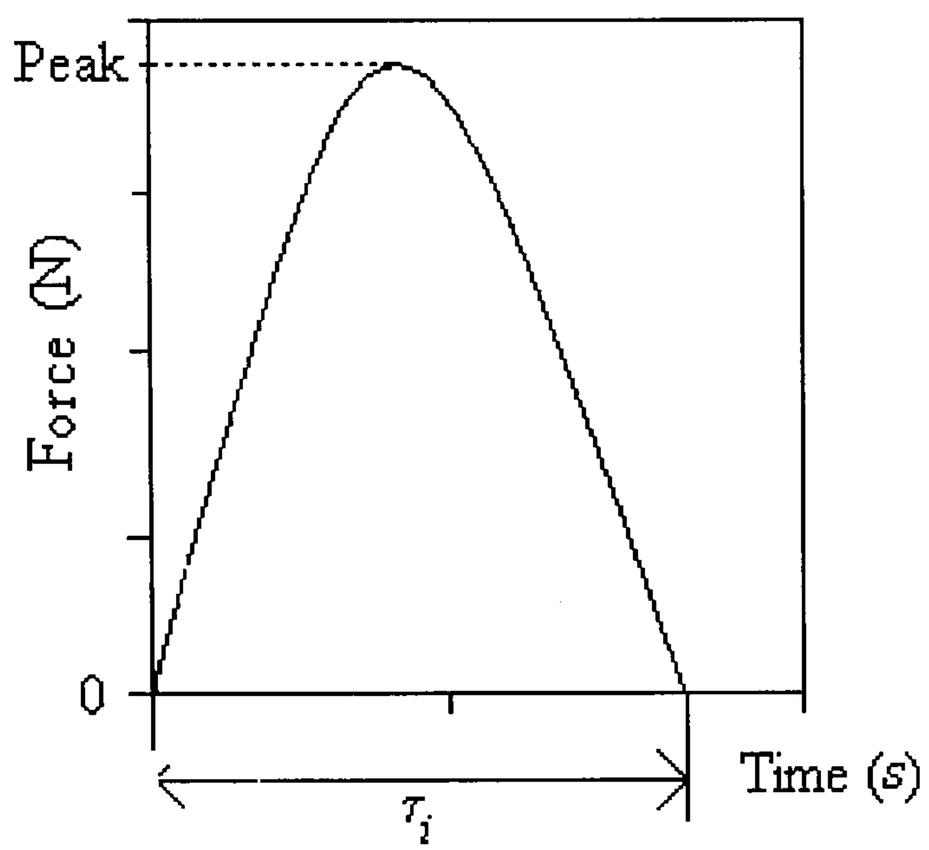

(b) Time History

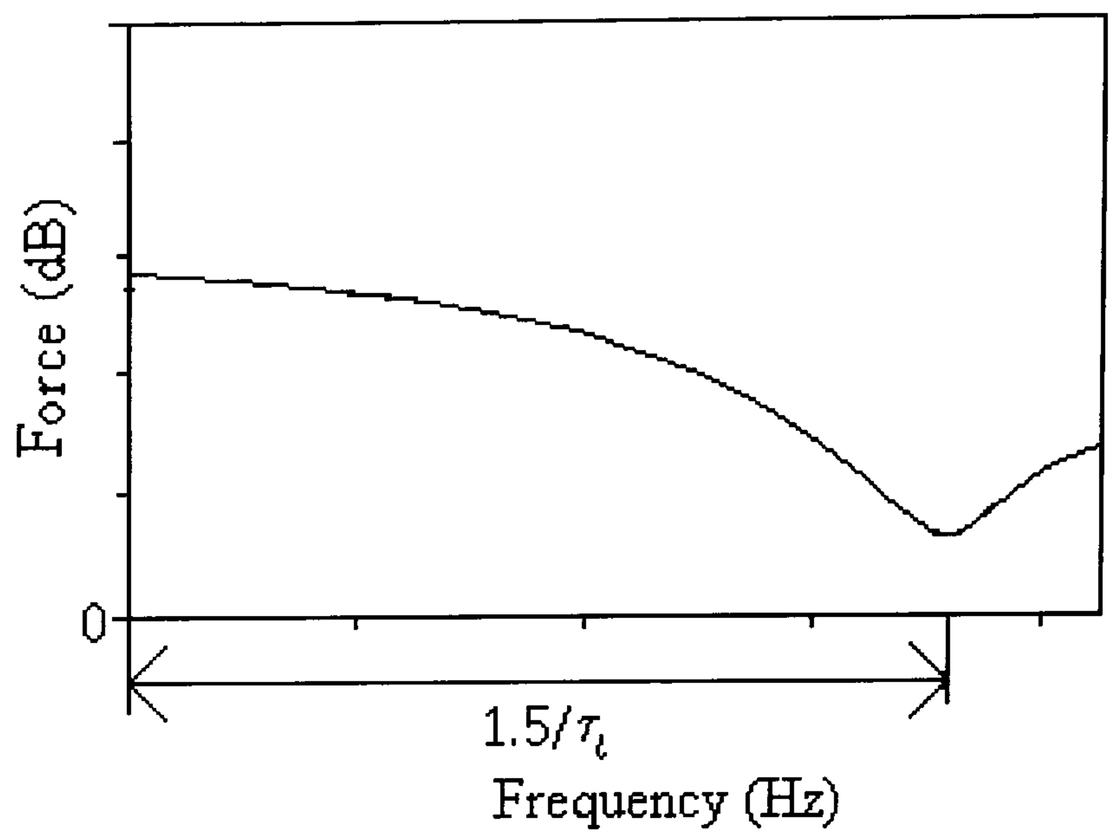

(c) Frequency Spectrum

Figure 4.1. Linear Elastic Collision

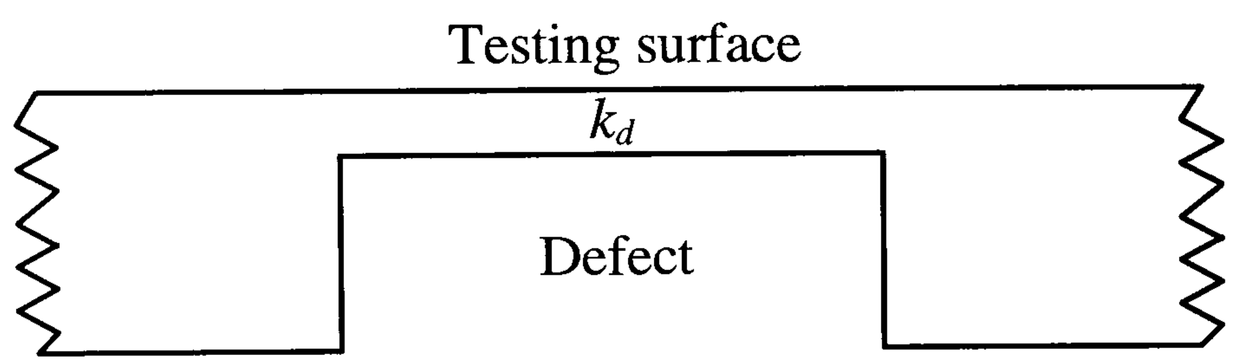

(a) Before Impact (side elevation)

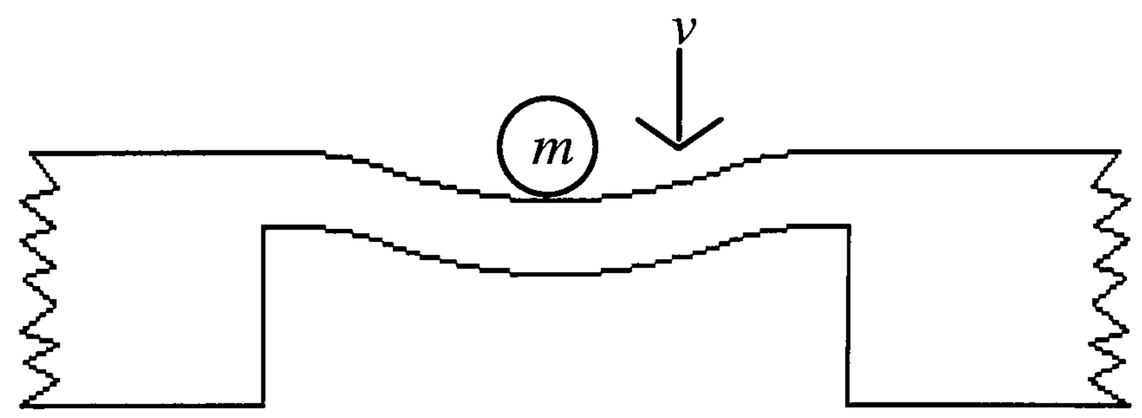

(b) Idealised Impact Scenario (side elevation)

Figure 4.2. Simplified Mechanical Impedance Model

where the amplitude is derived in Appendix A. The impulse duration τ_i, corresponds to half the period of the mass-spring system and is given by,

$$\tau_i = \pi/\omega_c \tag{4.6}$$

and the mass will rebound at speed v because the collision is perfectly elastic. From Newton's second law (the conservation of momentum) we get.

$$\int_0^{\tau_i} P\,dt = 2mv \tag{4.7}$$

Figure 4.1(b) and Figure 4.1(c) show force waveforms in the time and frequency domain respectively for the model described above. The time history has the shape of a half sine wave of period $2\tau_i$. The spectrum shown in Figure 4.1(c) is often plotted on logarithmic axes which present the amplitude as essentially constant (flat) below a certain frequency then rapidly falling to the first minimum.

The linear elastic theory is appropriate for an idealised impact scenario based on the simplified damage model assumed in the mechanical impedance method of testing (Cawley, 1984). In this model a defect in an unsupported beam is represented by a slot that traverses its width. The linear defect stiffness, k_d, is that of the part of the beam above the slot which is essentially fixed supported as shown in Figure 4.2 (a). A sinusoidally varying force, of frequency considerably less than the lowest resonant frequency, is applied to the structure. When a defect is present this causes a displacement that is assumed to be due to local bending above the defect. In the absence of a defect there is no bending. The impedance is determined from the ratio of peak force to peak displacement and, because of the aforementioned restriction on the frequency of excitation, this approximates to a measure of the local stiffness. In the idealised impact scenario the sinusoidally varying force is replaced by a half sine impulse provided by a mass, m, with incident velocity, v as shown in Figure 4.2 (b).

The above model assumes that the stiffness between the load and the structure is infinite. This assumption is inaccurate when considering a dynamic collision because of the large impulsive forces generated. In this case it is necessary to take account of the deformation of the contacting surfaces that occurs. Cawley (1984) suggested the inclusion of the contact *stiffness*, k_c, to take account of the finite stiffness of the dry contact used in the mechanical impedance method. The variation of the contact *force* between two elastic spheres as a function of the relative displacement of their centres is described, under static conditions, by the Hertz theory of contact (Hertz, 1881). This theory has also been extended to various dynamic collisions (Timoshenko and Goodier, 1934). A more accurate description of the impact process might also take account of the effects due to excited resonant vibrations. This theory has been applied to the case of a transverse collision between a mass and a beam by Raman (1920).

Figure 4.3 illustrates the impact scenario for an elastic sphere and beam with a finite contact stiffness. Figure 4.3 (a) is a snapshot at the instant when the sphere hits the structure with velocity, v. During the collision the separation of the beam and sphere is reduced from its initial value of d and the contacting surfaces become deformed. The sphere's kinetic energy is converted to elastic potential energy which is the integral of the contact force, $P(\delta)$ (assumed to be spread over a circular area of radius r) with respect to the relative displacement of the sphere and beam, δ, as shown in Figure 4.3 (b).

The contact stiffness predicted by Hertz's contact theory is non-linear with magnitude of impact. This is because the contact between a sphere of diameter d and an unyielding surface results in a non-linear relation between the contact force and the elastic compression of the sphere at the point of impact. Therefore the force, P, is not generally proportional to the relative displacement (except for very small displacements). Figure 4.3 (b) is a diagrammatic representation of a mechanical impedance model indicating the finite contact stiffness. The local stiffness measured by a tap on the structure is equivalent to that of a tap on either of the two springs in Figure 4.4. For the damaged beam it is due to the linear combination of the defect stiffness with the contact stiffness as shown in Figure 4.4 (a) whereas for the undamaged beam the defect stiffness is infinite and the local stiffness is due to the contact stiffness alone as shown in Figure 4.4 (b). In practice an improvement in

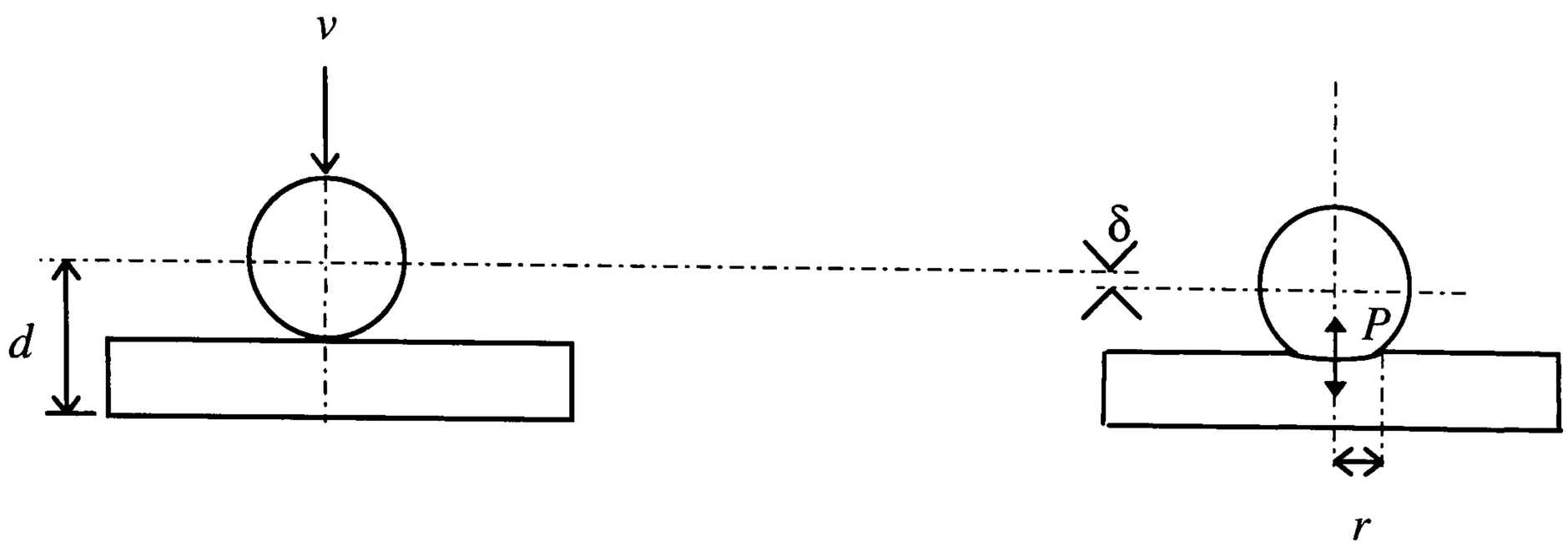

(a) Before Impact (b) During Impact

Figure 4.3. Elastic Sphere-Beam Collision

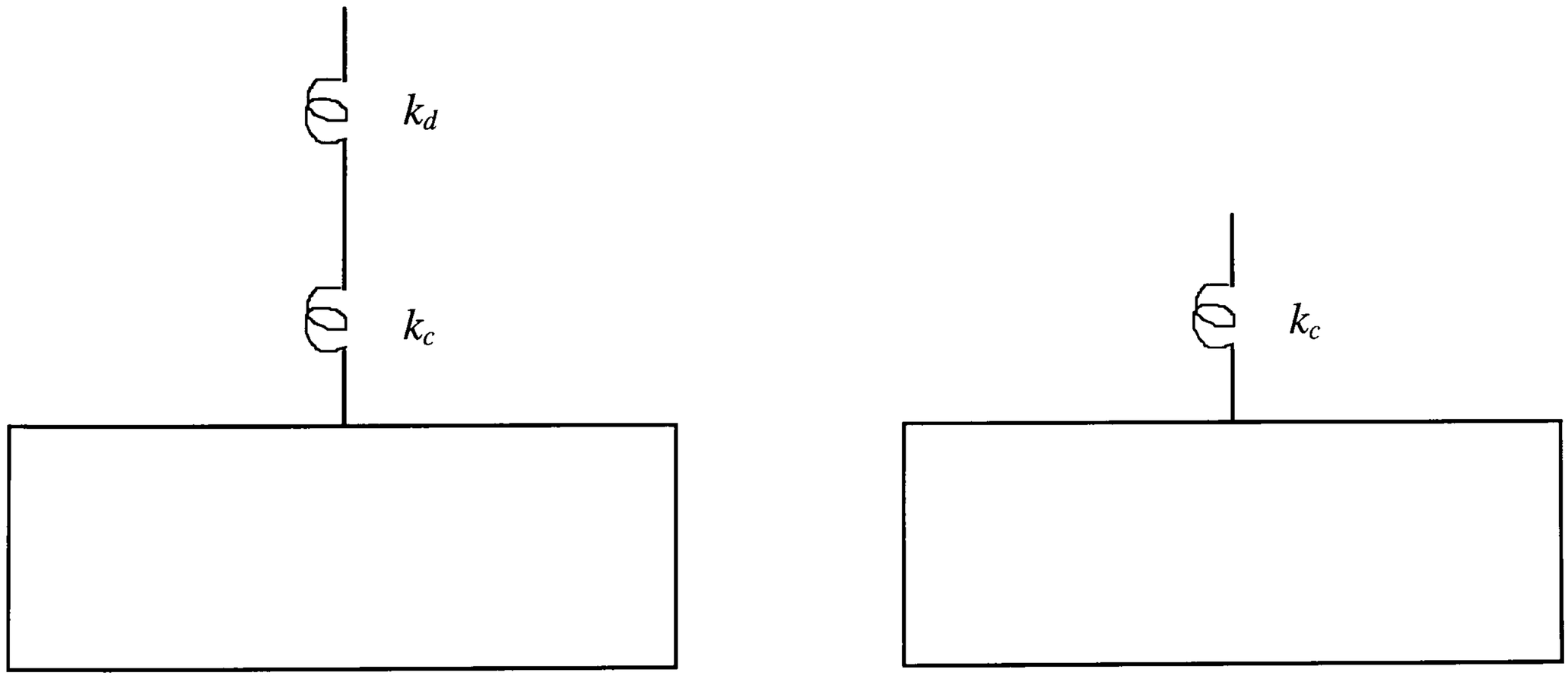

(a) Beam With Defect (b) Beam Without Defect

Figure 4.4. Mechanical Impedance Model

sensitivity can be achieved by increasing the contact stiffness, an infinite contact stiffness will give the maximum sensitivity to defects. Perfectly elastic conditions are in reality extremely rare and in a dynamic collision such as the one described some mechanical energy will inevitably be lost to sound and heat. One way in which this might happen is by plastic deformation at the contact point that occurs when the elastic limit is exceeded. The non-linear behaviour of a perfectly elastic contact stiffness breaks down under these circumstances and it is necessary to use an approximation.

Cawley and Adams (1988) tested the hypothesis that the behaviour of the contact stiffness was in practice approximately linear. In their experiment a rigid aluminium test block was impacted with a spherically tipped aluminium alloy striker of known mass, m, and incident velocity, v. The force versus time history during the collision was calculated by multiplying the signal provided by an accelerometer mounted behind the tip by the striker mass. According to the linear theory, the measured impulse duration, τ_i, should be related to the angular frequency according to equation 4.6, and the angular frequency is related to the peak force according to the first term on the RHS of equation 4.5. Using the measured velocity the peak force thus predicted was compared with that observed directly from the dynamic response. Similarly, the frequency of the first minimum in the spectrum is predicted from the impulse duration by $1.5/\tau_i$ (Cawley and Adams, 1988). This was also compared with the value observed from dynamic response. Furthermore, the initial momentum of the striker (observed) should be related to the total momentum transferred during the collision (predicted) by the conservation of momentum (equation 4.7) and these two values were compared. The results are summarised in table 4.1.

Table 4.1. Verification of Linearity (Cawley and Adams, 1988).

Quantity	Predicted	Observed
Total momentum (Ns)	0.030	0.034
Peak force (N)	220	198
First minimum in spectrum (kHz)	6.250	6.400

The agreement between predicted and observed results was regarded as close enough to justify the adoption of a linear representation of the contact stiffness in this case.

This discussion has shown that, using the mechanical impedance damage model, the impact scenario can be represented by an impact on a spring whose stiffness is a combination of the contact and defect stiffnesses. The linearity assumption, proposed by Cawley and Adams (1988) will hold for the manual impacts on structural steelwork described in later chapters if a comparable process occurs at the contact point.

4.3. Review of Measures for Damage Detection

This section presents new and established methods for identifying structural change, in order to detect damage from coin-tap test data. In the applications described in this thesis the methods are applied to data for the purposes of classification. For this reason both quantitative and qualitative methods of damage detection were considered appropriate. Quantitative methods involve the computation of some measure of structural change whereas qualitative methods involve some exercise in pattern recognition.

Experimental data usually contain some random noise from both the physical measurement and the electronic instrumentation used for data capture and processing. Therefore, in this application, insensitivity to background noise is a prerequisite of all useful methods. Furthermore, in order to obtain good statistical accuracy it is necessary to maximise the amount of experimental data included in any calculations used.

The coin-tap test indicates damage by changes in the local stiffness during an impact. Established measures have been devised to do this, indirectly, by detecting changes in the force input to the structure (section 4.3.1). However, it has emerged in the course of this study that, under certain circumstances, the interacting force contains direct information about the structural vibration. Changes in structural vibration can be detected directly and serve as an indicator of changes in structural damping. These findings are presented in section 4.3.2.

4.3.1. Damage Detection by Stiffness Changes

In this sub-section the impact response is assumed to be linear as discussed in section 4.2. Changes in local stiffness give rise to characteristic alterations in the waveform of the input force. These are illustrated in Figure 4.5 which presents the waveforms predicted for transverse impacts on a fixed supported bar with stiffness changes effected by changing the Young's modulus (E). It is assumed that the impact does not excite significant vibration in either the hammer or the bar.

In the time domain a reduction in local stiffness is accompanied by an increase in the impulse duration together with a reduction in the impulse amplitude. This is illustrated in Figure 4.5 (a), where τ_i^1 τ_i^2 and τ_i^3 represent the impulse durations obtained by impacts over an area with decreasing local stiffness such that $\tau_i^1 < \tau_i^2 < \tau_i^3$. In the frequency domain a reduction in local stiffness is accompanied by a more rapid rate of reduction in amplitude with frequency producing a spectrum with a lower high frequency content as indicated in Figure 4.5 (b).

The effect of impacts at the same location, but with different hammer velocities, is illustrated by the dotted curves. In the time domain a reduced velocity impact produces a lower peak force as shown in Figure 4.5 (a). The duration of the impulse is unchanged because this is only dependent on the hammer mass and local stiffness. In the frequency domain there is a reduction in the amplitude at zero frequency. This amplitude can be shown, in equation 3.2, to correspond to the mean force level in the time domain by substituting $f(t)$ with $P(t)$, putting $\omega = 0$, performing the integration and dividing the result by the impulse duration.

This illustrates why it is necessary, when experimental data is obtained by manual impact, to detect damage by calculating quantities sensitive to local stiffness that are also independent of hammer velocity. The change in impulse height is not therefore a useful measure of stiffness change. However, the first minimum frequency *is* independent of impact velocity as indicated by Figure 4.5 (b) in which the first minima for spectra

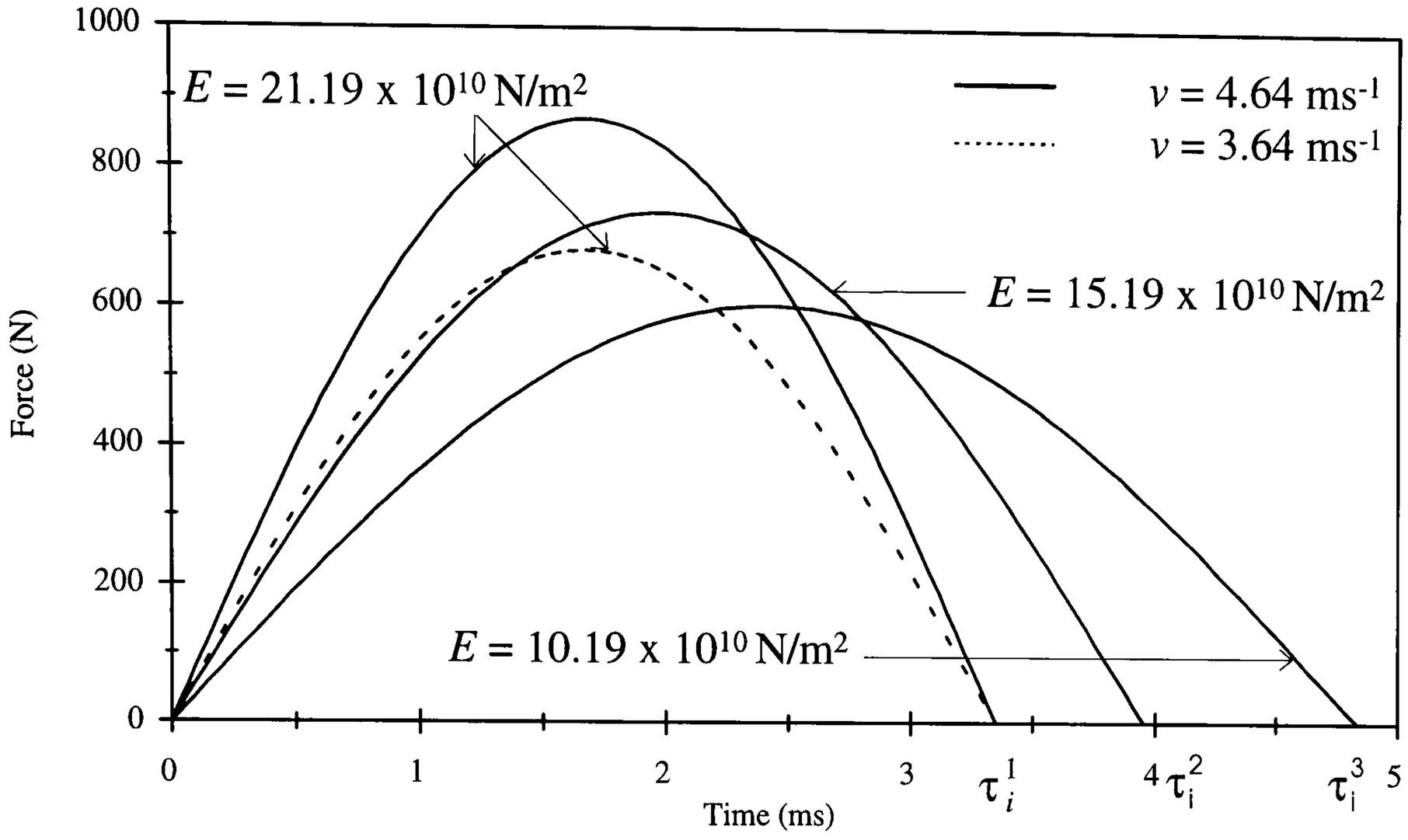

(a) Time Histories

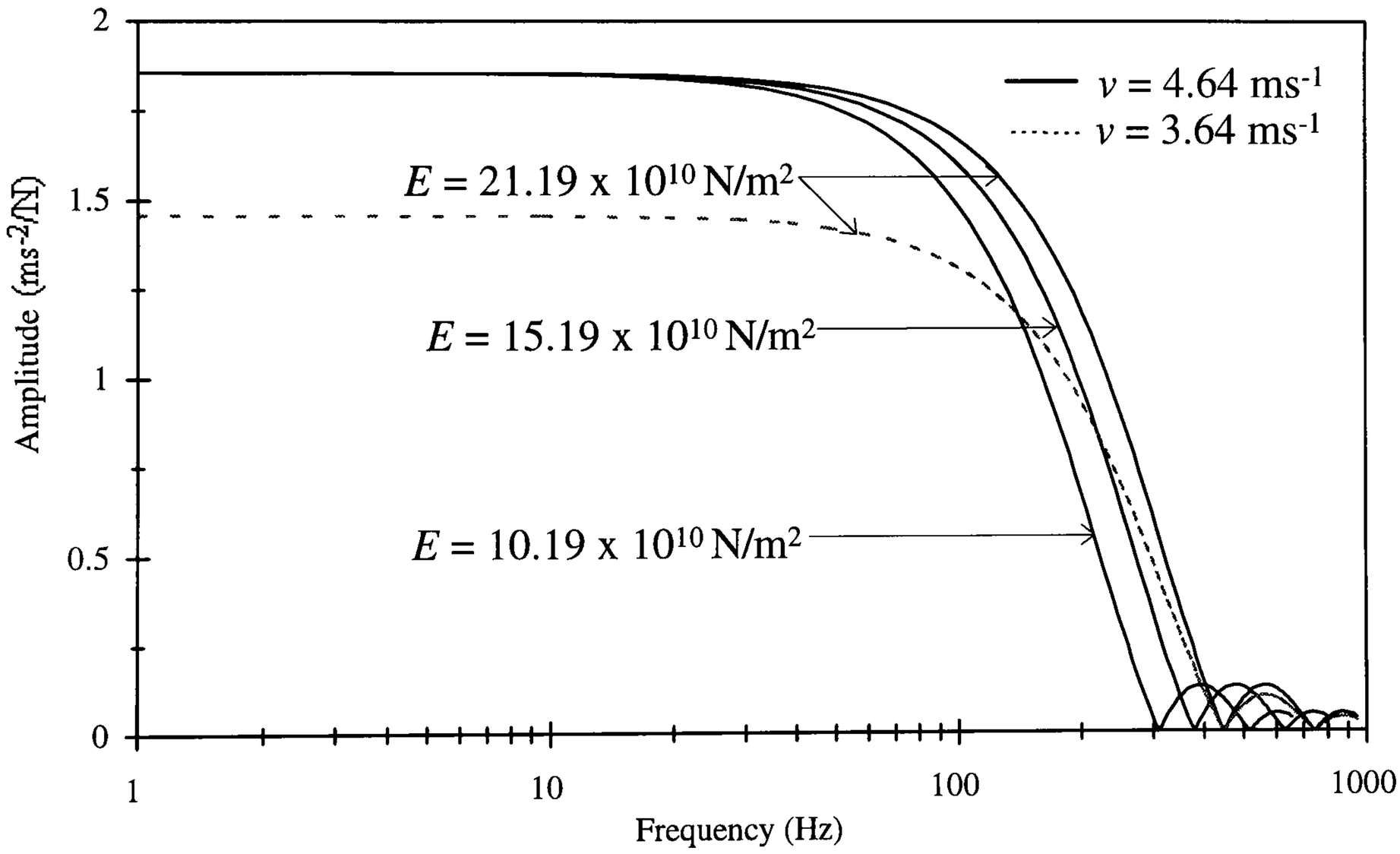

(b) Frequency Spectra (logarithmic scale on x-axis)

Figure 4.5. Effect of Hammer Velocity and Local Stiffness on Dynamic Waveforms

(Transverse Impact Near Support on Fixed Supported Steel Bar (1.8m), m = 200g)

corresponding to impacts at two different velocities both occur at approximately 455 Hz. Similarly, in the time domain the impulse durations for impacts at the two velocities are both approximately 3.4 ms. These would appear to be the ideal measures of stiffness change for manual impacts because of the expected variability in hammer velocity on impact. However, both are estimated in regions of the dynamic response where the amplitude is low and the signal to noise ratio is correspondingly high; consequently it would be difficult to obtain an accurate value.

There is a direct relationship between the impulse duration, the peak force and a frequency known as the first cut-off point. It is easier to measure the first cut-off frequency than the impulse duration because it occurs in a region of the spectrum where the signal to noise ratio is comparatively high and, unlike the peak force, the cut-off frequency is independent of hammer velocity. This measure of local stiffness is described in more detail in the following sub-section.

4.3.1.1. The First Cut-off Frequency

The frequency spectrm, $P(j\omega)$, of the internal force between the mass and spring for the linear elastic collision described in section 4.2 is obtained by substituting $P(t)$ from equation 4.5 for $\boldsymbol{f}(t)$ in equation 3.2 and integrating over the impulse duration.

$$P(j\omega) = \int_0^{\tau_i} P(t).e^{j\omega t}.dt \tag{4.8}$$

Therefore

$$P(j\omega) = \int_0^{\tau_i} P_{max}\sin(\omega_c t).e^{j\omega t}.dt$$

The constant P_{max} represents the peak force of the impulse defined in equation 4.5 as kv/ω_c. Substituting ω_c from equation 4.6 gives a general expression for the spectrum of the impulse.

Therefore

$$P(j\omega) = P_{max}\int_0^{\tau_i} \sin\left(\frac{\pi t}{\tau_i}\right).e^{j\omega t}.dt \tag{4.9}$$

Integrating this expression by parts gives the real and imaginary components. The spectrum can then be expressed in terms of its magnitude, $|P(j\omega)|$ and phase, $\phi(\omega)$ by the following expressions (Harris and Crede, 1961):

$$|P(j\omega)| = \frac{2\tau_i P_{max}}{\pi}\left|\frac{\cos(\omega\tau/2)}{1-(\omega\tau_i/\pi)^2}\right| \qquad \omega \neq \pi/\tau_i \tag{4.10}$$

$$|P(j\omega_c)| = \frac{P_{max}\tau_i}{2} \qquad \omega = \omega_c$$

$$\phi(\omega) = -\frac{\omega\tau_i}{2} + n\pi \tag{4.11}$$

The first cut-off frequency is defined as $\omega = \omega_c$ and therefore it is related to the impulse duration according to equation 4.6. The spectral amplitude at the cut-off frequency, $|P(j\omega_c)|$, is defined by equation 4.10. The amplitude at zero frequency, $|P(0)|$, is obtained by putting $\omega = 0$ in equation 4.10.

$$|P(0)| = \frac{2P_{max}\tau_i}{\pi} \tag{4.12}$$

A convenient method of finding the cut-off frequency in the spectrum is to measure the frequency interval corresponding to a reduction in amplitude from $|P(0)|$ to $|P(j\omega_c)|$. The spectral amplitude is commonly displayed on a logarithmic scale in units of decibels (dB).

$$\mathrm{dB}(\omega) = 20 \text{ x } \log |P(j\omega)| \tag{4.13}$$

The required amplitude reduction $\Delta P(j\omega)$ can be evaluated in decibels by substituting the corresponding expressions for the spectral amplitude:

$$\mathrm{dB}(0) - \mathrm{dB}(\omega_c) = 20 \text{ x } (\log |P(0)| - \log |P(j\omega_c)|)$$

Therefore

$$\Delta P(j\omega) = 20 \times log\left(\frac{|P(0)|}{|P(j\omega_c)|}\right)$$

$$= 20 \times \log\left(\frac{\left(\frac{2P_{max}\tau_i}{\pi}\right)}{\left(\frac{P_{max}\tau_i}{2}\right)}\right)$$

$$= 20 \times \log\left(\frac{4}{\pi}\right)$$

Therefore

$$\Delta P(j\omega) = 2 \text{ dB (1 s.f.)} \qquad (4.14)$$

Therefore the first cut-off frequency can be estimated by inversely mapping a spectral amplitude of 2 dB less than the amplitude at zero frequency onto the frequency axis. This frequency can be used with manual impacts to detect damage because it is independent of the hammer velocity but dependent on local stiffness.

Although the signal to noise ratio is comparatively high near the first cut-off frequency, this quantity is still vulnerable to random noise because it is based on the measurement of a single data point. The following two sub-sections describe quantities that are less sensitive to random noise because they are calculated from a larger amount of data.

4.3.1.2. The Ratio of Areas Under the Frequency Spectrum

Earlier in this section it was noted that a reduction in local stiffness had the effect of lowering the high frequency content of the spectrum as indicated by Figure 4.5 (b). Therefore, the changes in the high frequency content of the spectrum could be used to identify changes in local stiffness for manual impacts provided it was independent of the hammer velocity. It can be demonstrated that this is not the case by inspecting the spectra for impacts at two different impact velocities on a local stiffness corresponding to E=21.19x10^{10} Nm^{-2}. The areas are very different because of the amplitude difference.

This problem can be avoided by normalising the frequency spectrum to the (maximum) amplitude at 0 Hz. This has the effect of producing spectra with unit maximum amplitude that are identical for a particular local stiffness, regardless of the hammer velocity. However, a reduction in local stiffness still lowers the high frequency content of the normalised spectrum. The effect of normalisation is illustrated in Figure 4.6 (a) and Figure 4.6 (b) where the spectra are presented on a linear axis for greater clarity. Figure 4.6 (a) shows the spectra corresponding to two impacts with different hammer velocities on areas of differing local stiffness. The normalised spectra are shown in Figure 4.6 (b) and clearly the spectrum corresponding to impact over the area with higher local stiffness has a greater high frequency content. Therefore this property can be used to identify changes in local stiffness when significant random variations in hammer velocity are expected such as during manual impacts. The high frequency content of a spectrum can be defined as the area under the curve and beyond an arbitrary threshold frequency, ν_t. This was the basis of a quantity used by Cawley and Adams (1988) to detect stiffness change in aluminium beams with the coin-tap test. They calculated the ratio, R_f, of the high frequency area, B, to the total area enclosed below a maximum frequency, ν_{max}, near to the first minimum. Thus

$$R_f = B/(A + B) \tag{4.15}$$

where A is the area enclosed by the spectrum below the threshold frequency. This is illustrated in Figure 4.6 (c) where the threshold frequency and the maximum frequency are 200 Hz and 500 Hz respectively. The minimum recommended amplitude to be used in the calculation is 30 dB below the amplitude at zero frequency (Cawley and Adams, 1988). Figure 4.6 also shows the location of the maximum analysis frequency, ν_B.

The present discussion has revealed that, currently, the only methods of detecting local stiffness change that are suitable for this application, use spectral data. Modern spectrum analysers are capable of displaying both the time history and the frequency spectrum simultaneously from a single impact. In order to make full use of the available data it was decided to devise a measure sensitive to stiffness change that is also suitable for time domain data obtained by manual impact. A new quantity has emerged from this investigation and it is described in the following sub-section.

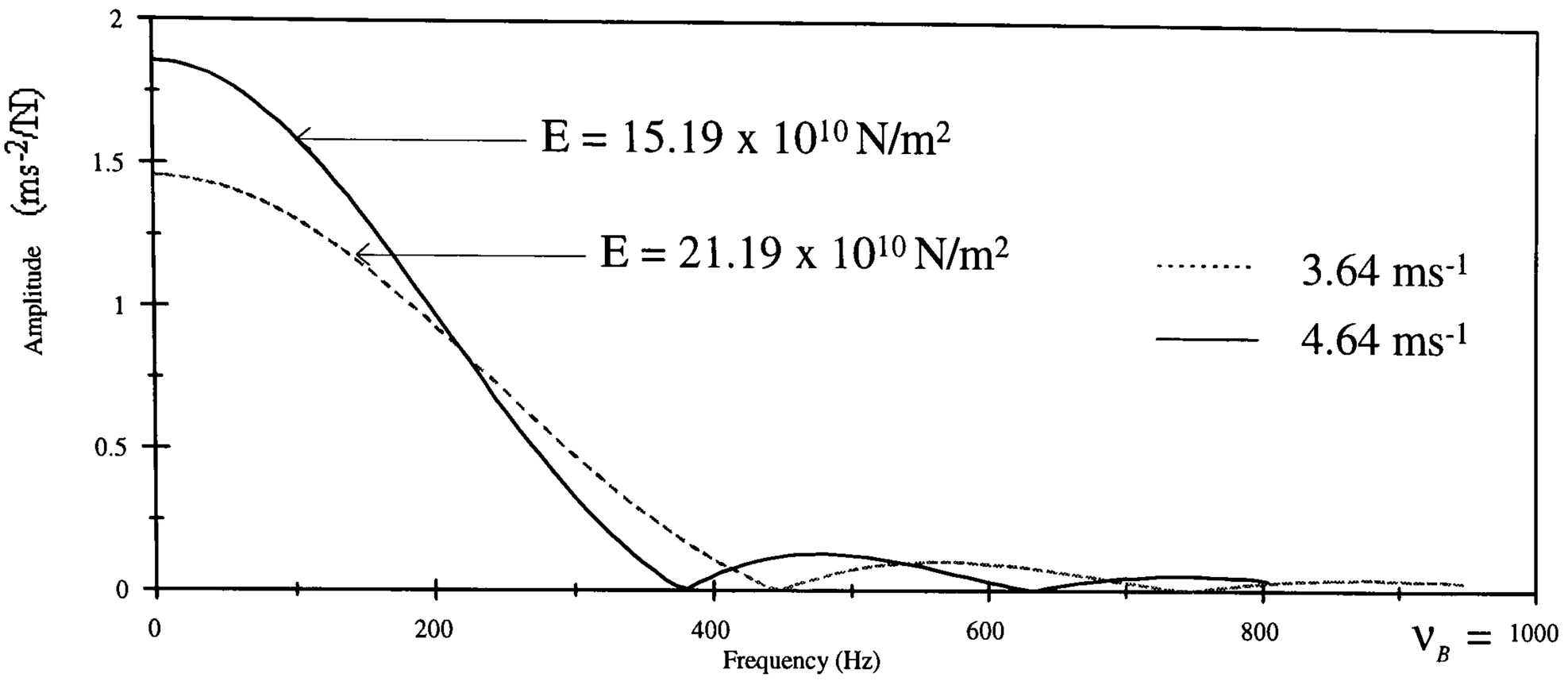

(a) Spectra for Different Impacts before normalisation

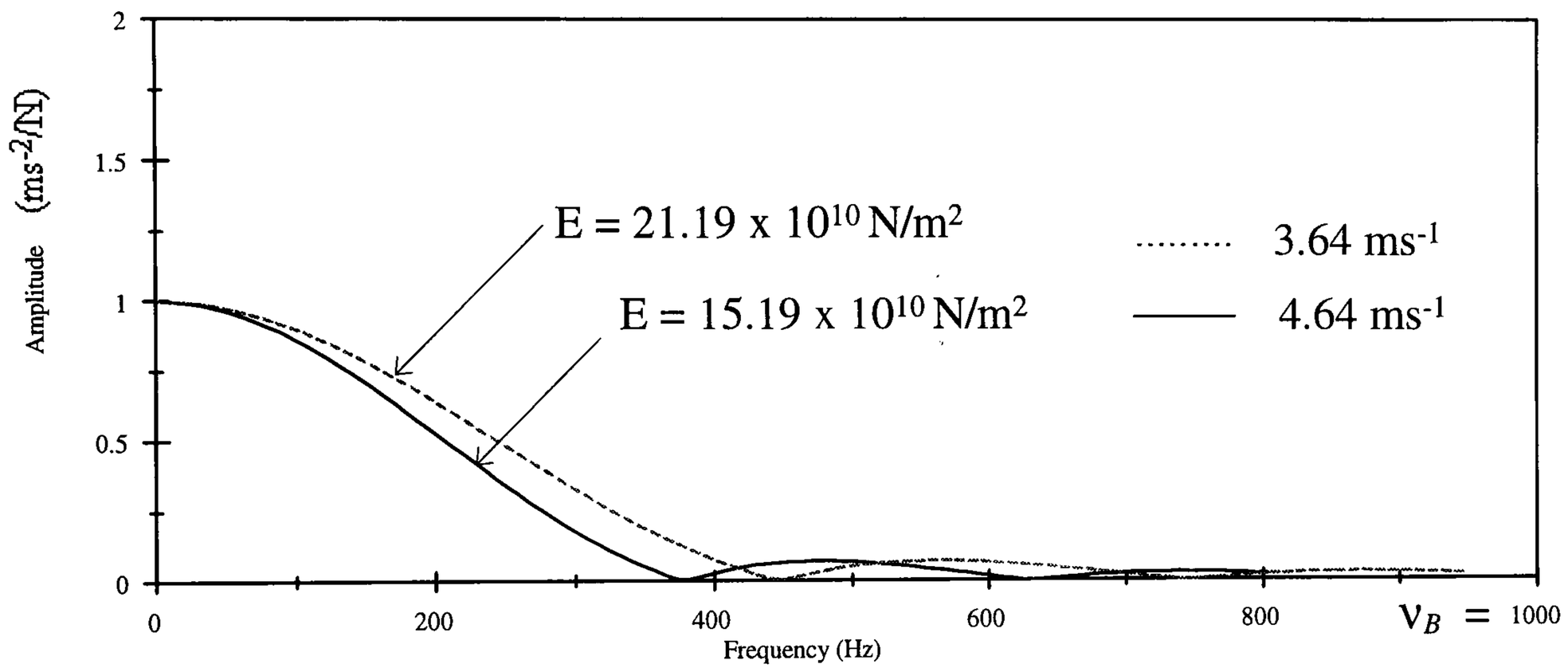

(b) Spectra for Different Impacts after normalisation.

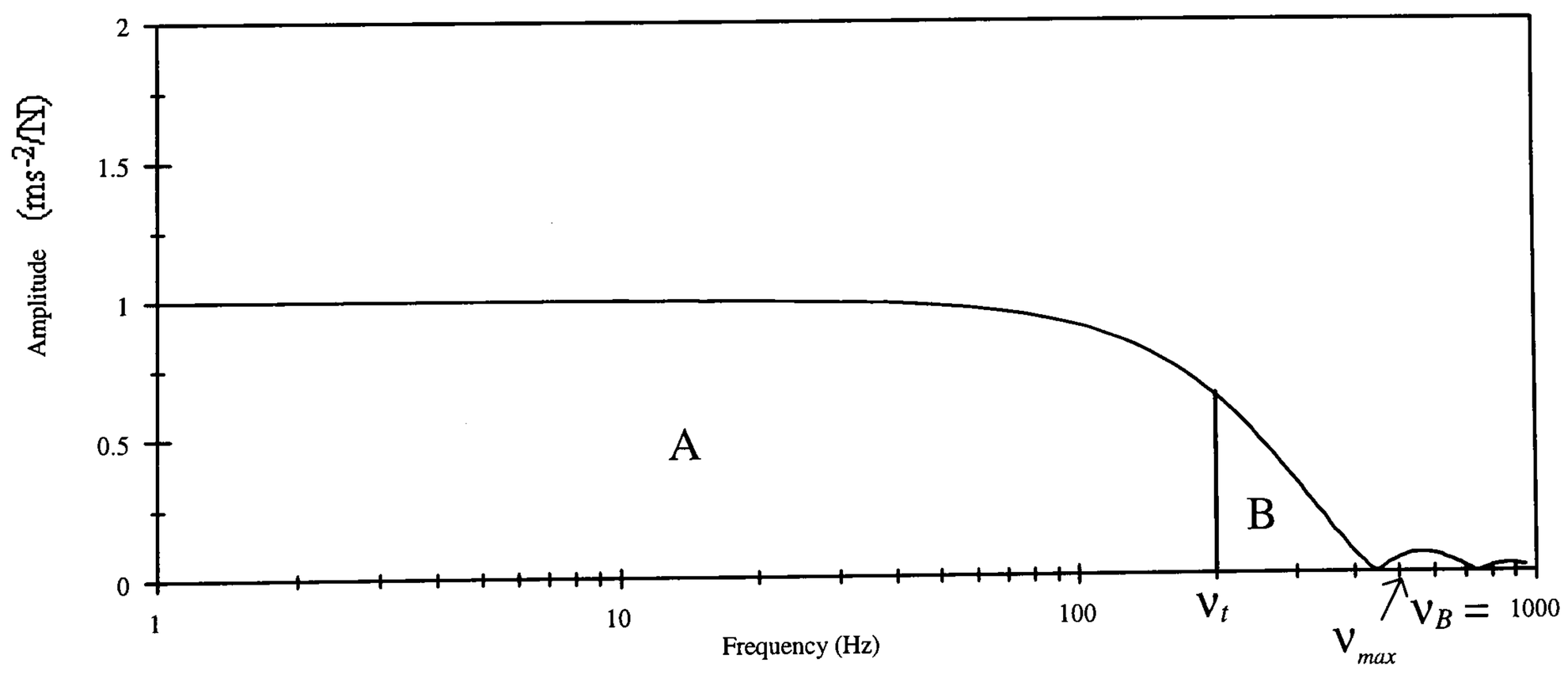

(c) Illustration of Area Measurements Under the Spectrum (logarithmic scale).

Figure 4.6. Ratio of Areas Under the Frequency Spectrum

4.3.1.3. The Ratio of Impulse Peak Force to Enclosed Area

This sub-section shows that the ratio, R_t, of the peak force to the total area under the impulse is a measure of local stiffness that is suitable for data obtained by manual impact.

The impulse width is dependent on the contact stiffness according to equation 4.4 and equation 4.6. Figure 4.5 (a) shows the impulses for impacts over three different local stiffnesses for a constant hammer velocity (4.64 ms^{-1}). In each case the total area under the impulse is a constant given by the conservation of momentum (equation 4.7). The peak force reduces with local stiffness so it follows that R_t will also reduce proving that it is an effective measure of local stiffness.

Figure 4.5 (a) shows the effect of impacts of different hammer velocity on the local stiffness corresponding to $E = 21.19\text{x}10^{10}\ Nm^{-2}$. Both impacts produce impulses with the same duration, τ_i. If the peak force corresponding to a hammer velocity of 4.64 ms^{-2} is $P_{max,1}$, the area, A_1, under this impulse is given by:

$$A_1 = P_{max,1}\int_0^{t_i} \sin(\omega_c t)\ d(t) \tag{4.16}$$

Therefore

$$A_1 = P_{max,1}\left[\frac{\cos(\omega_c t)}{\omega_c}\right]_0^{\tau_i}$$

Therefore

$$|A_1| = \frac{2\tau_i P_{max,1}}{\pi} \tag{4.17}$$

where $\omega_c = \pi/\tau_i$. The ratio for this impulse, $R_{1,t}$, is given by the equation.

$$R_{1,t} = \frac{\pi}{2\tau_i} \tag{4.18}$$

If the peak force corresponding to a hammer velocity of 3.64 ms^{-2} is, $P_{max,2}$, then the area, A_2, under this impulse is given by the following equation.

$$|A_2| = \frac{2\tau_i P_{max,2}}{\pi} \tag{4.19}$$

Clearly the ratio for this impulse is the same, i.e. $R_{1,t} = R_{2,t}$. This shows that R_t is independent of hammer velocity. Therefore it is a particularly useful measure of local stiffness when data is obtained by manual impact because significant random variations in hammer velocity are to be expected.

If there is noise on the signal, or insufficient data points are obtained to define the peak region precisely, then poor accuracy will result. In such cases, changes in local stiffness may be detected with a ratio, R'_t, derived by making a slight modification to the R_t calculation. The peak force is replaced by the area under the impulse within a small interval of width 2c centred on $\tau_i/2$.

If the angular frequency, peak amplitude and impulse duration for impact on the local stiffness corresponding to $E = 21.19\text{x}10^{10}$ Nm^{-2} at 4.64 ms^{-1} are ω_c $P_{max,1}$ and $\tau_{i,1}$ respectively, then the area, A'_1 under the impulse within the interval is given by the equation:

$$A'_1 = P_{max,1} \int_{(t_{i,1}/2)-c}^{(t_{i,1}/2)+c} \sin \omega_c t \, dt \tag{4.20}$$

Therefore $$A'_1 = P_{max,1} \left[\frac{\cos(\omega_c t)}{\omega_c} \right]_{t_1/2-c}^{t_1/2+c}$$

Therefore $$A'_1 = \frac{P_{max,1}}{\omega_c} \left(-2 \sin(\omega_c \tau_{i,1} / 2) \sin(c\omega_c) \right)$$

Therefore,

$$|A'_1| = \frac{2\tau_{i,1} P_{max,1}}{\pi}\left(\sin(\pi c / \tau_{i,1})\right) \tag{4.21}$$

where equation 4.21 is obtained by substituting $\omega_c = \pi/\tau$. Dividing equation 4.21 by equation 4.17 gives an expression for $R'_{t,1}$, the modified ratio of this impulse.

$$R'_{t,1} = \sin(\pi c/\tau_{i,1}) \tag{4.22}$$

For a fixed interval width this quantity is only dependent on the impulse duration. The impulse duration, $\tau_{i,2}$, for an impact on the local stiffness corresponding to $E = 10.19\text{x}10^{10}$ Nm^{-2} is greater than it is for the previous case ($E = 21.19\text{x}10^{10}$ Nm^{-2}) so $R'_{t,1}$ is reduced. Therefore, the ratio R'_t is an effective measure of local stiffness.

Impacts of different velocity on the same local stiffness have the same impulse duration (Figure 4.4a). Therefore, $\tau_{i,1}$ in equation 4.22 is constant and the modified ratio is also independent of impact velocity.

As the interval width approaches the impulse duration the ratio R'_t tends to 1 and its sensitivity to local stiffness change diminishes. Therefore, the optimum interval width will depend on the balance between accuracy and sensitivity appropriate for the available data.

This concludes the discussion of measures to detect structural change by identifying the associated changes in local stiffness. The three measures described will be used in tests on structural steelwork described in later chapters. The next section describes a method of detecting structural change by the identification of changes in local damping using coin-tap test data.

4.3.2. Damage Detection by Changes in Structural Damping

This section presents a brief discussion of the physical principles behind a new method for identifying changes in structural damping from the time history of a hammer impact. The method differs from those previously discussed in that it offers the possibility of detecting

damage by inspection of the structural vibrations rather than the local stiffness. A complete mathematical treatment of the propagation of vibrations within materials is outside the scope of this thesis but the reader is referred to the text by French (1971) which presents a comprehensive discourse on the subject matter.

According to the linear elastic model of impact the total kinetic energy is conserved so that the speed at which a hammer recoils from a fixed surface is the same as its incident speed. Although the linear elastic model may remain a valid approximation (section 4.2), these conditions are rarely achieved in practice and some of the hammer's initial energy is lost in the collision. A small amount of the energy deficit is due to energy dissipated immediately as sound and heat. However, the dominant factors are deformation at the contact surface and excited structural vibrations.

Deformation occurs because one of the contacting surfaces is usually curved and generates a high local stress which causes highly localised elastic and plastic deformation in one of the surfaces resulting in the dissipation of heat energy. Vibrations generally occur in the structure rather than the hammer because of design constraints on the latter. They are excited at the instant of contact and may persist for some time, even after contact has ceased, dissipating energy as sound and (primarily) heat. In the time domain this means that the contact duration is now dependent on the coefficient of restitution (Newton, 1686) which is the ratio of the final to the initial total velocity of the system in the direction of impact. The structural vibrations are of great importance because they are sensitive to changes in structural damping.

There are several factors that determine the magnitude and nature of the excited structural vibrations. These factors either affect the structure's FRF or the effective bandwidth of the frequency spectrum of the impulse. Structural vibrations are not significantly excited when the first natural frequency (fundamental) is significantly greater than the impulse bandwidth. In the time domain this means that the half period of the fundamental is small in comparison with the contact duration, which is largely determined by the hammer mass and the contact stiffness. The structural vibrations are weakly excited and occur well within the impulse

duration (Rayleigh, 1906). High natural frequencies are characteristic of structures with simple shapes exhibiting a low surface area to volume ratio.

This is not true of structural steelwork which consists of interconnected members exhibiting a high surface area to volume ratio. The first few natural frequencies of these structures are usually well within the bandwidth of a typical manual impact involving metal to metal contact. Under these conditions the contact duration (Goldsmith, 1960) becomes extended and the time history may be profoundly affected by structural vibrations.

What is of particular interest in the present discussion is the case whereby the contact duration is comparable with the half period of the fundamental. Strongly excited stress waves corresponding to higher order natural frequencies radiate a considerable distance from the impact location during the period of contact. This effect has been reported for longitudinal waves produced by the coaxial impact of cylindrical bars (Conway and Jakubowski, 1969). Impact testing of structural steelwork generates transverse stress waves, and higher order natural frequencies of vibrations are set-up when these are reflected from joints and interfaces and form standing waves. If this occurs during contact then these oscillations modulate the contact force, an effect known as ringing.

Therefore any structural damage that significantly affects the damping of a vibration mode can be identified by inspecting the impact time history for a reduction in the amplitude of oscillations due to that mode. This will be true provided that the hammer carries sufficient kinetic energy and impinges on the correct location to excite strongly a number of higher order modes as well as the fundamental.

The phenomenon of ringing is illustrated in Figure 4.7. In the absence of structural vibration the time history of the impact is assumed to approximate to a half-sine impulse with a duration of approximately 12.5 ms, as shown in Figure 4.7 (a). However, the impact is assumed to excite the fundamental, a low frequency structural mode at 75 Hz and a high frequency structural mode at 637 Hz. The time history, approximated by a linear superposition of the contact force with the modes of vibration, is shown in Figure 4.7 (c).

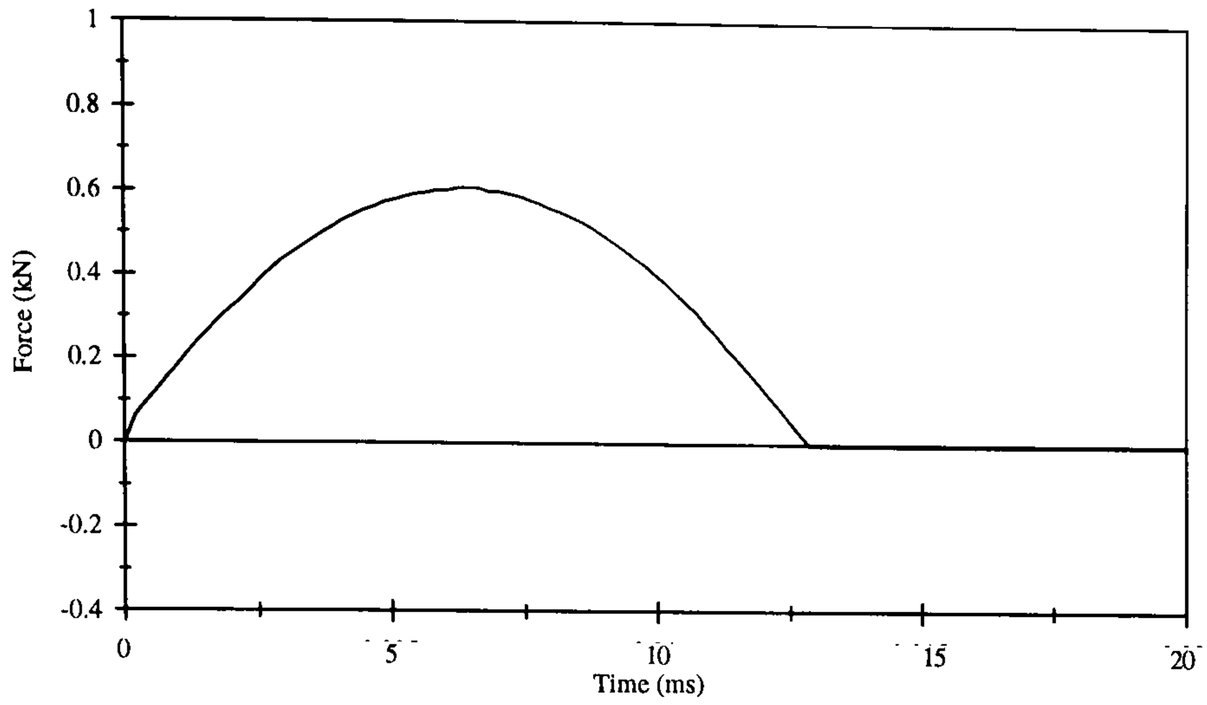

(a) Time History of Impact with no Ringing

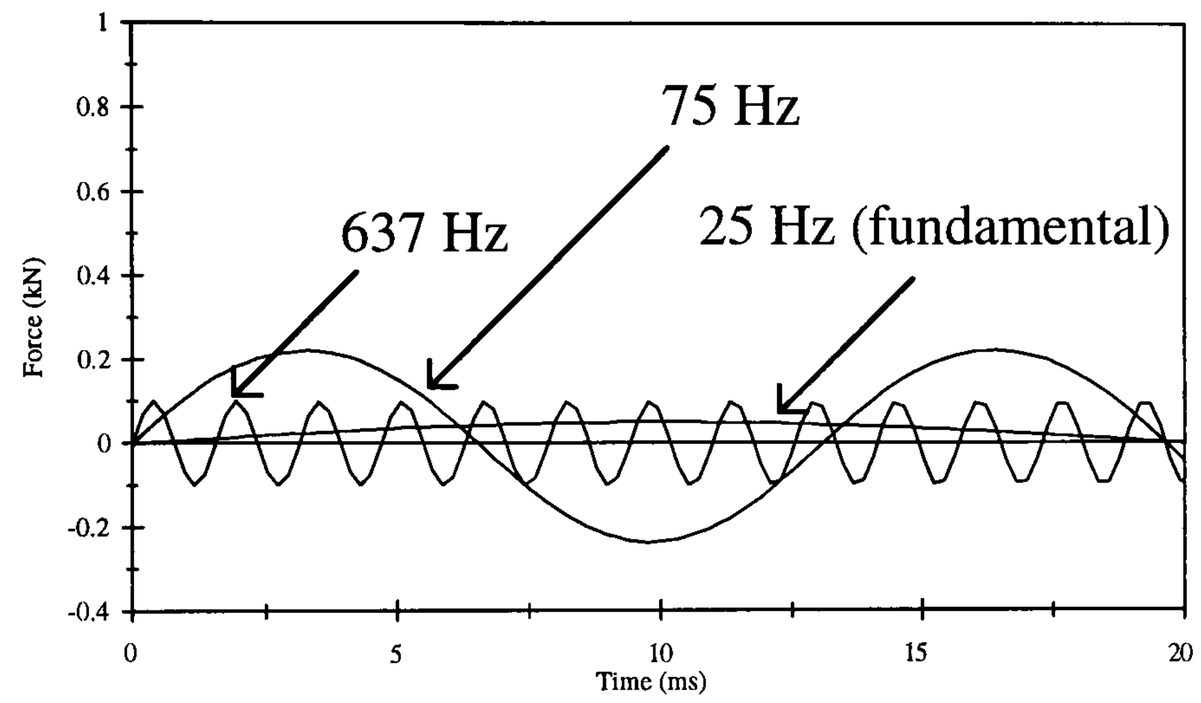

(b) Three Structural Modes Excited by Impact

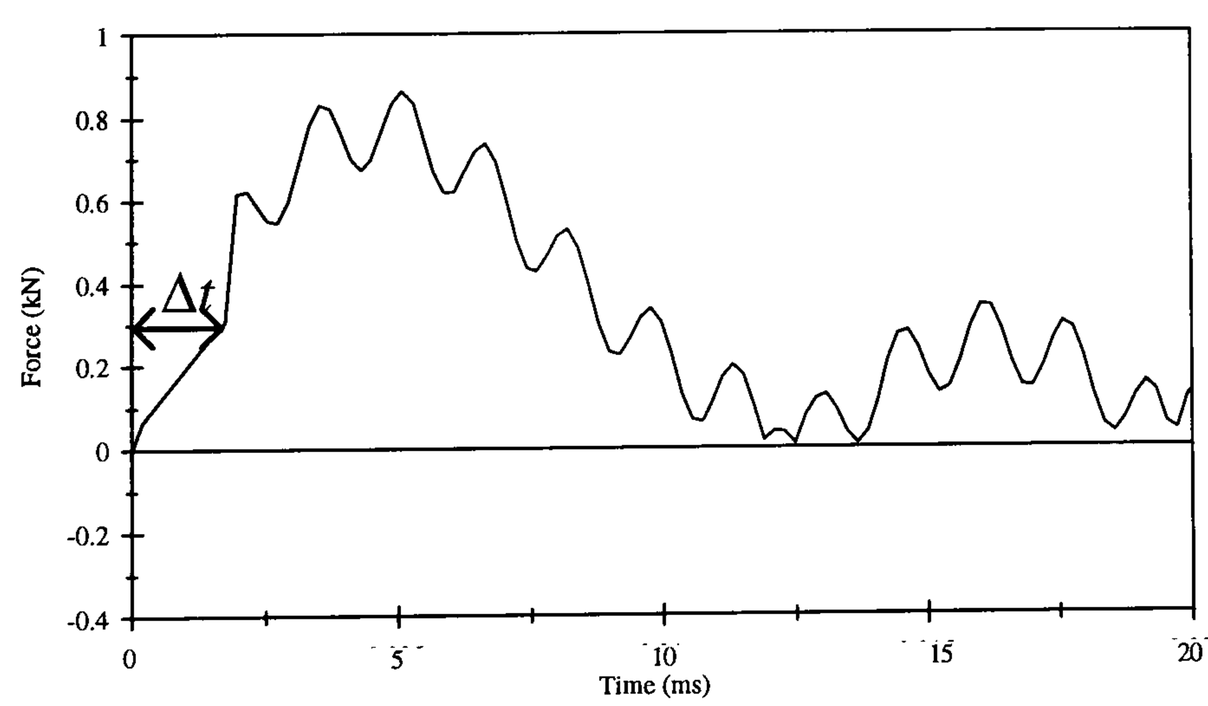

(c) Expected Time History

Figure 4.7. Illustration of 'Ringing'

Ringing effects becomes apparent after an interval of Δt which corresponds to the time taken for stress waves to return to the impact location after reflecting from the nearest joint or interface. At this point the time history becomes modulated with ripples caused by the high frequency mode. However, the effect of the low frequency mode is not apparent over the first 12.5 ms because its period is similar to that of the impulse duration which dominates because its amplitude is greater. The low frequency mode becomes apparent beyond 12.5 ms when the impulse amplitude has returned to zero but contact is maintained by the weakly excited fundamental.

4.4. Design and Fabrication of Instrumented Hammers

The previous section highlighted the importance of controlling impact parameters to optimise damage detection with the coin-tap test. The sensitivity of methods based on changes in local stiffness were shown to depend on the contact stiffness (section 4.2) and it was noted that the statistical accuracy was improved by obtaining a larger number of data points (section 4.3). The method based on changes in local damping required that the hammer carried sufficient energy to excite structural vibrations. To some extent these requirements could be met with some control over the specifications of the hammer. This section presents the dynamic and technical considerations involved in making two instrumented hammers for applying the coin-tap test to structural steelwork.

4.4.1. Dynamic Considerations

The dynamic waveforms of the interacting force between the hammer and structure are influenced by the contact stiffness. The contact stiffness, on which the local stiffness is dependent, is controlled by the choice of material for the hammer tip. In order of decreasing Young's modulus: steel, aluminium, nylon, plastic and polyurethane were available for making the tips. The influences of local stiffness on the dynamic waveforms of the impact force have been discussed in section 4.3.1. It follows that tips made of steel or aluminium will produce a wider impulse bandwidth than tips made of polyurethane or plastic and will therefore be more effective at exciting higher order structural vibrations. They will therefore be useful for the method of damage detection based on changes in

structural damping described in section 4.3.2. Furthermore, greater sensitivity will be obtained in methods based on stiffness change with steel and aluminium tips.

The influence of hammer mass on the dynamic waveforms is illustrated in Figure 4.8 which presents the waveforms predicted for transverse impacts on a fixed supported bar with both the Young's Modulus, E, and hammer velocity, v, fixed. It is assumed that the impact does not excite significant vibration in either the hammer or the bar.

In the time domain an increase in hammer mass is accompanied by an increase in both the impulse duration and the peak force. This is illustrated in Figure 4.8 (a) which shows the time histories corresponding to two impacts with hammers of different mass. For a given sample rate the heavier hammer generates an impulse with a longer duration. Therefore there are a larger number of data points and the statistical accuracy of damage detection methods is increased. In the frequency domain an increase in hammer mass is accompanied by an increase in the amplitude at zero frequency and a reduction in the frequency of the first minimum as indicated in Figure 4.8 (b). The 300 g hammer is more effective at exciting structural vibrations below approximately 200 Hz than the 200 g hammer because the amplitude of its spectrum is greater there. Therefore the method of damage detection based on changes in local damping would work better with a heavier hammer.

The final dynamic consideration is the resonant frequency of the hammer. If the lowest natural frequency of the hammer is within the spectral bandwidth of the impact force it will be excited and the measured spectrum will be due to structural vibrations of both the hammer and the structure. To avoid this the hammer is designed so that its lowest natural frequency is considerably greater than the force's spectral bandwidth for a typical impact. The spectrum in Figure 4.8 (b) for a 200g hammer is that predicted for a rigid tip impacting a mounted steel bar and its first minimum is about 450 Hz. The local stiffnesses are close enough to that of the experimental impacts described in Chapter 6 and Chapter 7 to provide an order of magnitude estimate of the expected bandwidth. The physical specifications were based on those of two commercial hammers (PCB, 1996). These had resonant frequencies of 31 kHz and 12 kHz, both considerably greater than the expected bandwidth. These were the PCB model GK291C01 and model GK291C20.

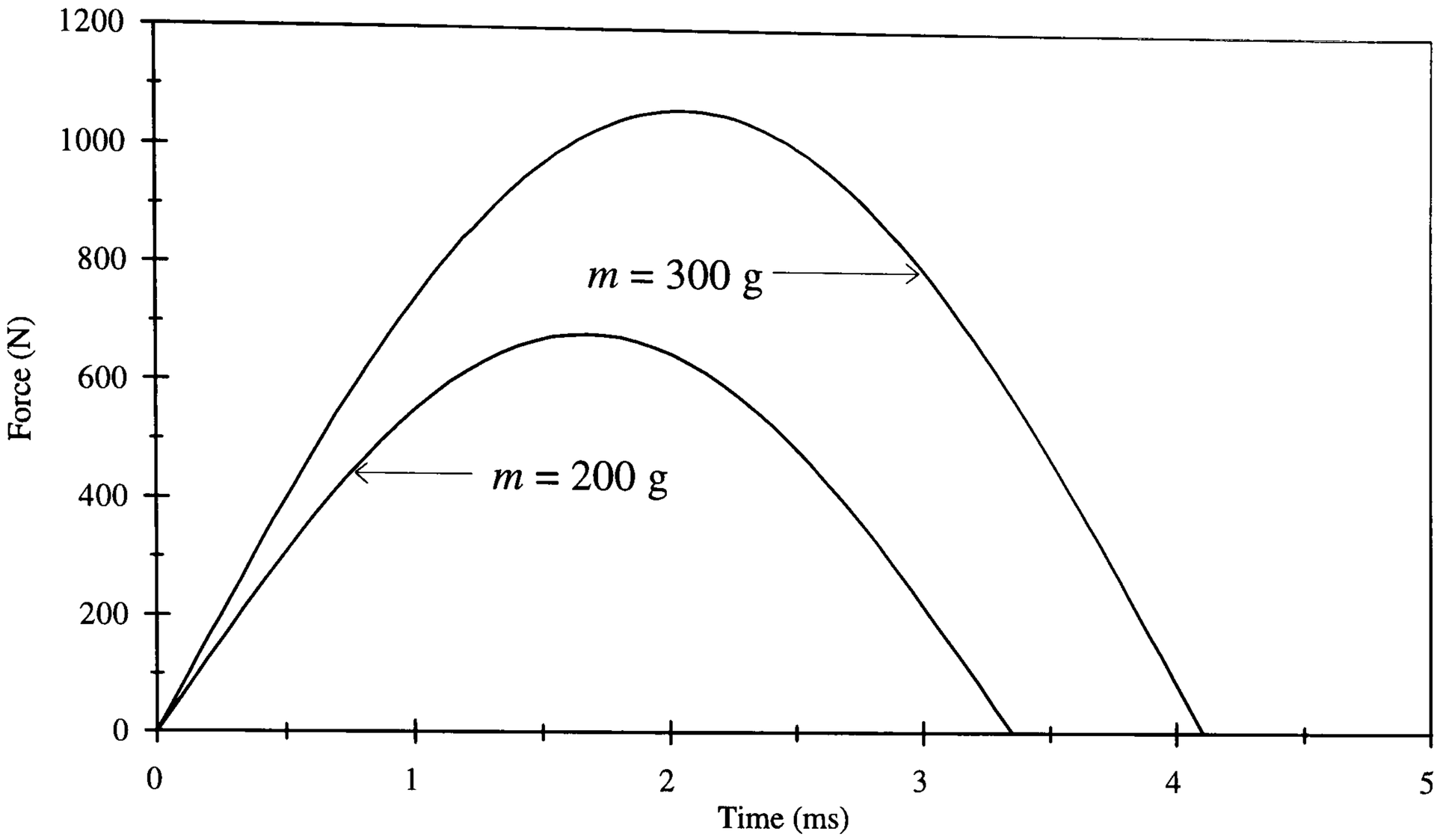

(a) Time Histories

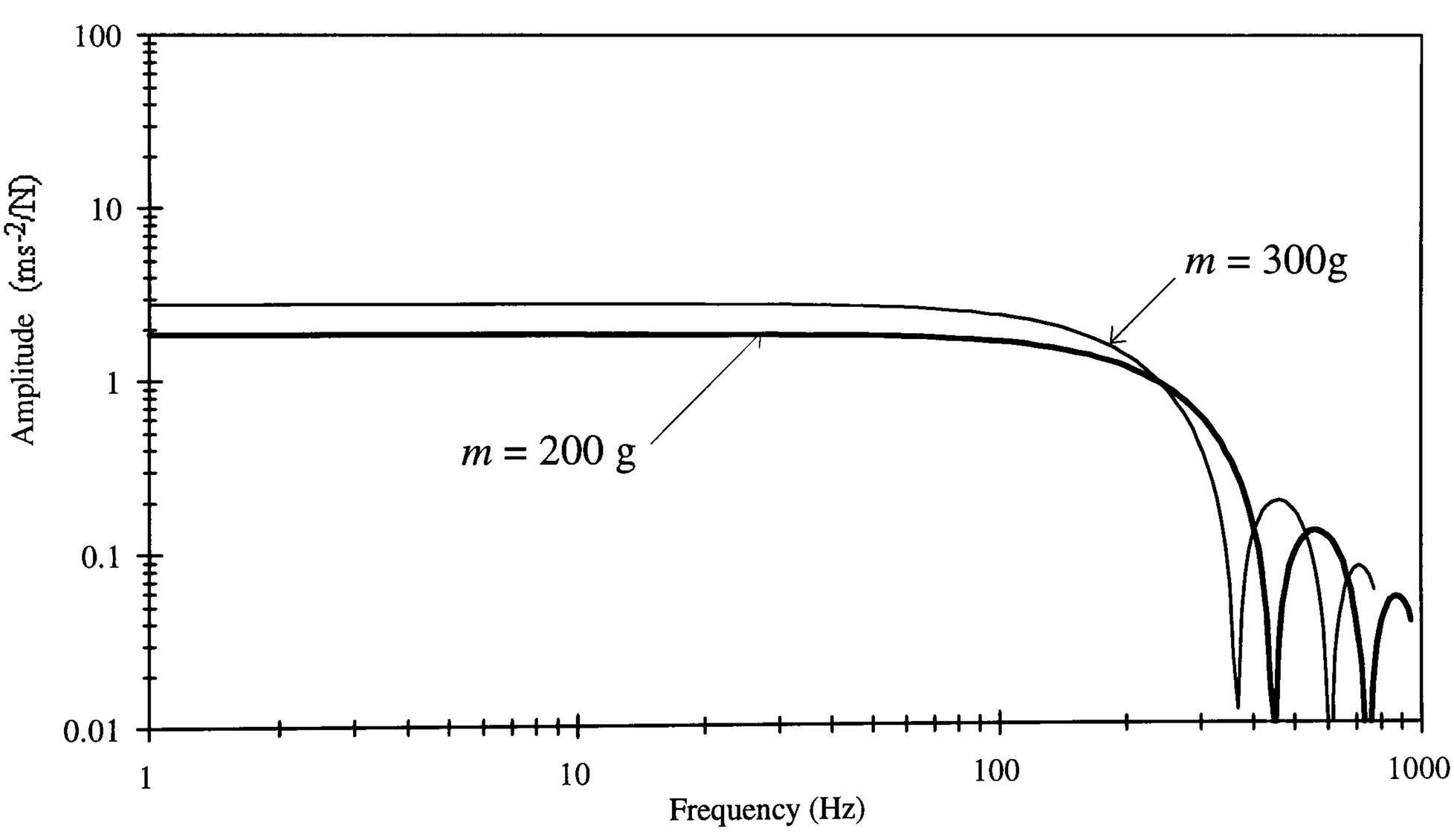

(b) Frequency Spectra (logarithmic scale on x and y axes)

Figure 4.8. Effect of Hammer Mass on Dynamic Waveforms of Fixed Supported Bar

(Transverse Impact Near Support, $E = 21.19 \times 10^{10}$ N/m^2, $v = 4.64$ ms^{-1})

4.4.2. Technical Considerations

The two instrumented hammers are shown in Figure 4.9. The larger one was designed for use on heavy structural steelwork such as I-sections. The smaller hammer was for lighter steelwork such as angle sections. The sections below detail the technical considerations involved in assembling both hammers.

4.4.2.1. Impact Tip and Load Cell

The load cell chosen for use in both hammers was the Dytran model 1051V5 (Dytran, 1996) which had a force range of 1000 lbf. This was an integrated circuit piezoelectric (ICP) type transducer and as such has its own built in signal amplifier. The advantage of using this instead of a charge mode device is that it is does not require an additional signal amplifier, making the equipment more portable. The measured force on impact is mainly due to the deceleration of the mass behind the load cell in the direction of impact. Therefore the load cell is mounted at the front of the hammer head so that the force delivered to the structure is close to the measured force (Figure 4.9). Another consequence of locating the load cell in this way is the possibility of damaging it if a substantial force acts on the tip at a large angle to the load cell axis. This is unlikely to occur with the smaller hammer because the tip diameter is less than that of the load cell, as shown in Figure 4.9 (a). The outer edge of the load cell protects it from impacts at large 'off-axis' angles. However, the tip diameter of the larger hammer is more than that of the load cell and therefore it is necessary to recess the cell into the hammer head. By doing this the cell is protected by the outer edge of the hammer head, as shown in Figure 4.9 (b).

The voltage signal produced by the load cell is due to the compression of an internal quartz plate mounted at right angles to the axis of the load cell. The impact tips are originally spherically shaped so that a force acting normal to the surfaces and at a small 'off-axis' angle is conducted to the tip's screw thread which is coaxial. Another advantage of the spherical tip is that the contact area when it impacts a flat surface is very small and this reduces spurious effects caused by trapped air.

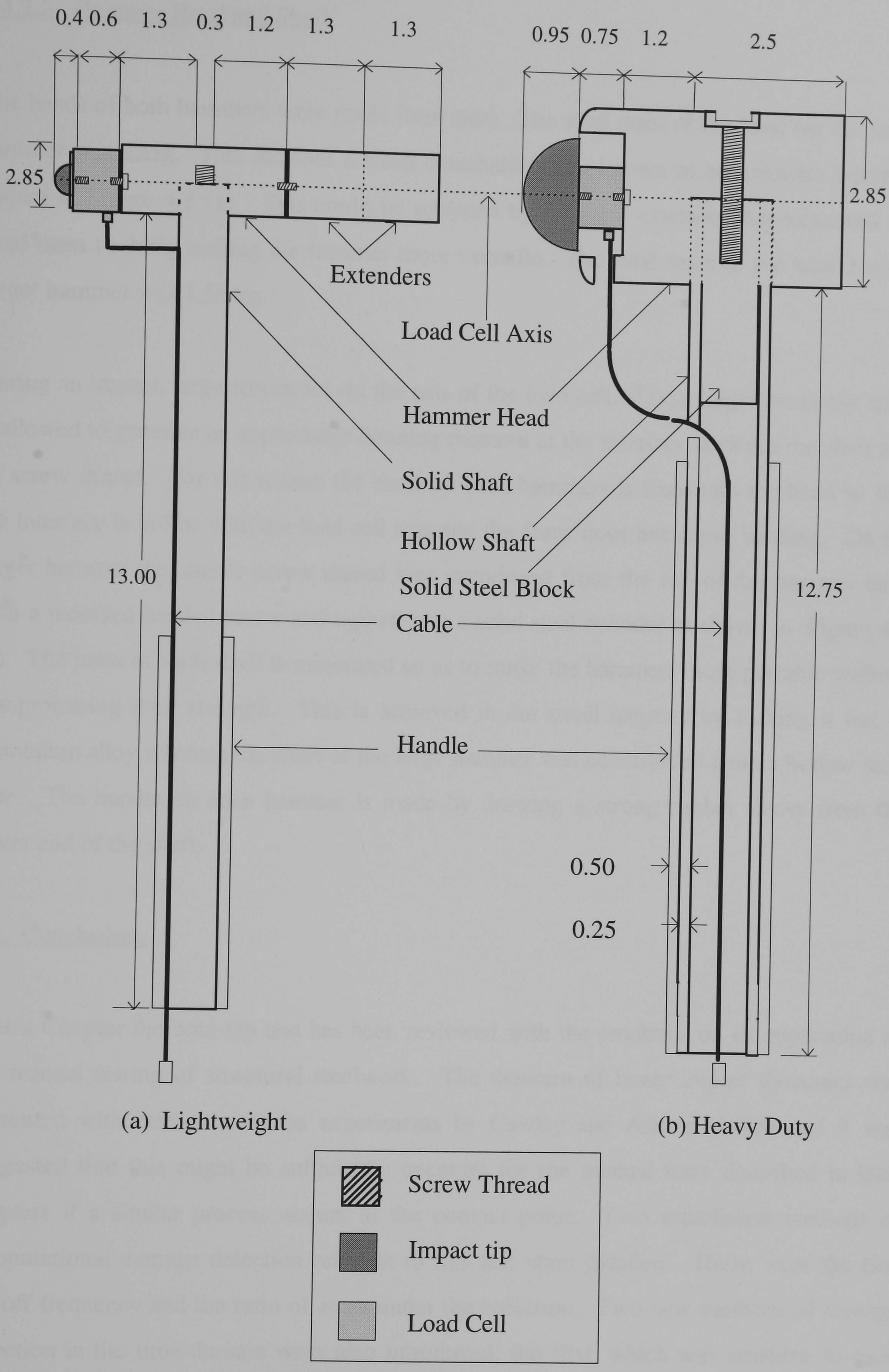

Figure 4.9. Instrumented Hammers Used for the Coin-tap Test (dimensions in cm)

4.4.2.2. Hammer Head and Shaft

The heads of both hammers were made from steel. The total mass of the head for the small hammer was 225g. This includes a small detachable mass known as an extender which is shown in Figure 4.8 (a). This could be replaced by a longer extender that increased the head mass to 300g making the hammer more versatile. The total mass of the head for the larger hammer was 1.56 kg.

During an impact, large forces act on the axis of the load cell. These might break the shaft if allowed to generate an appreciable bending moment at the interface between the shaft and its screw thread. For this reason the shaft on both hammers is fixed into the head so that the interface is in-line with the load cell axis and the force does not cause bending. On the larger hammer the shaft's screw thread was introduced from the top of the hammer head with a recessed headed screw and tapped into a solid steel cylinder as shown in Figure 4.9 (b). The mass of each shaft is minimised so as to make the hammers more portable without compromising their strength. This is achieved in the small hammer by making it out of aluminium alloy whereas the shaft of the large hammer was constructed from a hollow steel tube. The handle on each hammer is made by drawing a strong rubber sleeve from the lower end of the shaft.

4.5. Conclusions

In this Chapter the coin-tap test has been reviewed with the emphasis on its application to the manual testing of structural steelwork. The theorem of linear impact dynamics was presented with reference to the experiments by Cawley and Adams (1988) and it was suggested that this might be sufficiently accurate for the manual tests described in later chapters if a similar process occurs at the contact point. Two established methods of computational damage detection relevant to this test were detailed. These were the first cut-off frequency and the ratio of areas under the spectrum. Two new methods of damage detection in the time domain were also introduced: the first, which was sensitive to local stiffness changes, was the ratio of the peak impulse height to the enclosed area. The

second, which was sensitive to changes in local damping, was to inspect for changes in the amplitude and frequency of 'ringing' vibrations.

The methods described in this chapter will be applied to experimental data derived from the tests described in Chapter 6 and Chapter 7. In practice dynamic testing generates large volumes of experimental data and it is unrealistic to attempt to process it manually. Algorithms for the processing and computation of quantities sensitive to damage from experimental data are described in Appendix B. The following chapter describes the pattern recognition techniques employed to classify measurements automatically according to the condition of the joint or structure being tested.

5. PATTERN RECOGNITION

5.1. Introduction

Pattern recognition in general covers a wide range of applications. It can be described as a discrimination or classification of a set of processes or events that could be either a set of physical objects or mental states. Its goal is to clarify the complicated mechanisms of decision-making processes and to automate these functions using computers. Although pattern recognition is applied to biological problems, such as brain modelling, the present chapter is only concerned with its uses in engineering applications.

Because of the complex nature of the problem most pattern recognition research has been concentrated on relatively straightforward problems, particularly the recognition of Latin characters and the classification of waveforms. The different computational techniques used may be grouped into two general approaches; namely, the decision-theoretic approach, which includes statistical and neural classifiers, and the syntactic (or linguistic) approach, which includes knowledge based systems (KBS). Hansch et al. (1993) compared the performances of both recognition techniques on the waveforms of spectra from ultrasonic testing. It is the application of pattern recognition to the classification of waveforms produced by the coin-tap test that is the concern of this chapter.

In the decision-theoretic approach a set of critical features are extracted from each waveform measurement to form a feature vector. This is then assigned to a particular class, usually by partitioning feature space with a classifier. The method of feature extraction ranges from the primitive technique of sampling the waveform in the time or frequency domain, to the computation of quantities less sensitive to statistical variations such as those described in the previous chapter. The method of classification varies depending on the practical situation. It may be that given a set of feature vectors the aim is to determine their probability distribution by establishing the existence of classes or clusters amongst them. Alternatively, it may be known that there is a certain number of classes and the aim is to find a rule (discriminant) that partitions feature space allowing a new feature vector to be assigned into one of the existing classes. The former type of classification is known as *Unsupervised*, the latter as *Supervised*. Furthermore, the classification methods used in this

study fall into the two categories of *Neural* and *Statistical* computation. Both methods compute a probability of class membership for a vector and it is necessary to define a criterion based on this probability to classify the vector. General information on neural and statistical classifiers can be found in Hertz et al. (1993) and Fukunaga (1972) respectively. A broad review of methods of neural computation can be found in Lippmann (1987) and Hecht-Nielsen (1988).

Statistical classifiers are generally characterised by having an explicit underlying probability distribution and the method of feature extraction requires the computation of quantities as described above. Neural networks are computer models whose function mimics the knowledge acquisition and organisational skills of the human brain. They consist of layers of interconnected units, each producing a non-linear function of the total input. The input to a node may come from other nodes or directly from the input data. The output of the final layer of units represents the network output. Therefore the complete network represents a complex set of interdependencies allowing very general functions to be modelled. The input to a neural network can be either computed quantities or sampled waveforms.

The syntactic approach can be applied to patterns that are quite complex and possess a large number of features. In these cases it is often better to divide the pattern into a number of sub-patterns forming a hierarchical (tree-like) structure. This approach is often used for the recognition of continuous speech and it has been applied to waveform recognition. An example of the latter is a study carried out by Comerford (1989) who developed a KBS to classify data from seismic tests on a concrete pile. However, a considerable amount of time is required to set up a KBS including frequent interviews with experts (Brulé and Blount, 1989). Considering the limited time-scale of this study it was deemed inappropriate to employ a KBS in the present application. Further information on expert systems can be found in Jackson (1990).

This chapter is divided into two sections that discuss pattern recognition methods used with coin-tap test data. The first section covers supervised classifiers and includes the back-propagation neural network and two simple statistical techniques: the nearest mean and the

nearest neighbour. The second section describes an unsupervised classifier known as the probabilistic resource allocating network (PRAN).

5.2. Supervised Pattern Recognition

5.2.1. The Back-propagation Neural Network

These networks have a feed-forward architecture. Figure 5.1(a) shows a back-propagation network that has two layers. The five component feature vector, ξ, from a sampled waveform is 'clamped' to the input distribution which is represented by small solid circles. This forms the input to the first layer of processing units, V_j, represented by large open circles. However, the strength of the total signal, h_j, received by each of these units depends on the weight on each interconnection which is given by the matrix w_{jk}. The output from each unit is derived by applying the non-linear sigmoid activation function, θ_s, (also called the logistic function) to the total signal. The function is given by

$$\theta_s(h_j) = \frac{1}{1+\exp(-\beta h_j)} \tag{5.1}$$

where β is a constant and the *total* signal, h_j, received by a unit in the first layer is the sum of the weighted signals carried by each interconnection as given by the equation

$$h_j = \sum_{k=1}^{5} w_{jk}\xi_k \tag{5.2}$$

Sometimes the output level is adjusted by subtracting a threshold but this is neglected in the present discussion for clarity. The equivalent expression for the total signal, h_i, received by units in the second layer is obtained by replacing w_{jk} with W_{ij}, and replacing the feature vector with the output vector from the first layer, $\boldsymbol{h}_j$. The output of the second layer units, U_i, represents the network output. The sigmoid function is plotted in Figure 5.1(b) for values of h between -2 and +2 and for different values of the constant β. The function is 0.5 when $h = 0$ and tends to 1 or 0 as h approaches plus and minus infinity, respectively.

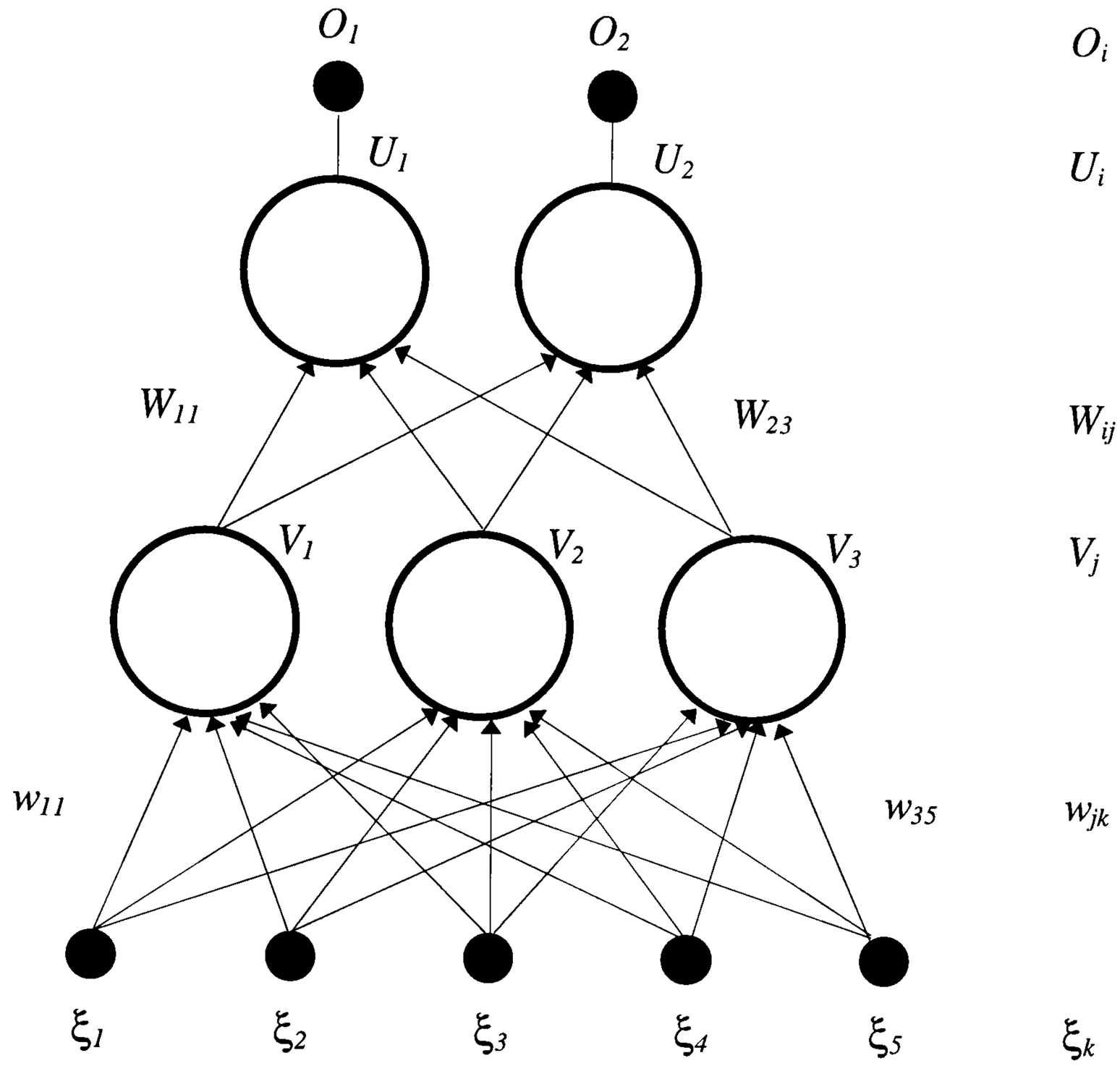

(a) Architecture

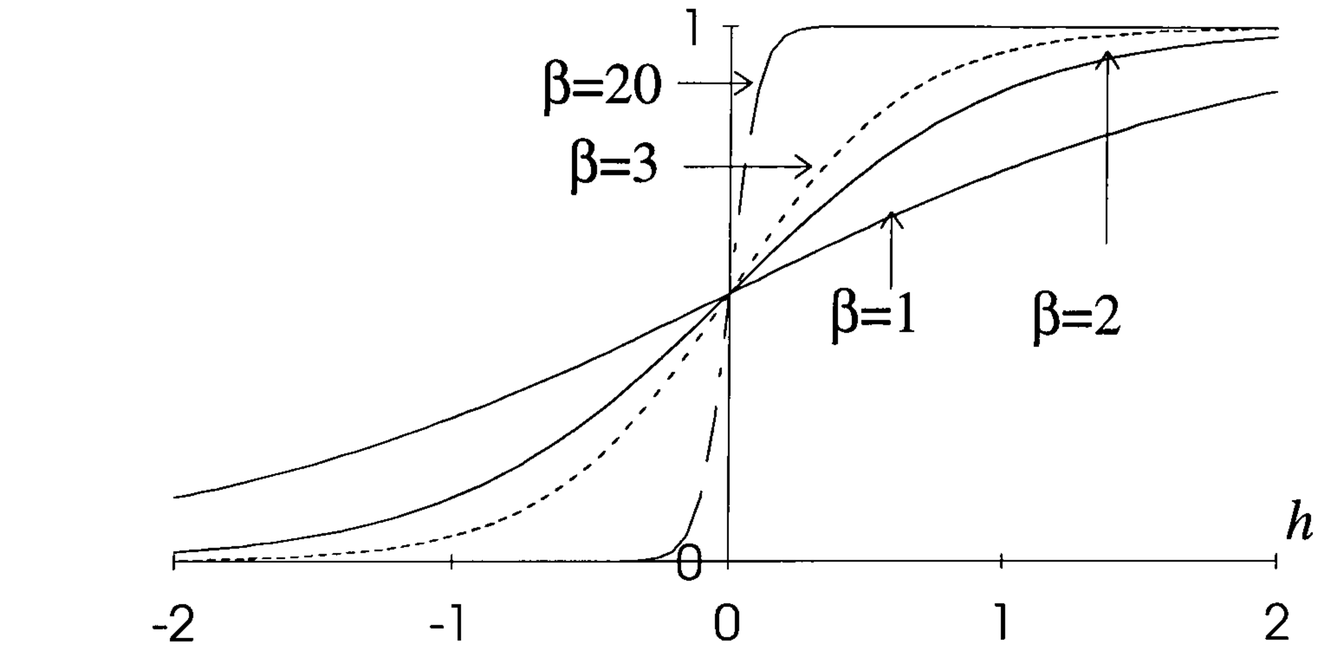

(b) The Sigmoid Function

Figure 5.1. The Back-propagation Neural Network

The curves indicate that for increasing values of β the sigmoid function tends to a step function. During a *training* phase feature vectors of known class membership, called training vectors, are clamped to the input distribution and a code representing the class, called the target vector, is clamped to the network output. For each sample vector adjustments are made to the weights on the interconnections. At the end of training the weight vectors represent a distributed store of information that allows the partitioning of feature space and the subsequent classification of unknown feature vectors that are presented during a *test* phase. There should also be some statistical variation between training vectors with the same target and this should be typical of the statistical variation inherent in obtaining the unknown feature vector.

Back-propagation networks adjust their weights by means of a gradient descent algorithm. The standard gradient descent, otherwise known as the *steepest descent method*, is described here. Before training the network weights are initialised and then, using the current set of weights, the network computes its output vector $\boldsymbol{O}_i$. This is subtracted from the corresponding target vector, $\boldsymbol{T}_i$, and the error for each training vector is the sum of the squared difference for each component. These values are then summed to give an error for each pattern. The error function, E (sometimes called the cost function) is the sum of the errors for each training vector,

$$E = \frac{1}{2}\sum_{i,\mu}\left(\boldsymbol{T}_i^{\mu} - \boldsymbol{O}_i^{\mu}\right)^2 \tag{5.3}$$

where μ is the number of the current training vector. The factor of 1/2 is for convention only. The signal produced by one unit in the output layer can be written in terms of the weight matrices (Hertz et al, 1993) as follows:

$$O_i^{\mu} = \theta\left(\sum_j W_{ij}\theta\left(\sum_k w_{jk}\xi_k^{\mu}\right)\right) \tag{5.4}$$

The inner parentheses represent h_j^{μ}, the total signal received by a unit in the first layer when the training vector μ is presented to the network. Therefore each output unit sums up the signals produced by units in the first layer and applies the sigmoid function to the result. When all the training vectors have been presented to the network a weight adjustment is performed so that each weight changes in proportion to the negative derivative of the error function with respect to the present value of the weight. The weight change equation for interconnections between the input distribution and first layer units is

$$\Delta w_{jk} = -\eta \frac{\partial E}{\partial w_{jk}} \tag{5.5}$$

where the constant η is called the learning rate. The equivalent expression for interconnections between the first and second layer units is obtained by replacing w_{jk} with W_{ij}. An epoch is completed when all the training vectors (the training set) have been presented to the network and all the weights have been adjusted. Weight adjustments, which back-propagate through the network in the opposite direction to the original signal, reduce the value of the error function for the next epoch. Training is complete once the error function is minimised; the network is then said to have converged. The rate of convergence can be increased either by adjusting the learning rate or by adding a momentum term to the weight change equation (equation 5.5) and adjusting the momentum constant α. This makes the weight change at iteration t+1 proportional to that at iteration t. For an interconnection between the input distribution and the first layer the time dependent weight change equation is given as follows:

$$\Delta w_{jk}(t+1) = -\eta \frac{\partial E}{\partial w_{jk}} + \alpha \Delta w_{jk}(t) \tag{5.6}$$

This term can also reduce the level of the error function by 'jiggling' it out of a local minimum allowing the network to converge on the global minimum.

Clearly the back-propagation neural network requires a large number of parameters to be defined. These can be grouped into algorithmic parameters that affect the way each unit

computes its output, and architectural parameters that affect the size and complexity of the network. Since the number of interconnections in an m-layered network with l units in each layer is ml^2 (provided that only interconnections between adjacent layers are allowed), larger networks result in a considerable increase in the duration of the training phase. The architectural parameters that control the network size are discussed below.

The first parameter to consider is the number of components in the feature vectors because this will determine the number of interconnections to first layer units. When the feature vector is composed of computed quantities only a few components will be necessary. For example Kirkegaard and Rytter (1993) computed a five component feature vector from the relative changes in the first five natural frequencies of a structure. Similarly, Elkordy et al. (1994) computed a five component feature vector from the relative changes in displacement at five locations on a structure. However, more components are generally necessary when the feature vector is a sampled waveform. For example Kudva et al. (1992) produced forty component feature vectors by sampling strain mode shapes, and Wu et al. (1992) produced two hundred component feature vectors by sampling FRFs over a 20 kHz band.

The next parameter to consider is the number of units in the first layer as this will determine the ability of the network to partition feature space in a way that groups the training set according to their class membership. If this can be done with a single linear discriminant only one first layer unit is required (the single layer perceptron). However, this situation is rare and more first layer units are required to represent increasingly complex discriminants (multi-layer perceptrons). The optimum number is usually determined by trial and error but it is widely recognised that a number of first layer units equal to half the number of components in the feature vector is sufficient. The number of units in the second layer is determined by the number of classes. If each unit represents one bit of a binary code, and each binary number represents a class, then 2^l classes can be represented with l second layer units. This architecture minimises the number of interconnections but takes longer to converge (and may fail altogether) than a network that has l equal to the number of classes.

The number of algorithmic parameters is large and may depend on the software package used. There is no generally agreed procedure on choosing the optimum values. Parameters

such as the learning rate and momentum constant are usually determined by trial and error to minimise the training time. Other gradient descent algorithms exist which result in shorter training times under certain circumstances (Simpson, 1990). The standard Newton method and the quasi-Newton are examples of such algorithms. However, the former method only tends to work well when the weights are initialised at specially chosen values, and the latter method is only suitable for small networks. Similarly, other refinements of the standard gradient descent method also have their drawbacks.

5.2.2. Nearest Mean and k-Nearest Neighbour Statistical Classifiers

These assume that each feature vector, ξ, belongs to a probability distribution $p(\xi)$ that is the superposition of a number of generator functions. They approximate the *posterior* probability, $p(C_q|\xi)$, that the vector belongs to a class, q, that has *conditional* probability density $p(\xi|C_q)$. Baye's theorem states the relationship between these quantities as,

$$p(C_q|\xi) = \frac{p(\xi|C_q)p(C_q)}{p(\xi)} \tag{5.7}$$

where $p(C_q)$ is the prior probability of membership of class q. Statistical classifiers approximate the posterior probability indirectly by either modelling the conditional probability with a standard distribution or by estimating it from the local 'lie of the data'. These two approaches are referred to as parametric and non-parametric methods respectively. It is then possible to classify unknown vectors by assigning them to the class with the highest conditional probability.

Parametric methods assume the minimal number of generator functions to represent the data adequately whereas non-parametric methods assume a generator function located at each feature vector. Consequently non-parametric methods are more computationally demanding. In this investigation two types of statistical classifier were used: k-nearest neighbour (k-NN) which is non-parametric and the nearest mean (NM) which is parametric (Michie et al, 1994).

In the nearest mean approach the centroid (mean) of each class of feature vectors is computed and the Euclidean distance between this and a feature vector of unknown class membership is computed. The unknown vector is assigned to the class corresponding to the shortest distance. The nearest mean technique models the conditional probability of the classes as symmetrical generator functions with equal spread and the highest classification success rate will be obtained when the feature vectors are distributed in this way. In the k-nearest neighbour approach a hypersphere centred on the feature vector of unknown class membership and containing k feature vectors of known class membership, is constructed. The conditional probability for a particular class is estimated from the vectors lying within the hypersphere by dividing the number belonging to that class by the total number. The unknown vector is assigned to the class corresponding to the highest conditional probability estimate. When $k = 1$ the unknown vector is assigned to the class of the feature vectors that lies closest to it. This special case is called the nearest neighbour technique. The success rate of k-NN classification does not depend on the form of the conditional probability distribution but is susceptible to spurious data because the conditional probability is estimated from only a small number of feature vectors.

The two techniques are illustrated in Figure 5.2. The feature vectors have two components and either belong to group 's' or group 'd'. 'X' marks the mean for each class of measurements. The unknown feature vector is labelled 'u'. In Figure 5.2(a) the nearest neighbour belongs to the 'd' group and the unknown measurement would be correctly classified by this technique. However, the 'd' class of vectors is not symmetrical and the unknown vector would be miss-classified by the nearest mean technique because the mean of the 's' class is nearer than that of the 'd' class. In Figure 5.2(b) the vector classes are symmetrical and of equal spread but a vector computed from a spurious measurement is the nearest neighbour to that of the unknown resulting in misclassification by this technique. However in this case the nearest mean gives the correct classification. When the number of components is greater than three it is not possible to visualise the distribution of feature vectors and consideration of results produced by both techniques is the best approach. The classification success rate improves with the number of components.

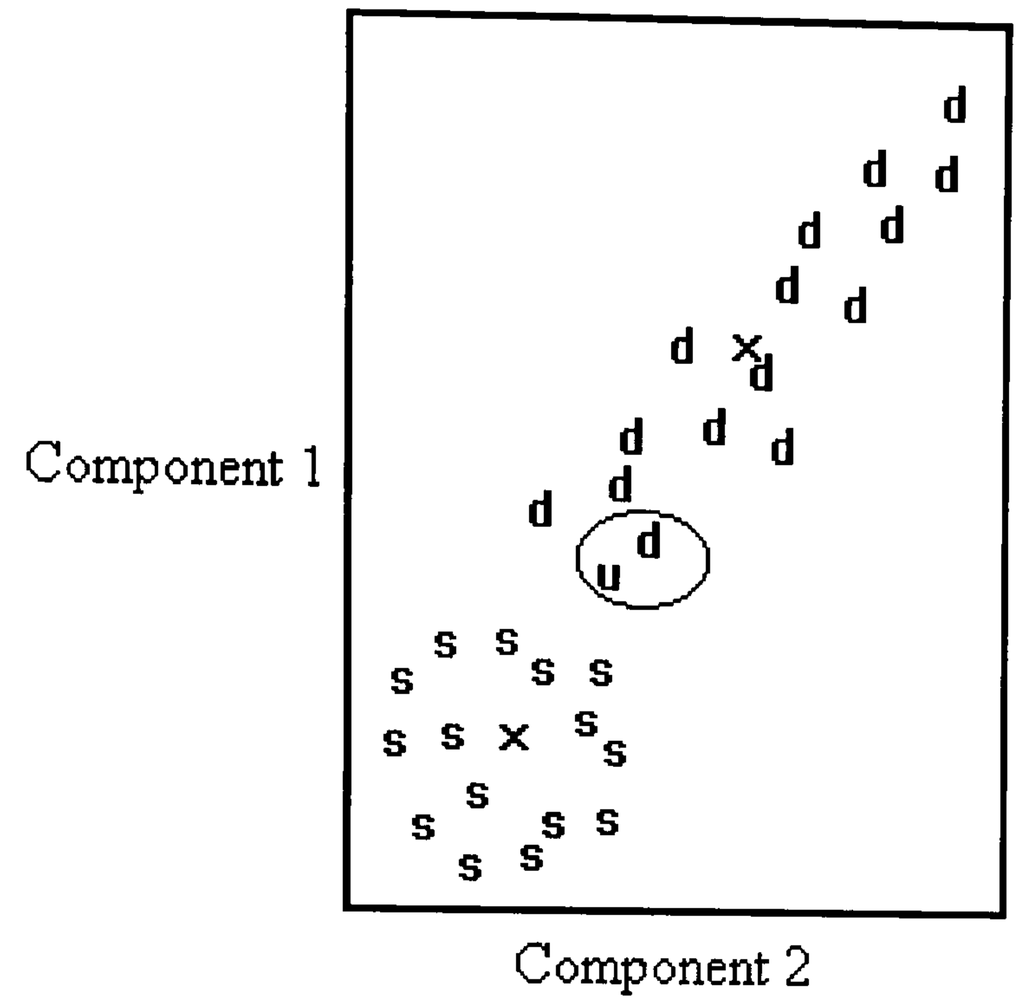

(a) The Nearest Neighbour Technique

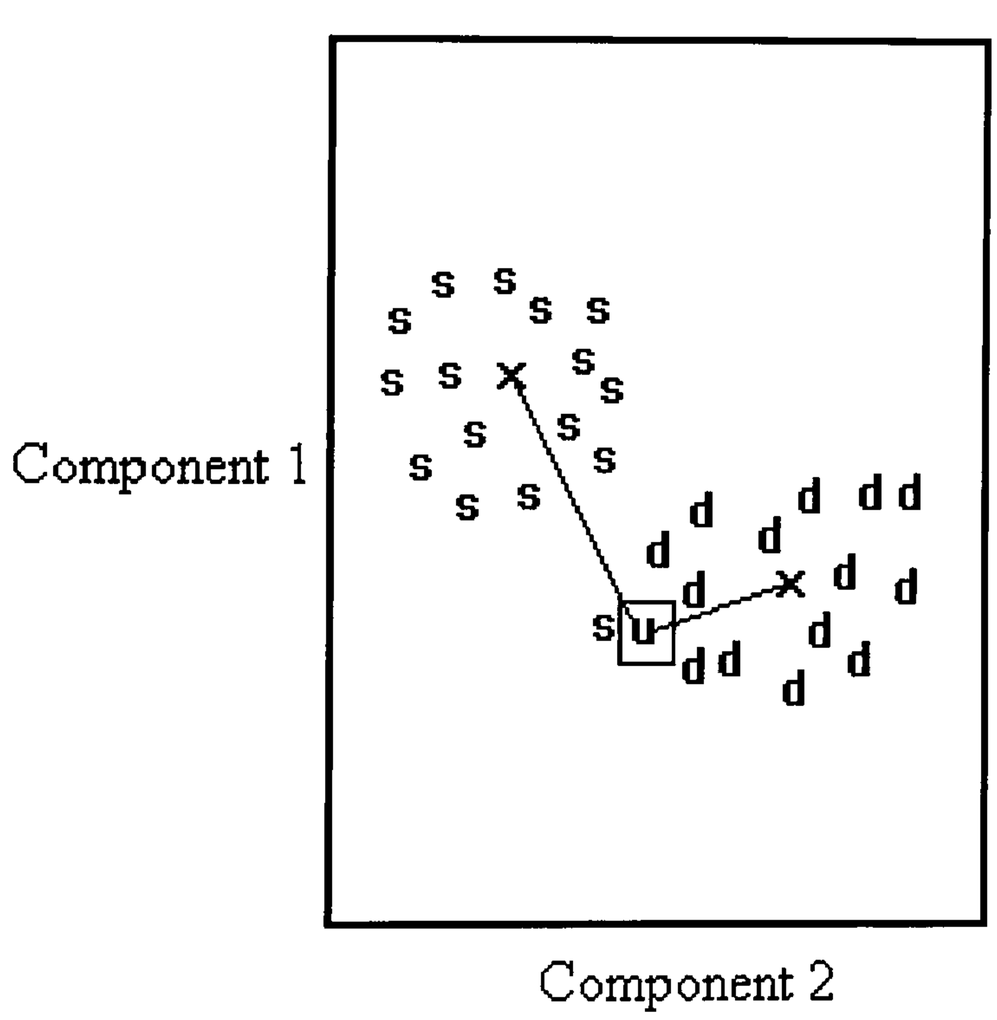

(b) The Nearest Mean Technique

Figure 5.2. Simple Statistical Classifiers

5.3. Unsupervised Pattern Recognition - The Probabilistic Resource Allocating Network

The Probabilistic Resource Allocating Network (PRAN) is a novelty detector and as such it can be thought of as a binary classifier: it either assigns an unknown feature vector to membership of a parent population, or excludes it. Its operation, which can be understood from both the neural and statistical perspectives, has many similarities to that of the Carpenter/Grossberg classifier (Carpenter and Grossberg, 1986). However, the input to the Carpenter/Grossberg classifier must be binary and therefore it is not suitable for sampled waveforms which are continuous valued. It trains by means of a constructive algorithm to optimise the number of processing units. Therefore it is more efficient than networks that have a fixed architecture such as Kohonen self-organising feature maps.

The PRAN's initial architecture is similar to a neural network that has one layer containing only one processing unit (also called a Gaussian kernel) as shown in Figure 5.3(a) where the solid black circles represent the input distribution and the large open circle represents the unit. The feature vector, ξ, is 'clamped' to the input distribution forming the input to the unit. The output of the unit is obtained by applying the non-linear Gaussian activation function θ_g, to the vector, $\boldsymbol{h}$, which is the difference between the feature vector and a vector, $\boldsymbol{m}$, representing the mean of the kernel. Hence $\boldsymbol{h}$ is given by

$$\boldsymbol{h} = \xi - \boldsymbol{m} \tag{5.8}$$

The Gaussian activation function is given by

$$\theta_g(\boldsymbol{h}) = A \exp\left[-\frac{1}{2}\left(\frac{\boldsymbol{h}^T.\boldsymbol{h}}{\sigma^T.\sigma}\right)\right] \tag{5.9}$$

where σ is a vector representing the standard deviation of the kernel. A is the maximum amplitude of the Gaussian function which is given by,

$$A = \frac{1}{(2\pi)^{N/2}\sigma} \tag{5.10}$$

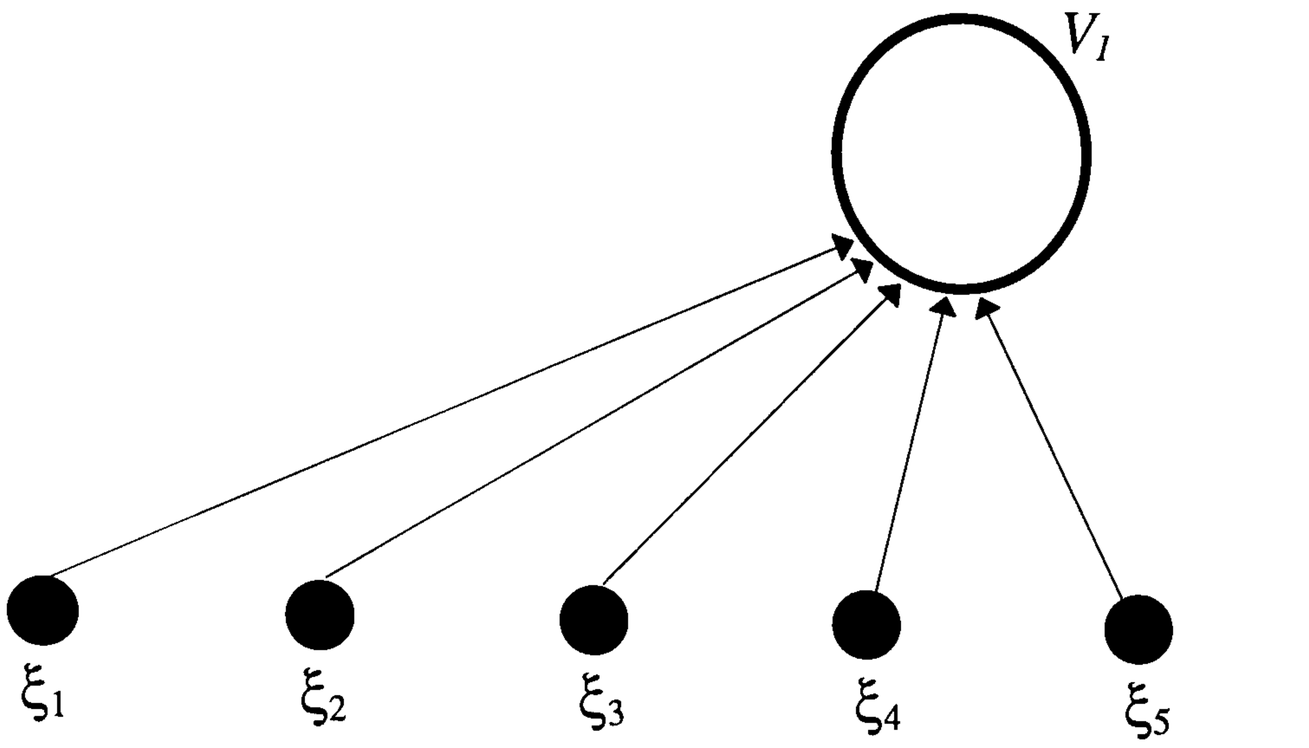

(a) Initial Architecture

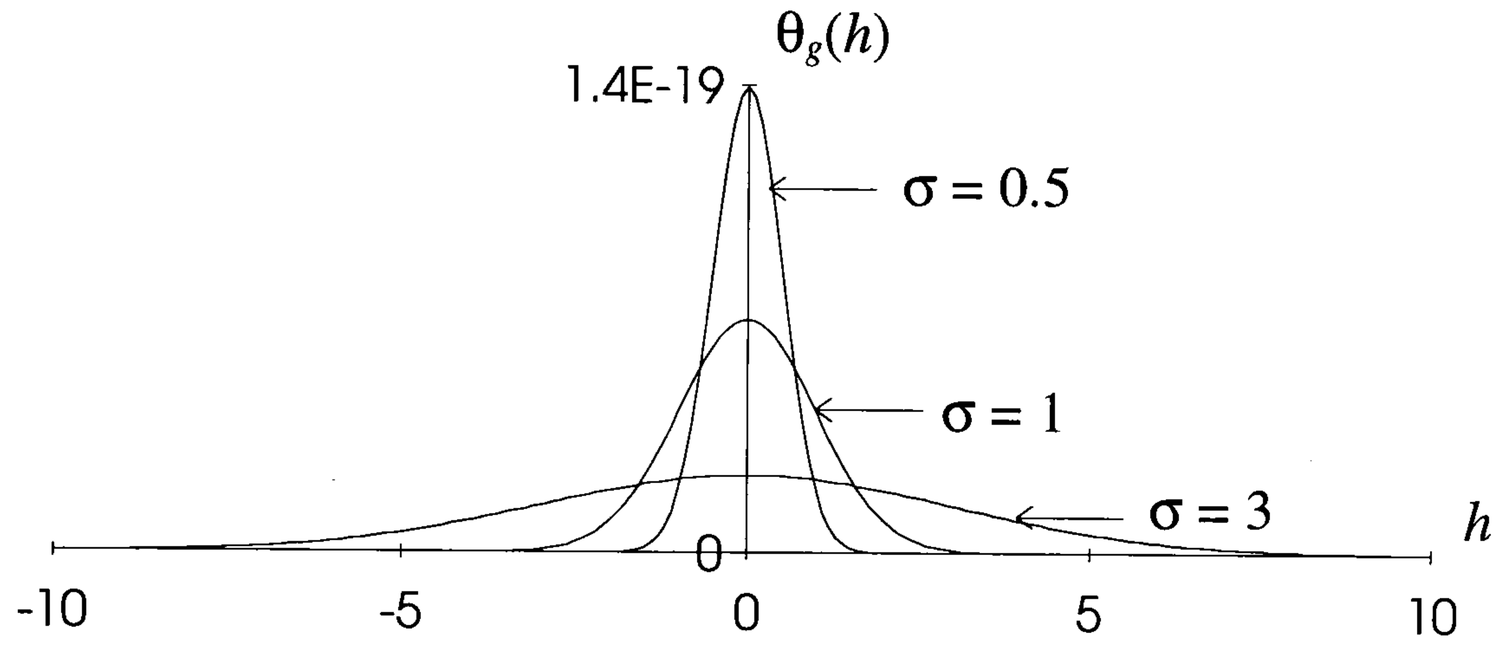

(b) The Gaussian Function

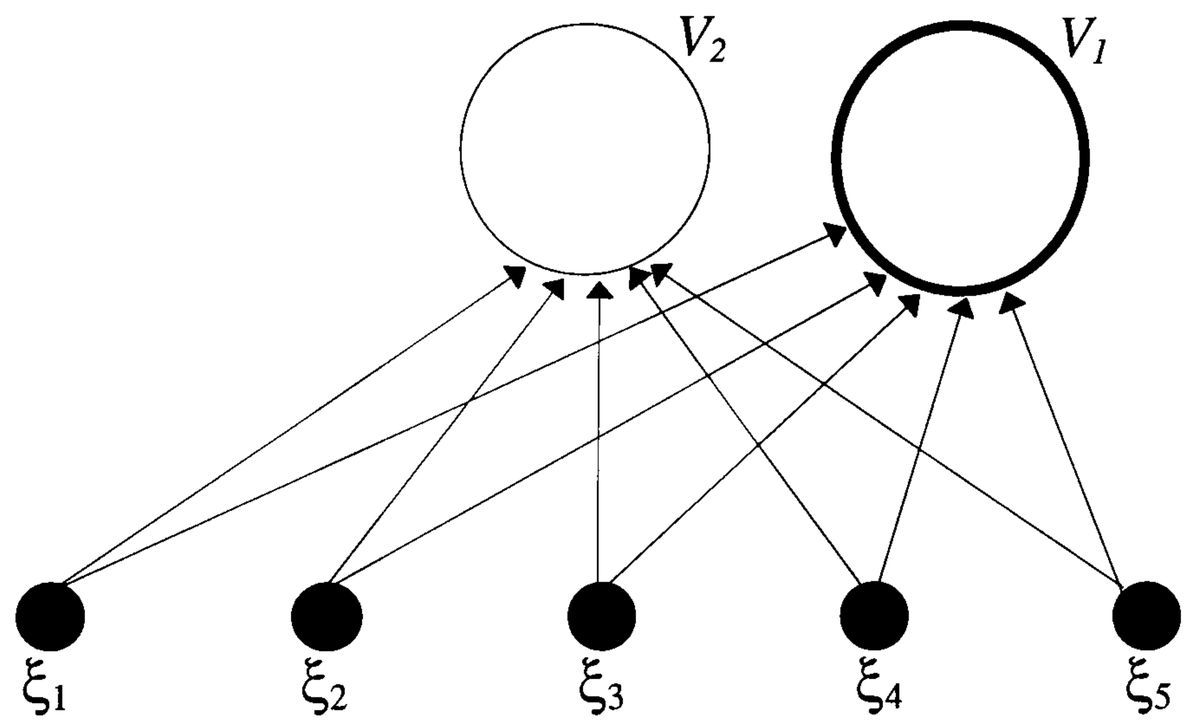

(c) Architecture After Growth of One Additional Unit

Figure 5.3. The Probabilistic Resource Allocating Network

where N is the number of components in the feature vector. Note that the scalar σ is the amplitude of the standard deviation vector $\boldsymbol{\sigma}$ for the kernel. Gaussian functions with zero mean are plotted in Figure 5.3(b) for $N = 48$, values of h between -10 and 10 and for different values of the standard deviation. The functions decrease smoothly from the maximum amplitude at $h = 0$ and approach zero as h tends to plus and minus infinity. The curves indicate that as the standard deviation decreases the Gaussian function tends towards a spike function localised on the mean.

The PRAN uses statistical principles for novelty detection and as such assumes that each feature vector, $\boldsymbol{\xi}$, belongs to a probability distribution $p(\boldsymbol{\xi})$ that is the superposition of a number of generator functions. The generator functions are assumed to be Gaussians each of which is defined by a processing unit or kernel. The number of these kernels required to represent the distribution adequately, together with the corresponding means and standard deviations are determined during the training phase. The final number of generator functions is generally less than that of parametric methods but more than non-parametric methods. Therefore this method is sometimes referred to as semi-parametric. Further general reading on Gaussian mixture models can be found in Bishop (1995).

The probability distribution, $p(\boldsymbol{\xi})$, is defined by Baye's rule which states that the probability of a feature vector $\boldsymbol{\xi}$ is the sum, over all K kernels, of each probability that it belongs to the kth kernel. The probability that the vector belongs to kernel k is the product of the *prior* probability of selecting that kernel, $p(k)$, with the conditional probability of $\boldsymbol{\xi}$ given that kernel k has been selected, $p(\boldsymbol{\xi}| k)$,

$$p(\boldsymbol{\xi}) = \sum_{k=1}^{K} p(k)\,p(\boldsymbol{\xi}|k) \tag{5.11}$$

where. $\quad 0 \le p(k) \le 1 \quad$ and $\quad \sum_{k=1}^{K} p(k) = 1$

The conditional probability is simply the Gaussian activation function (equation 5.9) which may be written in terms of the *i*th feature vector and the kernel mean, $\theta_g(\xi_i;\boldsymbol{m}_k,\sigma_k)$ by substituting equation 5.8 into equation 5.9.

$$\theta_g(\xi_i;\boldsymbol{m}_k,\sigma_k) = \frac{1}{2\pi^{N/2}\sigma_k} \exp\left[-\frac{1}{2}\left(\frac{(\xi_i - \boldsymbol{m}_k)^T(\xi_i - \boldsymbol{m}_k)}{\sigma_k^T.\sigma_k}\right)\right] \tag{5.12}$$

The sum over all ξ of the log of equation 5.11 is called the log-likelihood.

$$\sum_{i=1}^{N} \log p(\xi_i) \tag{5.13}$$

The required probability distribution is determined by seeking Gaussian kernels that maximise the log-likelihood. Substituting $p(\xi_i)$ from equation 5.11 into equation 5.13, differentiating and setting the result to zero gives (Tråvén, 1991)

$$\sum_{i=1}^{N} p(k|\xi_i) \frac{\partial}{\partial[\boldsymbol{m}_k,\sigma_k]} \log\theta_g(\xi_i;\boldsymbol{m}_k,\sigma_k) = 0 \tag{5.14}$$

Where $p(k|\xi_i)$ is the posterior probability that vector ξ_i belongs to kernel *k*. By substituting the corresponding quantities in equation 5.7 it can be written in terms of the prior probability of selecting kernel *k*, $p(k)$, the conditional probability of ξ given kernel *k* has been selected $\theta_g(\xi_i;\boldsymbol{m}_k,\sigma_k)$ and the probability distribution $p(\xi)$. Roberts and Tarassenko (1994) proposed an iterative solution to equation 5.14 together with a procedure for representing the probability distribution $p(\xi)$ by 'growing' units (Gaussian kernels) in the PRAN during a training phase.

A solution to Equation 5.14 was formulated which updates the *mean* and *variance*, $\boldsymbol{F}$, for the kernel at each iteration according to the following equations.

$$\boldsymbol{m}_{k,t+1} = \frac{\boldsymbol{m}_{k,t} + \alpha_t \left[p(k \mid \xi_t)\xi_t - \boldsymbol{m}_{k,t} \right]}{(1 - \alpha_t) + \alpha_t p(k \mid \xi_t)} \tag{5.15}$$

$$\boldsymbol{F}_{k,t+1} = \frac{\boldsymbol{m}_{k,t} + \alpha_t \left[p(k \mid \xi_t)(\xi_t - \boldsymbol{m}_{k,t})(\xi_t - \boldsymbol{m}_{k,t})^T - \boldsymbol{F}_{k,t} \right]}{(1 - \alpha_t) + \alpha_t p(k \mid \xi_t)} \tag{5.16}$$

Where $\boldsymbol{F} = \sigma.\sigma$ and α is called the *adaption* parameter which is given by,

$$\alpha_k(t_k) = \frac{\alpha_0}{t_k + \tau_\alpha} \tag{5.17}$$

where α_0 and τ_α are constants. The posterior probability is computed from equation 5.7 by substituting the probability distribution, $p(\xi)$ and prior probability, $p(k)$, as defined in equation 5.11, and by substituting the conditional probability as defined in equation 5.12. The first kernel is established at the first iteration with its mean equal to the first feature vector and its variance equal to the variance among the components of that feature vector. The kernel has a *time* index that is set to zero and a prior probability that is set to 1. At each subsequent iteration the mean and variance are updated according to equation 5.15 and equation 5.16, the time index is incremented and the adaption parameter is updated according to equation 5.17.

The decision as to whether or not another kernel should be grown is based on the proximity of the current vector to the kernel which in turn depends on the kernel's spread (standard deviation) as well as its location (mean). If the separation exceeds a certain *threshold* metric it is necessary to grow a new kernel to represent the probability distribution accurately. Considering the Gaussian functions in Figure 5.3(b) to be PRAN kernels, clearly a feature vector corresponding to $h = 4$ is distinctly separated from the kernels with $\sigma = 0.5$ and $\sigma = 1$ whereas it is closely associated with the kernel that has $\sigma = 3$. In the former cases one new kernel would be grown whereas in the latter case the vector should be simply 'added' to the kernel, i.e. its mean and standard deviation should be accordingly

updated. The metric is based on the difference between the maximum kernel amplitude, A, and the response $\theta_g(h)$ of that kernel to the feature vector. This is called the Malhalanobis distance (Roberts and Tarassenko, 1994). Figure 5.3(c) shows the PRAN architecture after one additional kernel has been grown. Subsequently there is one iteration for each existing kernel and if the growth criterion is met at any of these iterations a new kernel is generated before the next feature vector is presented. The initial variance of new kernels is different from that of the first. The ith component of the kth kernel's variance, $(F_k)_{ii}$, is given by,

$$(F_k)_{ii} = \frac{1}{N}\mathrm{Tr}[\boldsymbol{C}] \tag{5.18}$$

where $\boldsymbol{C} = (\boldsymbol{m}_k - \boldsymbol{m}_l)(\boldsymbol{m}_k - \boldsymbol{m}_l)^T$ in which l is the index of the kernel that, before growth, had the largest posterior probability for that vector. The set of feature vectors is presented cyclically and if the growth criterion is not met at any iteration during the presentation of all the vectors they are presented once more and then training is stopped. The network is then said to have converged.

Apart from the number of feature vectors used, the key factor that determines the training time is the growth threshold. For computational simplicity this is chosen between 0 and 1 and the Malhalanobis distance is replaced by the kernel response normalised between the same limits. Growth occurs if the normalised response is less than the threshold. The number of kernels grown, and consequently the training time, will increase with threshold because it becomes more likely that a kernel's response to a given vector will be less than the threshold. In addition to the constraints on the prior probabilities (equation 5.11) they are always equal and updated each time a new kernel is grown. The constants that determine the adaption parameter, α_0 and τ_α, are set to 0.7 and 1 respectively in this study.

Once the PRAN is trained, its kernels represent an approximation of the population distribution for the feature vectors. It has the advantage that the parameters of this distribution are easily accessible, being stored in the processing units. This permits the testing of the PRAN in two distinct ways depending on the practical situation. It may be

known that the feature vectors used to train the PRAN all belong to the same class of measurement and the aim is to determine whether or not new feature vectors also belong to this class. Those that do not may be identified as novel. Alternatively, it may be suspected that a minority of feature vectors used for training belong to a different class of measurement and the aim is to identify these vectors as novel.

In the first method of testing, the response of new feature vectors to each existing kernel is compared with the maximum threshold parameter. The vector is classed as novel if the growth criterion is met for any of the existing kernels. In the second method of testing it is assumed that when a kernel has only a few vectors closely associated with it those vectors are novel. These kernels can be identified as those that produce the lowest total posterior probability, T, over the all vectors. For a given kernel T is computed as follows.

$$T = \sum_{i=1}^{N} p(k|\xi_i) \tag{5.19}$$

The novel vectors can be identified by testing the network as described above after these kernels are removed (pruned) from the network. The pruning process is illustrated in Figure 5.4 for a network that had four kernels after training. A feature vector with two components is shown for clarity but vectors that represent sampled waveforms normally have considerably more.

The PRAN architecture after training is shown in the first diagram of Figure 5.4(a). The feature vectors are plotted in the second diagram together with an indication of the location and spread of the kernels (intersecting error bars). Clearly the third kernel has the fewest vectors closely associated with it and therefore the lowest total, T. The architecture of the PRAN after this kernel has been identified and pruned, is as shown in the first diagram of Figure 5.4(b). This effectively alters the probability distribution so that those vectors that were closely associated with the third kernel are now identified as novel.

The ability to visualise the layout of vectors and kernels in feature space provide an opportunity to compare the PRAN's classifications with those of the user. However, when

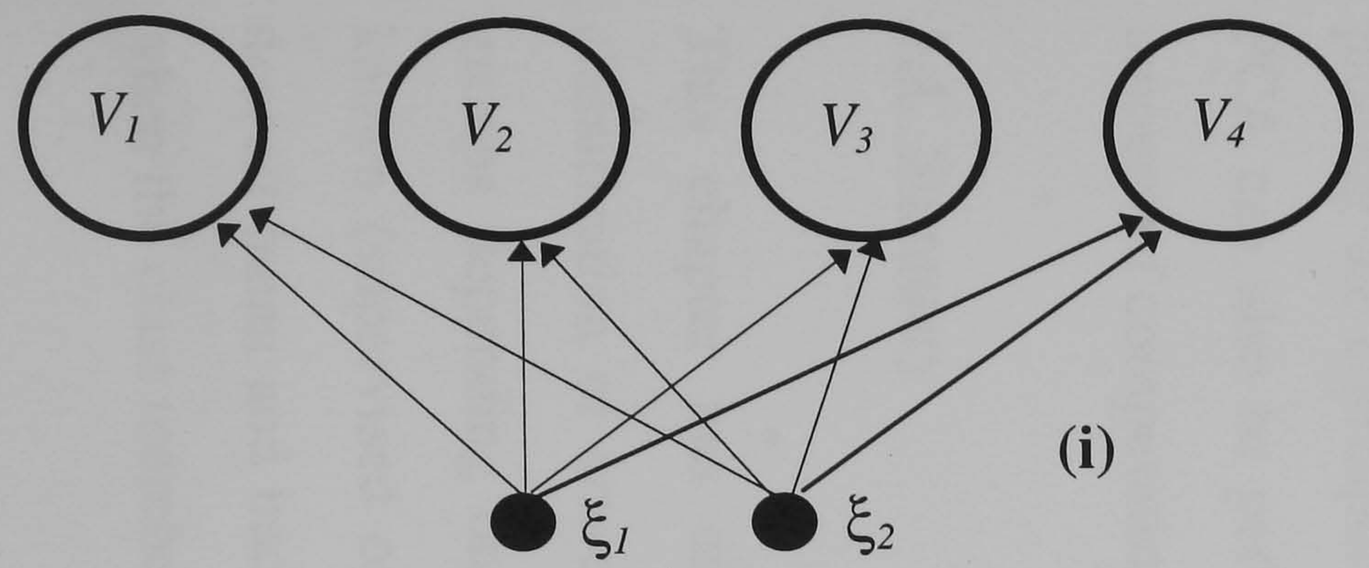

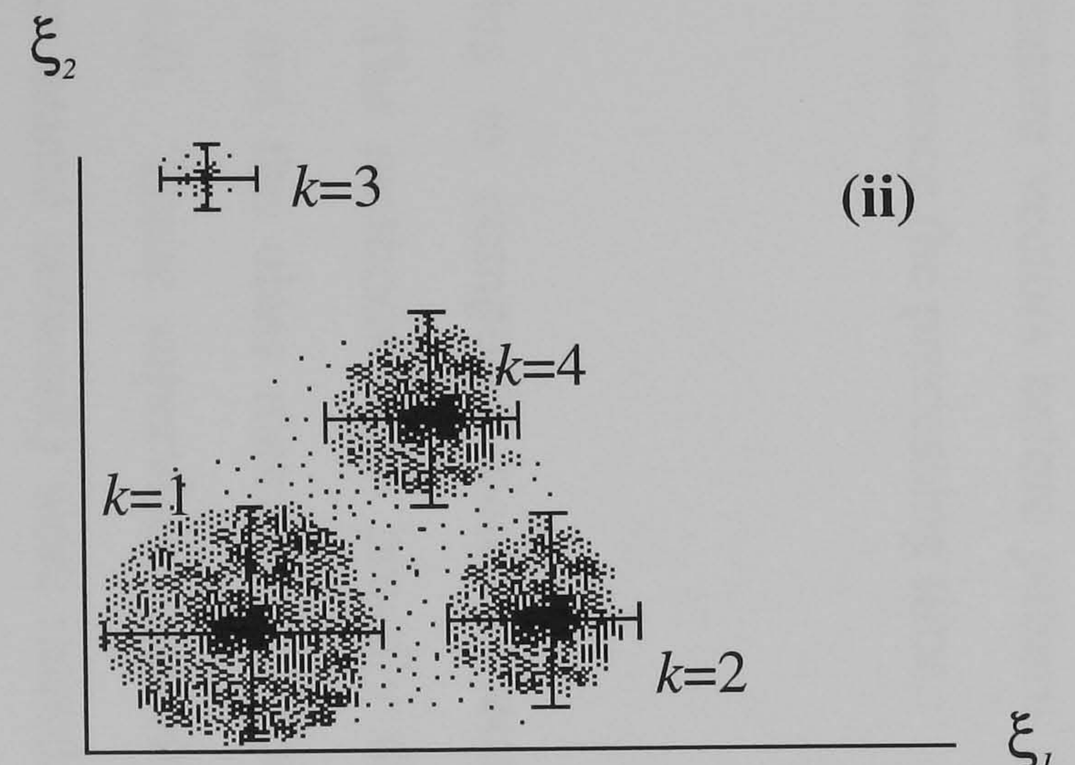

(a) After Training

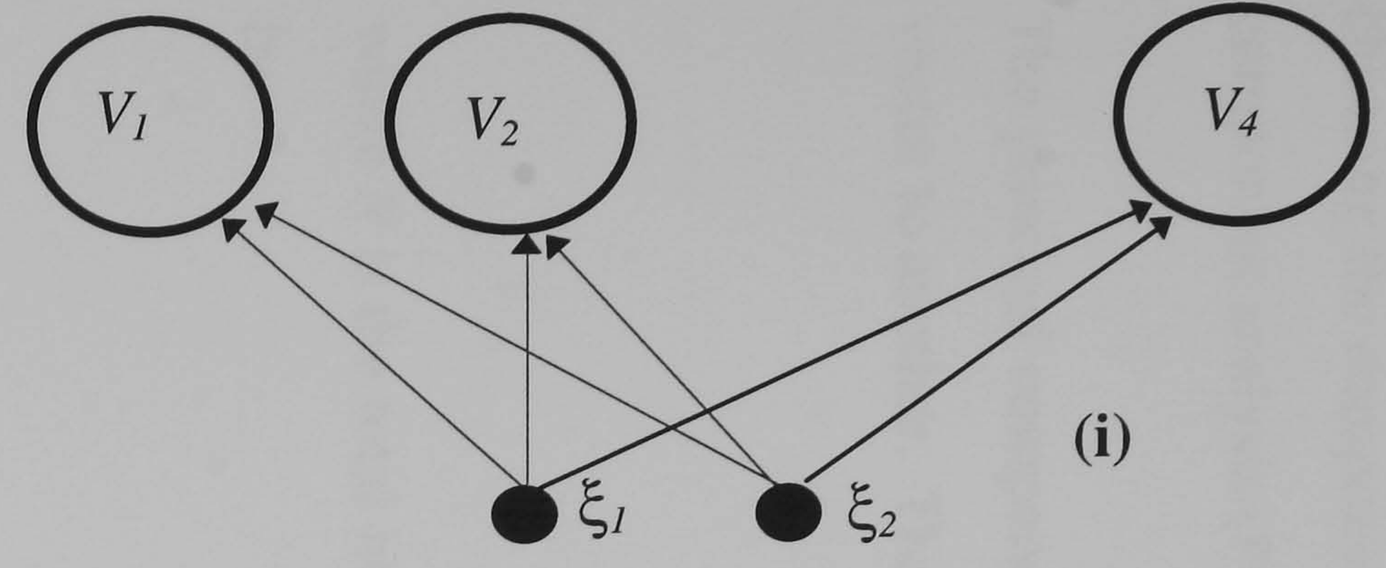

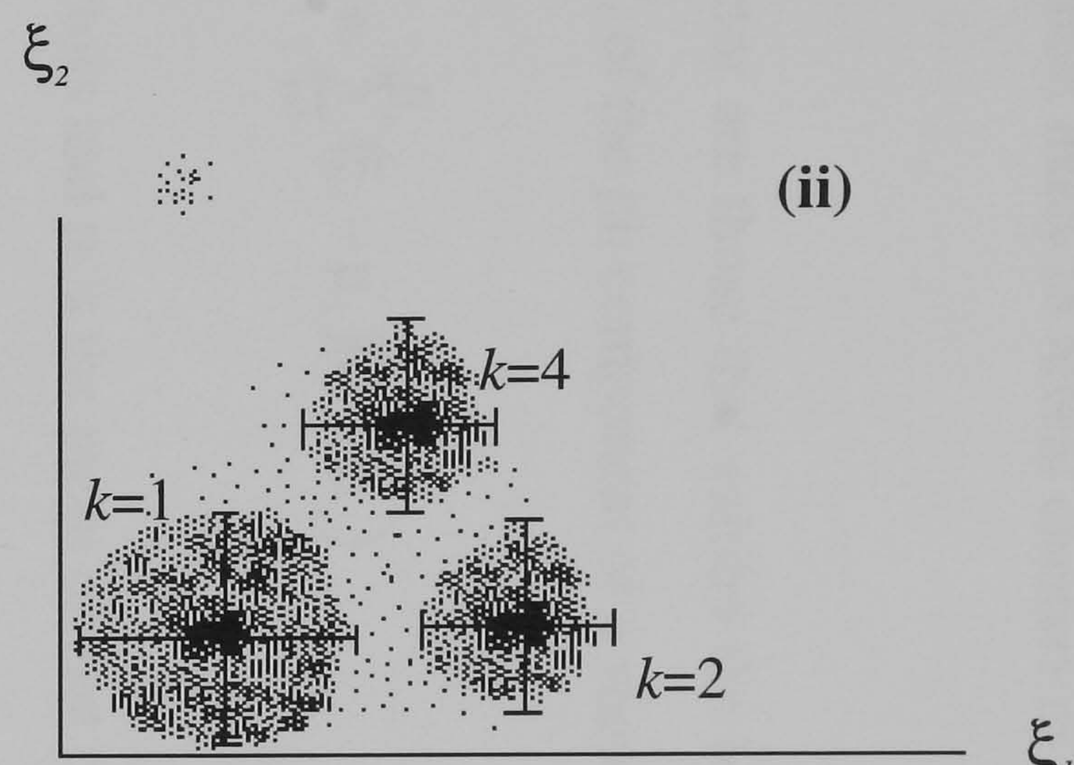

(b) After Pruning

Figure 5.4. Novelty Detection in the PRAN

the vectors have more than three components it is not possible to visualise them unless a group of two or three components from each vector are plotted. One technique for choosing the components that are most likely to reveal clusters of vectors is called principal component analysis (PCA).

The principal components of a vector are those that exhibit the highest variance from one vector to another. The variance, s^2, of the jth component of a vector is given by,

$$s^2 = \sum_{i=1}^{N} (\xi_i - \mu_\iota)(\xi_i - \mu_\iota) \tag{5.20}$$

where N is the total number of vectors and μ is the mean of that component which is given by.

$$\mu_i = \frac{1}{N} \sum_{i=1}^{N} \xi_i \tag{5.21}$$

PCA allows feature vectors with a large number of components, such as those that represent sampled waveforms, to be reduced to two or three component vectors that can be plotted on orthogonal axes. The location and spread of the kernels can also be visualised by plotting the corresponding components of the mean, $\boldsymbol{m}$, and variance, $\boldsymbol{F}$, for each kernel. PCA can also be performed on feature vectors before pattern recognition to reduce the amount of computation required and hence the processing time..

5.4. Summary

This chapter has discussed topics in computer pattern recognition relevant to the classification of waveform data. The methods were broadly divided into two classifier groups depending on whether or not the class membership for each measurement was known (supervised or unsupervised). Three supervised classifiers (k-nearest neighbour, nearest mean and back-propagation neural network) were introduced for use in situations when the class membership for each measurement was known and an unsupervised classifier

(the probabilistic resource allocating network or PRAN) for situations when the requirement is simply to identify novel measurements. Appendix B describes the interaction of the various algorithms designed and written by the author for the purpose of processing and classifying the waveform data from the coin-tap test. While the k-nearest neighbour and nearest mean algorithms were implemented with standard programming techniques, the PRAN required more advanced features to make the algorithm run more efficiently on a serial computer. Therefore, a description of the operation of the PRAN algorithm is also presented. The back-propagation neural network was implemented with a commercial software package (McClelland and Rumelhart, 1988). These methods will be used on data obtained by applying the coin-tap test to different structures in experiments described in the next two chapters.

6. TESTS ON BOLTED AND RIVETED STEEL JOINTS

6.1. Introduction

This chapter describes the application of the coin-tap test to the detection of corrosion deterioration in bolted and riveted joints in structural steelwork. Methods of pattern recognition described in the previous chapter were also used. The experience of ICI at their chemical works has shown that joints are particularly susceptible to corrosion damage in exposed structural steelwork because they act as moisture traps (Gallon, 1993). Capillary action draws water between the plies of bolted or riveted joints resulting in the formation of a layer of corrosion. Such a joint may be considerably weakened by loss of cross-section of bolts or rivets and by the expansive forces exerted by the corrosion products which occupy more volume than the original steel.

The first structure to be tested was a simple bolted joint constructed in the laboratory that was tested in various simulated conditions of deterioration due to corrosion. The methods were then applied to the detection of corrosion damage in the splice plates of the Clifton Suspension Bridge in Bristol. Two instruments were available for data acquisition: the first was a Diagnostic Instruments, PL202 spectrum analyser (Diagnostic Instruments, 1995); and the other was a Gould model OS4020 Digital Storage Oscilloscope (Gould, 1981).

6.2. Bolted Steelwork Joint

The layout of the bolted joint is shown in Figure 6.1. It consisted of an angle section connected to two fixed I-sections, both of which were made from black mild steel, as shown in Figure 6.1 (a). The angle was fixed to each I-section with two grade M10 bolts in each joint as shown in Figure 6.1 (d). This configuration represented the joint in its sound condition. Two conditions of deterioration were simulated: the first was a joint packed with corrosion products; the second was a joint that had suffered section loss. The first condition was achieved by introducing a layer of coarse iron filings, bound with grease into a stiff paste, at the interface between the plies before bolting up. The second was achieved by cutting away part of one leg of the angle close to the joint as indicated in Figure 6.1 (c) by the shaded rectangle.

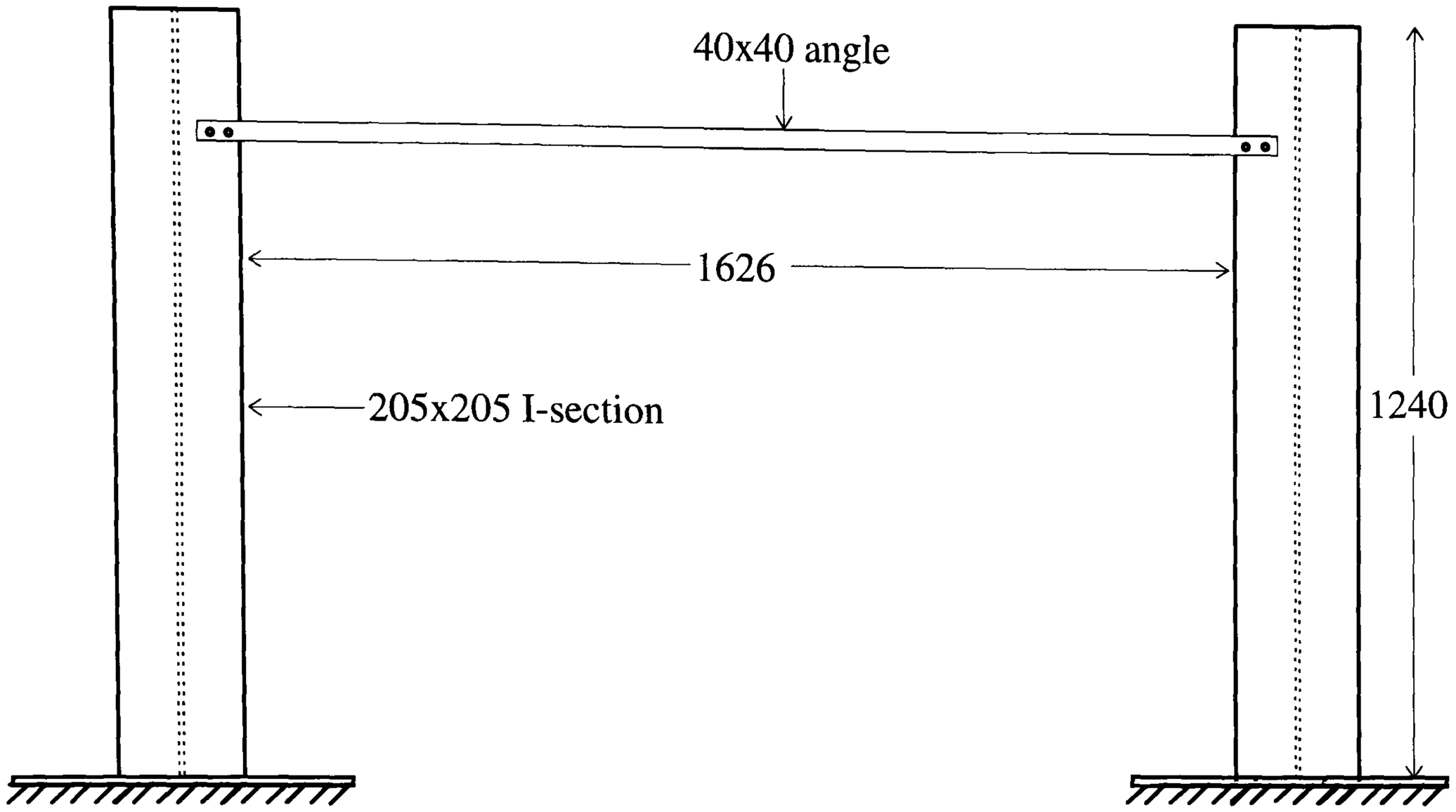

(a) Experimental Set-up (scale 1:16)

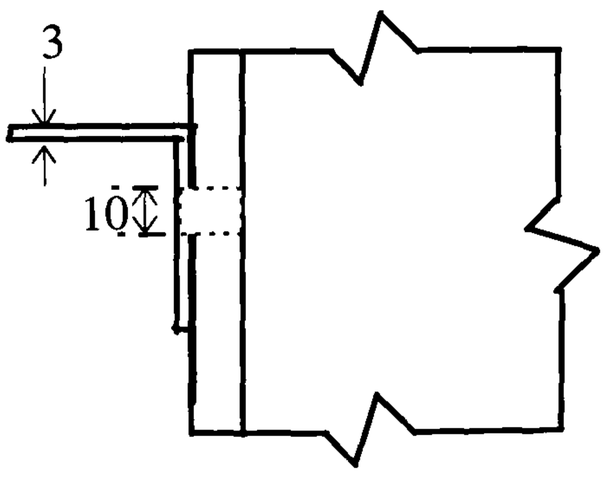

I- section

(b) Section (scale 1:3)

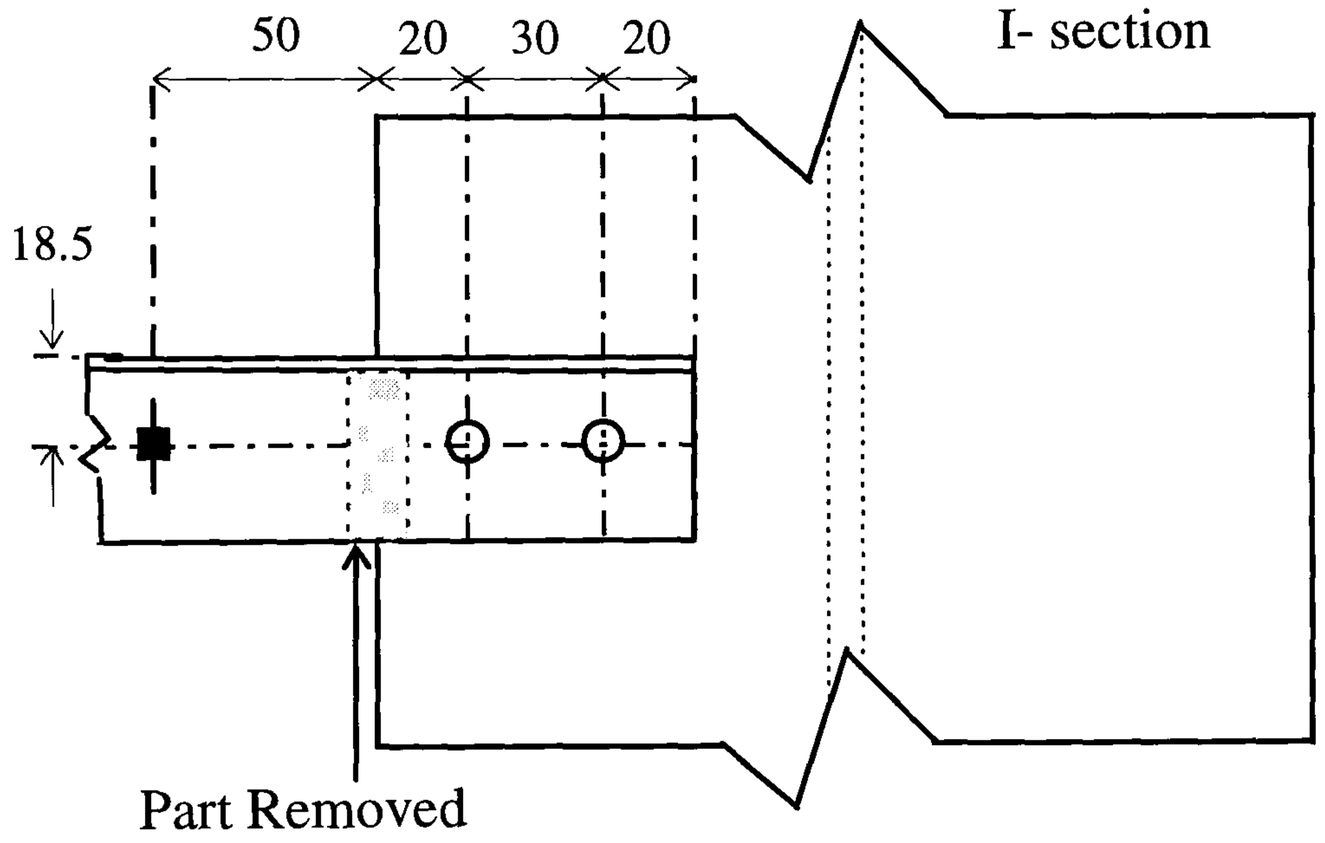

(c) Elevation (scale 1:3)

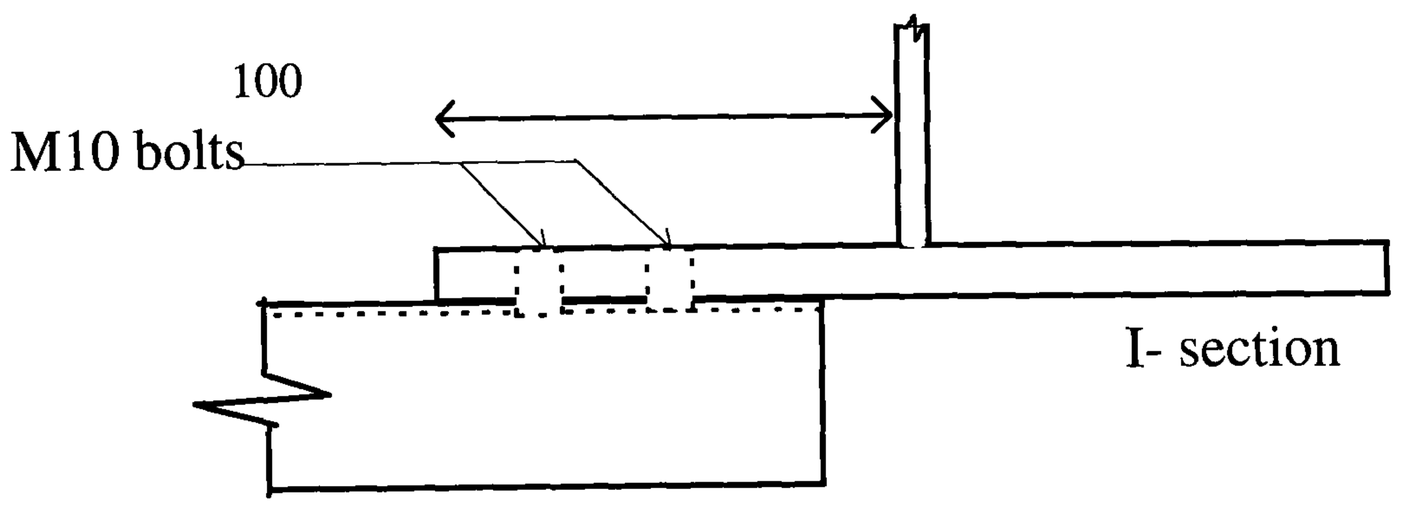

(d) Plan (scale 1: 3)

Figure 6.1. Bolted Steelwork Joint (dimensions in mm)

In the next section, the three categories of deteriorated joint that are referred to are described as follows:

sound : clean surfaces bolted firmly;

corroded : packed with corrosion products;

damaged : part of angle section removed.

6.2.1. Experimental Procedure and Results

The closer the location of impact is to the region affected by corrosion the greater will be the sensitivity to deterioration, provided that the damage significantly alters the structural properties in the direction of impact. In practice the location of impact may be limited by access to the joint and for this reason it was decided to test by impacting the angle section a short distance from the joint (see Figure 6.2). The angle was impacted at the mid-point of its lower leg in a direction that was perpendicular to the interface between the plies, this location being indicated on Figure 6.1 (c) by the black square. Owing to the dimensions of the angle it was only possible to impact at the desired location with the lightweight hammer, so this was used together with the long extender. The aluminium tip was used to maximise the contact stiffness and therefore the sensitivity.

Forty measurements of the impact force were taken by testing the joint as described above and acquiring the time history and frequency spectrum with the spectrum analyser. A rectangular window was used and the bandwidth was 20 kHz corresponding to a sample rate of 50 kHz (20 μs between samples). The frequency interval was 12.5 Hz. Each measurement was obtained by performing a process average on the time histories and spectra acquired from three impacts on the joint. The time histories and spectra for typical impacts on the joint in each condition are presented in Figure 6.3.

The impulse duration for the corroded joint is approximately 1.5 ms which is about the same as that of the sound joint as shown in Figure 6.3 (a) and Figure 6.3 (c). This suggests that the local stiffness of the corroded joint was not significantly less than that of the sound joint. Correspondingly, at approximately 300 Hz in the spectrum, the cut-off frequency

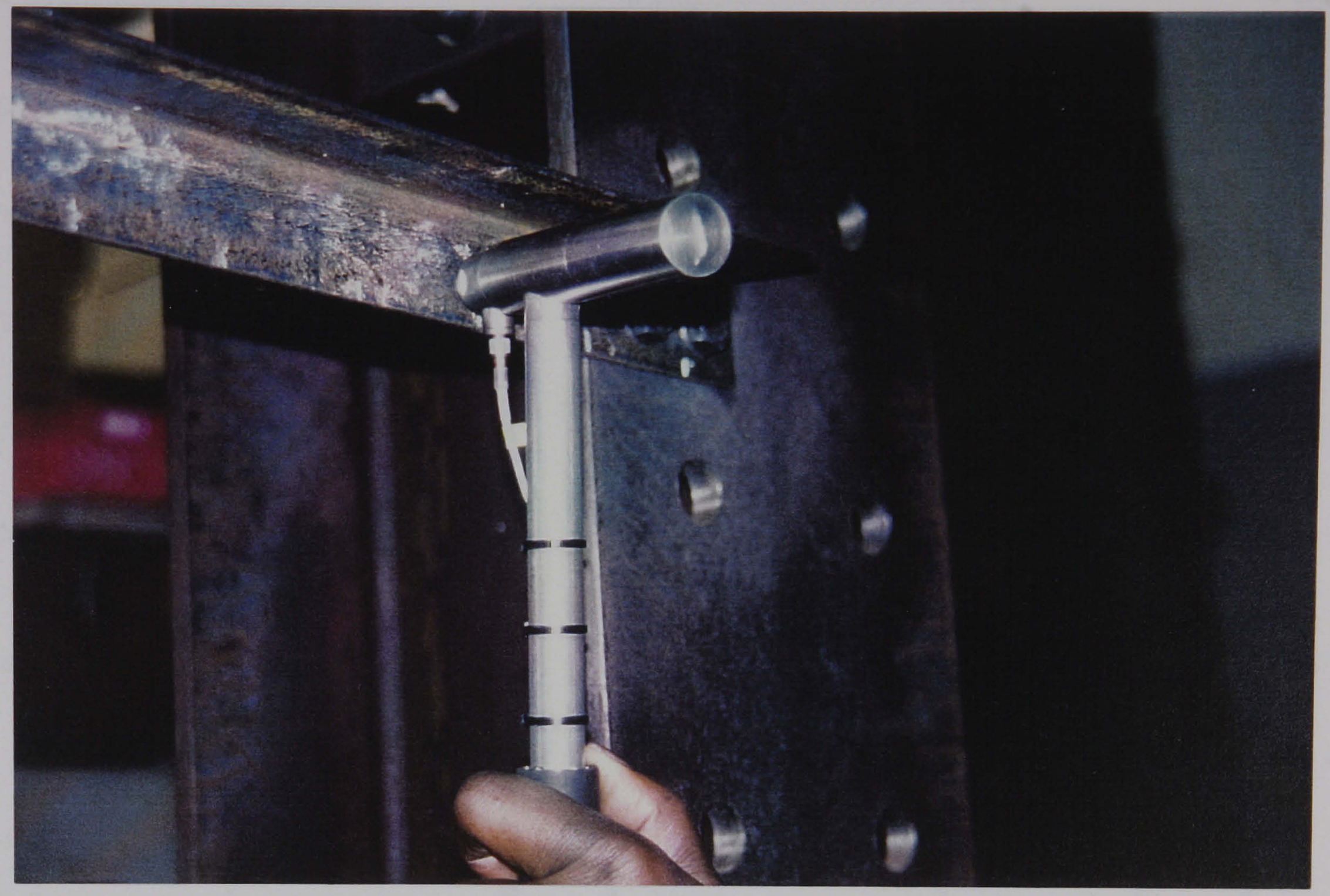

Figure 6.2. Applying the Coin-tap Test to the Bolted Steelwork Joint

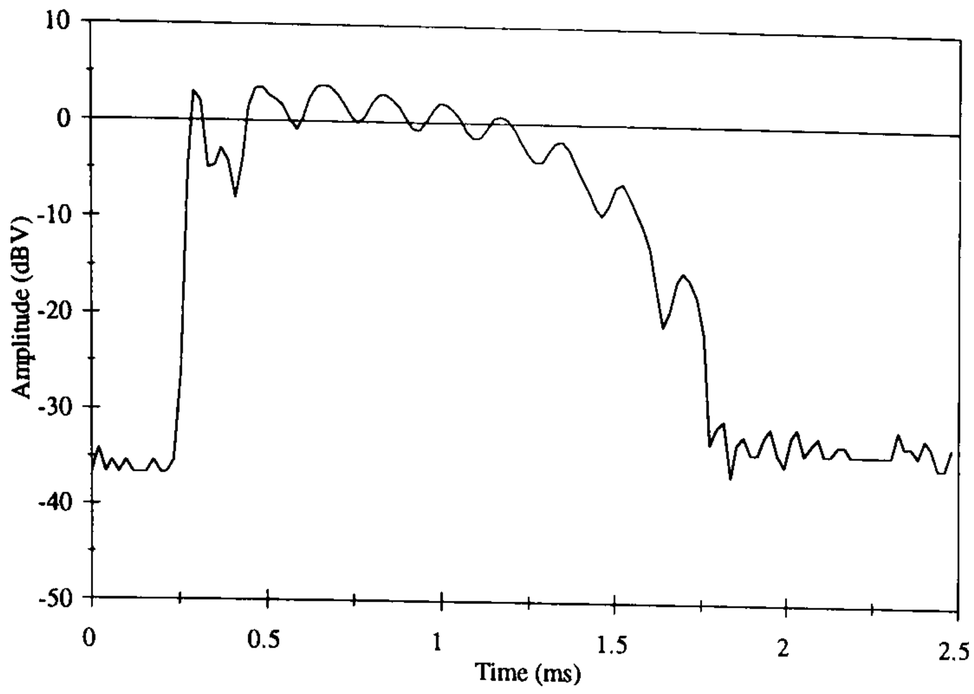

(a) Time History of Sound Joint

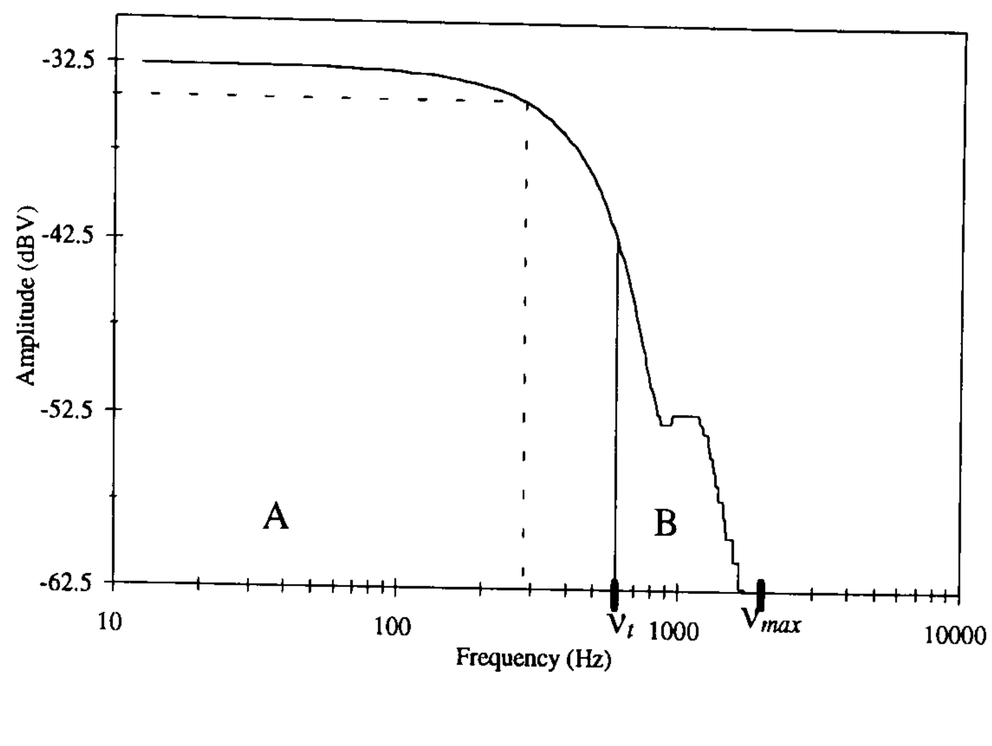

(b) Spectrum of Sound Joint

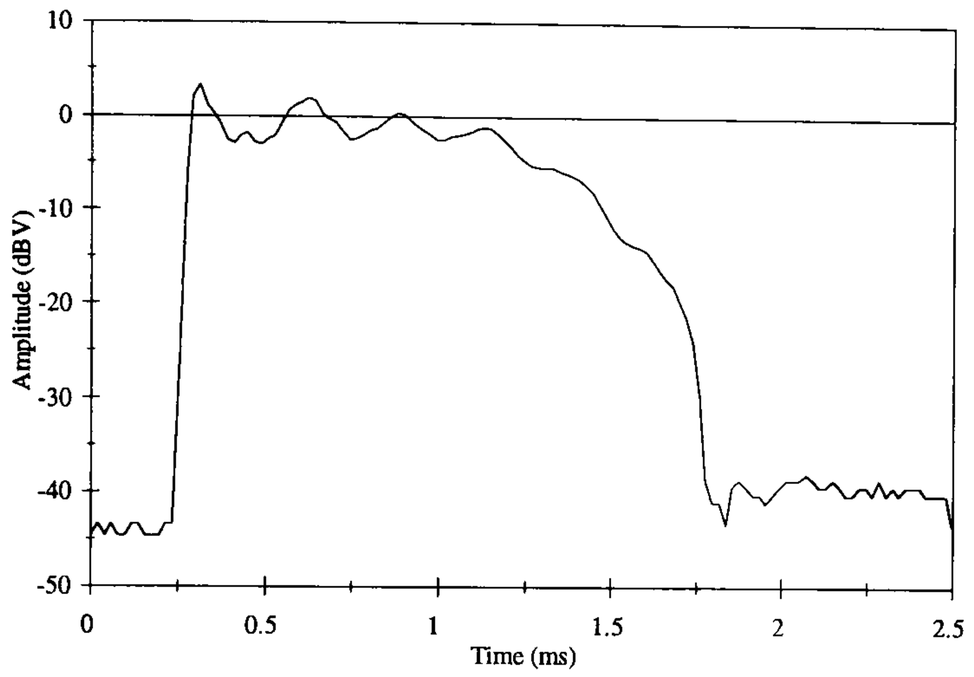

(c) Time History of Corroded Joint

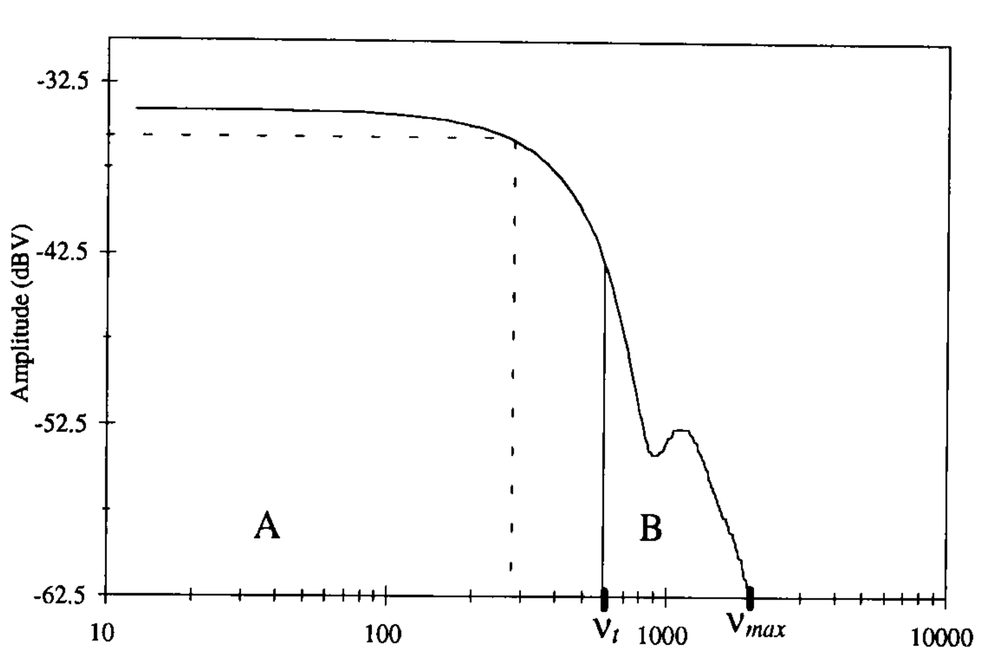

(d) Spectrum of Corroded Joint

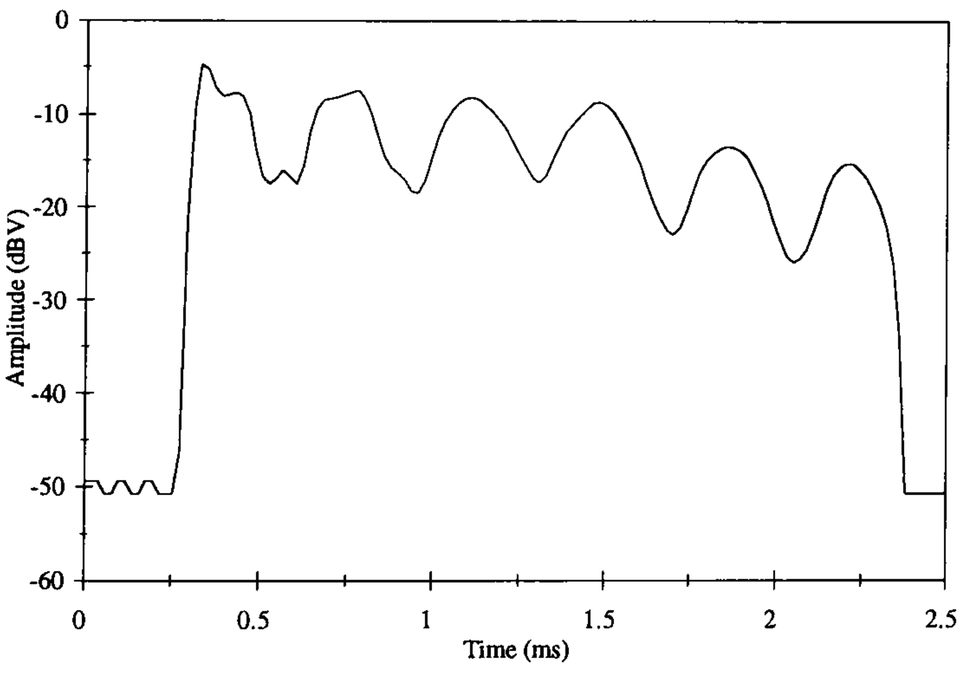

(e) Time History of Damaged Joint

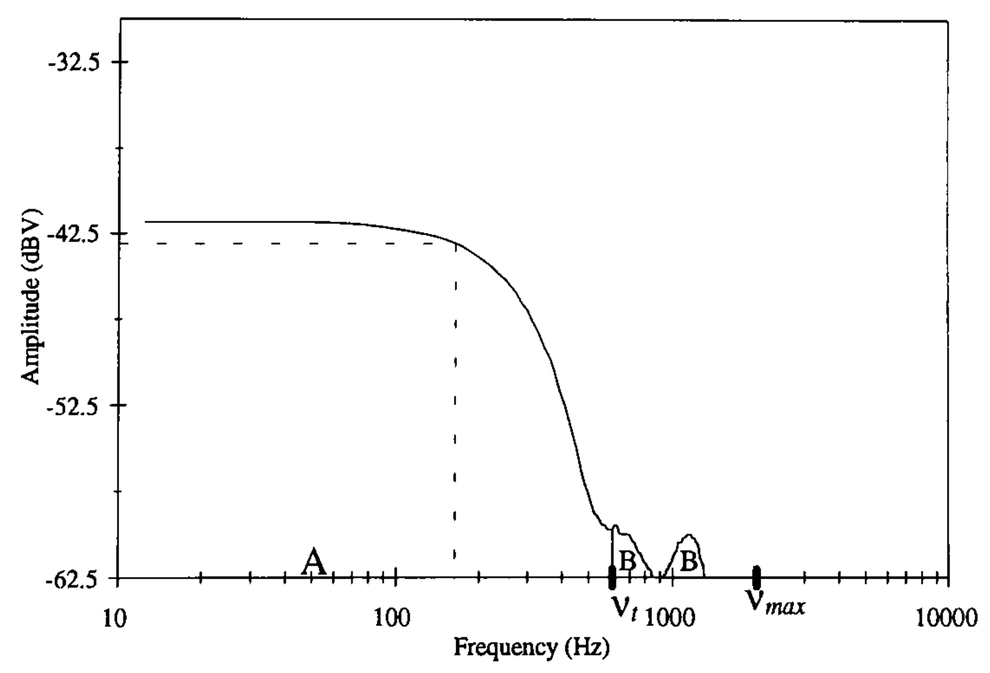

(f) Spectrum of Damaged Joint

Figure 6.3. Waveforms of Impact Force on Steelwork Joint (20 kHz Bandwidth)

(the frequency at which the spectral amplitude has fallen by 2 dB) for the sound joint is about the same as that of the corroded joint as indicated by the broken lines in Figure 6.3 (b) and Figure 6.3 (d). However, Figure 6.3 (e) shows that the impulse duration of the damaged joint is greater than 2 ms indicating a significant reduction in local stiffness compared with the sound joint. Figure 6.3 (f) shows that, at approximately 170 Hz, the cut-off frequency of the damaged joint is also significantly less than that of the sound joint.

Figure 6.4 shows the distributions of quantities sensitive to local stiffness for forty measurements on the joint in each of the three conditions. Figure 6.4 (a) shows a plot of the cut-off frequency versus the ratio of the area, B, between the threshold frequency (ν_t) and the maximum frequency (ν_{max}), to the total area (A+B) under the spectrum up to the maximum frequency. The threshold frequency was 600 Hz corresponding to 30% of the maximum frequency (2 kHz). These frequencies are also indicated on the spectra of Figure 6.3. It is clear that using both quantities, i.e. cut-off frequency and ratio of areas, it is possible to discriminate between all three conditions of the joint but this would not be possible using either one of the quantities on its own. The ratio of areas under the spectrum revealed a slight reduction in local stiffness in the corroded joint compared with the sound joint, that could not be identified from the cut-off frequency. The variability in a particular quantity for measurements on the joint in the same condition occurred because the location of impact between the supports varies from one blow to another and the local stiffness is generally very sensitive to this.

Figure 6.4 (b) shows a plot of the ratio of the impulse peak force to the enclosed area in the time domain versus the ratio of areas under the spectrum. It shows that the ratios in the time domain for measurements on the damaged joint were lower than those for measurements on either the sound joint or the corroded joint. This indicates that the ratio identified the stiffness reduction associated with the damaged joint and demonstrates the practical usefulness of this quantity. However, as with the cut-off frequency, it could not distinguish between measurements on the sound joint and measurements on the corroded joint. This is probably because the ratio in the time domain and the cut-off frequency are both related to the impulse duration and this does not change significantly because the local stiffnesses of the sound joint and the corroded joint are similar.

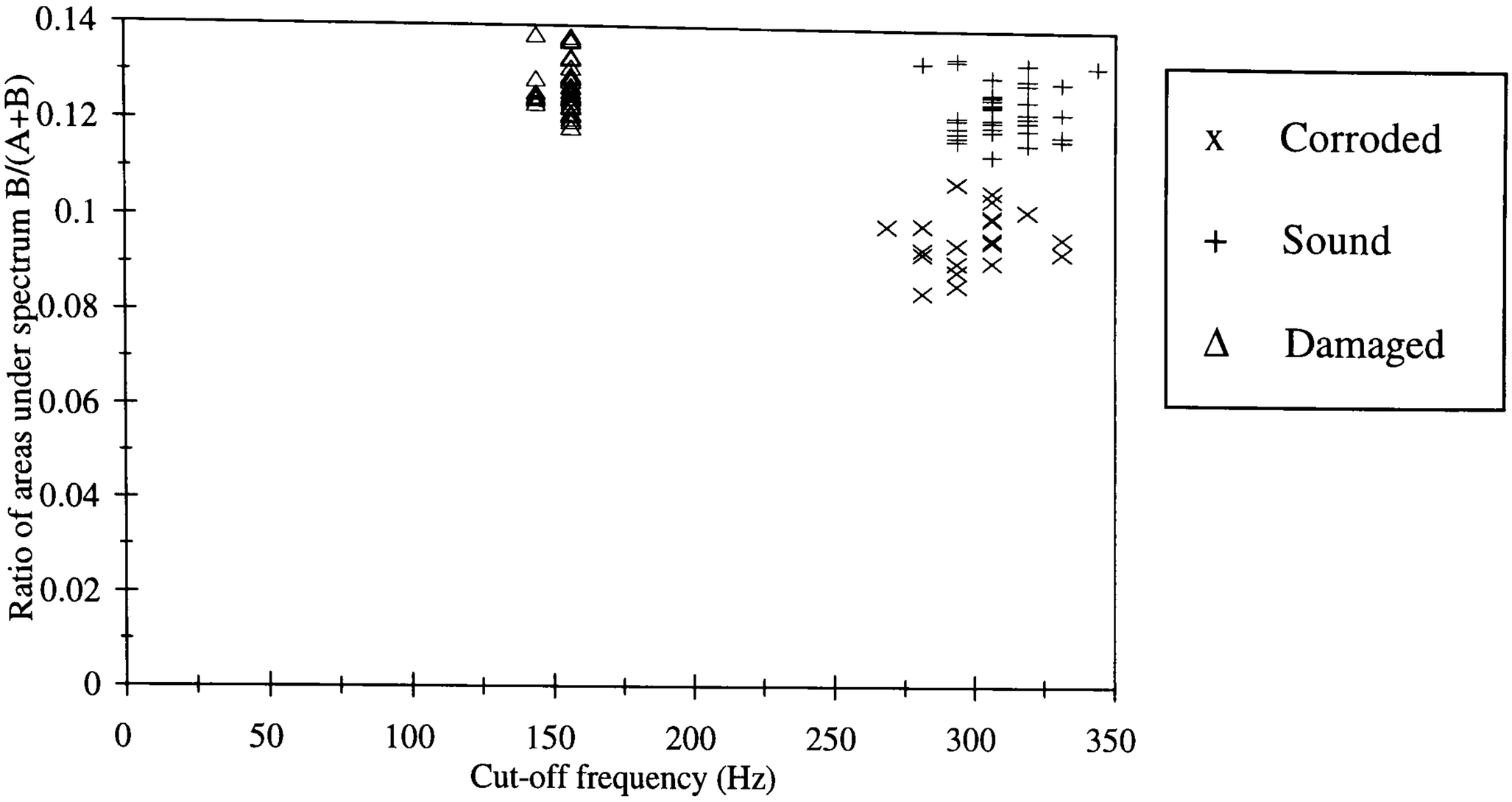

(a) Cut-off Frequency v Ratio of Areas Under the Spectrum

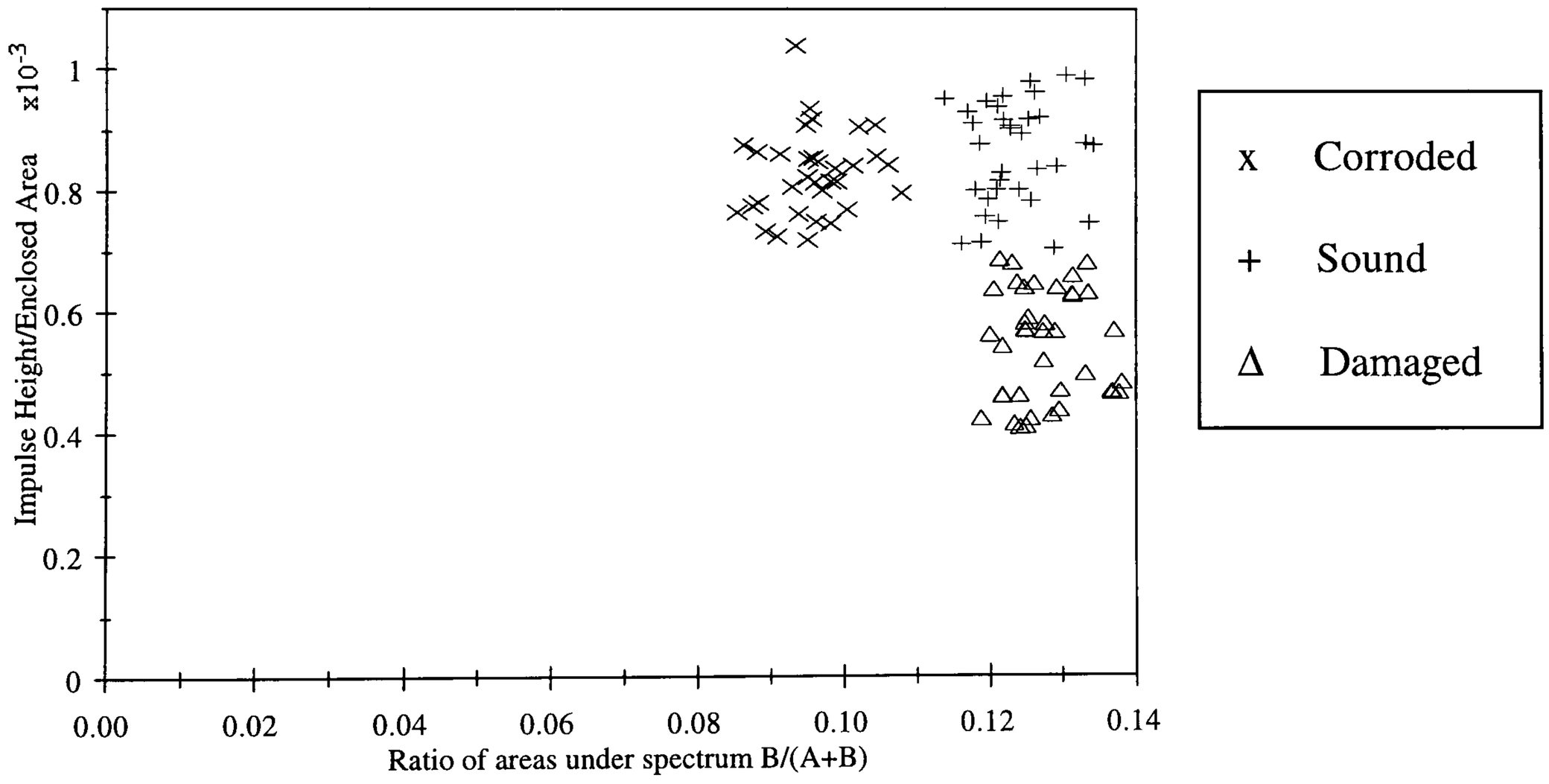

(b) Ratio of Impulse Peak Force to Enclosed Area v Ratio of Areas Under the Spectrum

Figure 6.4 Quantities Sensitive to Local Stiffness for Impacts on Steelwork Joint (20 kHz Bandwidth)

Figure 6.3 also shows the effect that corrosion damage has on the nature of the observed structural vibrations. Figure 6.3 (a) shows that there is significant 'ringing' on the sound joint's time history and it is clear from Figure 6.3 (c) that its *amplitude* is reduced in the corroded joint. This result suggests that vibrations, estimated from Figure 6.3 (a) at approximately 5.3 kHz, are effectively damped by the presence of corrosion products and that the time histories of the corroded joint and the sound joint can be distinguished on this basis. The damaged joint can also be distinguished from the sound joint by the changes in structural vibration. However, in this case it is the difference in the *frequency* of ringing vibrations on the damaged joint compared with that of the sound joint that is most significant. Figure 6.3 (e) shows that the damage reduced the 'ringing' frequency to approximately 2.5 kHz. Closer inspection of the time histories of the sound joint and the corroded joint after the impulse (time greater than 1.8 ms) reveals that the mean force level does not return to zero (the mean level of the pre-trigger between 0 and 0.25 ms). This indicates that contact persists for longer than 2.5 ms. Therefore the bandwidth was reduced to 5 kHz giving a sample rate of 12.5 kHz (80 μs between samples) which increased the duration of the time record to 10 ms. The time histories of these measurements are shown in Figure 6.5.

The time history of the sound joint is shown in Figure 6.5 (a). The interval between 2.5 ms and 10 ms reveals a 'ringing' frequency of approximately 625 Hz. Figure 6.5 (b) shows that the amplitude of these vibrations are reduced in the corroded joint indicating that there is strong damping by the corrosion products. The lower frequency vibrations are not visible on the time history obtained with a 50 kHz sample rate (Figure 6.3) because the period of these vibrations (~ 1.6 ms) is close to the impulse duration (~1.5 ms). The two coincide and it is the impulse that dominates. Although the Shannon theorem is not violated, the 5.3 kHz vibrations that are visible at the higher sample rate (Figure 6.3) are not visible at the lower rate. This is because the period of these vibrations is ~189 μs allowing only two samples per cycle at the lower sample rate compared with nine at the higher rate.

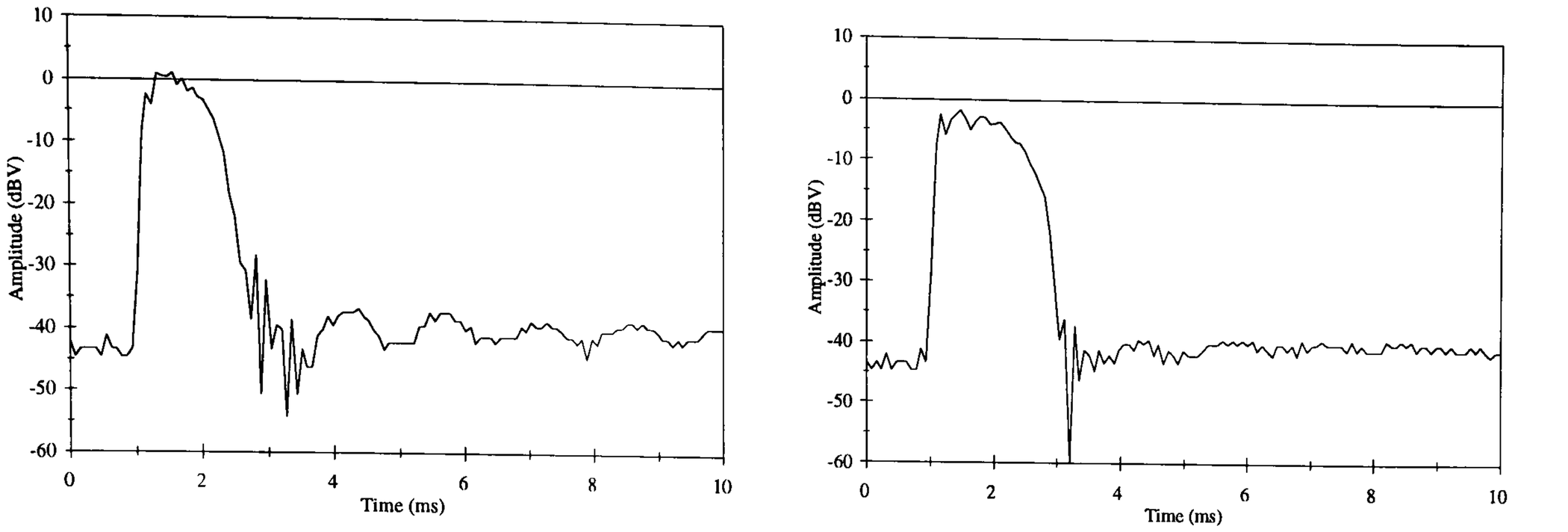

(a) Sound Joint (b) Corroded Joint

Figure 6.5. Time Histories of Impact Force on Steelwork Joint (5 kHz Bandwidth)

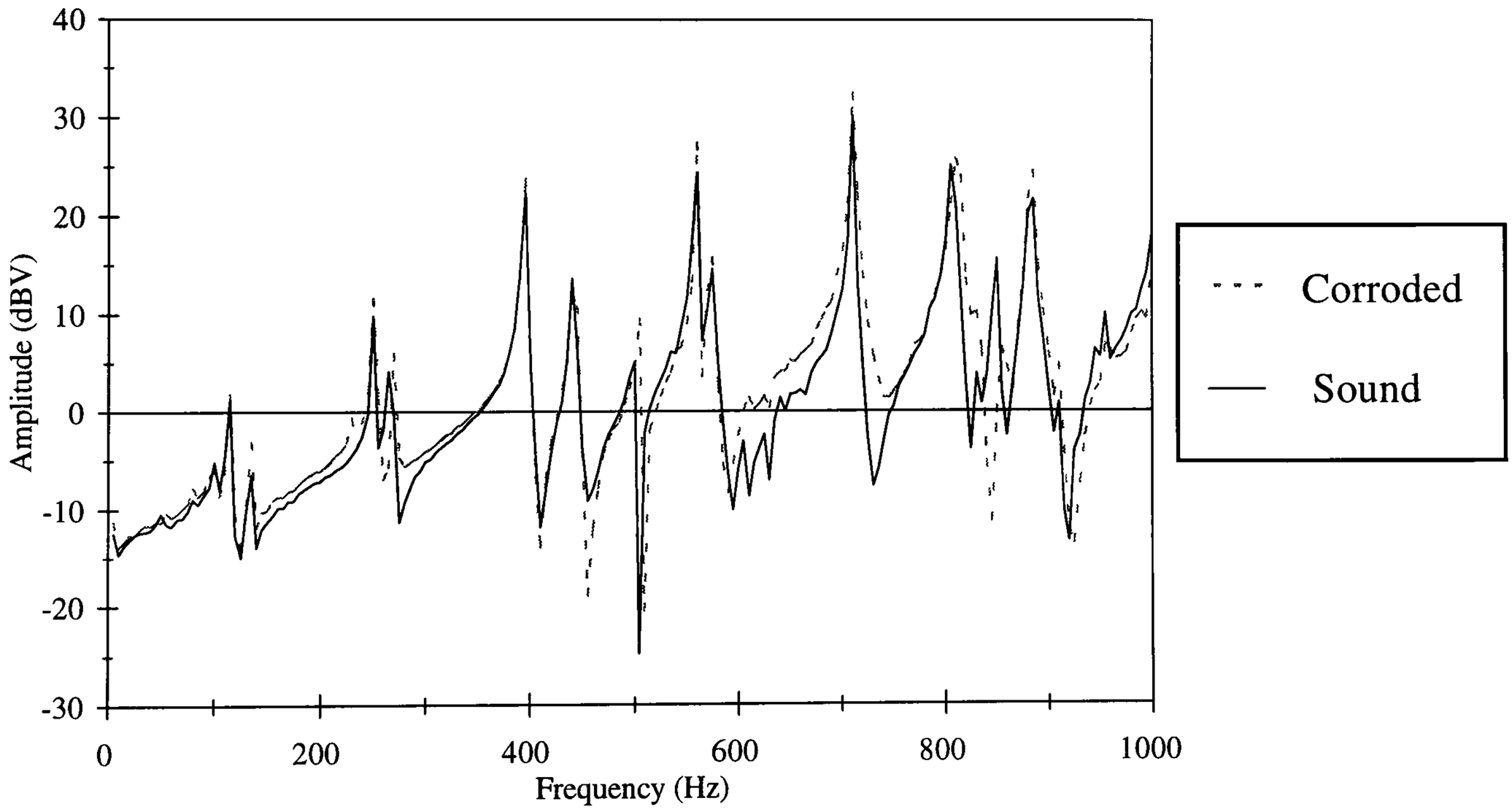

Figure 6.6. Accelerance of Mounted Angle Section Near Bolted Steelwork Joint

To verify this result the accelerance of the mounted angle section was measured by the impact method. The section was impacted with a polyurethane tip at the same location and the response of an accelerometer mounted on the other side of the angle directly opposite the impact location was measured. The less stiff tip had the advantage that it minimised the possibility of inducing non-linearities while still being capable of exciting the frequency band of interest.

The measured accelerances for the sound joint and the corroded joint are shown in Figure 6.6. It is clear from the general widening of the peaks that the corroded joint exhibits considerably more damping than the sound joint. The mode of vibration at approximately 700 Hz is affected more than the others and this probably corresponds to the 625 Hz structural vibrations. The modal frequency observed from the spectral response of an impact test is greater than the resonance frequency obtained using the oscillator because, unlike the latter, it is not influenced by structural damping. This confirms that the presence of corrosion products at the joint produces a significant change in local structural damping which in turn produces a noticeable reduction in the amplitude of 'ringing' vibrations. On a logarithmic amplitude scale the half-power points are the frequencies that correspond to an amplitude reduction of 3 dB. It is clear from Figure 6.6 that the corresponding frequency interval between the half power points for the mode of interest is very small and difficult to measure and therefore the damping factor in that mode is difficult to determine accurately.

To investigate the mechanism by which the structural vibrations are damped by corrosion products, the shape of the mode corresponding to the lower frequency 'ringing' vibrations, shown in Figure 6.5 (a), was measured using the resonance method. An electrodynamic oscillator, was connected to the angle section at the location of impact indicated by the black square in Figure 6.1 (c). The oscillator was tuned to the resonant frequency at 625 Hz and the response of an accelerometer attached at equally spaced locations along the mounted angle section was measured and plotted.

Figure 6.7 (a) shows that the mode shape, which was determined by fitting a smooth curve to the plotted points, had eight nodes between the flanges of the I-section. The response

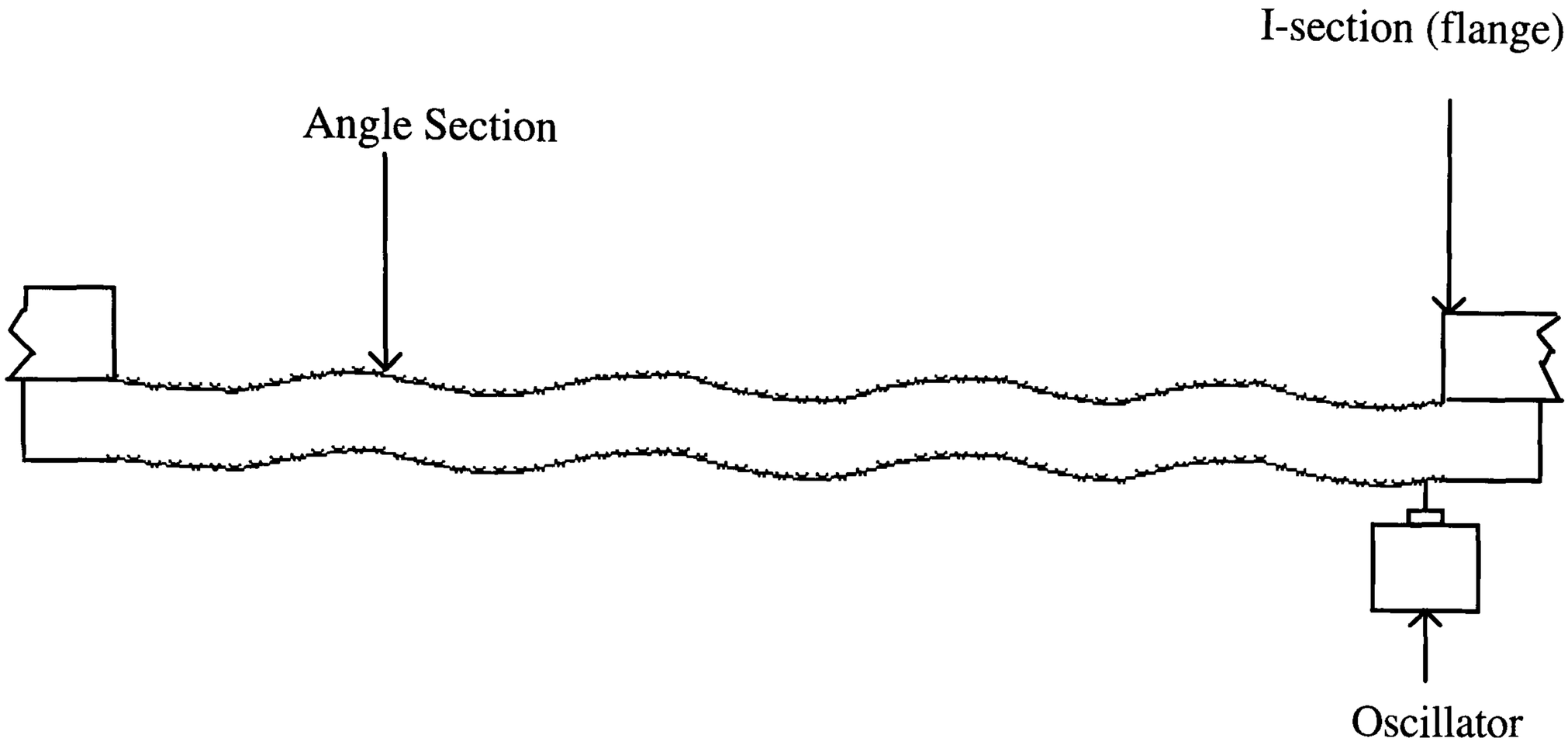

(a) Between I-section Supports (Horizontal Scale 1 cm :13 cm)

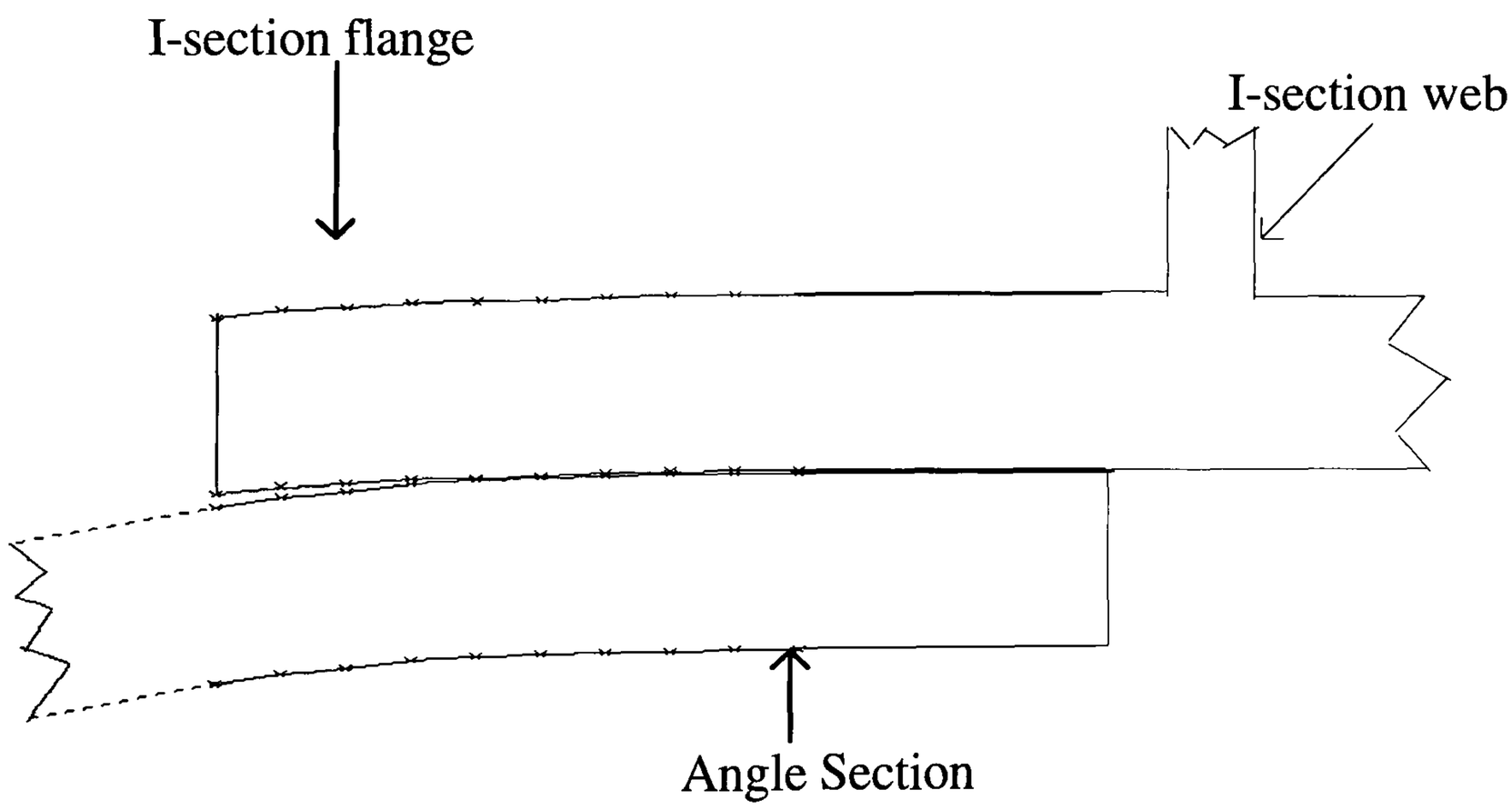

(b) At the joint (Horizontal Scale 1 cm : 1.3 cm)

Figure 6.7. Plan View of Mode Shape of Mounted Angle Section at 625 Hz

amplitude where the angle was connected to the I-section itself was comparatively low, so the mode shape in that region was sketched on a larger scale and is shown in Figure 6.7 (b). Evidently the region where simulated corrosion products were introduced is periodically compressed and expanded during the vibration of this mode. These vibrations are heavily damped by the corroded joint because mechanical energy is dissipated in the viscous paste whereas they are lightly damped in the sound joint because mechanical energy is dissipated in air.

This concludes the discussion of results obtained by applying the coin-tap test to the bolted steelwork joint under these specific experimental conditions. Other experimental approaches that were effective at detecting corrosion are presented in the section 6.2.3. The following section describes the methods of pattern recognition which were applied to this data in order to classify it automatically according to the condition of the corresponding joint.

6.2.2. Methods of Pattern Recognition

The coin-tap test measurements corresponding to known joint conditions that were acquired with a 50 kHz sample rate (20 kHz bandwidth) were used with methods of pattern recognition. The supervised methods assumed that the measurements belonged to one of three classes corresponding to each condition of the joint. The unsupervised method assumed that there were only two classes, those corresponding to measurements that were from the sound joint and those that were not. The methods were tested with feature vectors obtained from measurements on the joint after it had been dismantled then re-assembled in each of the three conditions. These represent the unknown vectors and are subsequently referred to as test vectors.

The first two supervised methods were simple statistical classifiers: the nearest mean and the nearest neighbour. Two dimensional feature vectors, composed of the cut-off frequency and the ratio of areas under the spectrum, were computed from measurements on the joint in each of its known conditions. These vectors formed a probability distribution with three

generator functions each comprising measurements from the joint in one of three conditions and representing one class.

The performance of the statistical classifiers was then tested with three test vectors, each representing a different condition of the joint. The cut-off frequencies were numerically on a scale of the order of 125 Hz to 360 Hz whereas the ratios of areas under the spectrum were of the order of 0.08 to 0.14 and the ratios in the time domain were of the order of $4x10^{-4}$ to $1x10^{-3}$. Because of the large differences in numerical scale it was found convenient to normalise these components by dividing each by the standard deviation of that component over all the vectors in the probability distribution. This standardises the scale of each component of the distance vector and prevents the largest component from dominating.

To determine the nearest mean the components of the mean for a class of vectors were computed and the distance of this mean from the test vector was computed by taking the square root of the sum of the square of each component of the scaled distance between the test vector and the mean. This process was repeated for all classes and the test vector was assigned membership of the class corresponding to the shortest distance. To determine the nearest neighbour the scaled distance between the test vector and each vector in the probability distribution was computed and the test vector was assigned membership of the class to which the nearest vector belonged. Table 6.1 summarises the results obtained.

Condition of Joint	Scaled test vector	Scaled Distance from Class Mean			Class of nearest neighbour
		Sound	Corroded	Damaged	
Sound	3.31, 7.78	**0.48**	1.67	2.58	Sound
Corroded	3.06, 6.09	1.73	**0.61**	2.20	Corroded
Damaged	2.06, 10.9	3.11	4.59	**2.81**	Damaged

Table 6.1. Classification of Impact Force on Bolted Joint with Statistical Techniques

For each test vector the class of its nearest neighbour is the same as the condition of the joint from which the measurement was taken and the test vector is closer to the mean of this class than that of any other class. The results show that both of the simple statistical methods were effective in classifying test vectors according to the correct condition of the bolted joint.

The second method of supervised classification was the back-propagation neural network. Forty-eight components of the feature vectors were obtained by sampling the dynamic waveforms of both time history and the spectrum. Feature vectors of the time history were composed of the first consecutive samples of the raw data after the pre-trigger, corresponding to a time interval of approximately 1 ms (Figure 6.3). This approach was preferred to that of doubling the interval by ignoring alternate raw data points and thereby representing the whole impulse. The reason was that such an approach does not preserve the details of the impulse caused by 'ringing' and these could be important in discriminating between corroded and sound joints because the impulse durations are very similar. However, the spectra were sampled to form feature vectors that represented the frequency content over the 2 kHz interval where its amplitude was significant (Figure 6.3). The first eight components were obtained by sampling at 125 Hz intervals and the remaining forty from 1.025 kHz to 2 kHz were obtained by sampling at intervals of 25 Hz.

The neural network was implemented on a commercial software package (McClelland and Rumelhart, 1988). The first layer had twenty units and the second layer had three units, one for each condition of the joint. Before training the weights on the network interconnections were initialised with random values as were the thresholds for each unit. The network was set to a training mode whereby it updated the weights after every training vector rather than after every epoch. The learning rate was 0.5, the momentum constant was 0.2 and the criterion for network convergence was defined as an error function that had been reduced to a value of 0.04 or less. Each training vector was normalised between 0 and 1 and the three target vectors were 100, 010 or 001 depending on whether the training vector corresponded to a sound joint, a corroded joint or a damaged joint. The network converged after 682 epochs (~17 hours) when trained with feature vectors sampled from the time histories and it

converged after 283 epochs (~7 hours) when trained with feature vectors sampled from the spectra.

The performance of the network was then tested with nine test vectors, three for each condition of the joint. Each vector was 'clamped' to the input distribution and the network output was computed with the weights computed during training. Table 6.2 summarises the results obtained. These show that the network correctly classifies all conditions of the joint with a high degree of certainty, particularly the time histories. For example, it estimates a 99.7% probability that a test vector representing the sound joint's time history belongs to that class and an 89.6% probability for the corresponding spectrum. The probability of misclassification is generally very low, the highest observed value being a 25.7 % probability that the second test vector representing the spectrum of the corroded joint belongs to the damaged class. The results show that the neural network was effective in correctly classifying test vectors according to the condition of the bolted joint.

Condition of sample	**Test No.**	**Target values**			**Output values**					
					Time history			**Frequency Spectrum**		
Sound	1	1	0	0	**0.992**	0.007	0.000	**0.921**	0.002	0.174
	2				**0.997**	0.001	0.005	**0.896**	0.008	0.053
	3				**0.991**	0.002	0.002	**0.916**	0.016	0.017
Corroded	1	0	1	0	0.001	**0.998**	0.001	0.000	**0.986**	0.103
	2				0.002	**0.998**	0.000	0.000	**0.948**	0.257
	3				0.001	**0.997**	0.005	0.001	**0.988**	0.040
Damaged	1	0	0	1	0.002	0.000	**0.999**	0.002	0.000	**0.999**
	2				0.009	0.000	**0.994**	0.001	0.000	**0.999**
	3				0.009	0.001	**0.995**	0.003	0.000	**0.999**

Table 6.2. Classification of Impact Force on Bolted Joint with Neural Network

The unsupervised method was the probabilistic resource allocating network (PRAN). The PRAN was trained by cyclically presenting it with 40 feature vectors that were obtained by

sampling the sound joint's time history at 48 points as for the neural network. The constant α_0 was set to 0.7 as recommended by Roberts and Tarrassenko (1994) and it was found that when the maximum threshold parameter was $6x10^{-3}$ the PRAN grew 17 units and subsequently classified test vectors representing the sound joint as normal whereas test vectors representing the corroded and damaged joints were classified as novel. It was found that when the maximum threshold was a higher value more units were grown and the PRAN classified some of the sound joint's test vectors as novel. When the maximum threshold was lower fewer units were grown and some of the test vectors representing the corroded or damaged joints were classified as normal. These results suggest that, given sufficient feature vectors to represent the sound joint and an empirically chosen maximum threshold, the PRAN can be used effectively to detect measurements from joints that have a deteriorated condition due to the effects of corrosion.

This section has described the results obtained when the coin-tap test was used to detect deterioration due to corrosion in a bolted steelwork joint under given experimental conditions. The ability to identify different states of deterioration due to corrosion is improved by obtaining more dynamic information on the structure being tested. One approach is to maximise the information obtained from one measurement by computing different quantities and sampling waveforms as described in this section. Another is to perform the test under new experimental conditions. The next section describes the experimental conditions that were found to be effective in identifying corrosion deterioration from the bolted joint's impact time histories, together with the results obtained. All experimental conditions other than those specified were the same as those described in this section.

6.2.3. Other Experimental Procedures

This section describes the results obtained when the coin-tap test was applied to the bolted joint under new experimental conditions. The time history of the impact force was captured on the oscilloscope and recorded on an x-y plotter. Identification of corrosion deterioration in the bolted joint was found to be possible by varying the location or direction of impact or by varying the tip stiffness.

The time history was found to be sensitive to the presence of corrosion when the location of impact was on the bolt itself. Figure 6.8 (a) shows the impulses for impacts on the bolt furthest from the I-section web. The impulses of the sound joint and the damaged joint are indistinguishable because the damage does not affect the local stiffness near the bolt. However, the impulse of the corroded joint is clearly distinguishable from that of the sound joint. Figure 6.8 (a) shows that the corrosion products reduce the local stiffness producing the characteristic increase in impulse duration. It can also be noted that the impulse durations are generally shorter than those of impacts on the angle a short distance from the joint indicating that the local stiffness at the bolts is greater. There is also less 'ringing' because the local response at the bolts is influenced by the I-section support which is heavier than the angle and therefore requires more kinetic energy to excite structural vibrations. Corrosion was also detectable by changing the direction of impact from horizontal to vertical as illustrated in Figure 6.9.

Figure 6.8 (b) shows the time histories obtained when the joint was impacted at the same distance from the I-section as the location indicated in Figure 6.1 but vertically and on the upper leg of the angle. The different conditions of corrosion deterioration can be discriminated according to their impulse durations. The local stiffness of the corroded joint is less than the sound joint and the local stiffness of the damaged joint is less than the corroded joint as indicated by the corresponding increases in impulse duration.

Figure 6.10 shows that different joint conditions could also be discriminated by differences in local stiffness when the aluminium tip was replaced with a plastic tip thereby reducing its stiffness. The differences in impulse duration indicate that all three conditions could be discriminated when the angle was impacted horizontally on its lower leg as shown in Figure 6.10 (a). Only the sound and corroded joints could be discriminated when it was impacted vertically on its upper leg as shown in Figure 6.10 (b).

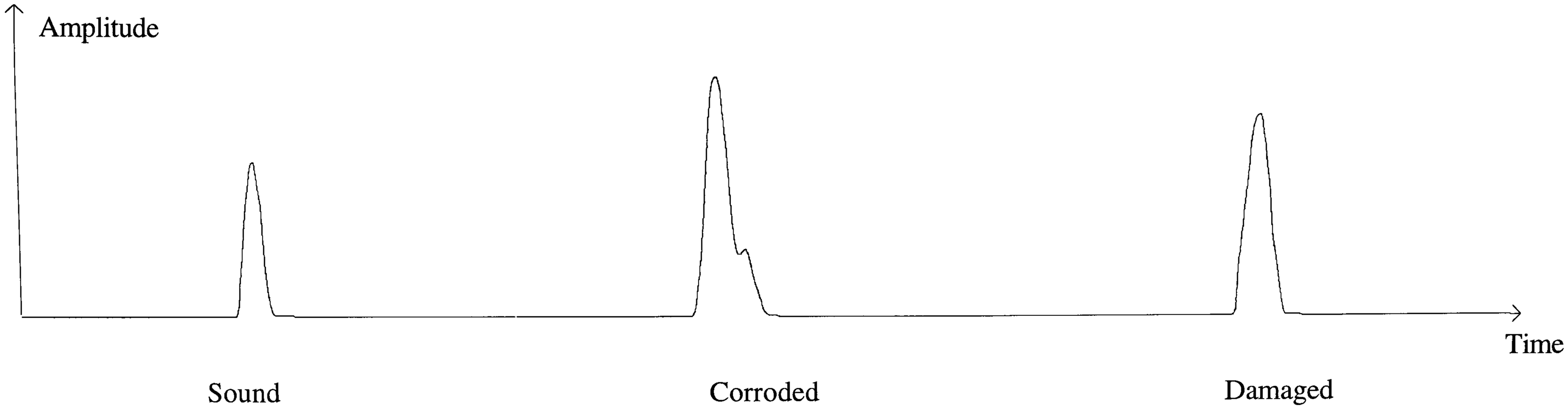

(a) Impact on Head of Bolt Furthest From I-section Web

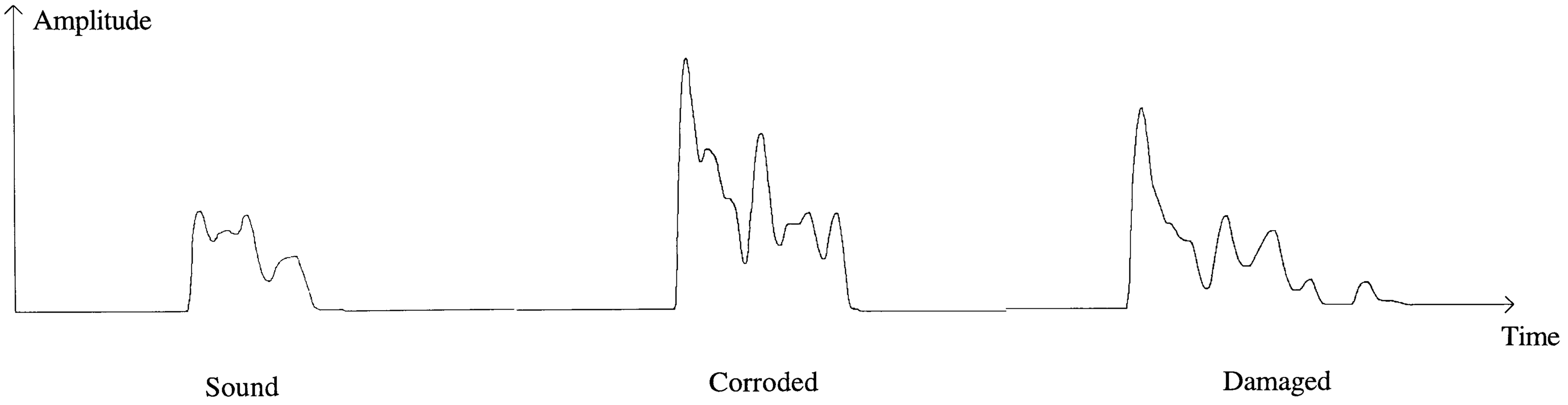

(b) Vertical Impact (12 cm from end of angle section on upper leg)

Figure 6.8. Effect of Corrosion on Force-Time History of Bolted Joint for Different Impacts (Time-scale: 0.8075 ms/cm)

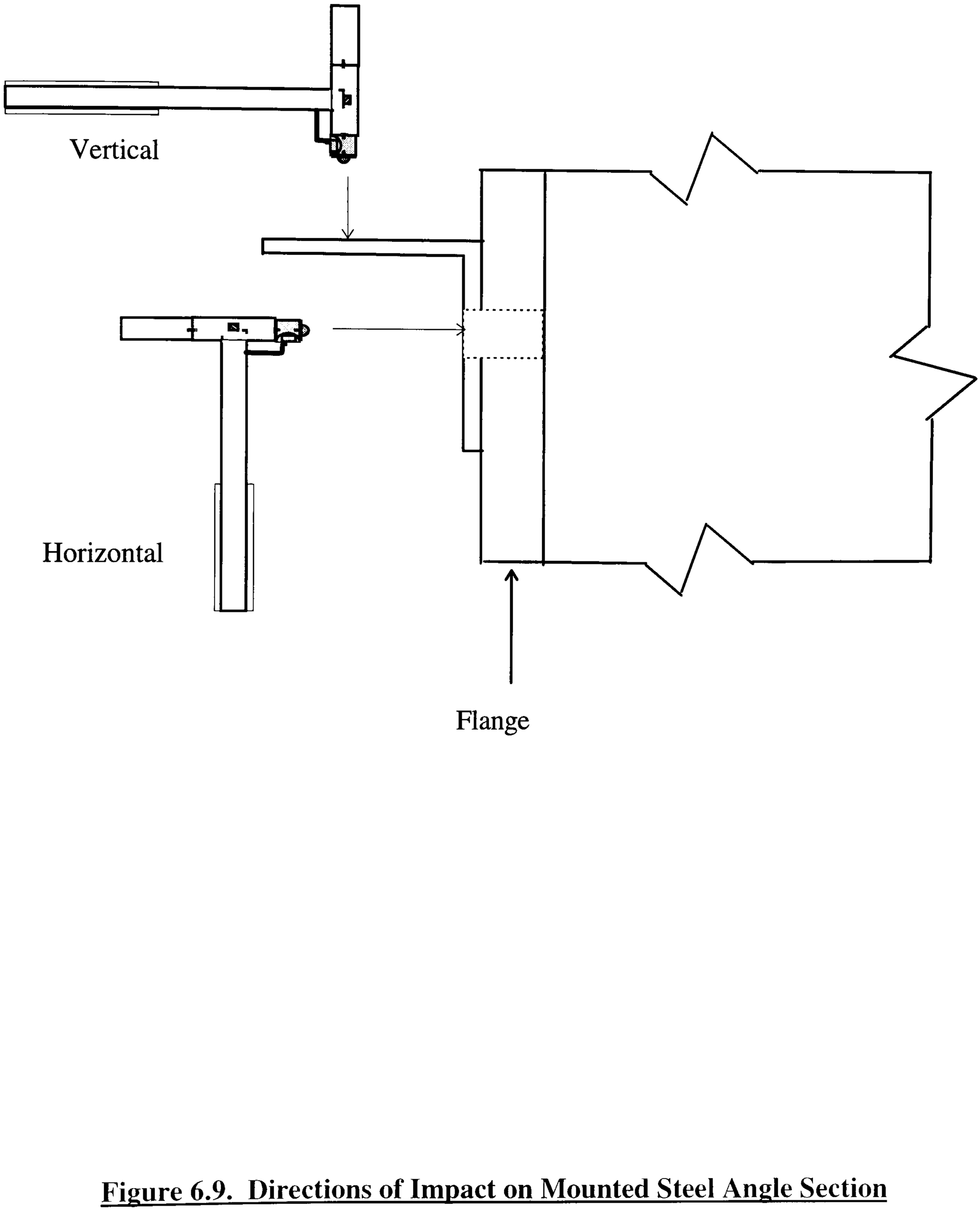

Figure 6.9. Directions of Impact on Mounted Steel Angle Section

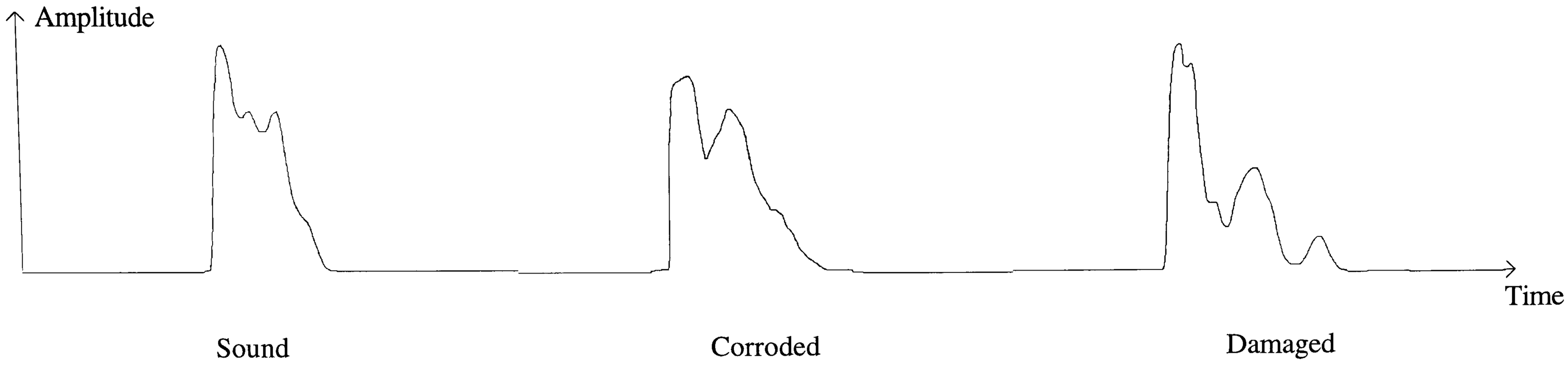

(a) Horizontal Impact (12 cm from end of angle section)

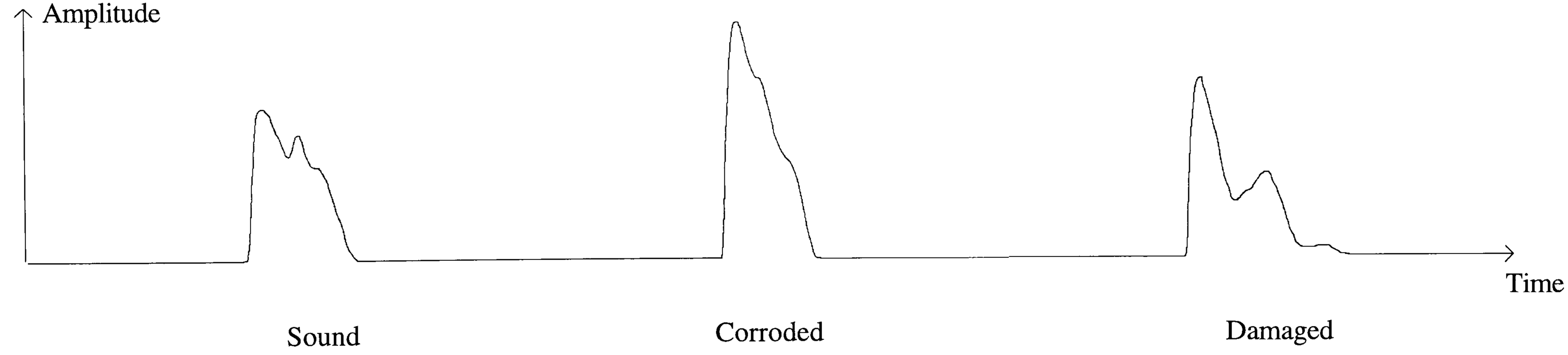

(b) Vertical Impact (12 cm from end of angle section)

Figure 6.10 Effect of Corrosion on Force-Time History of Bolted Joint Impacted with Plastic Tip (time-scale: 1.615 ms/cm)

6.3. Splice Plates

The splice plates provide continuity for the flanges of an iron lattice girder belonging to the Clifton Suspension Bridge in Bristol (built in 1864). There are two parallel rows of twenty-six splices and each row is located underneath the handrails near to the footways that border either side of the road (Figure 6.11). The splices had been painted some time ago but this could conceal corrosion that may develop at the joint interfaces when capillary action draws water through the damaged paint-work trapping it there. It has been found that many of these splices have worked loose over a period of time due to deterioration through corrosion and repeated loading.

Some splices appeared to be sound but the paint-work on others showed small cracks and discoloration indicating that deterioration due to corrosion was present. Other splice plates that were visibly very badly corroded had already been repaired by means of steel cover plates and friction grip bolts in place of the rivets. Therefore there were three different visual categories of splice plate: sound riveted; badly deteriorated riveted; and recently repaired bolted. A visual appraisal of the splices such as this may indicate deterioration due to corrosion but it is not always reliable. For example, a splice may be corroded even though the paint-work does not appear to be deteriorated. In such cases it should be possible to detect deteriorated splices using the coin-tap test.

The riveted iron splice plate is shown in Figure 6.12. It is made up with an iron cover plate riveted to the ends of the angle section flanges as shown. The test was performed by impacting the underside of the joint at the location indicated by the black square on Figure 6.12. Although inconvenient this was necessary because the timber handrail prevented access to the upper surface. It was also necessary to expose the steel surface by removing some paint at the location of impact; this improves the sensitivity because the contact stiffness is increased.

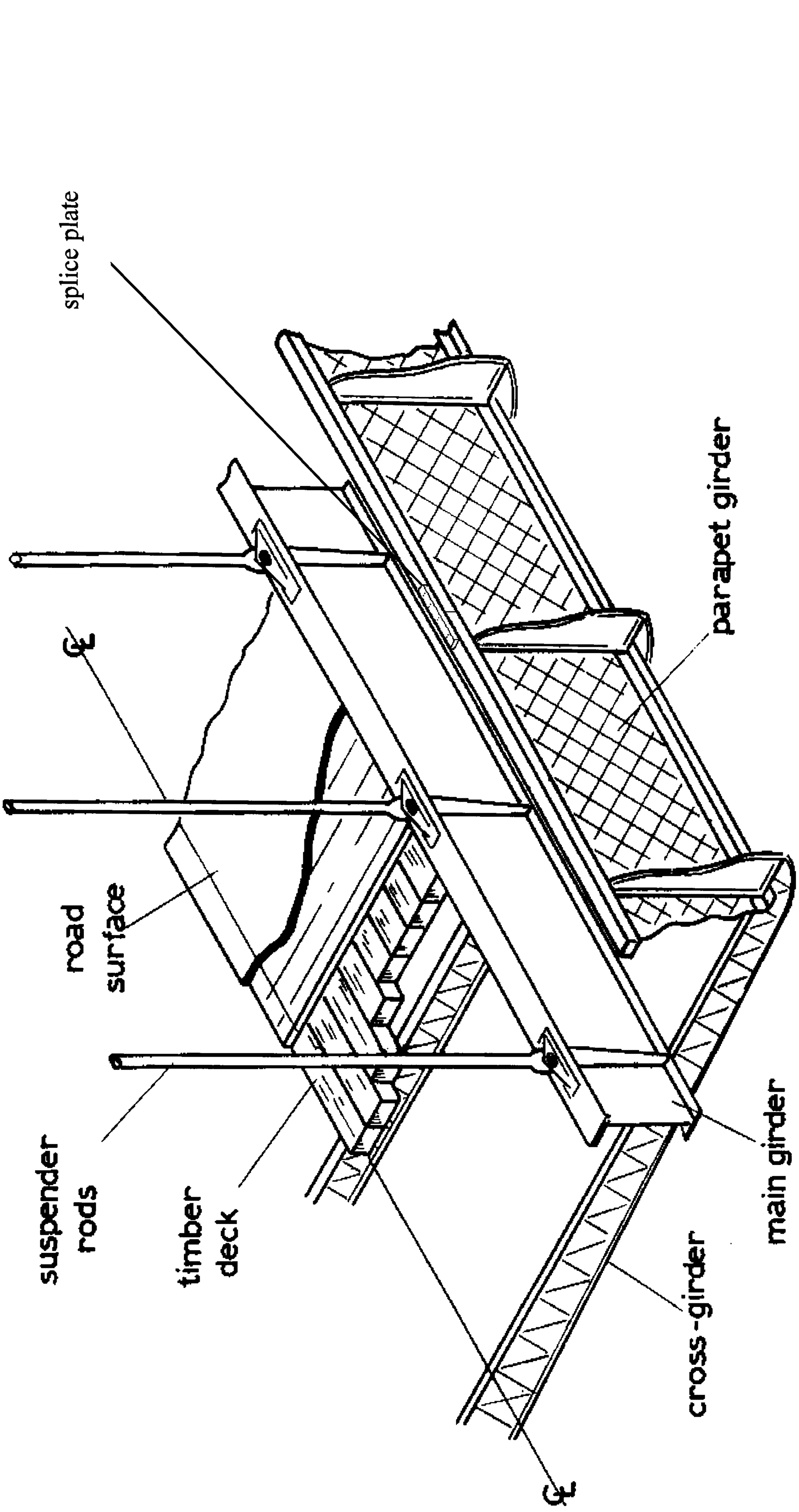

Figure 6.11. Structure of Clifton Suspension Bridge

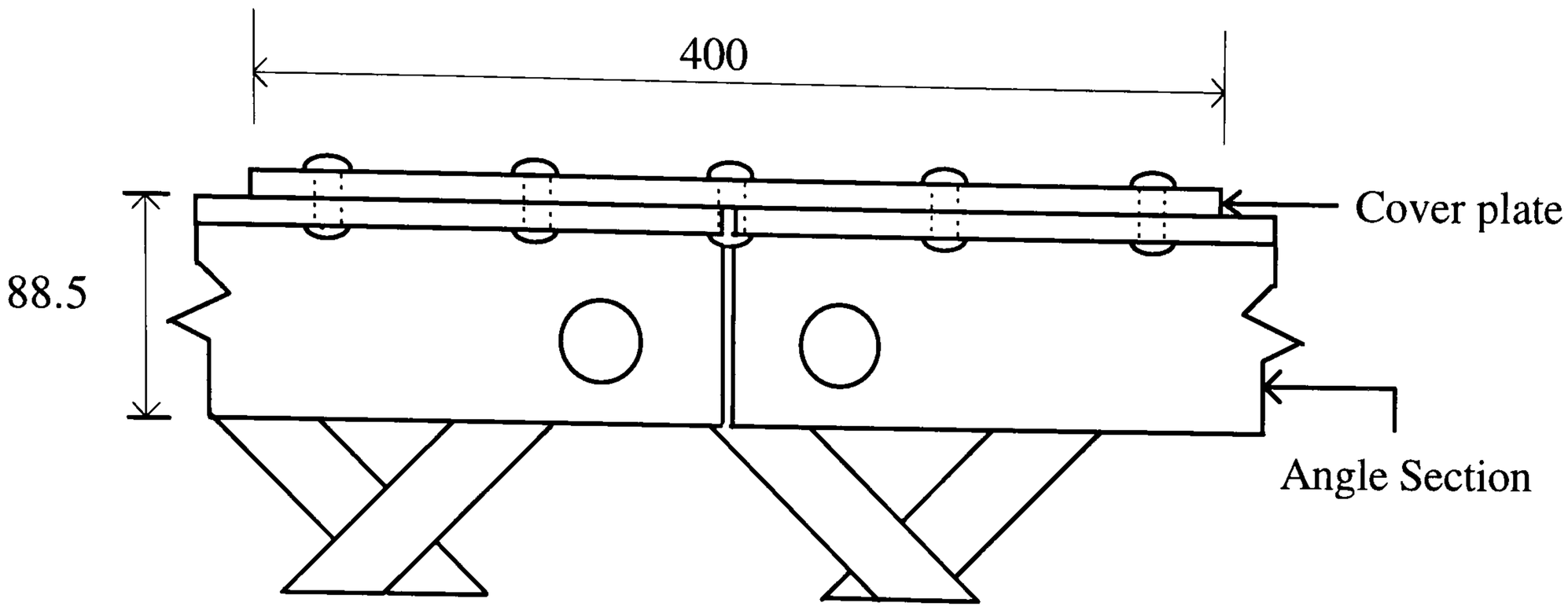

Elevation (horizontal scale 9 : 40)

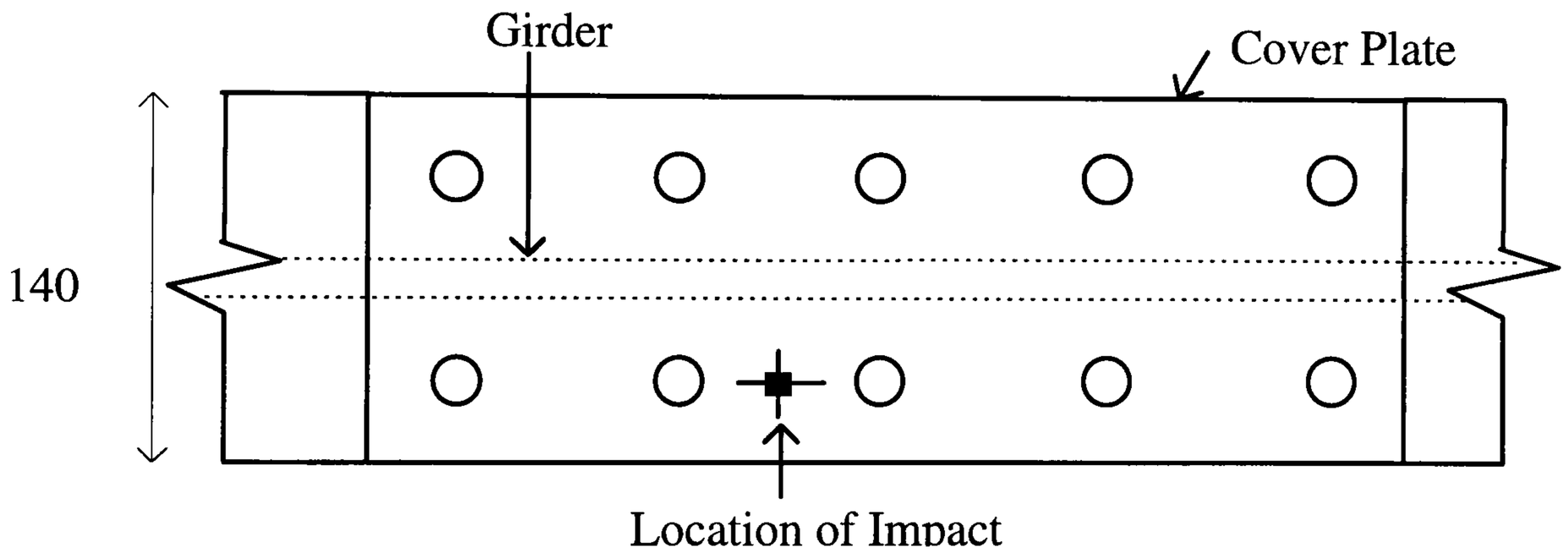

Plan

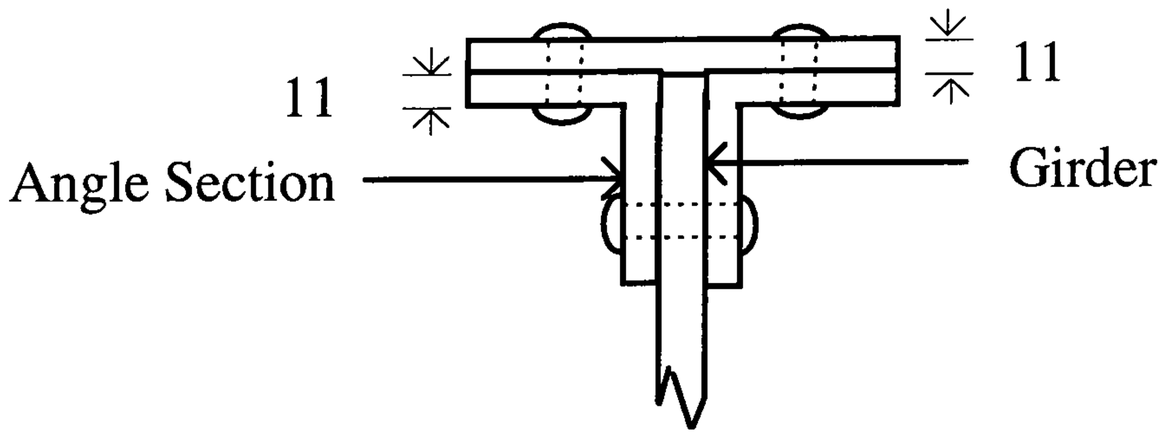

Section

Figure 6.12. Riveted Splice in Iron Lattice Girder (Scale 90 mm : 400 mm)

6.3.1. Experimental Procedure and Results

One measurement of the impact force for each of the fifty-one splices (one was temporarily inaccessible) was taken by testing as described above with the lightweight hammer (see Figure 6.13). The aluminium tip was used to maximise sensitivity. The time history and frequency spectrum were acquired with the spectrum analyser using a rectangular window and a bandwidth of 20 kHz corresponding to a sample rate of 50 kHz (20 μs between samples). The frequency interval was 12.5 Hz. Each measurement was obtained by performing a process average on the time histories and spectra acquired from three impacts on the splice. Figure 6.14 presents the force waveforms for typical impacts on two riveted splices: one appeared to be sound; and the other appeared to be badly deteriorated.

Figure 6.14 (a) and Figure 6.14 (c) both show that although there is a slight increase in the deteriorated splice's impulse duration compared with that of the sound splice; both are approximately 0.33 ms and neither exhibit the 'ringing' effect. For these reasons it would be difficult to use the time history to discriminate the deteriorated splice from the sound splice. The corresponding spectral cut-off frequencies, indicated by broken lines in Figure 6.14 (b) and Figure 6.14 (d), are also similar. However, the profiles are distinctively different between the deteriorated splice's first minimum (~4.5 kHz) and 10 kHz. The deteriorated splice's spectrum tends to increase to a maximum then fall off whereas the sound splice's spectrum just decreases to a minimum. This low amplitude, high frequency feature probably occurs because part of the deteriorated splice has worked loose causing a slight rattle and it is a possible means of discriminating deteriorated splices from sound splices.

Figure 6.15 shows a plot of the cut-off frequency versus the ratio of the area, B, between the threshold frequency (ν_t) and the maximum frequency (ν_{max}), to the total area (A+B) under the spectrum and below the maximum frequency. The threshold frequency was 2.8 kHz corresponding to 46% of the maximum frequency (6 kHz). Measurements from the bolted splices span the region of the diagram occupied by both conditions of riveted splice. The cluster of measurements from deteriorated riveted splices in the lower left region of the distribution confirms that the coin-tap test can discriminate between the two conditions of

Figure 6.13. Applying the Coin-tap Test to a Splice Plate

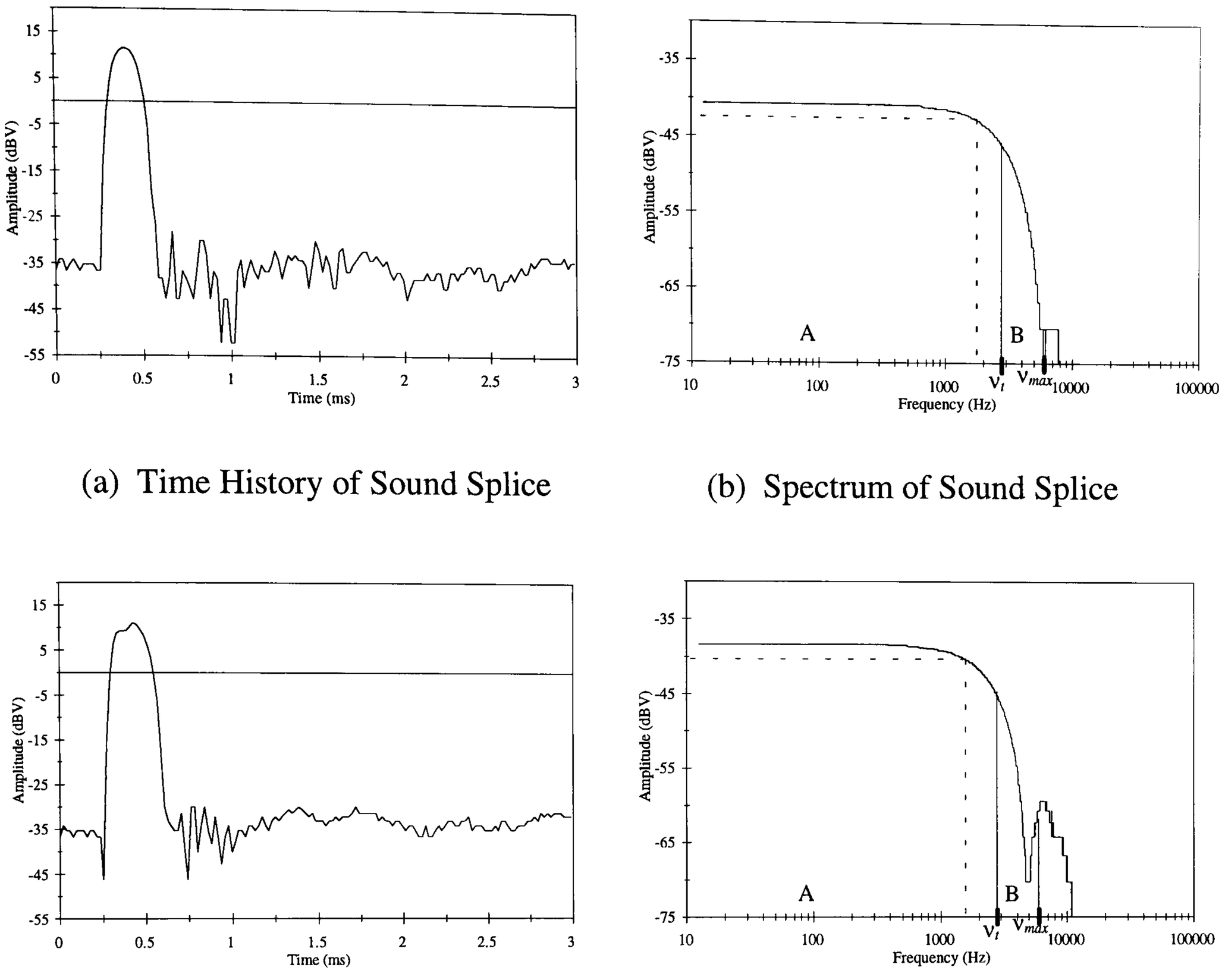

Figure 6.14. Force Waveforms for Impact on Splice Plates

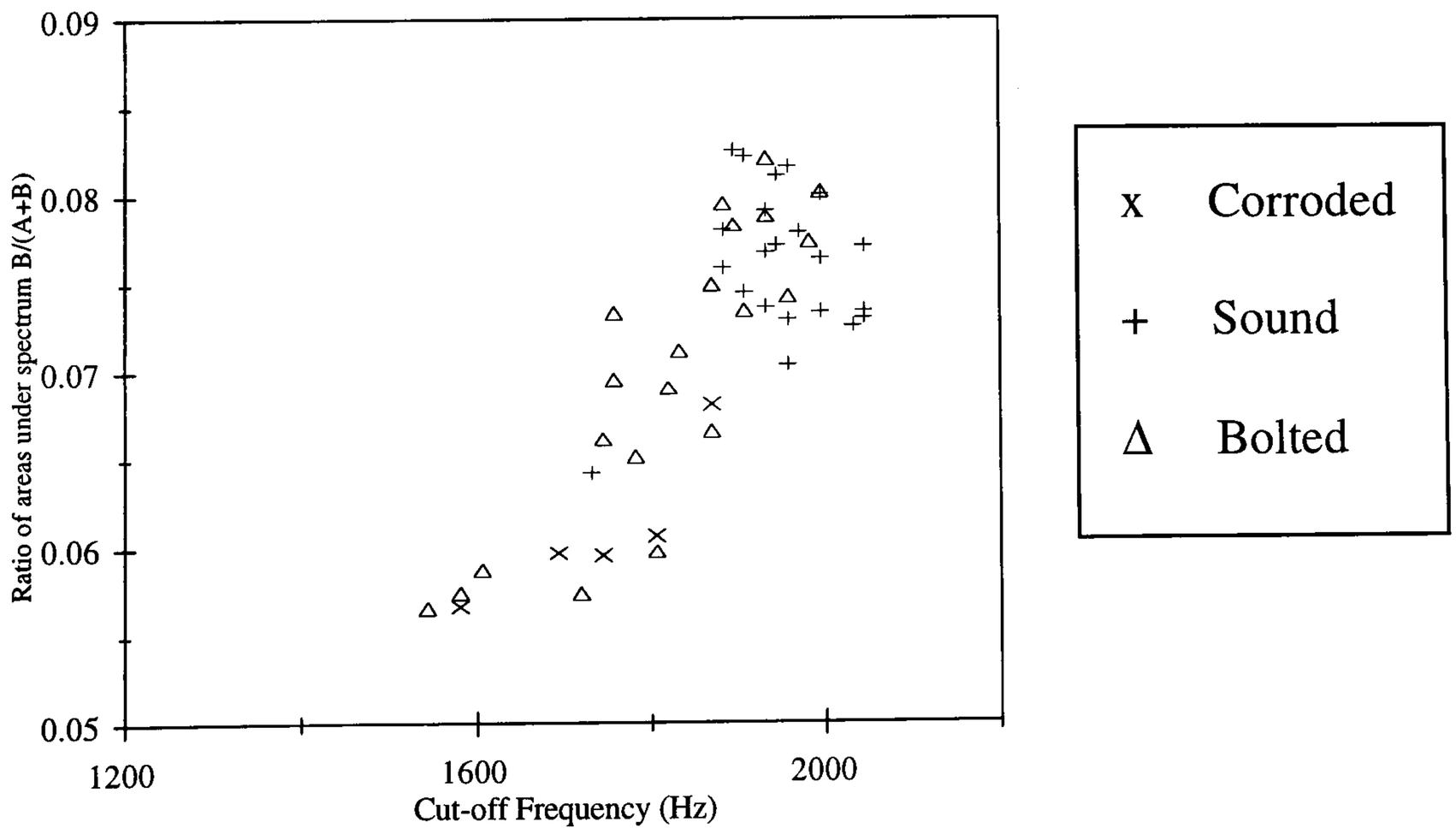

Figure 6.15. Cut-off Versus Ratio of Areas Under Spectrum for Splice Plates

riveted splice. The next section describes a method of pattern recognition employed to perform this task automatically.

6.3.2. Computer Pattern Recognition

The spectra were sampled to form feature vectors that represented the normalised spectrum over a 6 kHz frequency interval. The 48 components were obtained by sampling at 125 Hz intervals from 125 Hz to 6 kHz. The unsupervised probabilistic resource allocating network (PRAN) was trained by cyclically presenting it with the 51 feature vectors. Given the observed 'lie-of-data' when two quantities computed from the spectrum of each measurement were plotted (Figure 6.15), it was assumed that the probability distribution had about 4 generators. Therefore, the PRAN was trained to grow 4 units by repeatedly training and adjusting the parameters appropriately. By using this empirical approach the constant α_0, which determines the adaption parameter, was 0.6 and the maximum threshold was $1x10^{-5}$.

A principal component analysis, as explained in chapter 5, was then performed on the feature vectors. It was found that the first two principal components of the feature vectors were the 36th and 37th, corresponding to 4.5 kHz and 4.625 kHz. The approximate location of the principal components on the normalised spectrum is shown by the broken line on Figure 6.16 and this indicates that the magnitude of the sound splice's principal components is greater than those of the deteriorated splice. In Figure 6.17 the distribution of splice plate measurements is plotted on orthogonal axes corresponding to the two principal components. The measurements are represented by three types of symbol, one for each splice plate condition. Sometimes more than one vector with the same symbol coincide leading to an apparent discrepancy in the number of measurements. The kernels are represented by intersecting error bars, the width of which corresponds to the standard deviation of the kernel and the point of intersection corresponds to its mean. Clearly the measurements from deteriorated splices along with a few measurements from bolted splices are located in a sparsely populated part of the plane whereas measurements from sound splices are in a densely populated part. It would be possible to identify these

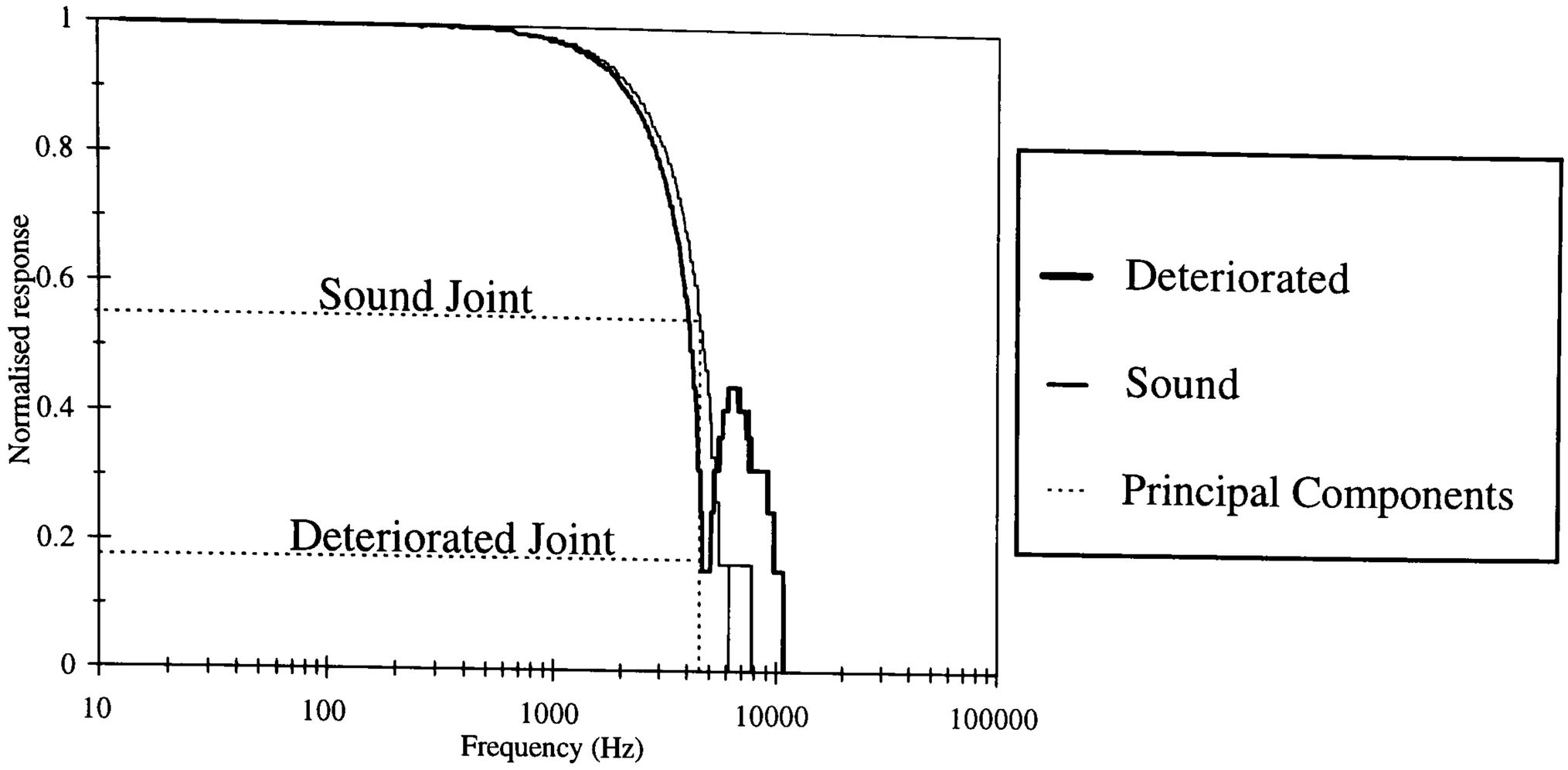

Figure 6.16. Normalised Spectra of Impact Force on Splice Plates (log scale on x-axis)

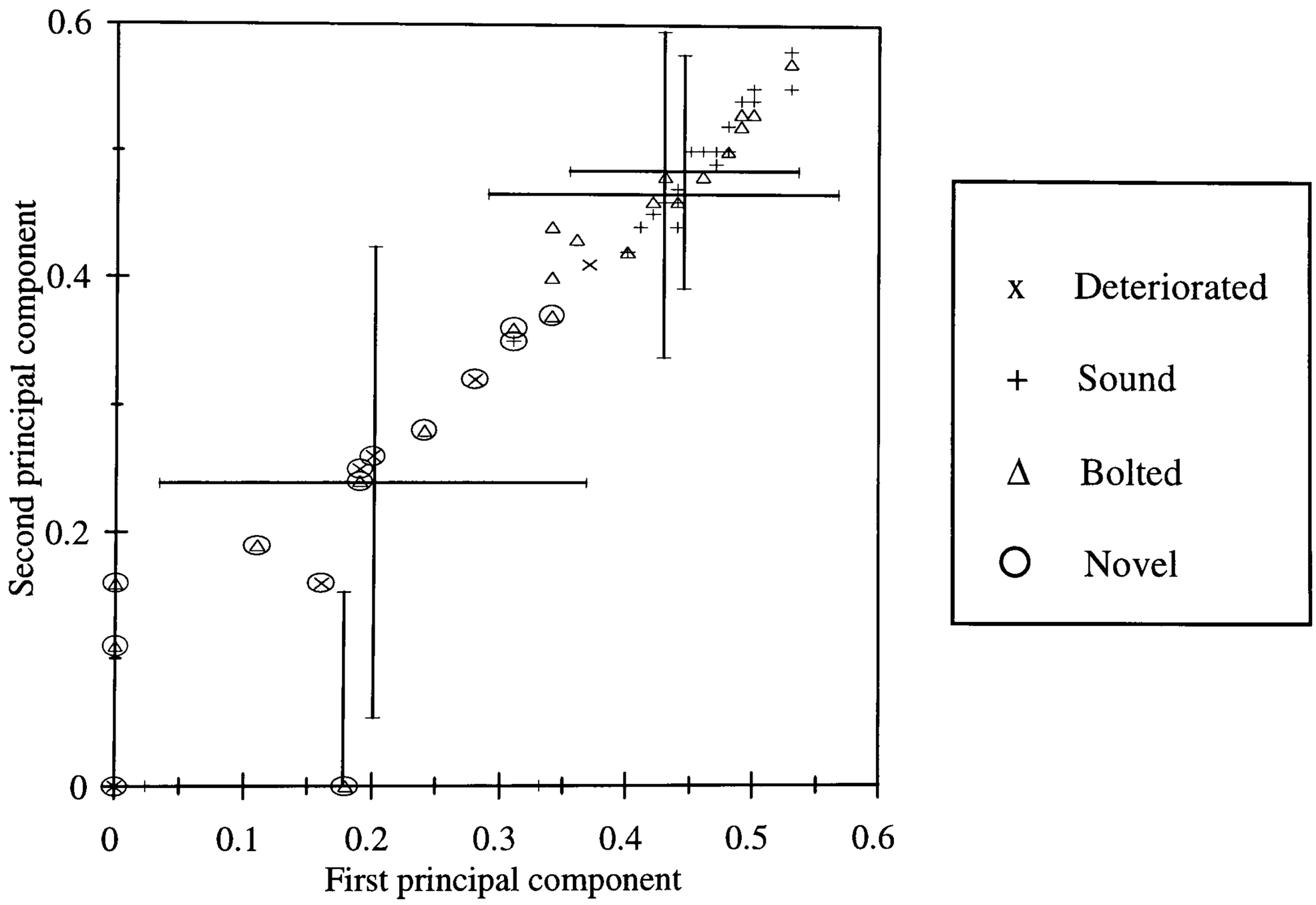

Figure 6.17. Plot of Feature Vectors of Normalised Spectra from Impact on Splice Plates after Two Dimensional Principal Component Analysis

measurements as novel by selectively pruning the two kernels that are closely associated with them.

The 51 feature vectors were presented to the PRAN again and for each kernel the posterior response was computed and added to a running total. After the two kernels with the lowest total response were pruned the feature vectors were presented again. The 14 vectors that were identified as novel are circled in Figure 6.17. Three of these vectors appear to be associated with one of the remaining kernels but they were more closely associated with another kernel that was pruned and therefore these measurements were identified as novel. This apparent anomaly occurs because the kernels are close and their error bars overlap. Eight of the novel vectors represented measurements on bolted splices suggesting that these might also be deteriorated. The other novel vectors corresponded to measurements on deteriorated riveted splices. Only one splice plate that appeared deteriorated was not identified as novel.

When only the kernel with the lowest total posterior response was pruned, two vectors were identified as novel: one represented a measurement on a riveted splice; and the other a measurement on a bolted splice. These vectors were closely associated with the kernel that lies at the lower extreme of the distribution indicating they represented measurements on splice plates with severe deterioration. This was verified by the external appearance of the riveted splice which was more badly corroded than the others and it was clear that its plates had separated allowing movement. The bolted splice did not display severe deterioration and the paint-work was largely intact. It is intended to dismantle this splice to determine whether corrosion has developed at the interface.

The measurements on all 51 splice plates were carried out again to test the repeatability of the coin-tap test in this application. Feature vectors were computed in the same manner and the two principal components were the 38th and the 39th corresponding to 4.75 kHz and 4.875 kHz. The distribution of vectors together with the 4 Gaussian kernels is plotted in Figure 6.18. The locations of vectors and kernels have changed but this is to be expected considering that the repeat measurements were carried out 3 months later. As before the

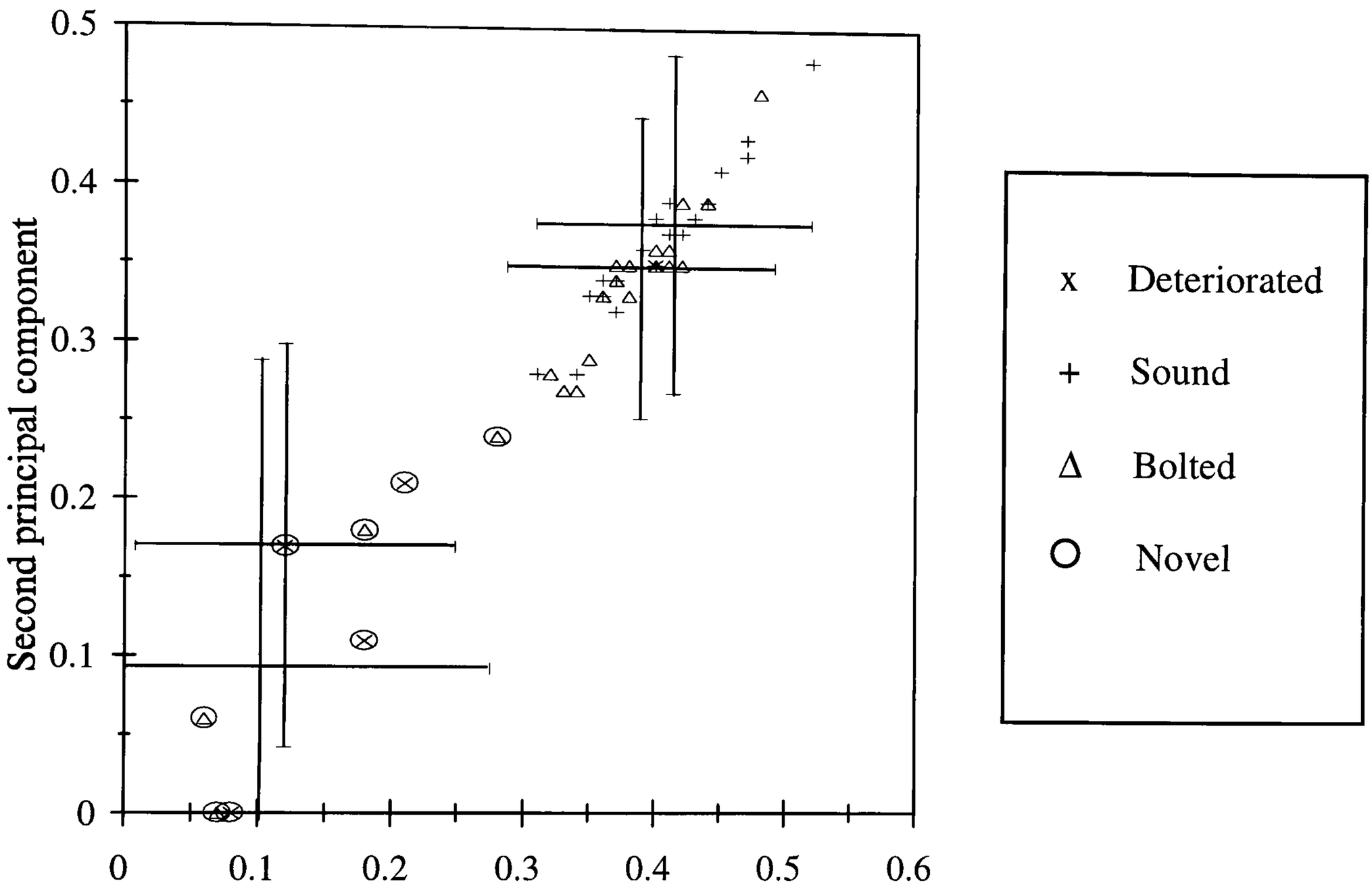

Figure 6.18. Plot of Feature Vectors of Normalised Spectra from Impact on Splice Plates after Two Dimensional Principal Component Analysis (Repeat)

upper right part of the distribution is densely populated and the lower left sparsely populated. Fewer vectors were identified as novel because some of the vectors representing bolted splices have shifted to the upper right, indicating that the bolted splice's responses are more variable with time. When only the kernel with the lowest total posterior response was pruned the two vectors representing measurements on the same bolted and riveted splices were identified as novel indicating, again, that the corresponding splice plates were severely deteriorated.

6.4. Summary

The coin-tap test has been applied to two types of joint: a bolted steelwork joint; and bolted and riveted splice plates.

The force waveforms for impact on the steelwork joint were found to exhibit features that allowed the identification of the presence of corrosion products and the loss of section. Both of these deteriorated conditions produced a reduction in local stiffness and furthermore the presence of corrosion products was found to increase local damping. In the second application it was not assumed that the visual appearance of splice plates was directly related to their actual condition. However, the coin-tap test revealed a reduction in local stiffness of deteriorated splices compared with sound splices and it was possible to distinguish between measurements on the two types of splice on this basis. Furthermore, measurements from some bolted splices that did not appear to be deteriorated were clustered with the deteriorated riveted splices, indicating the presence of concealed corrosion.

Methods of pattern recognition were employed to classify coin-tap test measurements according to the condition of the joint. In the case of the bolted steelwork joint, data from measurements on the joint in three known conditions were available. This permitted the use of two algorithms: a novelty detector (the probabilistic resource allocating network or PRAN) trained on data from the sound joint; and a supervised classifier (the back-propagation neural network) trained on data from all three joint conditions. The PRAN correctly classified new measurements as either being from a sound joint or from a

deteriorated joint, and the neural network correctly classified new measurements according the specific condition of the joint.

In the case of the splice plates the internal condition of the joint was assumed unknown and therefore it was necessary to use the unsupervised PRAN. This formed clusters of data from measurements on the riveted splices that corresponded with the visual categories. The distribution of feature vectors and kernels suggested that the data could be grouped into three categories corresponding to riveted splice plates that appear to be sound, deteriorated or badly deteriorated. The badly deteriorated group had two members, one of which was a bolted joint that did not show visible signs of serious deterioration. This implied that the bolted splice had concealed corrosion and that this could be automatically identified by the PRAN.

The chapter has shown that it is possible to detect and identify the effects of corrosion in steelwork joints by using the coin-tap test in conjunction with methods of pattern recognition.

7. OTHER APPLICATIONS

7.1. Introduction

This chapter describes the application of the coin-tap test and methods of pattern recognition to the detection of deterioration due to corrosion occurring at two further locations on structural steelwork: at the interface between chequer plate flooring and its support and within wire ropes under tension.

Chequer plate flooring is used in industrial buildings where it provides support for loads due to process equipment and personnel. At chemical works many such buildings are used for the storage or production of corrosive chemicals which, in situations of elevated humidity, result in an aggressive environment. Under these circumstances the gap between the chequer plate and the beam to which it is fixed may trap moisture leading to the development of corrosion products and compromising the strength of the flooring (Gallon, 1993). Limited access underneath the chequer plate makes visual inspection difficult, particularly when it requires the removal of ceiling coverings from the lower storey. There exists a need to detect corrosion by testing from the upper surface of the chequer plate where there is easy access.

Wire ropes used on suspension and cable stayed bridges are prone to deterioration because they are exposed to attack from environmental agents (Stafford and Watson, 1988). They are also subject to static and dynamic forces causing stress corrosion, corrosion fatigue and eventually fracture. Corrosion pits occurring on the outer surface of the rope provide water with access to the core leading to hidden corrosion. There are two principal techniques aimed at preventing contact between the steel and environmental agents; both have serious drawbacks. The first is to galvanise or paint the rope but these coatings quickly degrade under normal operational conditions. The other technique is to provide ropes with polythene sheathing but these have been found to split during service if not carefully stored during preparation. The best way to obviate failure is to detect hidden corrosion by testing on a regular basis.

The next section describes the application of the coin-tap test to the detection of corrosion occurring under chequer plate flooring in a chemical works building. This is followed by a description of the application of the coin-tap test to detect various simulated conditions of corrosion deterioration in a wire rope under tension mounted in the laboratory. Two instruments were available for data acquisition: the first was a Diagnostic Instruments, PL202 spectrum analyser (Diagnostic Instruments, 1991); and the other was a Gould model OS4020 Digital Storage Oscilloscope (Gould, 1981).

7.2. Chequer Plate Flooring

The region of flooring tested was directly above one of a series of small I-sections that supported the third floor of a packing shed for the production and storage of sodium nitrate (Nitram) as shown in Figure 7.1. The small I-section that was chosen for testing is shown in Figure 7.2. The flooring comprised 8 mm thick chequer plates fixed at regular intervals along their long edges to the flanges of two small I-sections by five steel bolts with countersunk heads, as indicated in Figure 7.3 (a). The short edges of the chequer plate were supported by two large I-sections that were perpendicular to the small I-sections. Visual inspection of this beam from the lower floor showed that, at the mid-span region, corrosion products were packed at its interface with the chequer plate, whereas the regions towards its ends were relatively free from corrosion. These regions were categorised as 'corroded' and 'sound' respectively. There were also intermediate regions where the condition was ambiguous because corrosion products were not clearly visible from the lower floor although they might have been present. These regions were categorised as 'suspect'.

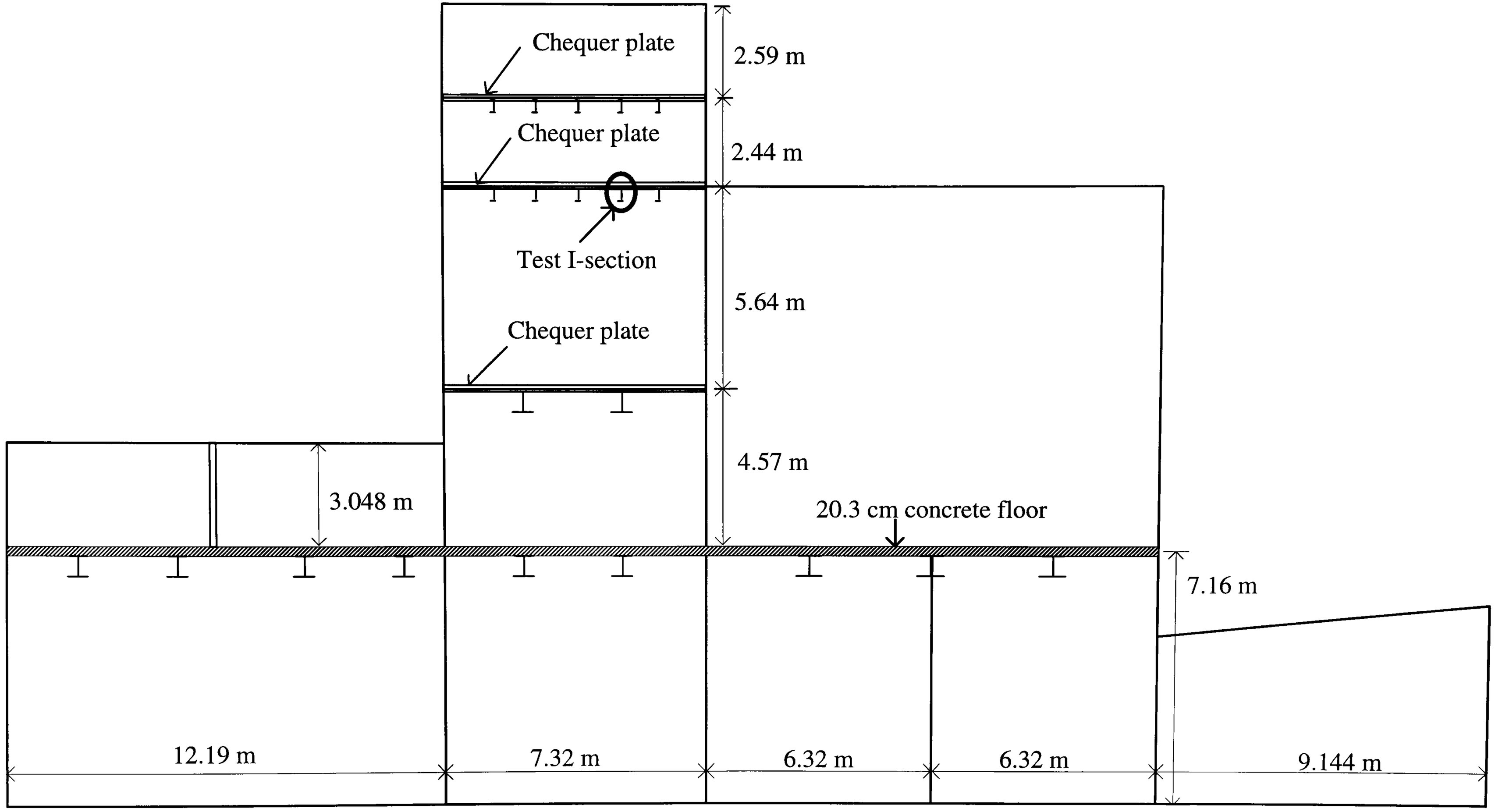

Figure 7.1. East-Side Section Through Nitram Packing Shed (dimensions in cm)

Figure 7.2. I-section to which Coin-tap Test was Applied

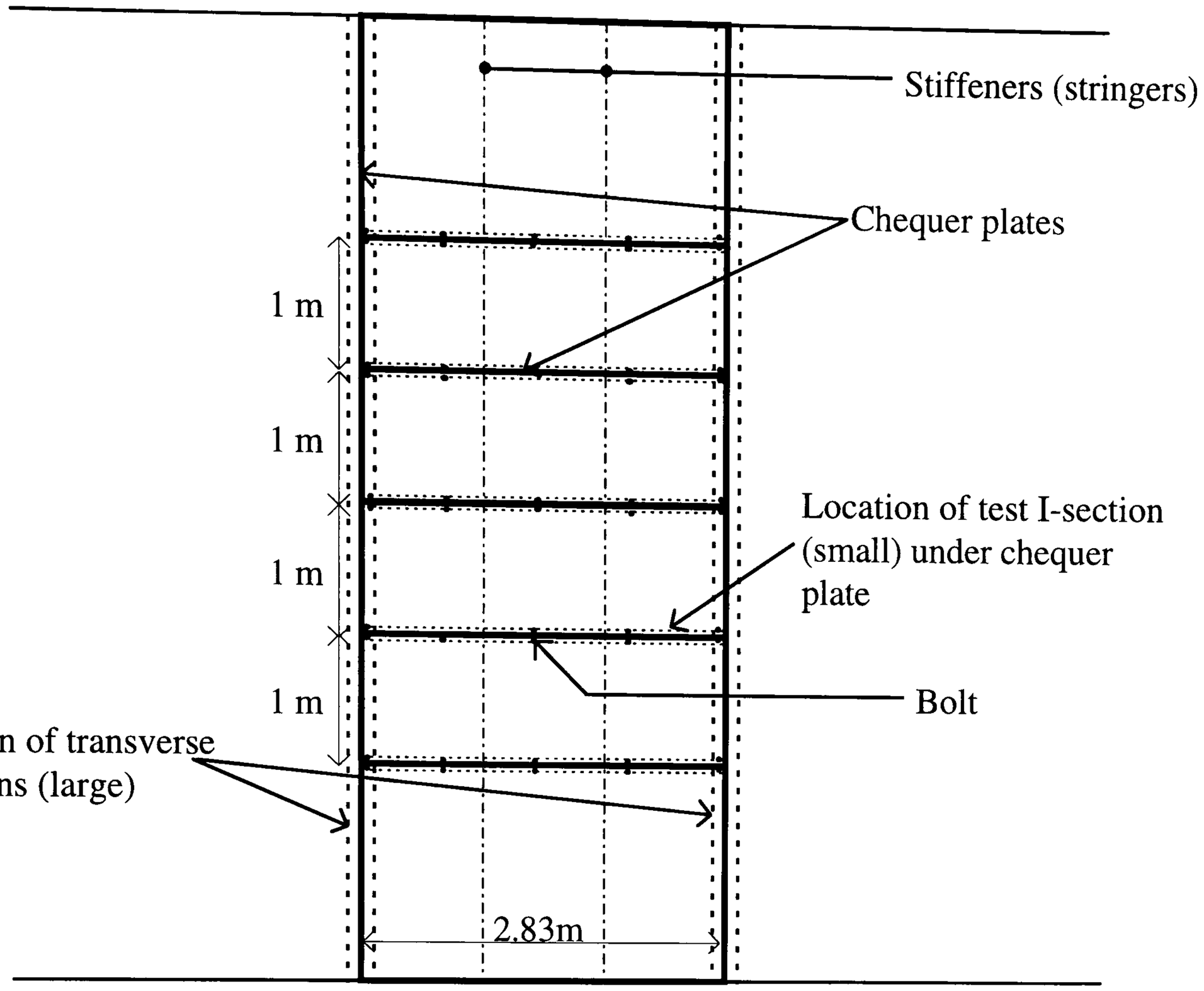

(a) Plan of Third Floor (scale 1m : 1.5 cm)

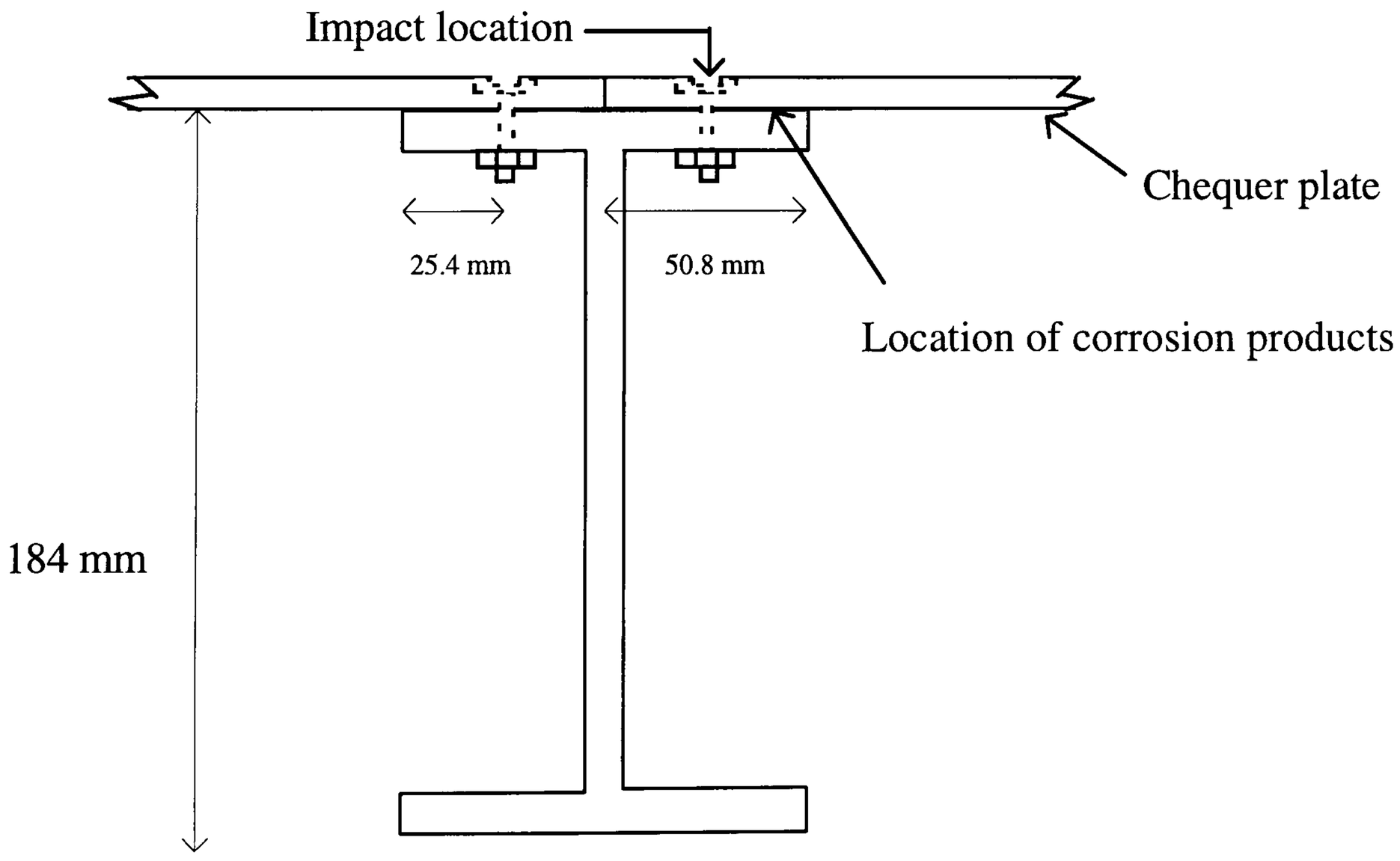

(b) Section Through Third Floor at Point of Testing

Figure 7.3. Detail of Third Floor of Nitram Packing Shed

7.2.1. Experimental Procedure

One measurement of the impact force was taken at each of forty equally spaced positions along the longer edge of the chequer plate that was supported by the test I-section. Measurements were taken directly above the flange along the line of the fixing bolts. Therefore five of the measurements corresponded to impacts on bolt heads as indicated in Figure 7.3 (b). The heavy duty hammer fitted with the aluminium tip was used (see Figure 7.4). The time histories and frequency spectra were acquired with the spectrum analyser using a rectangular window and a bandwidth of 10 kHz and a frequency interval of 6.25 Hz. The sample rate was 25 kHz (40 μs between samples). Each measurement was obtained by performing a process average on the time histories and frequency spectra acquired from three impacts at a particular position on the chequer plate. Figure 7.5 presents the force waveforms for typical impacts over regions known to be sound and corroded.

Figure 7.5 (a) and Figure 7.5 (c) both show that the presence of corrosion products under the point of impact has the effect of damping the structural vibrations of the chequer plate. This is clear because the time history of the sound region exhibits low frequency 'ringing'. This effect is also apparent by comparing the spectra shown in Figure 7.5 (b) and Figure 7.5 (d). Unlike the spectrum of the corroded region, the spectrum of the sound region exhibits peaks corresponding to modes of vibration. The apparent impulse duration of the sound region is greater than for the corroded region because of undamped structural vibrations feeding back into the hammer's force transducer. These are damped out rapidly by the corroded region resulting in a simple, clean force-time history as shown in Figure 7.5 (c). In the spectra the cut-off frequency of the sound region is approximately 138 Hz which is lower than for the corroded region at approximately 481 Hz, as indicated by the broken lines in Figure 7.5 (b) and Figure 7.5 (d). This is due to the relative increase in structural vibration of the sound region compared with corroded region. These differences in the spectra are a possible means of discriminating corroded regions from sound regions.

Figure 7.4. Applying the Coin-tap Test to Chequer Plate Flooring

Figure 7.6 shows a plot of the cut-off frequency versus the ratio of the area, B, between the threshold frequency (ν_t) and the maximum frequency (ν_{max}), to the total area (A+B) under the spectrum and below the maximum frequency. The threshold frequency was 1.2 kHz corresponding to 40% of the maximum frequency (3 kHz). Measurements over the suspect regions were grouped with those corresponding to corroded regions in the upper right of the distribution, suggesting that the suspect regions were actually corroded. Measurements on the bolts were also grouped with measurements on corroded regions suggesting that the force waveforms were similar and therefore structural vibrations of the chequer plate were also suppressed by the bolts. Measurements from the sound regions tend to be clustered in the lower left of the distribution whereas those from the corroded regions are clustered in the upper right of the distribution. This confirms that the coin tap test can discriminate impacts over corroded regions of the I-section from impacts over sound regions. The next section describes a method of pattern recognition employed to perform this task automatically.

7.2.2. Computer Pattern Recognition

The spectra were sampled to form feature vectors that represented the normalised spectrum over a 3 kHz frequency interval. The 48 components were obtained by sampling at 50 Hz intervals between 0 Hz and 250 Hz (eight components) and at 68.75 Hz intervals between 250 Hz and 3 kHz (40 components). This was done purely for convenience. The unsupervised probabilistic resource allocating network (PRAN) was trained by cyclically presenting it with the forty feature vectors obtained from measurements at each position on the I-section. Given the observed 'lie-of the data' when two quantities computed from the spectrum of each measurement were plotted (Figure 7.6), it was assumed that the probability distribution had two generators. Therefore, the PRAN was trained to grow two units by repeatedly training and adjusting the parameters appropriately. By using this empirical approach the constant α_0, which determines the adaption parameter, was 0.7 and the maximum threshold was 1×10^{-17}.

A principal component analysis, as explained in section 5, was then performed on the feature vectors. It was found that the first two principal components of the feature vectors

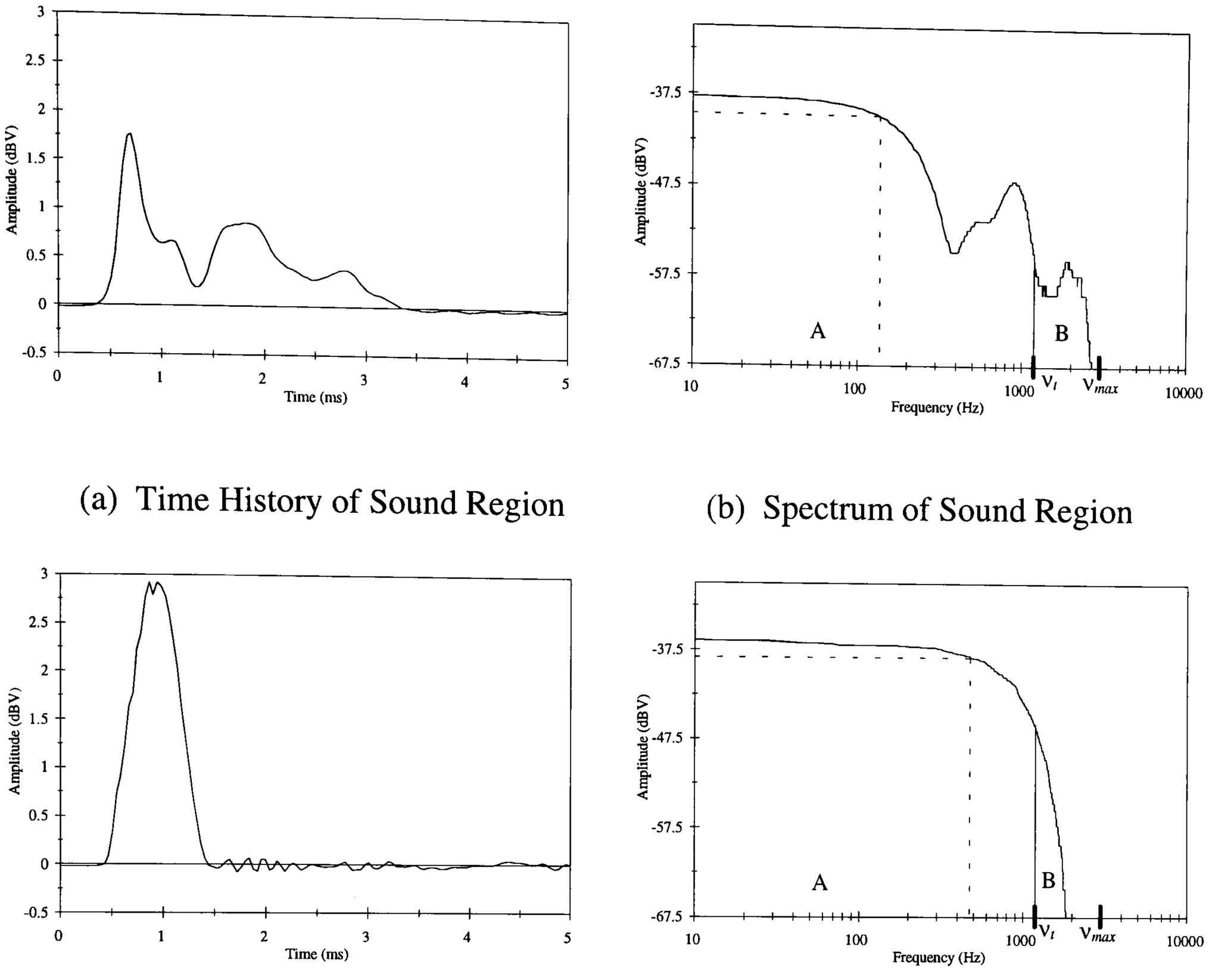

Figure 7.5. Force Waveforms for Impact on Chequer Plate Above Test I-section

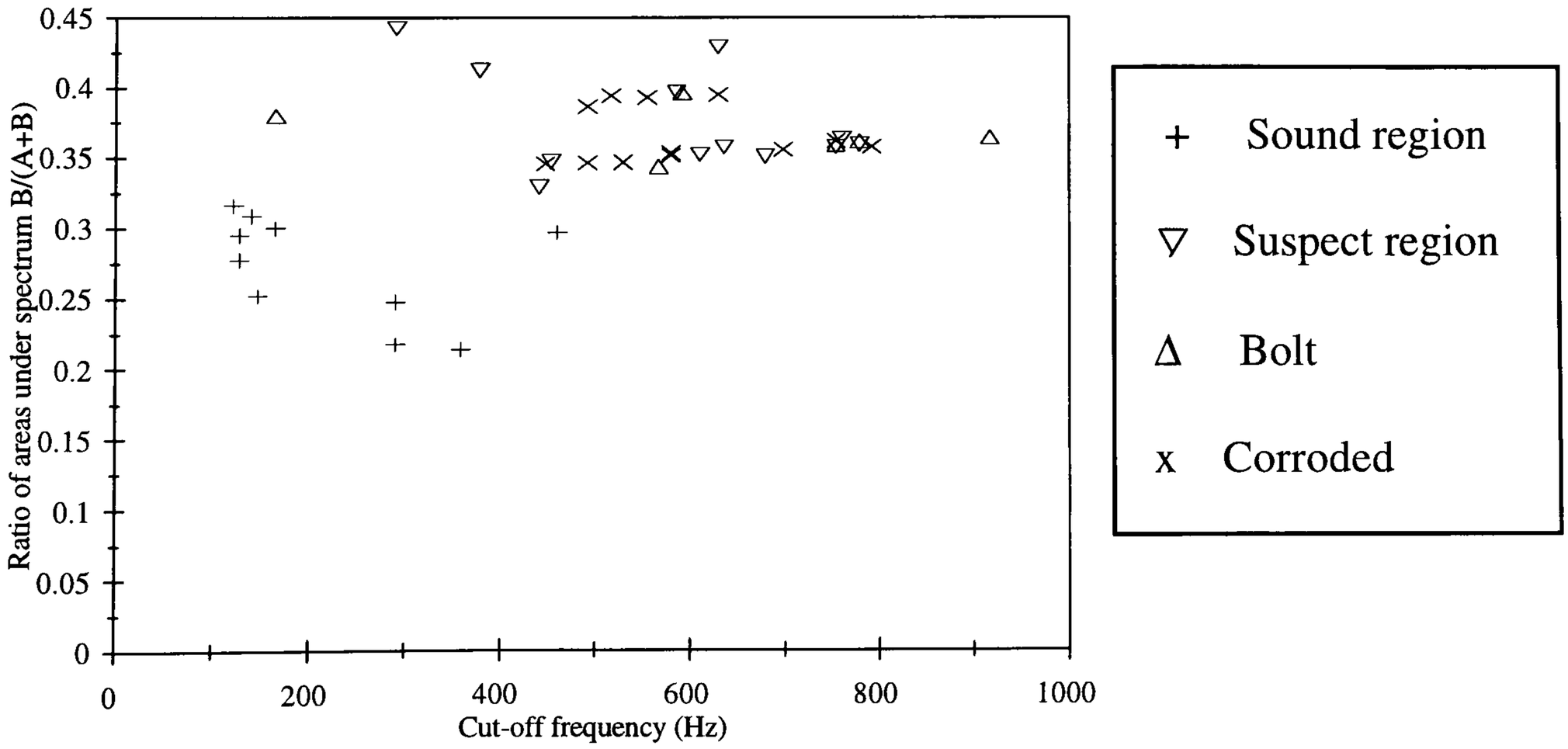

Figure 7.6. Cut-off Frequency Versus Ratio of Areas under Spectrum for I-section

were the 16th and 17th, corresponding to 950 Hz and 1018.75 Hz. The locations of the principal components on the normalised spectrum are indicated by the broken lines on Figure 7.7 and these show that the approximate magnitudes of the sound region's principal components are less than those of the corroded region. In Figure 7.8 the distribution of measurements on the chequer plate is plotted on orthogonal axes corresponding to the two principal components. The measurements are represented by four types of symbol, one for each category assigned to the condition of the interface between the I-section and the chequer plate. Sometimes more than one vector with the same symbol coincide, leading to an apparent discrepancy in the number of measurements. The kernels are represented by intersecting error bars, the width of which corresponds to the standard deviation of the kernel and the point of intersection corresponds to its mean. The measurements from the corroded regions are in a densely populated part of the plane whereas measurements from sound regions are in a sparsely populated part. It would be possible to identify these measurements as novel by pruning the kernel that is closely associated with them.

The 40 feature vectors were presented to the PRAN again and for each, the posterior response was computed and added to the running total. After the kernel with the lowest total response was pruned the feature vectors were presented again. The 11 vectors identified as novel are circled in Figure 7.8, all were from measurements on the sound region. Two of the vectors appeared to be more closely associated with the kernel that was not pruned. However, it must be remembered that the plot in Figure 7.8 is a projection of the feature vectors onto a two dimensional plane. The PRAN used all forty-eight components of the feature vectors to classify and it is likely that there were other components that identified these vectors as belonging to the kernel that was pruned. Measurements on the bolts and measurements on suspect regions were clustered with measurements on corroded regions. This confirms the observation made earlier that the suspect regions were actually corroded, and that the response of the bolts was similar to that of the corroded regions because both exhibited damping of the vibrations of the chequer plate.

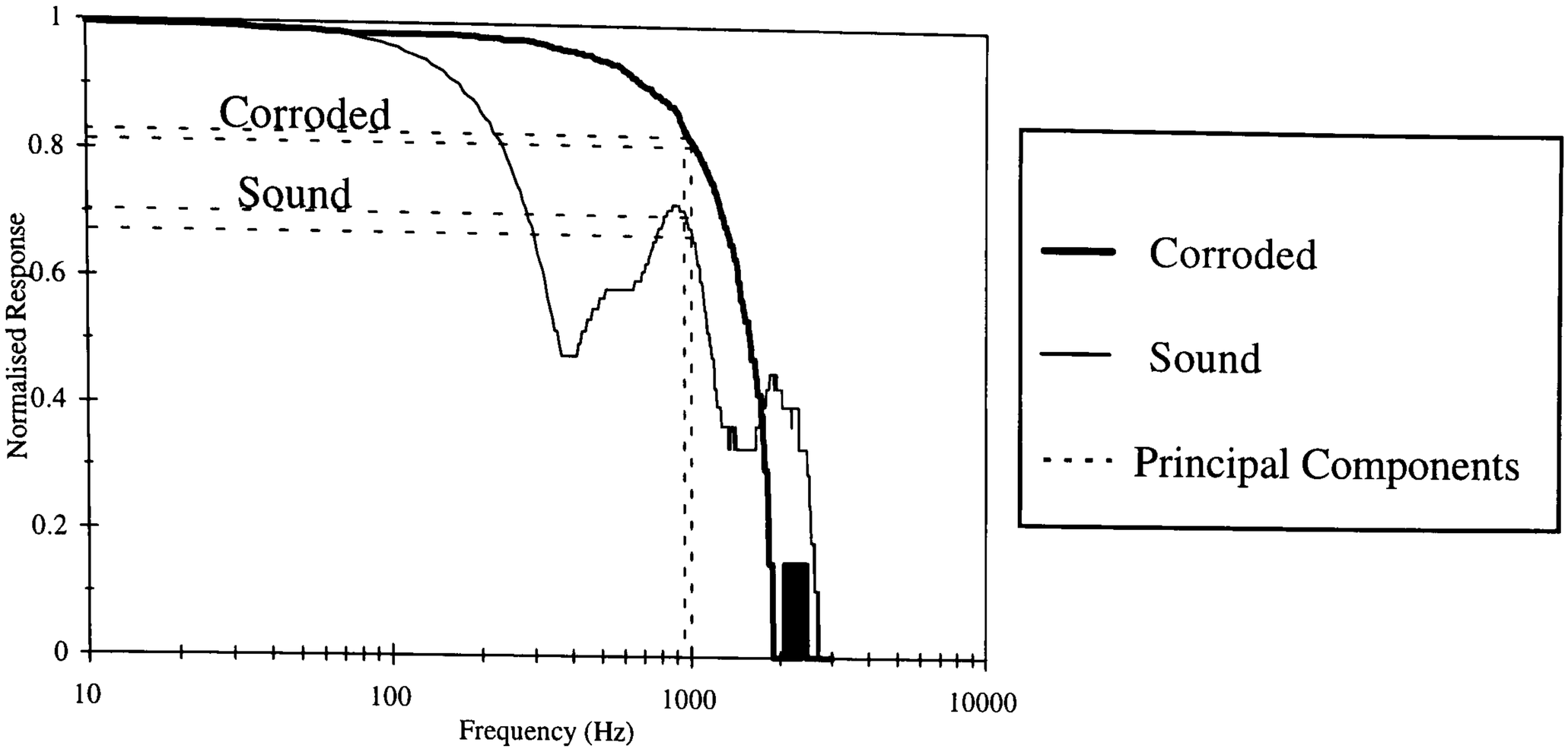

Figure 7.7. Normalised Spectra of Impact Force on Chequer Plate (log x-axis)

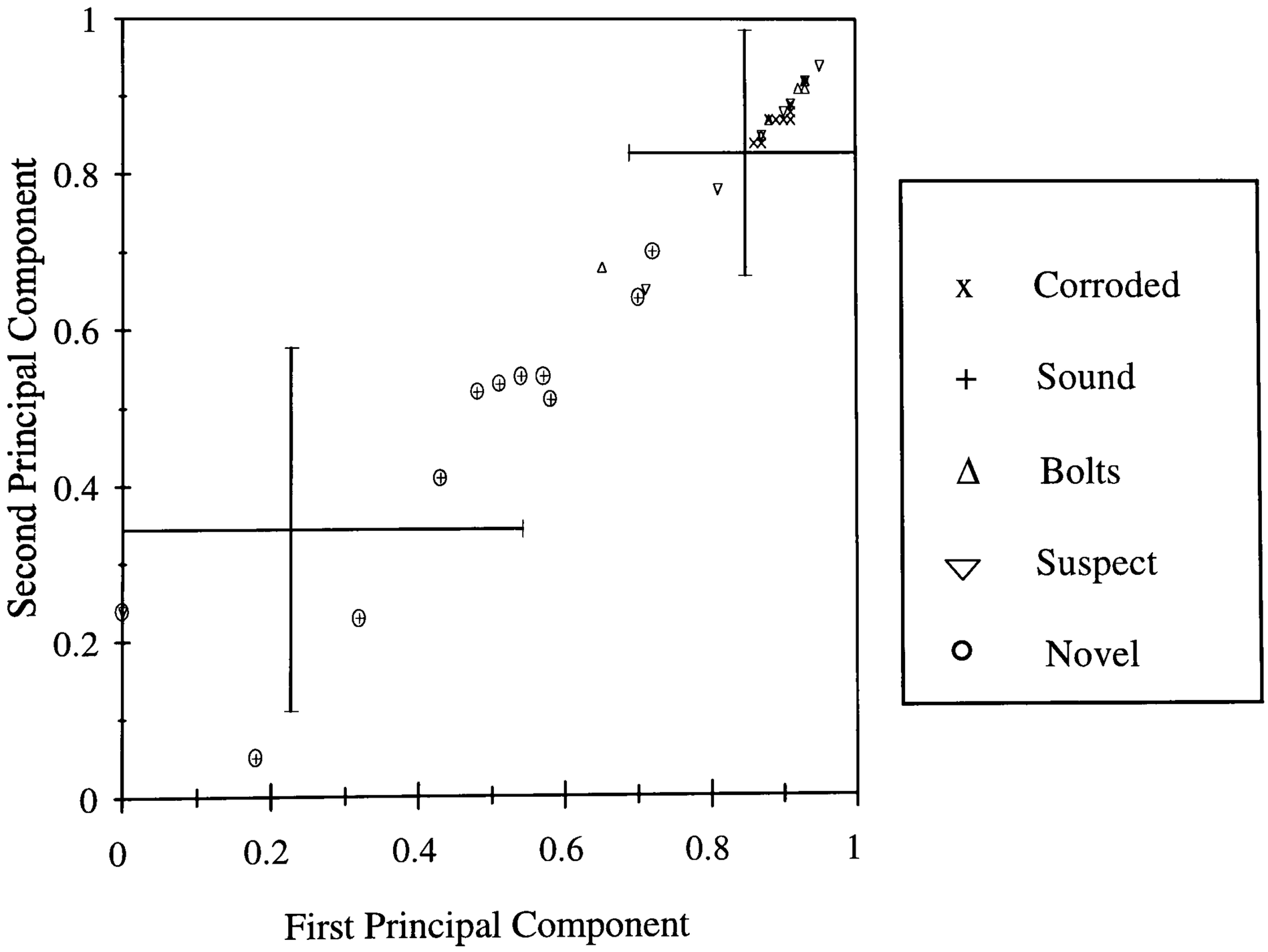

Figure 7.8. Plot of Feature Vectors of Normalised Spectra from Impacts on Chequer Plate after Two-dimensional Principal Component Analysis

7.3. Wire Rope Under Tension

The structure of a simple wire rope specimen is shown in Figure 7.9. It consisted of seven helical wires made of high tensile steel surrounded by a polythene sheath. The tensile properties of one of these wires are given below in Table 7.1.

Tensile Property	**Estimated Value**
Failure load	42 kN
Area of wire	
-before fracture	25.9 mm^2
-after fracture	24.4 mm^2
Stress at failure	1621.6 N/mm^2
Strain at failure	0.262 %
Yield stress	1177.6 N/mm^2
Young's modulus	211.9 kN/mm^2

Table 7.1. Tensile Properties of a Single Wire

A length of wire rope was installed in a Losenhausen UHS 60 fatigue testing machine (Losenhausen, 1971) and put under tension. The layout of the apparatus is given in Figure 7.10.

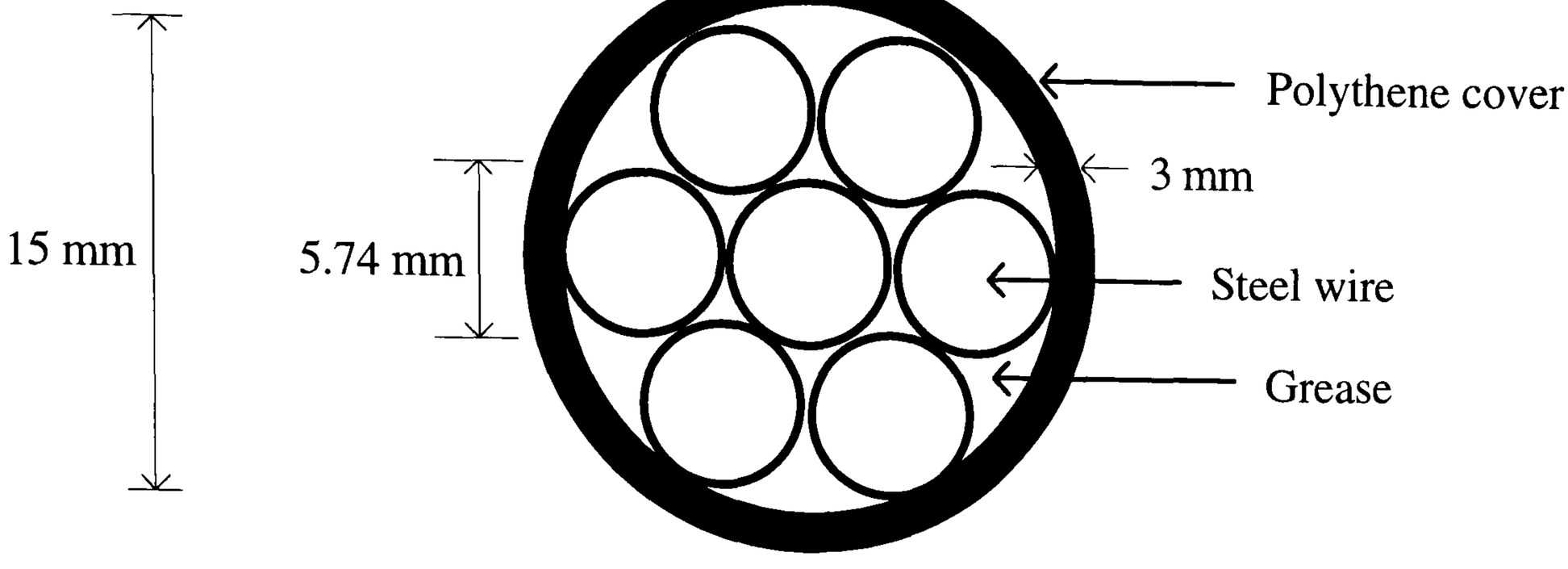

Figure 7.9. Cross-section of the Wire Rope

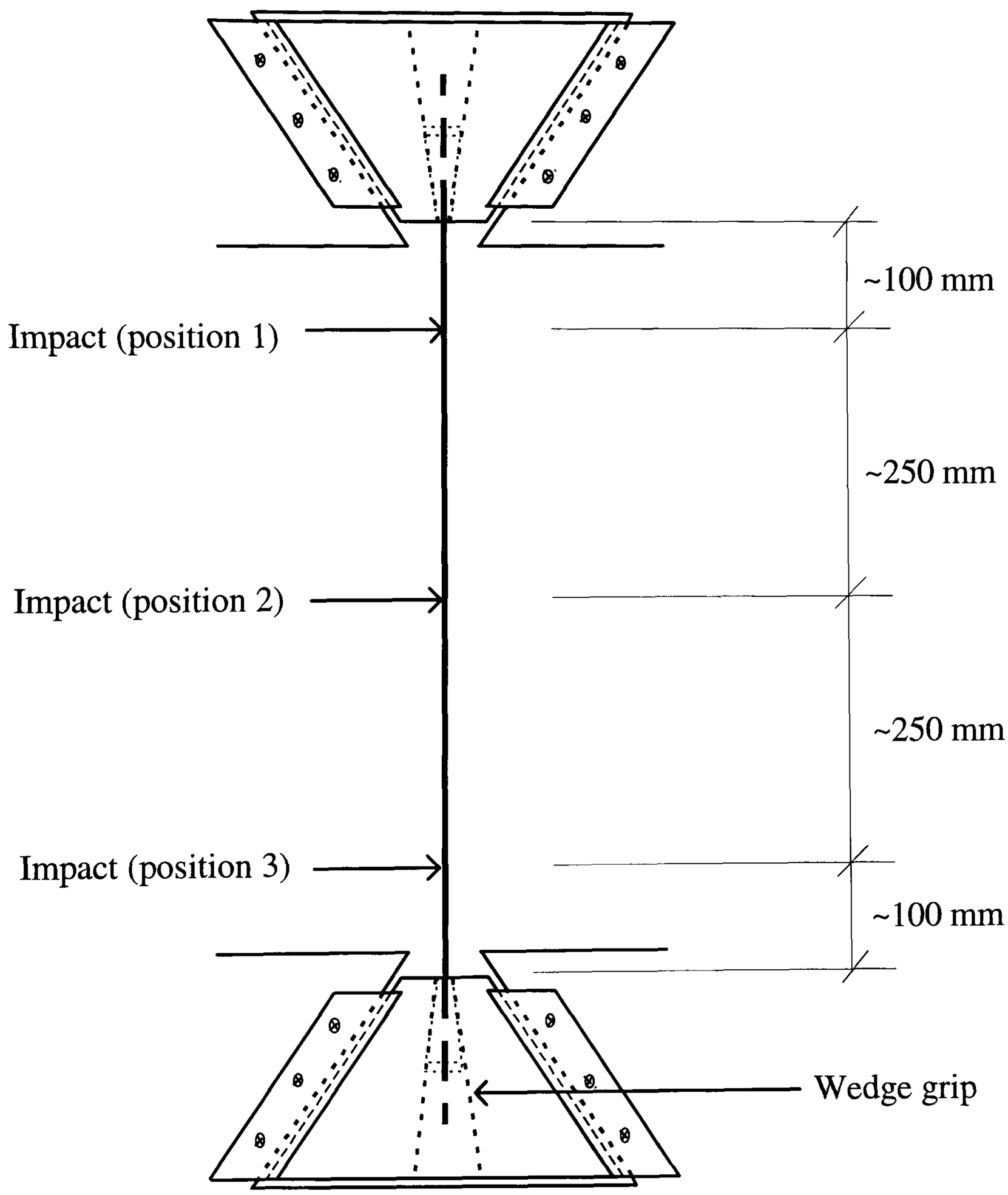

Figure 7.10. Wire Rope under Tension for Coin-tap Test (Not to Scale)

7.3.1. Experimental Procedure

The first three experiments were to determine the effect of changes in the experimental condition of the wire rope, other than damage to the rope itself, that might influence the force-time history and thereby reduce the sensitivity of damage detection.

The first two tests investigated the effect of the polythene cover:

Experiment 1 - The specimen was fixed at both ends with the cover removed.

Experiment 2 - The specimen was fixed at both ends with the cover intact. The experiment was carried out over a range of tension from 0 kN to 120 kN.

The third test investigated the effect of changing the support conditions:

Experiment 3 - The strand with cover intact was fixed at both ends. In addition a clamp (Figure 7.11) was installed at the middle section. The purpose of the clamp was to standardise the supporting conditions at different positions on the strand, as shown in Figure 7.12. When the unclamped rope is impacted centrally, as indicated in Figure 7.12 (a), the local displacement profile is markedly different from that obtained when it is impacted near a support, as shown in Figure 7.12 (b), because of the large difference in the amount of lateral restraint at the two positions. However, when the clamp is installed centrally, the amount of lateral restraint is similar to that obtained when it is installed near the support and the deflection profiles obtained at both positions would be similar to that indicated in Figure 7.12 (c).

The fourth experiment was to determine the effect that minor damage might have on the force-time history of the impact test:

Experiment 4 - An artificial defect was made to the specimen in the middle section by sawing one of the wires to a depth of approximately 1 mm. It was tested with the clamp in place and with the cover intact.

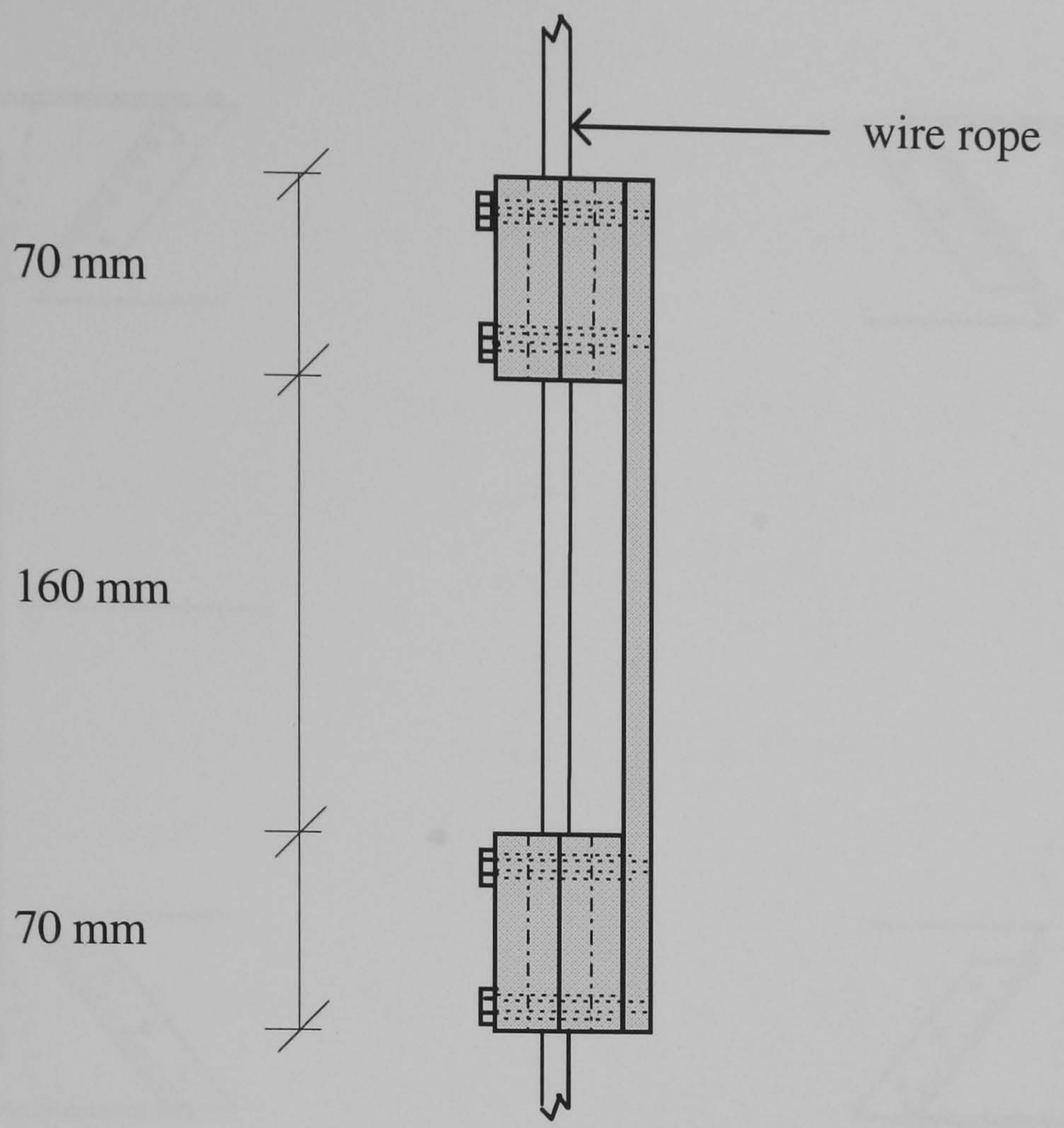

Side-View (Scale 1 : 4)

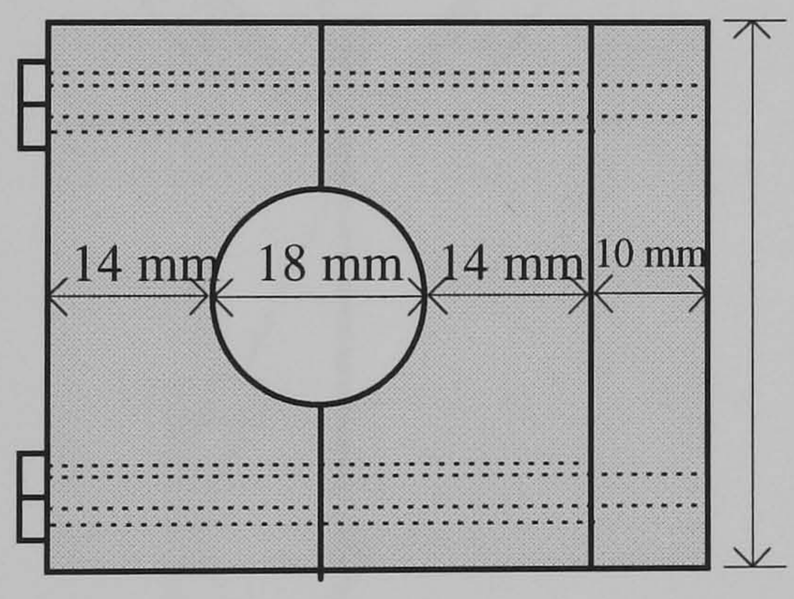

End View (Scale 1 : 1.25)

Figure 7.11. Supporting Clamp for Wire Rope

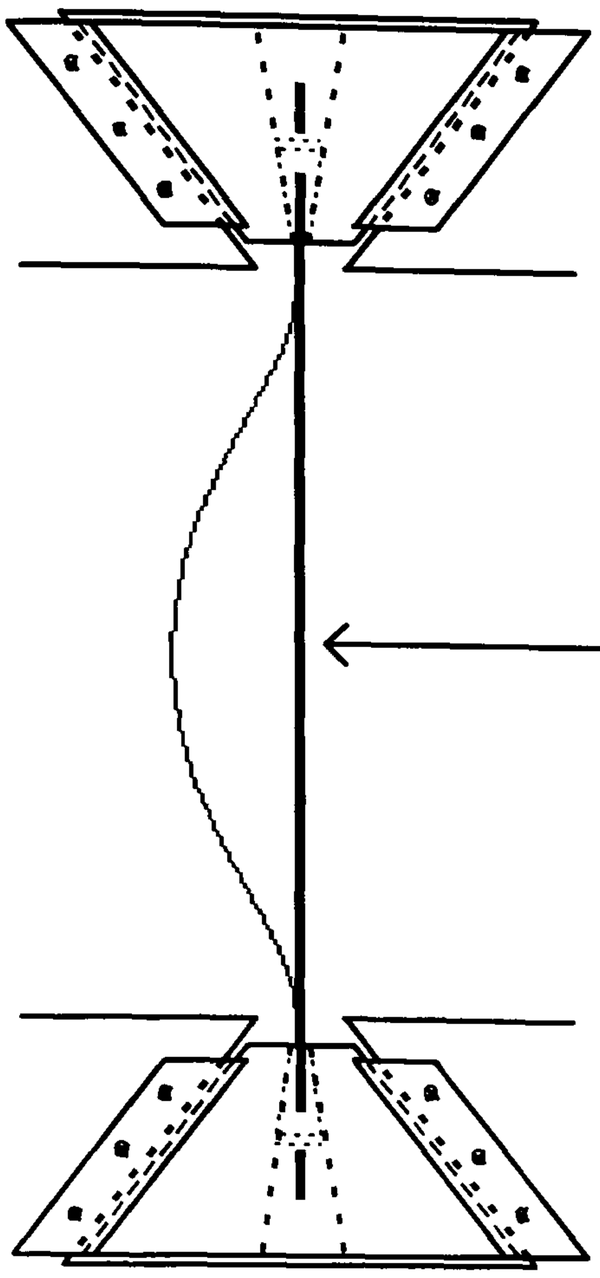

(a) Central Impact (no clamp)

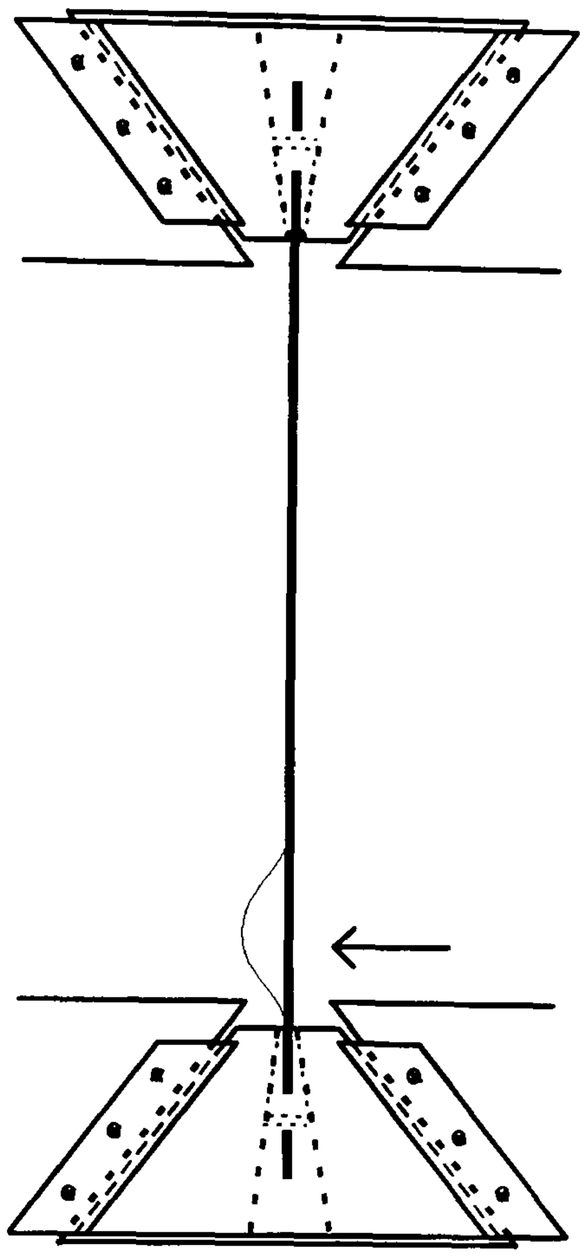

(b) Off-centre Impact (no clamp)

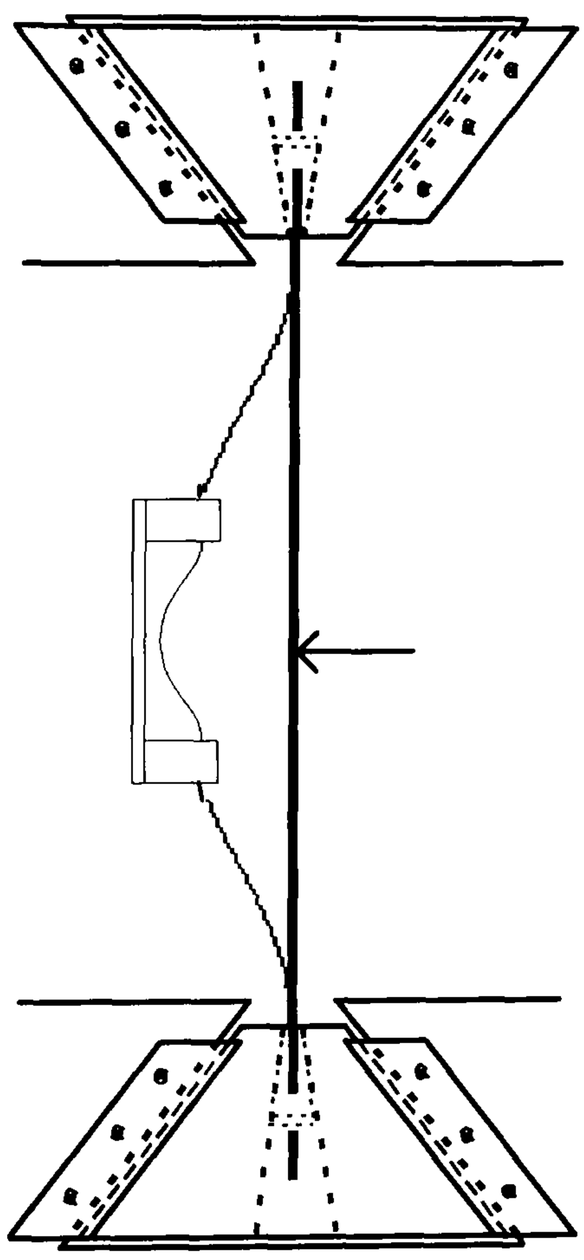

(c) Central Impact (clamp installed)

Figure 7.12. Effect of Clamp on Deflection Profile of Wire Rope

In each experiment the rope was subjected to a four-stage test in which it was impacted with the lightweight hammer fitted with the long extender and aluminium tip. The force-time history was acquired with the oscilloscope and recorded on an x-y plotter.

The first two stages were to determine whether changes in applied tension and position of impact had a significant effect on the force-time history, thus reducing the damage sensitivity.

(a) Impacts were made to the specimen (see Figure 7.13) at the positions shown in Figure 7.10 starting at 40 kN tension.

(b) This was repeated at every 40 kN increment of tension until 200 kN (except experiment 2 which was limited to 120 kN).

The last two stages were to determine the effect that substantial damage to the rope might have on the force-time history:

(c) One of the wires was cut and then the specimen was loaded until the wire ruptured. This normally occurred at a load greater than 200 kN.

(d) The load was reduced to 200 kN and impacts were made at the same positions as before.

7.3.2. Theoretical Model of Transverse Stiffness of Rope under Impact

The effects on the measured local stiffness of different tensions, different positions of impact and different rope conditions were compared with a theoretical model that predicted the local stiffness of a wire rope subjected to a transverse point load. The model assumes a static point load and therefore it does not take account of the effects of any structural vibrations that may be excited by the hammer on impact. It also assumes a uniform cross-sectional area. Furthermore, it does not include the finite contact stiffness between the tip of the hammer and the rope.

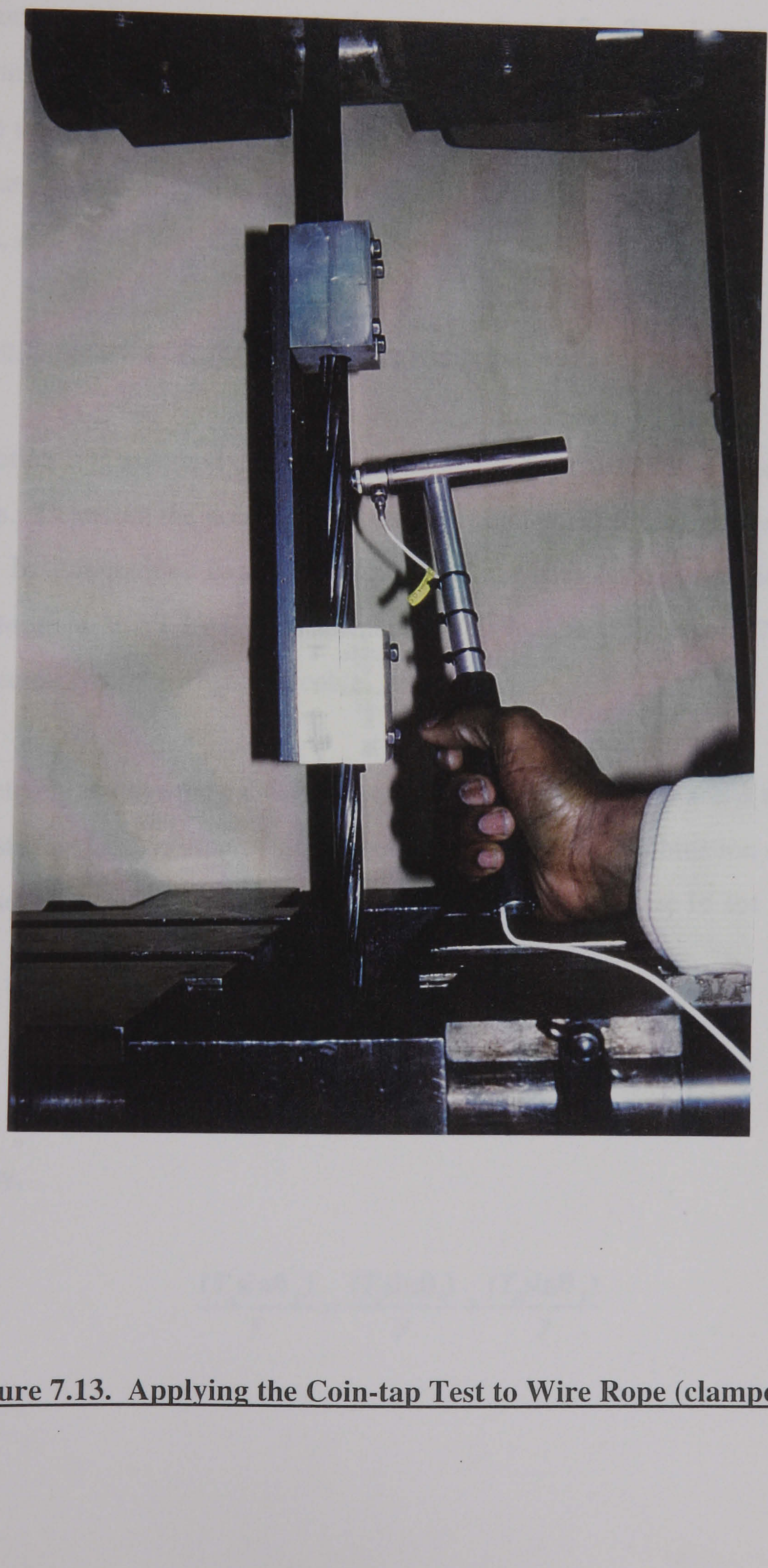

Figure 7.13. Applying the Coin-tap Test to Wire Rope (clamped)

7.3.2.1. Variations in Local Stiffness With Position Along a Mounted Wire Rope

This discussion concerns the variation with location of the local stiffness, k, measured by a small point load applied to a tensile wire rope in a direction perpendicular to its length. It is assumed that the displacement caused by the load is small compared with the rope's length. The rope is mounted between two pinned supports, A and B. The discussion is therefore equally valid in these cases. Figure 7.14 (a) shows the mounted wire rope. The bold line represents the undistorted rope which has an initial horizontal tension. The initial length of the rope is L and the point load is applied at L_1. Its Young's modulus is E and it has cross-sectional area, A.

(a) Wire Rope Supporting Negligible Bending Moment

In this sub-section it is assumed that the rope can be treated as a cable because it has a small shear modulus. Therefore the point load produces a negligible bending moment in it and the rope deforms by longitudinal extension that is uniform over its cross-section. The point load, $\boldsymbol{P}$, produces a small local displacement, y, as indicated in Figure 7.14 (b) which clarifies the geometry of the displaced cable.

The load effectively divides the cable into two sections with lengths a and b and tensions T_a and T_b. The stiffness, k_1, of one of these sections is the linear combination of the stiffness due to longitudinal extension of the cable, $k_{1,e}$, and the stiffness due to the initial tension, $k_{1,T}$.

$$k_1 = k_{1,e} + k_{1,T} \tag{7.1}$$

This is given by,

$$\frac{(T_a \sin\theta_1)}{y} = \frac{(T_e \sin\theta_1)}{y} + \frac{(T_0 \sin\theta_1)}{y} \tag{7.2}$$

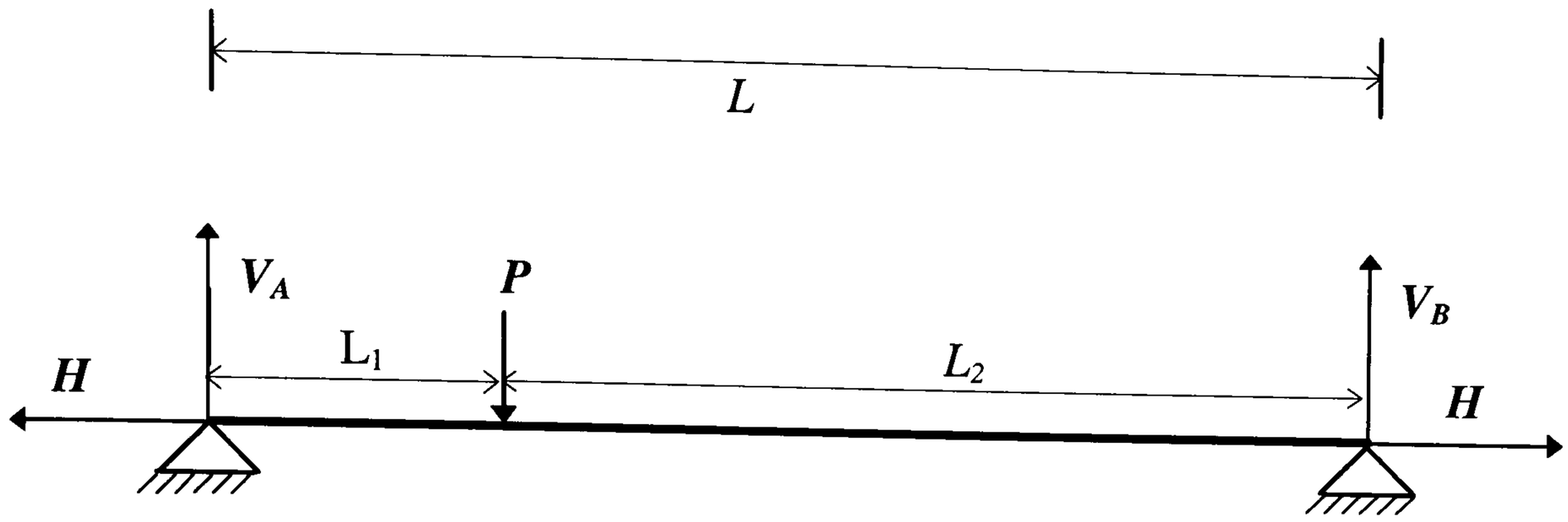

(a) Geometry Before Application of the Point Load

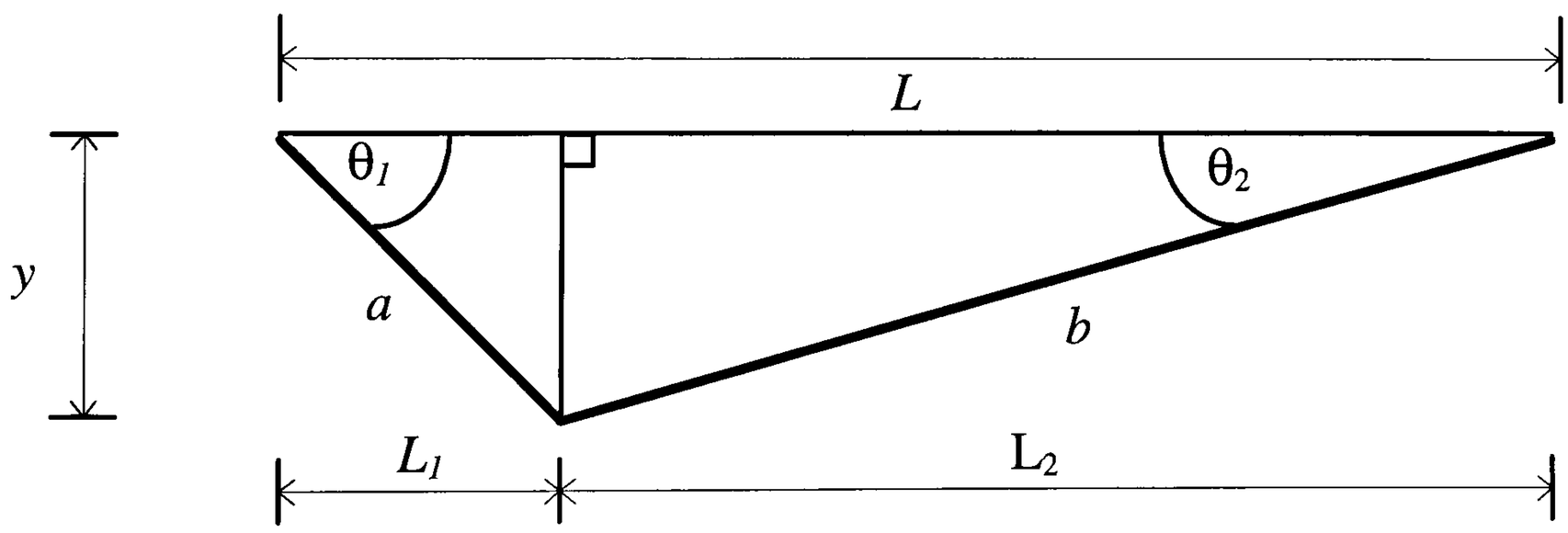

(b) Displaced Geometry

Figure 7.14. Cable Subjected to Transverse Static Point Load

where T_e is the increase in tension due to the extension of section a, and T_0 is the tension before the point load was applied (in this case equal to $\boldsymbol{H}$). The first term on the right hand side (RHS) of equation 7.2 represents $k_{1,e}$ and it can be written as follows:

$$\frac{(T_e \sin\theta_1)}{y} = \frac{T_e}{y} \times \frac{y}{a}$$

Therefore

$$\frac{(T_e \sin\theta_1)}{y} = \frac{T_e}{a} \tag{7.3}$$

T_e is derived from Hooke's law:

$$T_e = EA \times \frac{(a - L_1)}{L_1} \tag{7.4}$$

Therefore

$$k_{1,e} = EA \times \frac{(a - L_1)}{aL_1}$$

Therefore

$$k_{1,e} = EA \times \frac{(a - L_1)}{L_1^2} \tag{7.5}$$

Where the substitution $a \sim L_1$ was made in the denominator of equation 7.5 because the displacement y is small. The extended length of rope, a, can be written as,

$$a = \left(L_1^2 + y^2\right)^{1/2} \tag{7.6}$$

The RHS of equation 7.6 can be expanded as the first two terms of a Taylor series. This yields

$$a \cong L_1 + \frac{1}{2}\frac{y^2}{L_1} \tag{7.7}$$

This can be substituted into equation 7.5 to give

$$k_{1,e} = \frac{EA}{L_1^2}\left(L_1 + \frac{1}{2}\frac{y^2}{L_1} - L_1\right) \tag{7.8}$$

Therefore

$$k_{1,e} = \frac{EAy^2}{2L_1^3} \tag{7.9}$$

The load acts on both sections of cable simultaneously so the local stiffness in the load direction due to longitudinal extension of the cable, k_e, is obtained by the linear addition of the contribution of each section.

$$k_e = k_{1,e} + k_{2,e} \tag{7.10}$$

Therefore

$$k_e = \frac{EAy^2}{2}\left[\frac{1}{L_1^3} + \frac{1}{(L - L_1)^3}\right] \tag{7.11}$$

The second term on the RHS of equation 7.2 represents $k_{1,T}$ and it is derived from the relation,

$$T_0 \text{ Sin } \theta_1 = \frac{yT_0}{a} \tag{7.12}$$

The length, a, is approximately L_1 because the displacement, y, is small hence,

$$k_{1,T} = \frac{(T_0 \sin\theta_1)}{y} = \frac{T_0}{L_1} \tag{7.13}$$

The load acts on both sections of cable simultaneously so the local stiffness in the load direction due to the initial tension in the cable, k_T, is obtained by the linear addition of the contribution of each section.

$$k_T = k_{1,T} + k_{2,T} \tag{7.14}$$

Therefore

$$k_T = \frac{T_0}{L_1} + \frac{T_0}{(L - L_1)}$$

Therefore
$$k_T = \frac{LT_0}{L_1(L-L_1)} = T_0\left(\frac{L}{L_1(L-L_1)}\right) \tag{7.15}$$

(b) Wire Rope Supporting Significant Bending Moment

In this sub-section it is assumed that the rope can be treated as a bar because it has a large shear modulus. Therefore the point load produces a substantial bending moment in it and the rope deforms by bending forming a curved profile.

The displacement, y, produced by a point load, P, acting at a distance of L_1 from one of the supports of a fixed supported bar with length L is given by (Owens and Knowles, 1992).

$$y = \frac{PL_1^3(L-L_1)^3}{3EIL^3} \tag{7.16}$$

Where I is the bar's second moment of area. Therefore the local stiffness due to bending, k_b, is given by,

$$k_b = \frac{P}{y} = \frac{3EIL^3}{L_1^3(L-L_1)^3}$$

Therefore
$$k_b = 3EI\left(\frac{L}{L_1(L-L_1)}\right)^3 \tag{7.17}$$

(c) General Case

In this sub-section no assumptions are made concerning the behaviour of the rope when subjected to a transverse load. Therefore, the local stiffness, k, in the wire rope can be modelled by a combination of the stiffness due to longitudinal extension, k_e (equation 7.11), the stiffness due to tension, k_T (equation 7.15) and the stiffness due to bending, k_b (equation 7.17).

$$k = k_e + k_T + k_b \tag{7.18}$$

An approximation of the contribution of each stiffness component can be found by substituting the appropriate values for the rope into equation 7.11, equation 7.15 and equation 7.17. For impact at $L_1 = L/2$ with a tension of 100 kN, and assuming a displacement of 14 mm for y, this gives a value of 441 N/m for k_e, 5.7 x 10^5 N/m for k_T and 3.1 x 10^5 N/m for k_b. Clearly, the stiffness due to longitudinal extension is significantly less than the stiffness due to bending or the stiffness due to tension.

Therefore
$$k \cong k_b + k_T \tag{7.19}$$

$$= \frac{3EIL^3}{L_1^3(L-L_1)^3} + \frac{LT_0}{L_1(L-L_1)}$$

Therefore
$$k = \frac{3EIL^3 + L_1^2(L-L_1)^2 LT_0}{L_1^3(L-L_1)^3} \tag{7.20}$$

where E, I, L and T_0 are the Young's modulus, the second moment of area, the rope's original length and the applied tension, respectively. This is approximate because k_T assumes the displacement profile of a cable but, considering that the displacement at the load is small, the error should be insignificant.

The load is applied at a distance L_1 from one of the supports. The local stiffness at the mid-point of the rope can be obtained by substituting $L_1 = L/2$ and rearranging equation 7.20 to yield.

$$k = \frac{3EI + \frac{L^2}{16}T_0}{\left(\frac{L}{2}\right)^3} \tag{7.21}$$

Using the values of cross-sectional area and Young's modulus quoted in Table 7.1, and assuming a rope with a circular cross-section that is seven times the area of one wire, the

first term in the numerator, which represents the influence of bending on local stiffness, has a magnitude of 1.666 x 10^3 Nm^2. The rope's length was 0.7 m so the magnitude of the $L^2/16$ factor was 3.0625 x 10^{-2} Nm^2. This means that the second term in the numerator, which represents the influence of applied tension on local stiffness, is of the same order of magnitude as the first term when the applied tension is of the order of 100 kN. Consequently, the measured local stiffness would be expected to vary significantly over the 40 kN to 200 kN range used in these experiments.

The model makes two assumptions that could reduce the accuracy of its predictions in this application. The first is that the model assumes a rope with uniform cross-section whereas the experimental rope was made up of seven wires. Although its cross-sectional area is the same, the experimental rope has a smaller shear modulus and its local stiffness will be less. The second assumption is that the contact stiffness between the hammer and the model rope is infinite whereas in practice it is finite. This would also tend to increase the local stiffness of the theoretical rope relative to the experimental rope. Therefore, the impulse durations predicted by the model are expected to be shorter than those measured experimentally. However, the model should predict the relationship between the variables correctly and it is these trends that are of most interest in the present discussion.

7.3.3. Test Results

Factors that affect the force-time history, other than damage to the rope, may affect the sensitivity of the coin-tap test. The effects of differences in the applied tension, position of impact, support conditions and the presence of the cover were considered.

Figure 7.15 shows that the shape of the force-time history was not affected by change in the applied tension. Figure 7.15 (a) shows that the force-time history during impacts at $L/7$ from the support (position 1) on the uncovered rope (experiment 1) exhibits four cycles of ringing vibration over the duration of the impulse for tensions in the 80 kN to 200 kN range. Similarly, Figure 7.15 (b) shows that the impulses from impacts at the mid-point (position 2) of the covered rope (experiment 3) approximate to a half-sine shape for tensions in the 120 kN to 200 kN range.

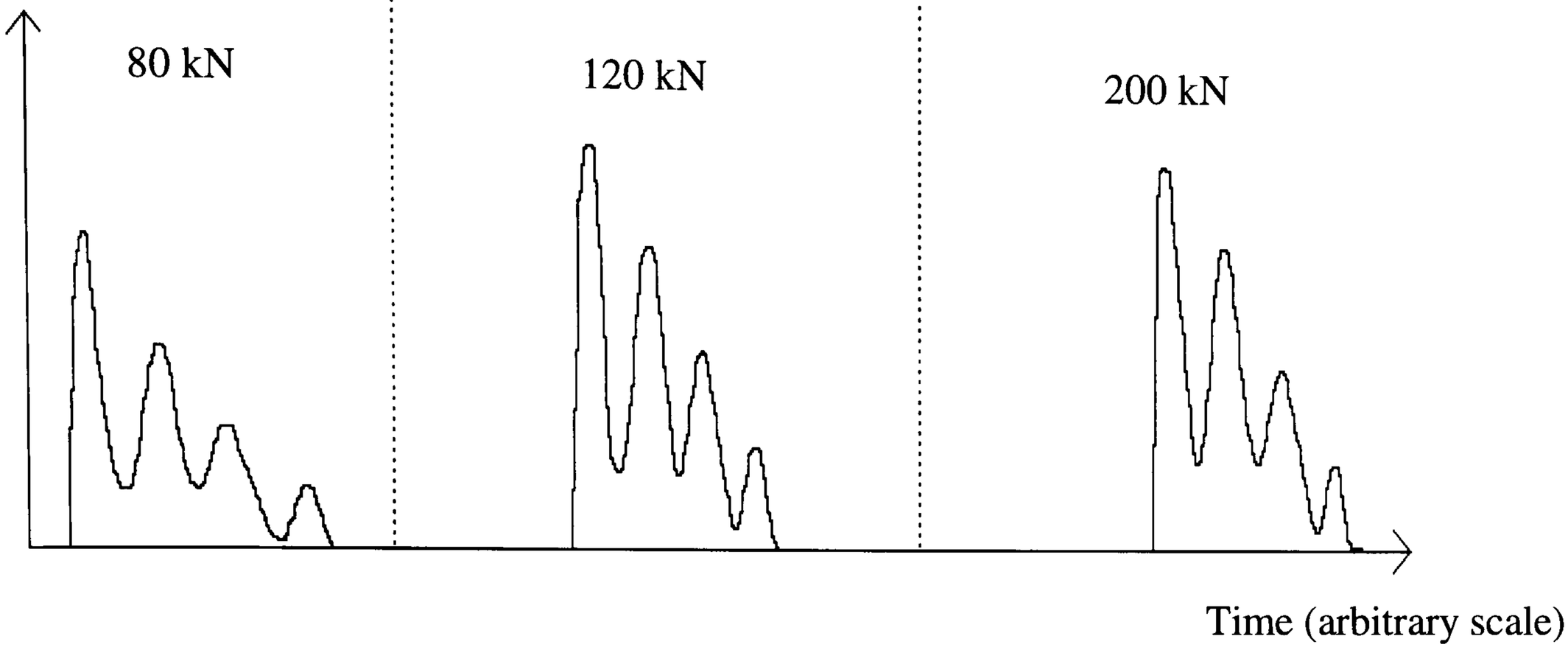

(a) Impact at *L*/7 From Support (Position 1) of Uncovered Rope (Experiment 1)

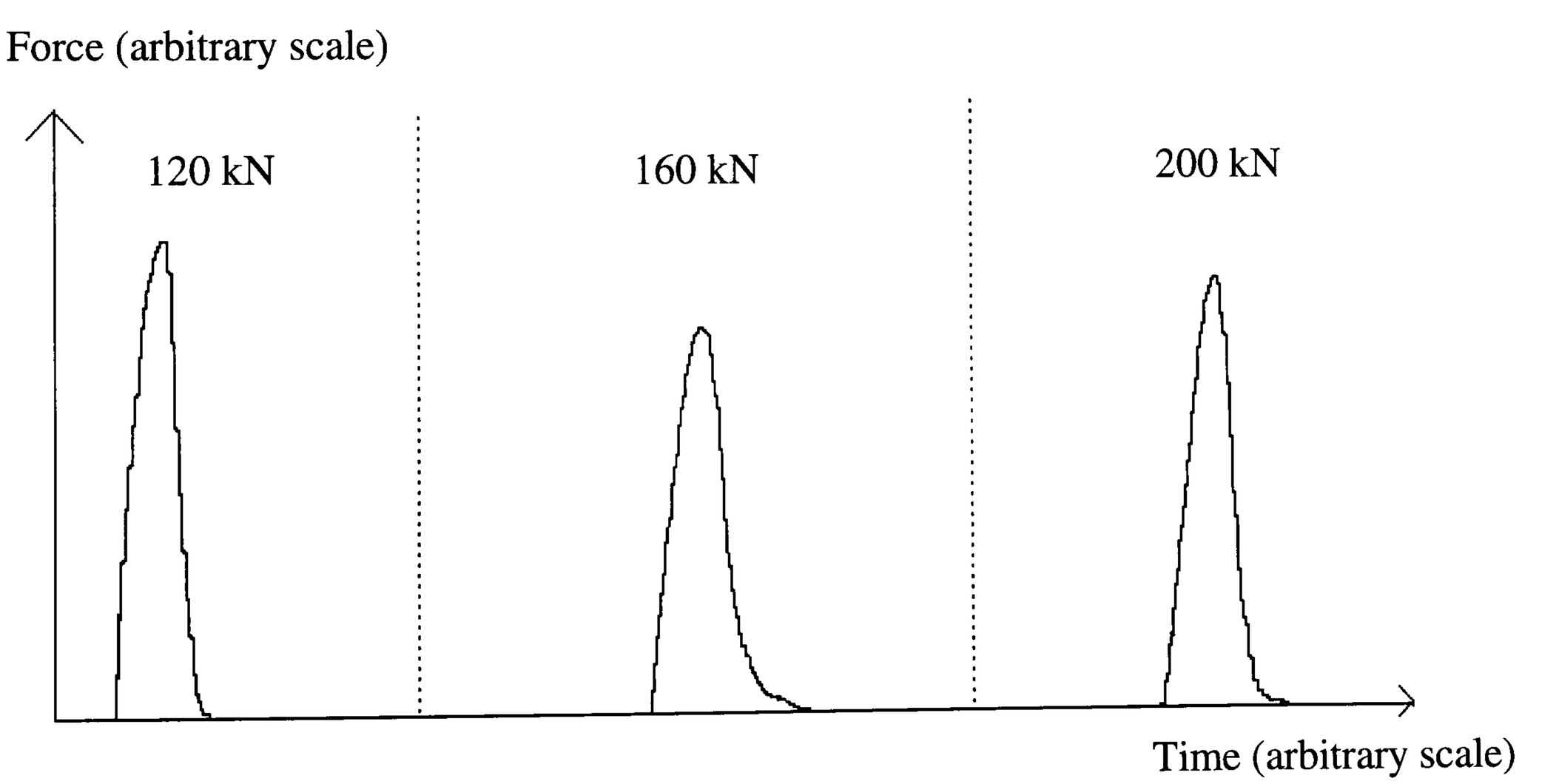

(b) Impact at Mid-Point (Position 3) of Covered Rope (Experiment 3)

Figure 7.15. Effect of Rope Tension on Shape of Force-time History

Figure 7.16 shows that the impulse's duration decreased with increasing applied tension. The figure shows the trends for impacts at the mid-point of the uncovered rope (experiment 1) over the 5 kN to 200 kN tension range. Clearly the rate at which the impulse duration decreases with increasing tension is greater at lower tensions such as 40 kN, than at higher tensions such as 160 kN. Similar trends were observed for other experimental conditions of the rope but the magnitudes of the impulse durations were different. The impulse durations at different tensions with stiffnesses predicted by equation 7.20 for impacts at the mid-point (position 2) of the rope are also plotted. The predicted impulse durations are shorter than those obtained experimentally because of the assumptions of the theoretical model or the missing term accounting for longitudinal extension.

The effect of different positions of impact is illustrated in Figure 7.17. The Figure shows three observed impulse durations for impacts on the uncovered rope (experiment 1) at 80 kN tension. Clearly the impulse duration at the mid-point (position 2) is greater than it is at position 1 and position 2. The impulse durations at different positions on the rope with stiffnesses predicted by equation 7.20 and at a tension of 80 kN are also plotted. The experimentally observed trend appears to be similar to that predicted theoretically although the impulse durations are generally shorter. Similar trends were observed for other experimental rope conditions.

The supporting condition was found to affect the force-time history. The impulse durations were found to reduce when the support condition was altered by fitting the clamp to the rope, indicating that the clamp had the effect of increasing the local stiffness of the rope. For example, at 200 kN tension the impulse duration was 0.94 ms when the unclamped rope (experiment 1) was impacted at $L/7$ (position 1) from the support. However, the duration was 0.78 ms when the clamped rope (experiment 3) was impacted at the same position. At $L/2$ from the supports the corresponding durations were 2.06 ms (experiment 1) and 0.78 ms (experiment 3). The clamp increased the local stiffness even though the polythene cover, which would tend to reduce the local stiffness and increase the impulse duration, was also present.

The results also show that the clamp performed its intended function in making the local stiffness at different positions along the rope constant by standardising the amount of lateral restraint. When the clamp was not installed the difference between the impulse duration at *L*/2 and its duration at *L*/7 was 1.12 ms, this was greater than the corresponding difference when the clamp was installed (0 ms).

This concludes the discussion of factors that reduce the damage sensitivity. The discussion that follows is concerned with the sensitivity of the coin-tap test for discriminating between time histories of impacts on the wire rope when its condition was either deteriorated by a fractured wire or by an artificial defect.

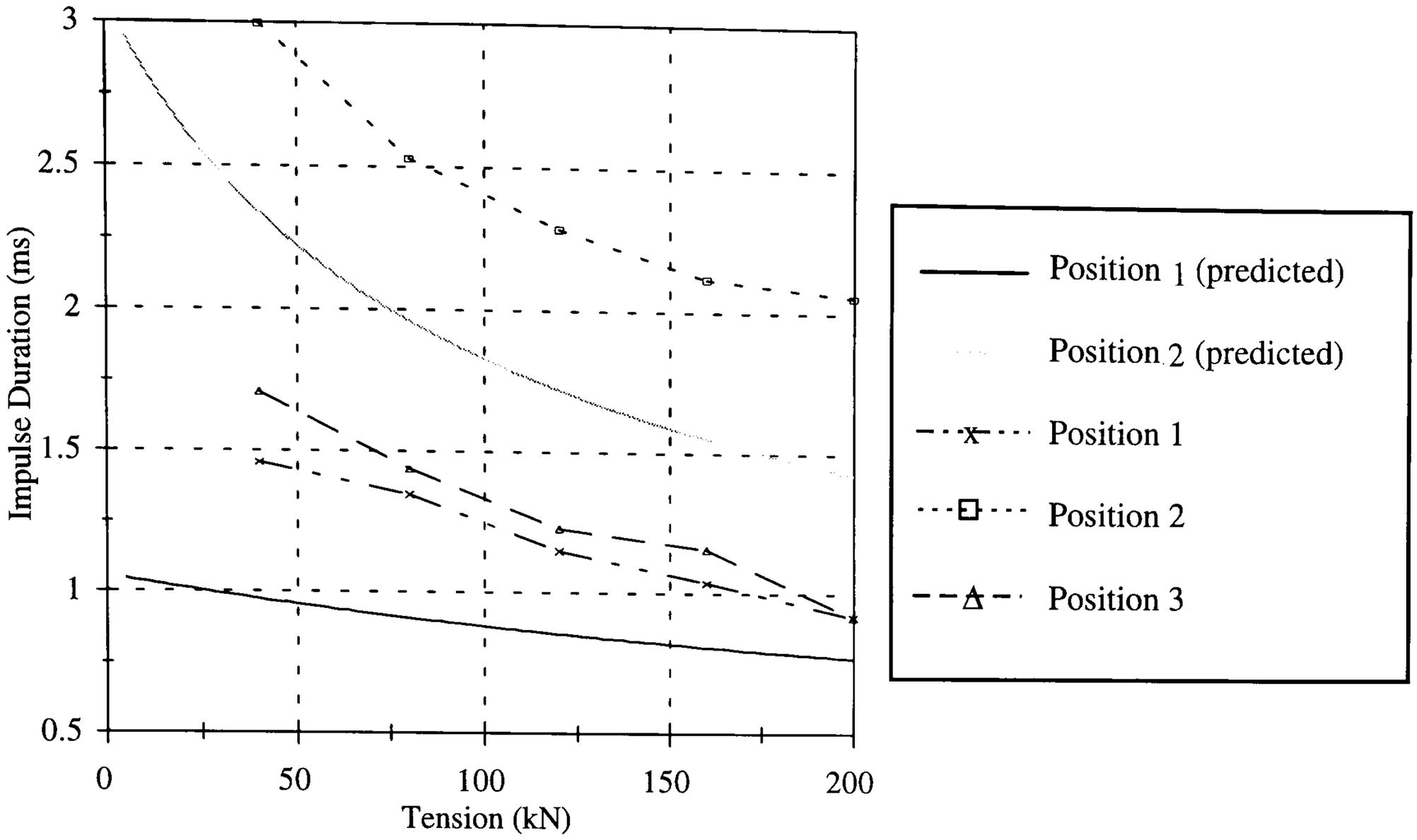

Figure 7.16. Effect of Applied Tension on Impulse Duration for Uncovered Rope (Experiment 1)

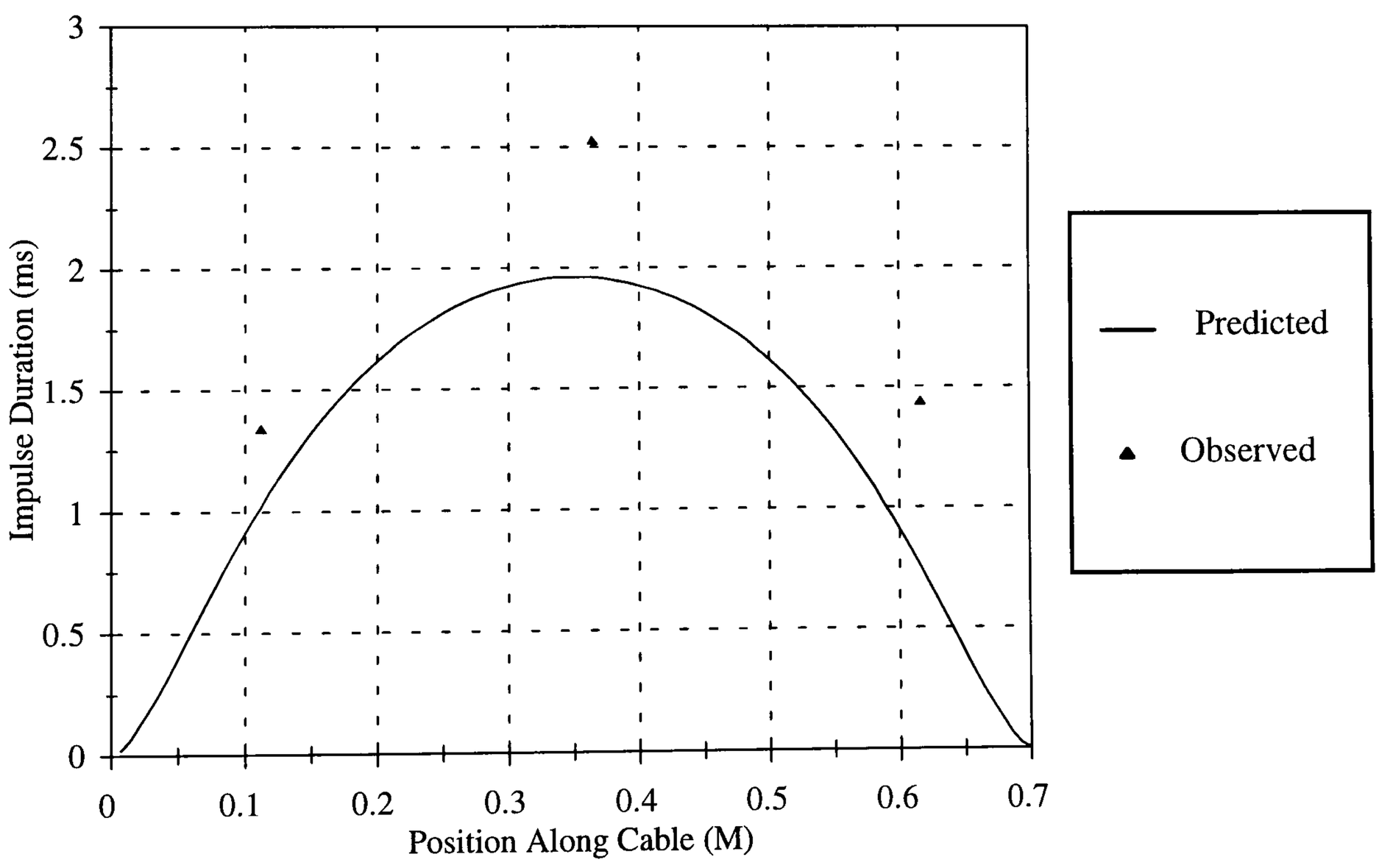

Figure 7.17. Effect of Impact Position on Impulse Duration for Uncovered Rope (Experiment 1) at 80 kN Applied Tension

The presence of a fractured wire was found to affect only the shape of the time history for impacts on the uncovered rope (experiment 1). Figure 7.18 shows that there was a sharp 'spike' after the impulse's tail. This feature, believed to be caused by the rebounding free ends of the fractured wire, could be a potential indicator of fracture. The shape of the time histories for impacts on the rope in other experimental conditions was unaffected, probably because the ends of the fractured wire were restrained by the cover.

The change in impulse duration due to the presence of a fractured wire was found to be inconsistent. Table 7.2 presents the results for the uncovered rope (experiment 1) and the covered, supported rope (experiment 3). In some cases the duration for the fractured rope was less than the unfractured rope. However, the duration of the fractured rope should always be greater because its cross-sectional area is effectively reduced by the area of one wire producing a corresponding reduction in the second moment of area (assuming the cross-section remains approximately circular) and the local stiffness (equation 7.20). The inconsistent experimental results were probably due to inaccuracies in measuring the width of the impulse because its boundaries were not well defined.

	Experiment 1 (uncovered)		Experiment 3 (covered)	
	Fractured	Non-fractured	Fractured	Non-fractured
Position 1	1.25	0.94	0.60	0.78
Position 2	2.06	2.06	0.95	0.78
Position 3	1.16	0.93	0.69	0.93

Table 7.2. Duration of Force-time Histories (ms) for Impacts on Wire Rope at 200 kN

Equation 7.21 suggests that the sensitivity of the coin-tap test to changes in local stiffness caused by fracture could be improved by reducing the tension. The first term in the numerator is dependent on the second moment of area whereas the second term is dependent on the tension. The tension on the rope was 200 kN giving a value of 6125 Nm^2 for the second term. The first term was 1666 Nm^2 for the unfractured rope whereas it was 1199 Nm^2 for the fractured rope. The change in the numerator and therefore the local stiffness is very small (6%). However, when the tension is reduced to 5 kN, the second

term is 153 Nm^2 producing a larger local stiffness change (26%) and increasing the sensitivity of the test.

This is illustrated in Figure 7.19 which shows the variation in impulse duration as a function of the rope's cross-sectional area at 200 kN and at 5 kN. The dotted vertical bars indicate the cross-sectional areas of the fractured and the non-fractured ropes. Clearly at both positions of impact the difference between the fractured and non-fractured rope impulse durations is greater for the lower tension. At position 2 the predicted difference is 0.44 ms which, given the variation in experimentally measured values (table 7.2), would be large enough to produce a consistent measurable reduction in impulse duration.

The presence of a defective wire with a small notch on it did not produce noticeable changes in the shape of the force-time history. It did not produce a measurable change in the impulse duration either, despite the rope being tested at a low tension (4 kN). The reason for this is thought to be because the reduction in cross-sectional area was not large enough to produce a measurable change in local stiffness.

7.3.4. Computational Damage Detection

It was mentioned in the previous section that the shape of the force-time history of an impact on the uncovered rope is changed by the presence of a fractured wire. This section describes computational methods of discriminating between the impact force on the rope in its fractured and non-fractured states. At a tension of 200 kN, five measurements were made at five positions on the uncovered rope; position 1, position 3 (Figure 7.10) and at three intermediate positions separated by 125 mm. The impact positions were then consecutively re-numbered from 1 to 5 in order of distance from the upper clamp. The time histories and frequency spectra were acquired with the spectrum analyser using a rectangular window and a 20 kHz bandwidth (50 kHz sample rate). Each measurement was obtained by performing a process average on the data from three impacts at each position on the rope.

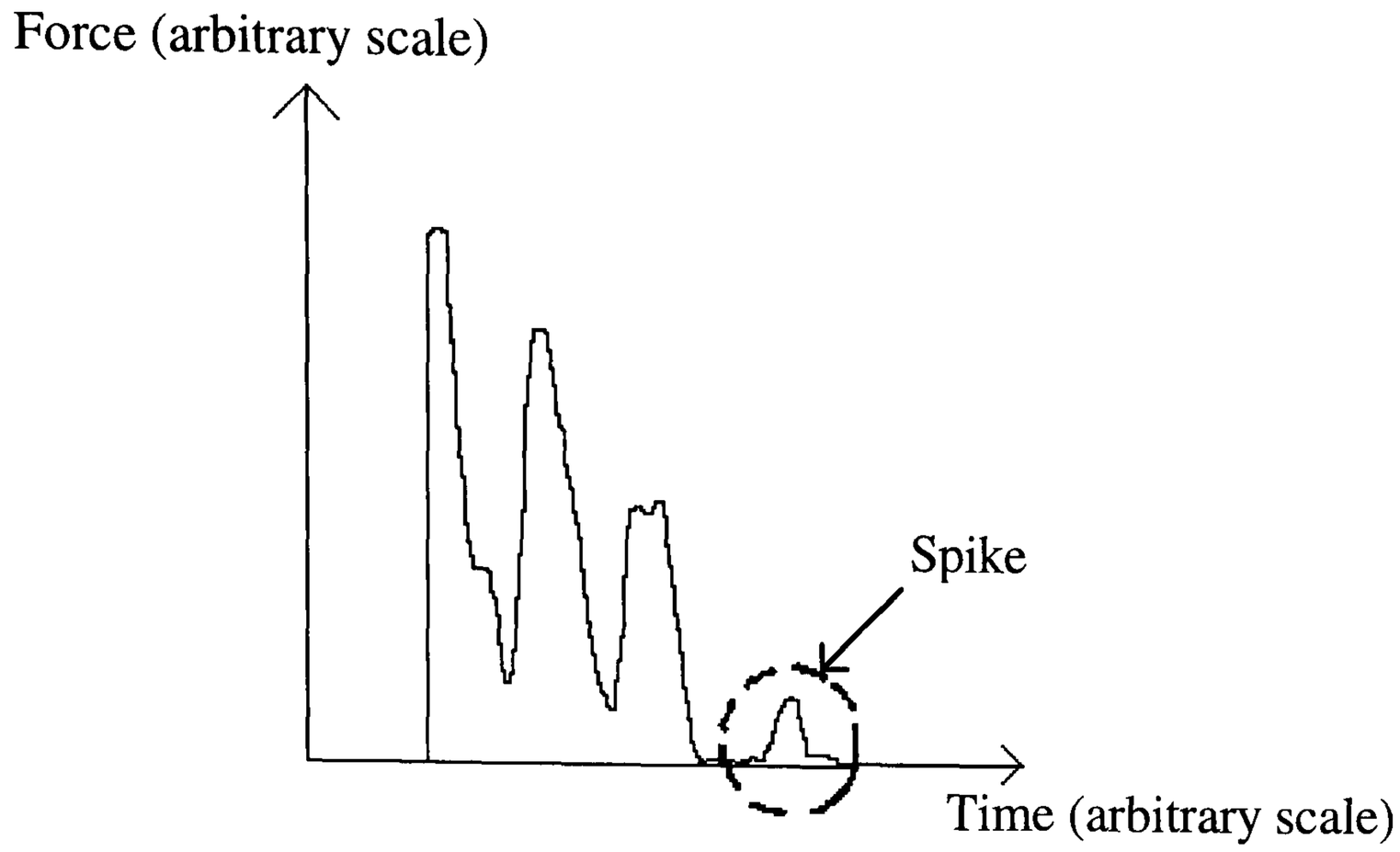

Figure 7.18. Effect of Fracture on Shape of Uncovered Rope Force-time History (Experiment 1)

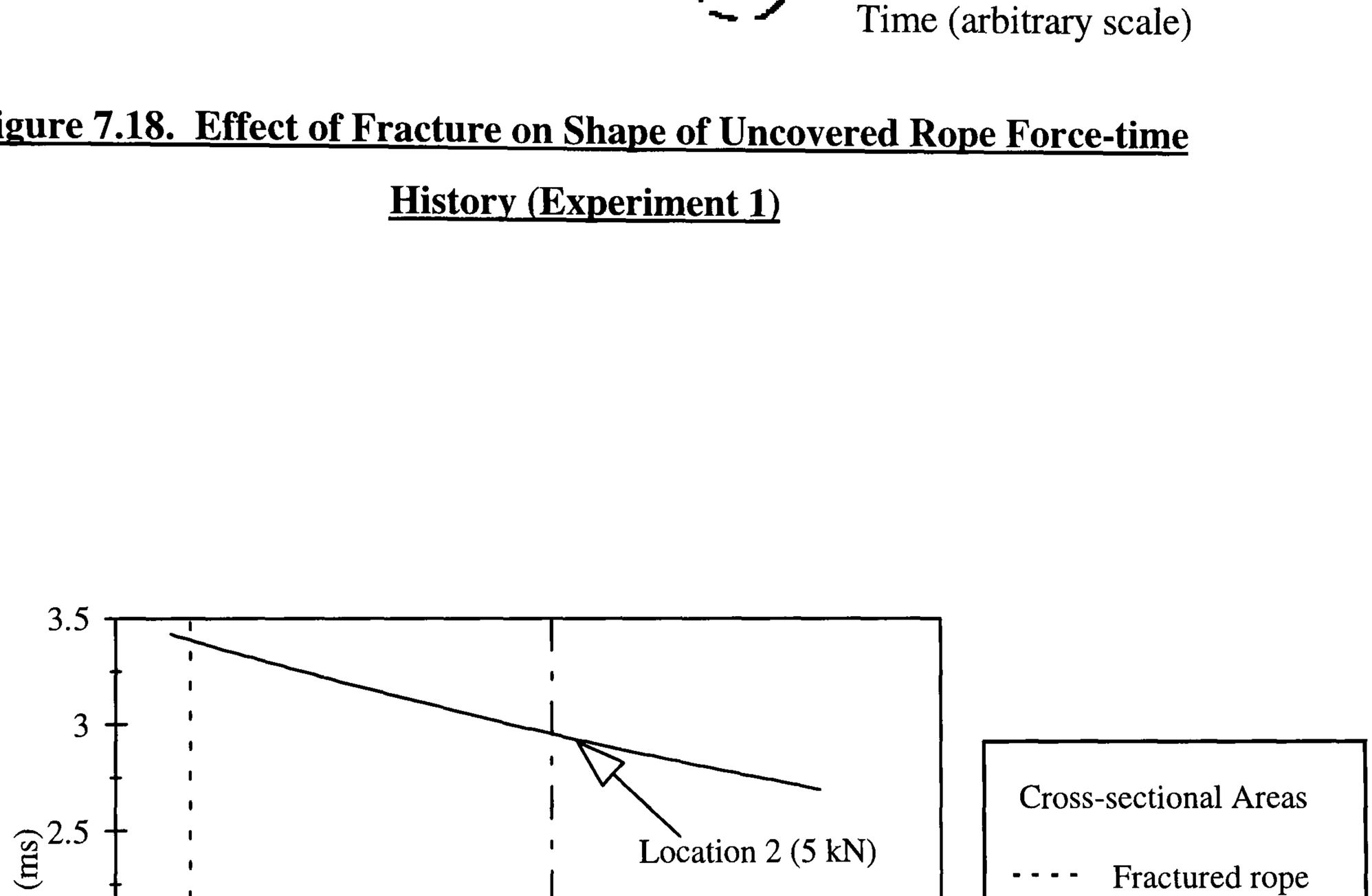

Figure 7.19. Predicted Effect of Rope Cross-sectional Area on Impulse Duration

The first method was to use a back-propagation neural network, as described in chapter 5, to classify automatically the time history waveforms according to the condition of the rope. The network had 20 first layer units and a single output unit. Thirty-six component feature vectors were obtained by sampling the waveforms over a fixed interval and normalising between 0 and 1. For each condition of the rope thirteen of the fifteen measurements taken at position 3 and the two neighbouring positions were used for training. Therefore there was a total of twenty-six training vectors. The targets for training vectors from the fractured rope and unfractured rope were 0 and 1 respectively. The learning rate was 0.5, the momentum constant was 0.2 and the criterion for network convergence was defined as an error function that had been reduced to a value of 0.04 or less. Training was complete after approximately 5 hours.

The network was then tested with four randomly chosen feature vectors; two were from measurements on the fractured rope and two were from measurements on the unfractured rope. Using the weights computed during training, the network computed an output for each test vector and these are presented in Table 7.3. Clearly the network correctly classifies test vectors from the fractured rope and the unfractured with a high degree of accuracy. This is probably because the 'spike' in the force-time history is such a distinctive feature of the response of the fractured rope.

Condition of rope	Test Vector	Target	Network Output
Unfractured rope	1	1.0000	1.0000
	2	1.0000	1.0000
Fractured rope	1	0.0000	0.0000
	2	0.0000	0.0000

Table 7.3. Classification of Impact Force on Wire Rope with Neural Network

The second method of discriminating between impacts on the fractured rope and the unfractured rope was to compute the ratio of areas under the spectrum, as described in Chapter 4, and compare these. Figure 7.20 shows typical spectra of impacts at position 3 on the rope in each condition for a 10 kHz bandwidth. Near the cut-off frequency (~175 Hz) the spectrum of the fractured rope is almost indistinguishable from that of the

unfractured rope. This agrees with the earlier observation that, at a tension of 200 kN, the test was not sensitive enough to detect the changes in the impulse duration caused by rope fracture. However, at frequencies above 1 kHz, the amplitude of the spectrum of the fractured rope is frequently greater and a larger area is enclosed between it and the frequency axis. Therefore the ratio of the area, B, between the threshold frequency (ν_t) and the maximum frequency (ν_{max}), to the total area (A+B) under the spectrum and below the maximum frequency would be greater for the fractured rope (provided that a substantial proportion of the area B is above 1 kHz). The increased high frequency content of the spectrum for the fractured rope is probably caused by the rebounding loose wire and corresponds to the 'spike' previously observed in the time history.

The ratio was computed with different values for ν_t and ν_{max}. The greatest sensitivity was obtained when ν_t was 178 Hz corresponding to approximately 10% of ν_{max}, which was 1.78 kHz. The locations of these frequencies on the spectra are indicated on Figure 7.20. By comparison it can be noted that for damage that primarily reduces the local stiffness, it is recommended that ν_t is chosen between 30% and 50% of ν_{max} for greatest sensitivity (Cawley and Adams, 1988).

The sensitivity was also found to vary at different positions on the rope. Table 7.4 shows that the difference between the ratio of the fractured rope and that of the unfractured rope diminished as the position of impact neared the supports but reached a maximum at the mid-point of the rope. This suggests that maximum sensitivity is obtained by impacting at the mid-point of the rope, as predicted for damage that primarily reduces the local stiffness.

This discussion has shown that it is possible to detect fracture in wire ropes by applying computational techniques to the dynamic waveforms of impact forces on them. It has been demonstrated, with the neural network, that pattern recognition can be employed to classify the time histories directly. These results indicate the potential feasibility of using a computer to perform the classification process and thereby automate the process.

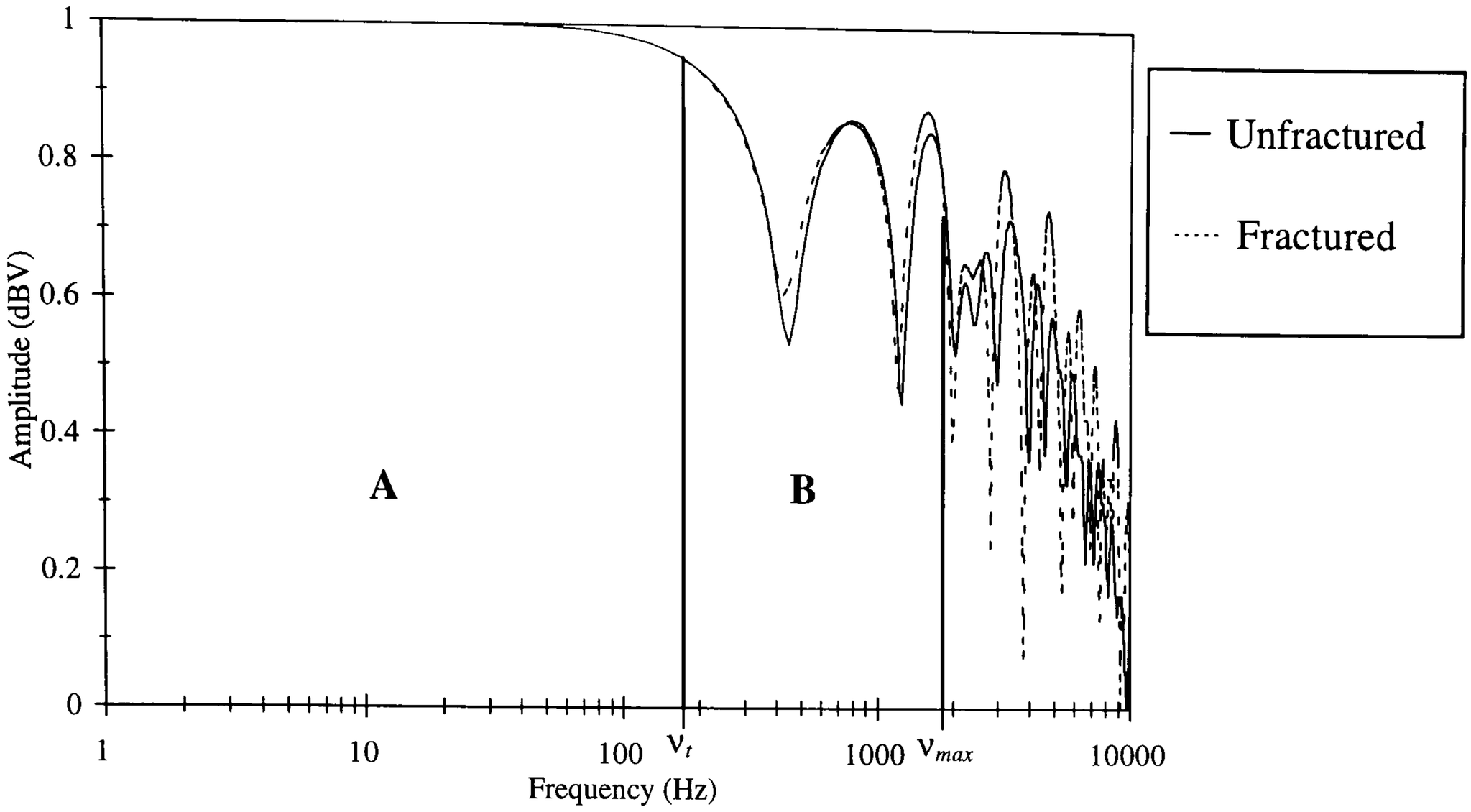

Figure 7.20. Spectra of Impact Force on Wire Rope (20 kHz Bandwidth)

Position on Wire Rope	Ratio of Areas Under the Spectrum B/(A+B) (ν_t = 178 Hz; ν_{max} = 1.78 kHz)	
	Fractured	Non-Fractured
1	0.51	0.5
2	0.48	0.48
3	0.57	0.48
4	0.48	0.48
5	0.49	0.50

Table 7.4. Variation in Ratio of Areas Under Spectrum with Position on Wire Rope

7.4. Summary

The coin-tap test has been applied to two types of structural steelwork: wire rope under tension and chequer plate flooring.

In the first application the presence of corrosion products between the chequer plate and the supporting I-section was found to dampen structural vibrations of the chequer plate when impacted and therefore the resulting force waveforms were distinctively different from those obtained by impact over a sound region. This allowed the presence of corrosion products to be identified. Furthermore, measurements taken at regions where it was suspected that there may be corrosion products also exhibited increased damping, indicating the presence of concealed corrosion. The force waveforms for impact on the wire rope were found to exhibit a feature that allowed the presence of a loose fractured wire to be identified (provided that the rope's protective cover had been removed). The fractured wire was found to reduce the local stiffness which in turn was affected by the supporting conditions, the position of impact and the applied tension. The sensitivity of the test to a fractured wire was best when the rope had no additional support, and it was impacted at its mid-span point under minimum tension.

Methods of pattern recognition were employed to classify coin-tap test measurements automatically, according to the condition of the steel structure. In the case of the wire rope, two known conditions were available. This permitted the use of the supervised back-propagation neural network which successfully classified new measurements as either being from the fractured rope or from the unfractured rope. In the case of the chequer plate flooring the condition of the interface between the chequer plate and the supporting I-section at the exact position of impact was not known and therefore it was necessary to use the unsupervised probabilistic resource allocating network (PRAN). This formed two clusters of data from measurements on the chequer plate. The distribution of feature vectors and kernels suggested that the data could be grouped into two categories corresponding to corroded regions and sound regions.

8. DISCUSSION

8.1. Introduction

In Chapter 1 the three objectives if this project were stated, these were:

i) to review current methods of non-destructive testing and identify a method suitable for the inspection of corrosion damaged steelwork;

ii) to review selected methods of intelligent computing suitable for categorising field test data automatically;

iii) to identify the components of a self-contained monitoring system capable of detecting and classifying corrosion damage in steel structures.

The coin-tap test has been shown to be effective in detecting corrosion deterioration at four locations on steel structures: bolted steelwork joints; bolted and riveted splice plates; wire ropes under tension; and I-sections under chequer plate flooring. Supervised and unsupervised methods of pattern recognition were used to classify the measurements automatically.

The test was advanced by the introduction of a new quantity sensitive to local stiffness change; the ratio of the peak impulse force to the area enclosed by the impulse. It was also advanced by identifying changes in structural vibration ('ringing') due to damping caused by corrosion products.

The next section reviews the findings of these investigations and it is followed by a section that draws on this information to identify the components necessary for a self-contained on-line monitoring system capable of detecting and classifying deterioration due to corrosion on-site. The last section makes suggestions for future research.

8.2. Research Findings

Corrosion deterioration was identified by inspection of the interacting force time history from an impact on the structure. The characteristic changes produced by *local stiffness reduction* were found to be useful for identifying corrosion deterioration of a bolted steelwork joint, in particular when there was considerable loss of section. The reduction in 'ringing' produced by *damping increase* was found to be effective in identifying the presence of corrosion products at the steelwork joint and at the interface between chequer plate flooring and its supporting I-section.

Severe corrosion deterioration may cause certain parts of the structure to work loose. This will increase the frequency response function amplitude at higher frequencies and in extreme cases it produces a 'spike' in the time history. These effects were found to be useful for identifying looseness in corroded splice plates and for identifying the presence of a fractured wire in a strand of wire rope under tension.

The method of pattern recognition employed to classify the force waveforms depended on the availability of structures of known condition for training. When structures of known condition were available, supervised methods of pattern recognition could be employed, whereas when they were not, unsupervised methods had to be used.

The steelwork joint and the wire rope were assembled in the laboratory under experimental conditions and therefore it was convenient to prepare them in known conditions and employ the supervised back-propagation neural network to classify new measurements automatically according to the condition of the structure. In the case of the wire rope the deteriorated condition was a fractured wire whereas the steelwork joint was prepared in two deteriorated conditions: the first had corrosion products at the joint interface; and the other had suffered loss of section.

The splice plates and the I-section under the chequer plate flooring were tested on-site and, at the time of testing, examples of the structures in known conditions were not available. Therefore it was necessary to employ the unsupervised probabilistic resource allocating

network (PRAN) to group the measurements automatically into clusters representing the different conditions of the structure. The clusters containing measurements from deteriorated parts could then be identified.

In circumstances when structures that are known to be in good condition are available on-site, it will be possible to use the PRAN to form a probability distribution of measurements from these structures and then test it on measurements from other structures. An example of this is when comparatively new I-sections that have not suffered corrosion deterioration are present under chequer plate flooring. In this case the PRAN could be used to form a probability distribution of measurements over the new beam and then it could be tested with measurements over other beams.

8.3. On-line Monitoring System

The system would comprise an instrumented hammer to perform the coin-tap test, data acquisition software to convert analogue signals to digital signals in the time and frequency domains, and pattern recognition software to classify measurements according to the condition of the test structure.

Both types of software could be installed on a portable lap-top microcomputer. This would have two main advantages over a spectrum analyser and a desktop computer, as used in this study. The first is that it would allow the condition of the structures tested to be classified on-site without the need to return to the office. The second advantage is that, unlike spectrum analysers that have limited storage capacity, it would allow a large number of measurements to be included in the training and testing stages.

Data processing software would also have to be installed so that measurement data could be normalised and compressed and so that anomalies generated by the electronics (e.g. 'spikes') could be removed from the acquired data. The operation of the monitoring system's pattern recognition software would consist of two stages; training and testing.

The purpose of training is to determine the distribution of measurements in feature space. The neural network performs this function by adjusting its weights to define discriminants that partition feature space, dividing the measurements into groups representing specific structural conditions. The PRAN performs this function by clustering the measurements in feature space.

The time taken for training depends on the following factors:

- the number of measurements that are to be included;
- the size of the feature vectors and the distinctiveness between them for different structural conditions;
- the pattern recognition algorithm and architecture chosen and;
- the processor speed.

For tests on the steelwork joint, a back-propagation network implemented on a 25 MHz processor was found to require seventeen hours to train when presented with one hundred and twenty time history feature vectors, each containing forty-eight components. However, when frequency spectrum feature vectors were used only seven hours were required because the differences between them for different structural conditions were more distinct. The PRAN generally requires a much shorter time to train than the back-propagation network because it uses a constructive algorithm. Under the same experimental conditions as those described for the back-propagation network, the PRAN took typically less than ten minutes to train.

The tests on the steelwork joint and wire rope were performed under laboratory conditions. However, under conditions of field testing the variability of measurements on wire ropes will be increased by wind loads and live loads, and the variability of measurements on steelwork joints will be affected by various difficulties in testing and other factors (paint, spills of products, dirt etc.). Under these circumstances it would be prudent to train the pattern recognition software with measurements taken under the widest possible range of operational loads.

The purpose of the test stage is to classify feature vectors from measurements on structures with unknown condition (test vectors). The trained pattern recognition software is presented with the test vectors which are then assigned to the classes defined during training. The PRAN is a novelty detector, so test vectors would be either classified as 'normal' when they are similar to those in the training set; or they would be classified as 'novel' when they do not. The neural network could be trained with feature vectors representing two or more structural conditions and therefore, there would be as many different classes to which new test vectors could be assigned. For example, if the possible conditions of a steelwork joint were 'sound', 'corroded' and 'damaged', then a test vector would be classified as belonging to one of these three classes.

8.4. Future Work

The condition monitoring of deterioration due to corrosion on structural steelwork could be advanced by applying the methods developed in this thesis to other locations on structural steelwork. In his report, Gallon (1993) identified a number of locations on structural steelwork at petrochemical sites that were particularly vulnerable to hidden corrosion. Therefore, those locations to which the coin-tap test has not been applied in this thesis would be ideal subjects for future research.

One such location would be to detect corrosion at steelwork joints that are hidden behind slabs of concrete fireproofing in chemical storage sheds. In this case the closest access to joints at floor level is often a considerable distance along the associated members where they become exposed from behind the concrete slab. The on-line monitoring system could be trained on examples of similar joints that are exposed and then tested on concealed joints. The test is likely to be more sensitive to changes in structural damping than local stiffness because of the large distance from the joint at which the member would be impacted.

Another application would be to test for corrosion occurring between back-to-back angles. The member would be impacted directly over the suspect region and corrosion could be

identified by the change in local stiffness or local damping relative to regions known to be sound.

The pattern recognition software could be improved with more efficient algorithms which would speed up the time for training. The back-propagation algorithm employed in this project was effective but in some cases training took several hours. This is acceptable for research but in an industrial application it would not be cost-effective.

Salomon and Hemmen (1996) have shown that the training time can be significantly reduced by introducing a learning rate that is adjusted iteratively according to the error function. Chen and Chang (1996) showed that significant reductions in the training time could also be achieved by introducing an activation function, the shape of which changes iteratively to prevent saturation. In the case of the sigmoid function this can be achieved by adjusting the constant β as described in Chapter 5. It would be worthwhile to implement these refinements to the back-propagation network and investigate the algorithms' performances in classifying waveforms.

The number of local minima in the error function of a given back-propagation network is a critical factor in determining the training time. This is an inevitable consequence of using a non-linear activation function and it would appear to limit the speed of supervised classifiers in these applications. However, radial basis function (RBF) networks (Michie et al, 1994) have hybrid architectures (first layer is trained unsupervised and second layer is trained supervised) and the activation functions of the second layer of units are linear.

Roberts and Tarassenko (1993) suggested that the PRAN could be used to grow kernels that represent the first layer (also called the hidden layer) of RBF networks and thereby ensure that the optimum number of units are obtained. The output of each first layer unit is connected to each unit in the second layer (also called the output layer). The second layer units of RBF networks have weighted inputs that are computed by the standard gradient descent algorithm with the same training set used by the PRAN to grow the first layer.

Because the activation functions of the second layer units are linear the error function has no local minima and the training time for the second layer is reduced considerably. The PRAN only takes a short time to grow the first layer so the total training time would be considerably less than a two-layered back-propagation network. It would be worthwhile to implement this combined architecture and investigate the algorithm's performance in classifying waveforms.

8.5. Summary

The coin-tap test has been shown to be an effective diagnostic tool for detecting deterioration due to corrosion at four common locations on structural steelwork. Furthermore, two new techniques for identifying deterioration were introduced. The classification of different categories of deterioration can be automated with supervised and unsupervised methods of pattern recognition.

However, the scope of the coin-tap test should be widened by applying it to other steel structures and the efficiency of methods of pattern recognition could be improved with more sophisticated algorithms. A complete self-contained, portable monitoring system would be possible by the inclusion of a laptop microcomputer. This would allow large quantities of data to be stored and processed on-site.

9. CONCLUSIONS

1. The coin-tap test is effective in detecting deterioration due to corrosion at a variety of locations on structural steelwork including: bolted steelwork joints; wire ropes under tension; I-sections under chequer plate flooring, and bolted and riveted splice plates on an iron bridge.

2. It is possible to identify the increase in local damping associated with the presence of corrosion products by inspecting the time history for changes in the amplitude or frequency of 'ringing' vibrations.

3. It is possible to identify the reduction in local stiffness associated with severe deterioration due to corrosion by computing the ratio of the impulse height to the area enclosed by it. This quantity is also independent of the velocity of impact.

4. The measurement data produced by the coin-tap test can be classified automatically according to the condition of the structure. The back-propagation neural network can be employed for supervised classification whereas the probabilistic resource allocating network (PRAN) can be employed for unsupervised classification.

5. Situations are common where classification is a question of identifying unusual measurements and in these cases the PRAN has considerable potential as a novelty detector. This is because:

   i) it is easy to obtain the internal representation of the measurement data within the PRAN

   ii) the distribution measurement data within the PRAN can be visualised by performing a principal component analysis.

6. A self-contained on-line monitoring system for detecting corrosion in structural steelwork could be assembled. Such a system would comprise an instrumented hammer connected to a portable microcomputer with pattern recognition and data processing

software installed. The total time required to perform and classify measurements would be considerably less than that of a system in which the acquisition and processing software were separate because there is no longer a need to transfer data and because the on-line storage capacity is greater.

REFERENCES

Adams R. D. and Cawley P (1985)
Vibration Techniques in Non-Destructive Research. Research Techniques in Non-Destructive Testing (edited by Sharpe R. S). Academic Press, London, Volume VIII, pp 303-360.

Allemang R. J. and Brown D. L (1982)
A Correlation Coefficient for Modal Vector Analysis. Proceedings of the First International Modal Analysis Conference. Orlando, Florida, USA.

American Society For Metals (ASM, 1976)
Metals Handbook, Eighth edition. Ed. Boyer H. E.. American Society For Metals, Metals Park, Ohio. Volume 11, pp 1-276.

ASTM Designation (1983)
E165 Standard Practice for Liquid Penetrant Inspection Method. 1990 Annual Book of ASTM Standards, Volume 03.03, ASTM, pp 54-68.

ASTM Designation (1985)
E837 Standard Practice for Magnetic Particle Examination. 1990 Annual Book of ASTM Standards, Volume 03.03, ASTM, pp 287-313.

ASTM Designation (1984)
E1004 Standard Test Method for Electromagnetic (Eddy-current) Measurements of Electrical Conductivity. 1990 Annual Book of ASTM Standards, Vol. 03.03, ASTM, pp 427-430.

ASTM Designation (1989)
E94 Standard Guide for Radiographic Testing. 1990 Annual Book of ASTM Standards, Vol. 03.03, ASTM, pp 1-10.

ASTM Designation (1985)
E569 Standard Practice for Acoustic Emission Monitoring of Structures During Controlled Simulation. 1990 Annual Book of ASTM Standards, Vol. 03.03, ASTM, pp 231-234.

ASTM Designation (1988)

E164 Standard Practice for Ultrasonic Contact Examination of Weldments. 1990 Annual Book of ASTM Standards, Vol. 03.03, ASTM, pp 33-53.

Bishop C. M (1995)

Neural Networks for Pattern Recognition. Clarendon Press, Oxford, pp 59-73.

Biswas M, Pandey A. K and Samman M. M (1989)

Diagnostic Experimental Spectral/Modal Analysis of a Highway Bridge. International Journal of Experimental and Modal Analysis, Volume 5 Number 1, pp 33-42.

Brandon J. A (1996)

Impulse Testing of Civil Engineering Systems With Characteristic Non-linearities. International Conference on Identification in Engineering Systems, Swansea, pp 407-416.

Brulé J. F. and Blount A (1989)

Knowledge Acquisition. McGraw-Hill Publishing Company, New York.

Burdekin F. M (1993)

Nondestructive Testing of Structural Steelwork. Proceedings of the Institute of Civil Engineers, Structures and Buildings. Volume 99, pp 89-95.

Carpenter G. and Grossberg S (1986)

Neural Dynamics of Category Learning and Recognition: Attention Memory Consolidation, and Amnesia, in Davis J, Newburgh R and Wegman E (Eds.). Brain Structure, Learning and Memory, AAAS Symposium Series.

Cawley P (1984)

The Impedance Method of Non-Destructive Inspection. NDT International, Volume 17, pp 59-65.

Cawley P. and Adams R. D (1979)

The Location of Defects in Structures From Measurements of Natural Frequencies. Journal of Strain Analysis. Volume 14 Number 2.

Cawley P. and Adams R. D (1988)
The Mechanics of the Coin-Tap Method of Non-Destructive Testing. Journal of Sound and Vibration. Volume 122 Number 2, pp 299-316.

Cawley P. and Adams R. D (1989)
Sensitivity of the Coin-Tap Method of Non-Destructive Testing. Materials Evaluation, Volume 47, pp 558-563.

Chen C and Chang W (1996)
A Feedforward Neural Network with Function Shape Autotuning. Neural Networks, Volume 9 Number 4, pp 627-641.

Conway H. D. and Jakubowski M (1969)
Axial Impact of Short Cylindrical Bars. Journal of Applied Mechanics, Volume 36, p 809.

Cooley J. W. Tukey J. W (1965)
An Algorithm for the Machine Calculation of Complex Fourier Series. Mathematics of Computation, Volume 19 Number 90, pp 297-301.

Comerford J. B (1989)
The use of Knowledge-Based Systems in Interpretation of Measurements. University of Bristol PhD Thesis.

Cygnus Instruments Ltd (1996)
Saving Time on Bridge Inspections. INSIGHT Non-destructive Testing and Condition Monitoring, Volume 38 Number 11, pp 772-773.

De Bruyn H. J (1996)
Current Corrosion Monitoring Trends in the Petrochemical Industry. International Journal of Pressure Vessels and Piping. Volume 66 Numbers 1-3, pp 293-303.

Diagnostic Instruments (1995)
2 Michaelson Square, Kirkton Campus, Livingston, West Lothian EH54 7DP.

Dobmann G. and Höller P (1980)
Physical Analysis Methods of Magnetic Flux Leakage. Research Techniques in Non Destructive Testing (Edited by Sharpe R. S.). Academic Press, London, Volume IV, pp 39-69.

Dos Reis H. L. M (1990)
Nondestructive Testing of Wire Ropes using Analytical Ultrasonics. In International Advances in Nondestructive Testing. Edited by McGonnagle W. J. Gordon Breach, Volume 15, pp 149-158.

Dytran Instruments Inc (1996)
21592 Marilla Street, Chatsworth, CA 91311.

Elkordy M, Chang K. C. and Lee G. C (1994)
Applications of Neural Networks in Vibrational Signature Analysis. Journal of Engineering Mathematics (ASCE). Volume 120 Part 2, pp 250-265.

Evans D. T (1959)
Nondestructive Testing Handbook. The Ronald Press, New York. Volume 2, p 4420.

Ewins D. J (1984)
Modal Testing: Theory and Practice. Research Studies Press, Taunton, p 1.

Freedman A. J, Troscinski E. S. and Dravnieks A (1958)
An Electrical Resistance Method of Monitoring in Refinery Equipment. Corrosion, Volume 14 Number 4, pp 29-32.

French A. P (1974)
Vibrations and Waves. Van Nostrand Reinhold (UK) Company Limited, Wokingham, Berkshire, England.

Fourier J. B. J (1822)
Theorie Analytique de la chaleur. Didot, Paris.

Fu K. S (1976)
Digital Pattern Recognition. Springer-Verlag, Berlin, Heidelberg, New York.

Fukunaga K (1972)
Introduction to Statistical Pattern Recognition. Academic Press, New York and London.

Gallon M. J (ICI Engineering, 1993)

Managing Structural Corrosion in Chemical Plants. New Steel Construction, February pp 14-15.

Gericke O. R (1963)

Determination of the Geometry of Hidden Defects by Ultrasonic Pulse Analysis Testing. Journal of the Acoustical Society of America, Volume 35, pp 364-368.

Glaskov Y. A (1993)

Effect of Heat Treatment of Turbine-Blades in Hydrogen on the Effectiveness of Dye Penetrant Inspection. Russian Journal of Nondestructive Testing. Volume 29 Number 5, pp 391-395.

Goldsmith W (1960)

Impact. Edward Arnold Limited, London, pp 108-129.

Gould (1981)

Service Department, Roebuck Road, Hainault, Essex, IG6 3UE.

Green A. T, Lockman C. S. and Steele R. K (1964)

Acoustic Verification of Structural Integrity of Polaris Chambers. Society of Plastic Engineers, Atlantic City, New Jersey, USA.

Grimberg R, Olteanu I, Cristea T, Goia M, Gradinariu D, Plavanescu R, Bacanu T, Andreescu A and Apavaloaie D (1990)

Eddy Current Examination of Steel Wires. NDT International , Volume 23 Number 4, pp 201-205.

Halmshaw R (1966)

Physics of Industrial Radiology. Heywood Books, London, pp 219-263.

Halvorsen W. G. and Brown, D. L (1977)

Impulse Technique for Structural Frequency Response Testing. Journal of Sound and Vibration. Volume 11, pp 8-21.

Harris C. M and Crede C. E (1961)

Shock and Vibration Handbook. Volume 2, Chapter 23, pp 8-9.

Harrop I and Summerscales J (1989)
Acoustic Emission Testing of the Structural Integrity of Multicore Cable. British Journal of Nondestructive Testing, Volume 31 Number 7, pp 383-387.

Hansch M. K. T, Neundorf B and Stegemann D (1993)
Ultrasonic Pattern Recognition For Use in Surface Layer Recognition. European Journal of NDT, Volume 3 Number 2, pp 59-65.

Hecht-Nielsen R (1988)
Neurocomputing: Picking the Human Brain. IEEE Spectrum, Volume 25 Number 3, pp 36-41.

Hertz H (1881)
Ueber die Berührung fester elastischer Körper. Journal für die reine und angewandte Mathematik (Crelle). Volume 92, pp 156-171.

Hertz J, Krogh A. and Palmer R. G (1993)
Introduction to the Theory of Neural Computation. Addison-Wesley Publishing Company, Reading Massachusetts, pp 115-130.

Herz R. H (1969)
The Photographic Action of Ionising Radiations. Wiley Interscience, New York, pp 400-482.

Hochschild R (1958)
Progress in Non-Destructive Testing (Edited by Stanford E. G. and Fearon J. H.). Heywood, London, Volume 1, pp 59-109.

Hinsley J. F (1959)
Non-Destructive Testing. Macdonald and Evans Ltd., London, pp 294-325.

Hughes D. E (1879)
Induction-Balance and Experimental Researches Therewith. Philosophical Magazine, Series 5, Volume 8, pp 50-56.

ICI Engineering, June (1990) [1]
Procedure For: Requirements for Inspection of Plant Structures and Pipebridges. Standards and Technical Information Services, ICI Engineering. Cheshire, England.

ICI Engineering, June (1990) [2]
Procedure For: Condition Categories for Inspection of Plant Structures and Pipebridges. Standards and Technical Information Services, ICI Engineering. Cheshire, England.

Iffland J. S. B. and Birnstiel C (1993)
Guide to Nondestructive Test Methods. Bridge Management 2. Thomas Telford, London, pp 921-930.

Ifeachor C. E. and Jervis W. B (1993)
Digital Signal Processing: A Practical Approach. Addison-Wesley Publishing Company, Wokingham.

Jackson P (1990)
Introduction to Expert Systems. Second Edition. Addison Wesley, Wokingham.

Jung B (1968)
On the Application of 185 MeV Protons in Radiography and Densitometry. Report GWI-R 2/68. Gustav Werner Institute, Uppsala, Sweden.

Kozin F and Natke H. G (1986)
System Identification Techniques. Structural Safety, Volume 3, pp 269-316.

Krautkramer J and Krautkramer H (1983)
Ultrasonic Testing of Materials. Third edition. Berlin: Springer.

Kirkegaard P. H. and Rytter A (1993)
Vibration Based Damage Assessment of Civil Engineering Structures Using Neural Networks. Proceedings of the Third International Conference on the Application of Artificial Intelligence in Civil and Structural Engineering, pp 90-104.

Kudva J. N, Munir N and Tan P. W (1992)
Damage Detection in Smart Structures Using Neural Networks and Finite-Element Analyses. Materials Structures, Volume 1, pp 108-112.

Lewis D. M (1951)
Magnetic and Electrical Methods of Non-Destructive Testing. Allen and Unwin Ltd., London.

Lippmann R. P (1987)
An Introduction to Computing with Neural Nets. IEEE ASSP Magazine, April, pp 4-22.

Lord W (1985)
Electromagnetic Methods of Nondestructive Testing. Gordon Breach Science, New York.

Maguire J. R (1984)
The Dynamic Characteristics of Elevated Piled Tanks and Other Selected Prototype Structures. University of Bristol Ph.D. thesis.

Mannan M. A and Richardson M. H (1990)
Detection and Location of Structural Cracks using FRF Measurements. Proceedings of the Eighth International Modal Analysis Conference, Volume 1, pp 653-657.

Marshall W. T. and Nelson H. M (1977)
Structures. Second edition. Longman Scientific & Technical, Singapore, pp 48-51.

McClelland J. L. and Rumelhart D. E (1988)
Explorations in Parallel Distributed Processing. A Handbook of Models, Programs and Exercises. The MIT Press, Cambridge, Massachusetts, London, England.

McEleney P. C (1992)
Electromagnetic (Eddy Current) Testing (Edited by Berger H. and Mordfin L.). Non Destructive Testing Standards - Present and Future, chapter 25 pp 63-70.

Mason W. P, McSkimin J. H. and Shockley W (1948)
Ultrasonic Observation and Twinning of Tin. Physical Review, Volume 73 Number 10, pp 1213-1214.

Messina A, Jones I. A. and Williams E. J (1996)
Damage Detection and Localisation Using Natural Frequency Changes. International Conference on Identification in Engineering Systems, Swansea, pp 67-76.

Michie D, Spiegelhalter D. J. and Taylor C. C (1994)
Machine Learning, Neural and Statistical Classification. Ellis Horwood, New York, pp 29-49.

Migliori A, Sarrao J. L, Visscher W. M, Bell T. M, Lei M, Fisk Z. and Leisure R. G (1993)

Resonant Ultrasound Spectroscopic Techniques for Measurement of Elastic Moduli of Solids. Physica B: Condensed Matter. Volume 183 Numbers 1-2, pp 1-24.

Moss R. M. and Matthews S. L (1993)

In-Service Structural Monitoring. A state-of-the-art review. The Structural Engineer. Volume 73 Number 2, January.

Newton I (1686)

Philosophia Naturalis Principia Mathematica. (Translated into English by A. Motte, D. Adee, New York, 1848).

Owens G. W. and Knowles P. R (1992)

Steel Designers Manual. Fifth edition. Blackwell Scientific Publications, pp 1031, 1040.

Pandey A. K and Biswas M (1994)

Damage Detection in Structures Using Changes in Flexibility. Journal of Sound and Vibration, Volume 169 Number 1, pp. 3-17.

Pandey A. K, Biswas M and Samman M. M (1991)

Damage Detection from Changes in Curvature Mode Shapes. Journal of Sound and Vibration, Volume 145 Number 2, pp 321- 333.

Papoulis A (1962)

The Fourier Integral and its Applications. McGraw-Hill.

Park H. S and Lee S. S (1988)

Weighted Error Matrix Application to Detect Stiffness Damage by Dynamic Characteristic Measurement. Journal of Modal Analysis, July, pp 101-107.

PCB Piezotronics Inc (1996)

3425 Walden Avenue Depew, New York 14043-2495, USA.

Raman C. V (1920)

On Some Applications of Hertz's Theory of Impact. Physical Review, Volume 15 Number 4, p 277.

Rayleigh J. W. S (1906)

On the Production of Vibrations by Forces of Relatively Long Duration, with Applications to the Theory of Collisions. Philosophical Magazine, Series 6, Volume 11, p 283.

Roberts S and Tarrasenko L (1994)

A Probabilistic Resource Allocating Network for Novelty Detection. Neural Computation, Volume 6 pp 270-284.

Rockley J. C (1964)

An Introduction to Industrial Radiology. Butterworths, London.

Roderick R. L. and Truell R (1952)

The Measurement of Ultrasonic Attenuation in Solids by the Pulse Technique and Some Results in Steel. Journal of Applied Physics, Volume 23 Number 2, pp 267-279.

Russell T. J, Schuster V. E. and Waidelich D. L (1962)

The Impedance of A Coil Placed on a Conducting Plane. Transactions of the American Institute of Electrical Engineers, Volume 81 Number 1, pp 232-237.

Salane H. J. and Baldwin J. W (1990)

Identification of Modal Properties of Bridges. Journal of Structural Engineering, Volume 116 Number 7, pp 2008-2021.

Salomon R and Hemmen J (1996)

Accelerating Backpropagation through Dynamic Self-Adaptation. Neural Networks, Volume 9 Number 4, pp 589-601.

Samman M. M. and Biswas M (1994)

Vibration Testing for Nondestructive Evaluation of Bridges. Journal of Structural Engineering (ASCE). Volume 120 Number 1, pp 269-289, pp 290-306.

Samman M. M, Biswas M. and Pandey A. K (1991)

Employing Pattern Recognition For Detecting Cracks in a Bridge Model. International Journal of Analytical and Experimental Modal Analysis. Volume 6 Number 1, pp 35-44.

Scott I. G (1991)

Basic Acoustic Emission. Gordon Breach Science, New York.

Simpson P. K (1990)
Artificial Neural Systems. Pergamon Press.

Stafford D. G. and Watson S. C (1988)
A Current World Condition Survey of Cable Elements on Stayed-Girder Bridges. First Oleg Kerensky Memorial Conference, Session 2.

Stubbs N. and Osegueda R (1987)
Global Non-destructive Evaluation of Offshore Platforms Using Modal Analysis. Proceedings of the 6th International Offshore Mechanics and Arctic Engineering Symposium. Volume 2, pp. 517-524.

Szilard J (1982)
Ultrasonic Testing: Non-Conventional Testing Techniques. Wiley-Interscience, Chichester.

Thewlis J (1956)
Neutron Radiography. British Journal of Applied Physics. Volume 7, p. 345.

Timoshenko S and Goodier J (1934)
Theory of Elasticity. McGraw-Hill Book Company, New York, pp 420-422.

Tråvén H. G. C (1991)
A Neural Network Approach to Statistical Pattern Classification by "Semiparametric" Estimation of Probability Density Functions. IEEE Transactions on Neural Networks, Volume 2 Number 3, pp 366-377.

Uygur E. M (1980)
Nondestructive Dynamic Testing. Research Techniques in Nondestructive Testing. Volume IV, Academic Press, London, pp 205-244.

Vann A. M. and Davis J. M (1994)
Interpretation Systems for Structural Monitoring.
Proceedings of the first EG-SEA-A1 Workshop, Lausanne, Switzerland, March, pp 77-89.

Weischedel H. W (1988)
Quantitative In-service Inspection of Wire Ropes. Materials Evaluation, Volume 46 Number 4, pp 430, 432-437.

Weischedel H. R and Ramsey R. P (1989)

Electromagnetic Testing, a Reliable Method for the Testing of Wire Ropes in Service. NDT International, Volume 22 Number 3, pp 155-161.

Winchester R. G. J (1991)

Apparatus for Magnetic Particle Inspection with an Adjustable Cable for Magnetising Inspection Areas of Variable Dimensions. U.S. Patent Number 5, 053, 702.

Williams S. M (1995)

Condition Monitoring of Damaged Steel Structures. Progress report, University of Bristol, Department of Civil Engineering.

Wu X, Ghaboussi J and Garrett J. H (1992)

Use of Neural Networks in Detection of Structural Damage. Computers and Structures, Volume 42 Number 4, p 649.

Zivica V (1993)

Improved Method of Electrical Resistance - a Suitable Technique for Checking the State of Concrete Reinforcement. Materials and Structures. Volume 26, pp 328-332.

BIBLIOGRAPHY

The following list of references are not referred to in the thesis but were used for the research work carried out.

Baruh H and Ratan S (1993)

Damage Detection in Flexible Structures. Journal of Sound and Vibration, Volume 166 Number 1, pp 21-30.

Bishop C. M (1994)

Novelty Detection and Neural Network Validation. IEE Proceedings on Visual Image Signal Processing, Volume 141 Number 4, pp 217-222.

Brandon J. A (1994)

Dynamic Testing Of Bridges : Current Practice and Future Concepts. Proceedings of the Centenary Year Bridge Conference.

Capron M. D. Williams F. W. and Symons M. V (1987)

The Parametric Study Of the Free Vibrations of an Offshore Structure. Proceedings of the International Conference on Steel and Aluminium Structures, U. K.

Caudhill M. and Butler C (1992)

Understanding Neural Networks: Computer Explorations . Volume 1 Basic Networks. The MIT Press, Cambridge.

Crohas H and Lepert P (1982)

Damage Detection Method is Field Tested. Oil and Gas Journal, 22 February, pp 94 103.

Cosenza E, De Luca A, Faela C, Mazzadani F. M (1987)

Imperfection Sensitivity of Industrial Steel Frames. Proceedings of the International Conference on Steel and Aluminium Structures, Cardiff.

Dempster A. P, Laird N. M and Rubin D. B (1977)

Maximum likelihood from incomplete data via the EM algorithm. Journal of the Royal Statistical Society, Volume 39 Part 1, pp1-38.

Flesh R. G and Kernbichler K. A (1988)

A Dynamic Method for the Safety Inspection of Large Prestress Bridges. Proceedings of the International Workshop on Non-Destructive Evaluation Performance on Civil Structures, Editors Agbabian M. S and Masri S. F, University of Southern California, pp 218-230.

Flood I. and Kartam N (1994)

Neural Networks in Civil Engineering. I: Principles and Understanding. Journal of computing in Civil Engineering, Volume 8 Number 2, pp 131-145.

Hablowetz T and Lieven N (1994)

Provision of Damping Models for Use in Neural Networks. University of Bristol Report Number 702, August.

Hickman G. A, Gerardi J. J and Feng Y (1991)

Application of Smart Structures to Aircraft Health Monitoring. Journal of Intelligent Systems and Structures, Volume 2, pp. 411-430.

Kenley R. M and Dodds C. J (1980)

West Sole WE Platform: Detection of Damage by Structural Response Measurements. OTC 3866, Twelfth Annual Offshore Technology Conference, ASME, Volume 4, pp 111-118.

Kirkgaard P. H. and Rytter A (1993)

The Use Of Neural Networks For Damage Detection and Location In A Steel Member. Proceedings of the Third International Conference On the Application of Artificial Intelligence In Civil and Structural Engineering.

Loland O and Dodds C. J (1976)

Experiences in Developing and Operating Integrity Monitoring Systems in the North Sea. Proceedings of the Eighth Annual OTC Conference, Volume 2, pp 313-319.

Lowe D (1991)

On the Iterative Inversion of RBF Networks: A Statistical Interpretation. Proceedings of the Second IEE International Conference on Neural Networks, pp 29-33.

Martin J. H (1991)

Inferring Large Dam Behaviour from Measurements and Uncertain Qualitative Knowledge. University Of Bristol PhD thesis.

Matthews J. R (1983)

Acoustic Emission. Gordon and Breach Science, New York.

Nataraja R (1983)

Structural Integrity Monitoring in Real Seas. OTC 4538, Fifteenth Annual Offshore Technology Conference, ASME, Volume 2, pp 221-228.

Smith J. W (1993)

Mechanical Properties of Samples of Structural Steel Affected Severely by Corrosion. University of Bristol Report No. UBCE/JWS/93/01, February.

Szewczyk Z. P and Hajela P (1992)

Damage Detection in Structures Based on Feature-Sensitive Neural Networks. Journal of Computing in Civil Engineering (ASCE), Volume 8 Number 2, pp 163-178.

Vandiver J. K (1975)

Detection of Structural Failure On Fixed Platforms By Measurement Of Dynamic Response. American Society of Mechanical Engineering. Proceedings of the Offshore Technology Conference, Volume 7.

Worden K, Ball A. D and Tomlinson G. R (1993)

Neural Networks For Fault Location. Proceedings of the 11th International Modal Analysis Conference.

Yang J. C. S, Chen J and Dagalakis N. G (1984)

Damage Detection in Offshore Structures by the Random Decrement Technique. Journal of Energy Resources Technology, ASME, Volume 106 Number 1, pp 38-42.

Yang J. C. S, Dagalakis N. G. and Hirt M. (1980)

Application of the Random Decrement Technique In the Detection of an Induced Crack on an Offshore Platform Model. Computational Methods for Offshore Structures (ASME), Editors: Armen H and Stiansen S, New York, pp 55-67.

Yin Z. K, Jun G. A and Wen L. J (1992)

Diagnosis of a Slot Fault on a Frame Structure. Proceedings of the Tenth International Modal Analysis Conference, pp. 549-553.

APPENDIX A

The Peak Interacting Force Between a Linear Elastic Spring and a Mass Resulting from a Dynamic Collision

When a mass, m, travelling with velocity, v, collides with a grounded linear elastic spring of stiffness k, the duration of interaction will be half the period, τ, of oscillation for the combined system provided the mass has sufficient kinetic energy. The time history of the contact force, F, at the mass-spring interface will be half sine shaped,

$$F = F_o \sin \omega t \qquad 0 \le t \le \tau/2 \qquad \text{(A1)}$$

where F_o is the peak force and ω is the angular frequency of the combined system. At time $\tau/2$ the mass will rebound and lose contact with the surface. The strain energy stored in the spring is given by

$$U = \frac{kx^2}{2} \qquad \text{(A2)}$$

where x is the displacement. The mass converges on the spring with velocity, v and therefore has kinetic energy, E_k given by.

$$E_k = \frac{1}{2}mv^2 \qquad \text{(A3)}$$

To find the maximum force the maximum displacement, x_0, must be determined. At this instant all of the kinetic energy of the mass has been used up.

Therefore $$\frac{1}{2}mv^2 = \frac{kx_0^2}{2} \qquad \text{(A4)}$$

Therefore $$x_0 = \sqrt{\frac{mv^2}{k}} \qquad \text{(A5)}$$

It can be readily shown that the natural frequency, ω, of a mass spring system in radians per second is given by,

$$\omega = \sqrt{\frac{k}{m}} \tag{A6}$$

therefore,

$$x_0 = \frac{v}{\omega} \tag{A7}$$

and the maximum force can be found by substituting this result into Hooke's law:

$$F_m = \frac{kv}{\omega} \tag{A8}$$

which on substitution into equation A1 gives the force-time history.

$$F = \frac{kv}{\omega} \sin \omega t \qquad 0 \leq t \leq \tau/2 \tag{A9}$$

APPENDIX B

Data Processing and Classification System

1. System Description

The system consists of four basic modules, the first two perform data processing and analysis whereas the third and fourth perform classification.

The first, 'compress' reads files in the form of two columns of data, each pair of data items being separated by a delimiter such as a space or a comma. This is the typical output format for data acquisition instruments where one column represents the x-axis (for example time or frequency) and the other represents the y-axis (usually amplitude or phase). In order to minimise the required storage space, the x-axis can be removed, provided that the initial value, the interval size and the number of data items are known. 'Compress' also checks for 'spikes' which are abnormally high amplitudes that corrupt the data files.

The compressed files can then be used by the second module, which is multi-functional, called 'impulse'. This converts the dynamic waveforms into feature vectors which are either sampled waveforms (normalised between 0 and 1) or computed quantities sensitive to structural change (the ratio of areas under the frequency spectrum for example). Each component of the feature vector is represented by numbers on a single line preceded by an identifier and separated by white space. The last component is followed by a label that represents the class of the data.

The third module, 'classify', implements the k-nearest neighbour and nearest mean supervised classifiers. Its input is feature vectors composed of computed quantities and its output is the appropriate class label. The fourth module, 'NoveltyNet', implements the unsupervised Probabilistic Resource Allocating Network (PRAN). 'NoveltyNet' ignores the class labels that follow the sampled waveform that form its input. Its output has only two states that indicate whether a feature vector belongs to the parent population ('normal') or whether it does not ('novel'). 'NoveltyNet' can also perform principal component

analysis on the feature vectors. In this case it outputs, for each sampled waveform, the required number of principal components on a single line. It also outputs the mean and standard deviation of each kernel, so that the distribution can be plotted on orthogonal axes. The sampled waveform can also be used by the parallel distributed programming (PDP) commercial software package that implements the back-propagation neural network (McClelland and Rumelhart, 1988).

The layout of the data processing and analysis system is summarised in Figure A1.

2. Operation of the Probabilistic Resource Allocating Network (PRAN) Module

The PRAN (Roberts and Tarrasenko, 1994) is a network that is trained with a constructive algorithm. It can be implemented with standard programming procedures but a large amount of memory would be required because the size of the network is not known before growth. Therefore, it is more efficient to use dynamic variables which allocate the required amount of memory as the network grows.

Each processing unit represents a Gaussian kernel and it is implemented with a record that has six fields (variable names are in italics):

(i) the *mean* (a real variable);

(ii) the *variance* (a real variable);

(iii) the *adaption* parameter (a real variable);

(iv) the *iteration* number (an integer variable);

(v) the *total* response (a real variable) and

(vi) the link to the *next* processing unit (a pointer variable).

The network is initialised with one processing unit by the procedure 'CreateNet'. The mean is set to the first feature vector in the training set and the variance is set to the square of the standard deviation between the components of that feature vector. The adaption

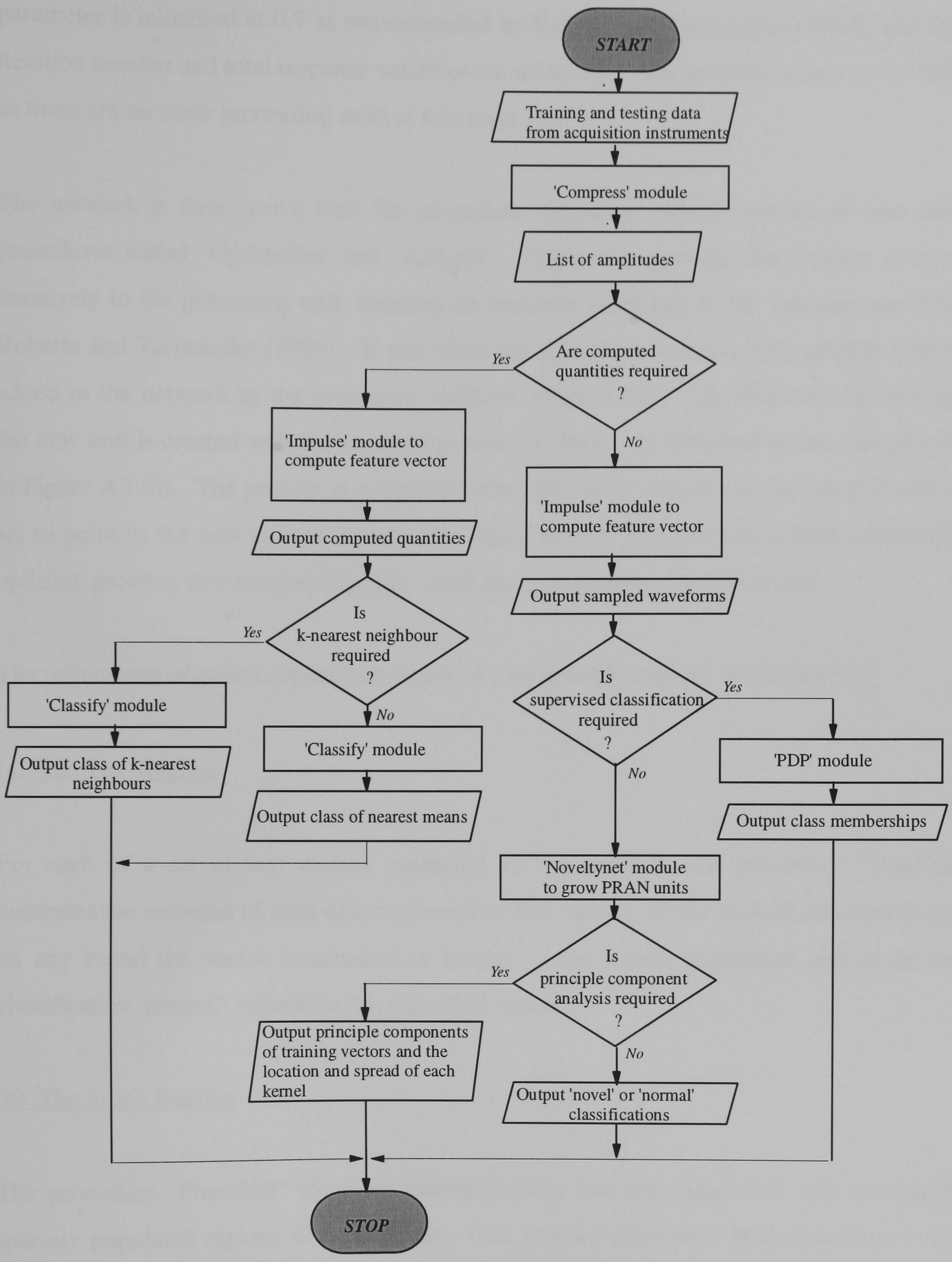

PDP => Parallel Distributed Programming
PRAN => Probabilistic Resource Allocating Network

Figure A1. Data Processing and Classification System

parameter is initialised at 0.7 as recommended by Roberts and Tarrasenko (1994), and the iteration number and total response variables are set to zero. The variable *next* is set to NIL as there are no other processing units at this stage.

The network is then grown with the procedure 'GrowNet' which consists of two sub-procedures called 'UpdateNet' and 'Addunit'. UpdateNet presents the training vectors iteratively to the processing unit, updating its variables according to the formulas given by Roberts and Tarrasenko (1994). If and when the growth criterion is met, another unit is added to the network by the procedure 'Addunit' (Figure A2). The Memory required for the new unit is created with the standard procedure 'New', as indicated by the shaded unit in Figure A2 (b). The process is completed when the *'next'* variable of the original unit is set to point to the new unit, as indicated in Figure A3 (c). The network is then continually updated, growing new units as required , until the convergence criterion is met.

The next course of action depends on which of four possible regimes was selected.

(a) The Test Regime

For each of a set of test vectors presented to the network, the procedure 'TestNet' computes the response of each existing kernel to that vector. If the growth criterion is met on any kernel the vector is assumed to belong to the parent population and given the classification 'normal', otherwise it is classified 'novel'.

(b) The Prune Regime

The procedure 'PruneNet' identifies feature vectors that are associated with kernels in sparsely populated regions of input space. The pruning process is illustrated Figure A3. The kernels are identified by summing up the posterior response of each kernel to the training set and storing the result in the 'total' field. The most sparsely populated kernel is that with the lowest response and this is indicated by the shaded processing unit in Figure A3 (a). The unit that points to the lowest response kernel is then set to point to the same location that the lowest response kernel points to by making the appropriate changes to its *next* variable, this is illustrated in Figure A3 (b). The lowest response kernel is removed

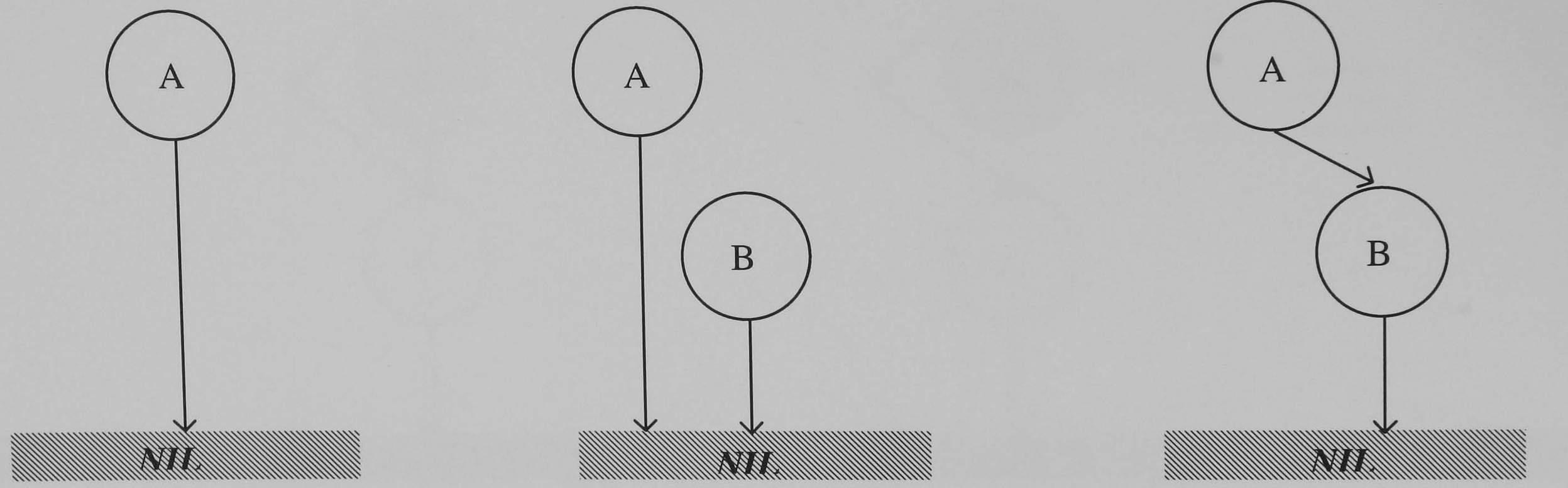

(a) Original Network (b) After creation of new unit (c) After pointer change

A2. Illustration of the Process of Adding a Unit to a One Unit Network

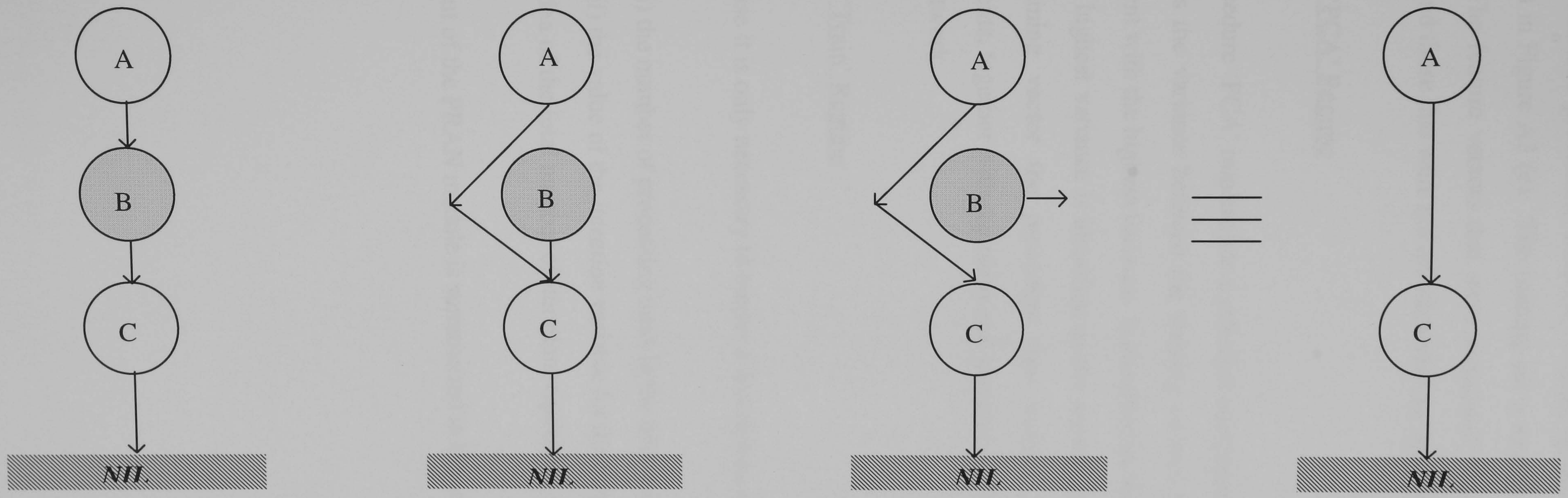

(a) Original Network

(b) After Pointer Change

(c) After Disposing of Memory Occupied by Unwanted Unit

Figure A3. Illustration of Pruning in a Three Unit Network (arrows indicate pointer locations)

with the standard procedure 'Dispose', freeing up the previously occupied memory space, as shown in Figure A3 (c). The training set is then presented to the pruned network once again. The feature vectors that were associated with the pruned kernel are identified as 'novel' and those that were not are identified as 'normal'.

(c) The 'PCA' Regime

The procedure 'PCA' implements a principal component analysis on the training vectors. It computes the variance between the training vectors for each of their components. The component with the highest variance is identified as the first principal component, that with the next highest variance is identified as the second principal component, and so on. For each training vector the procedure then outputs the required number of principal components, together with the mean and standard deviation for each of the processing units in the network.

(d) The 'Train' Regime

In this case it is only necessary to output a description of the network. This includes:

(i) the number of processing units in the network and

(ii) the value of the *iteration* variable for the original network unit. This gives an idea of the total number of iteration required to grow the network.

The layout of the PRAN module is summarised in Figure A4.

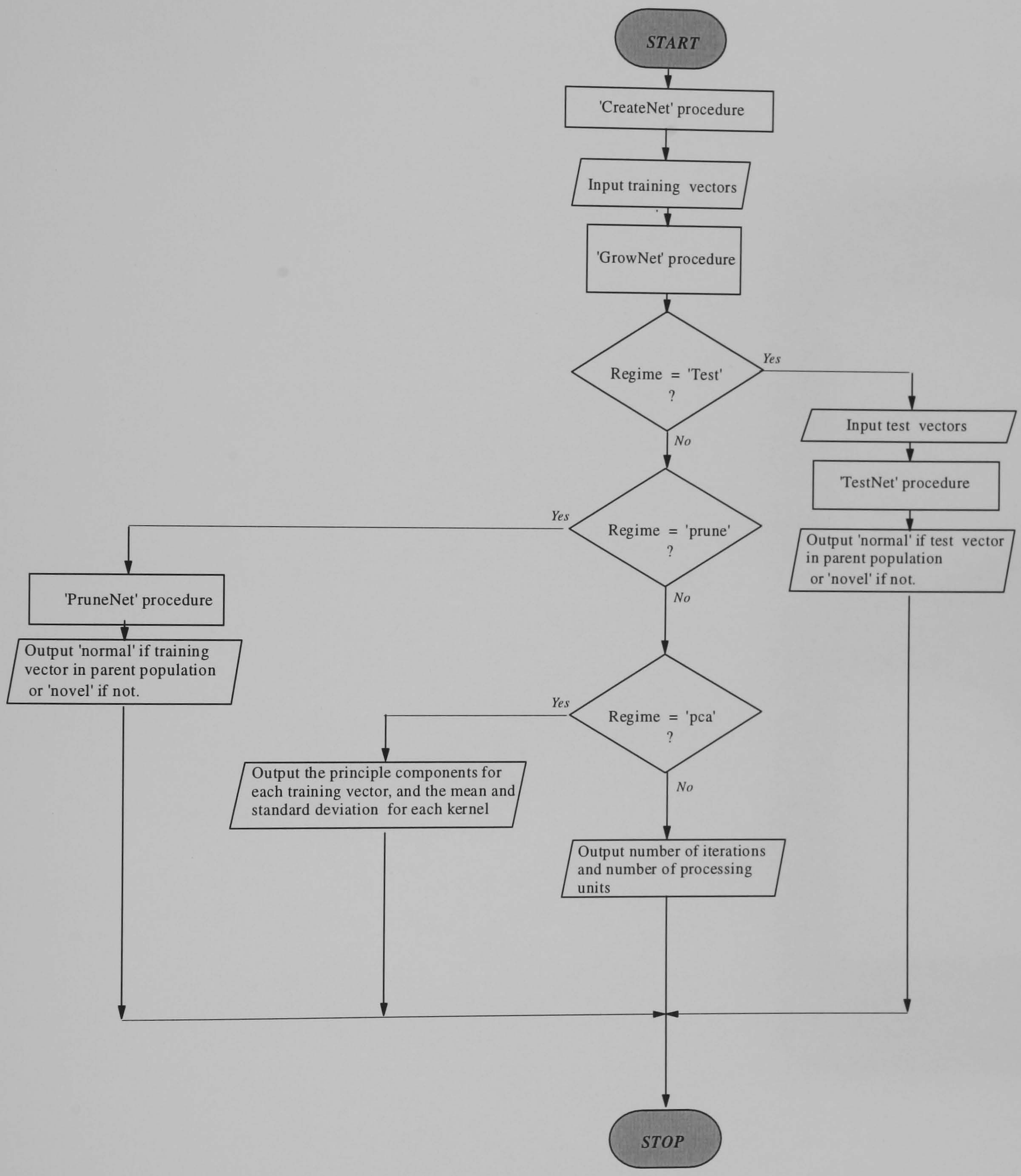

Figure A4. Layout of Probabilistic Resource Allocating Network (PRAN) Module